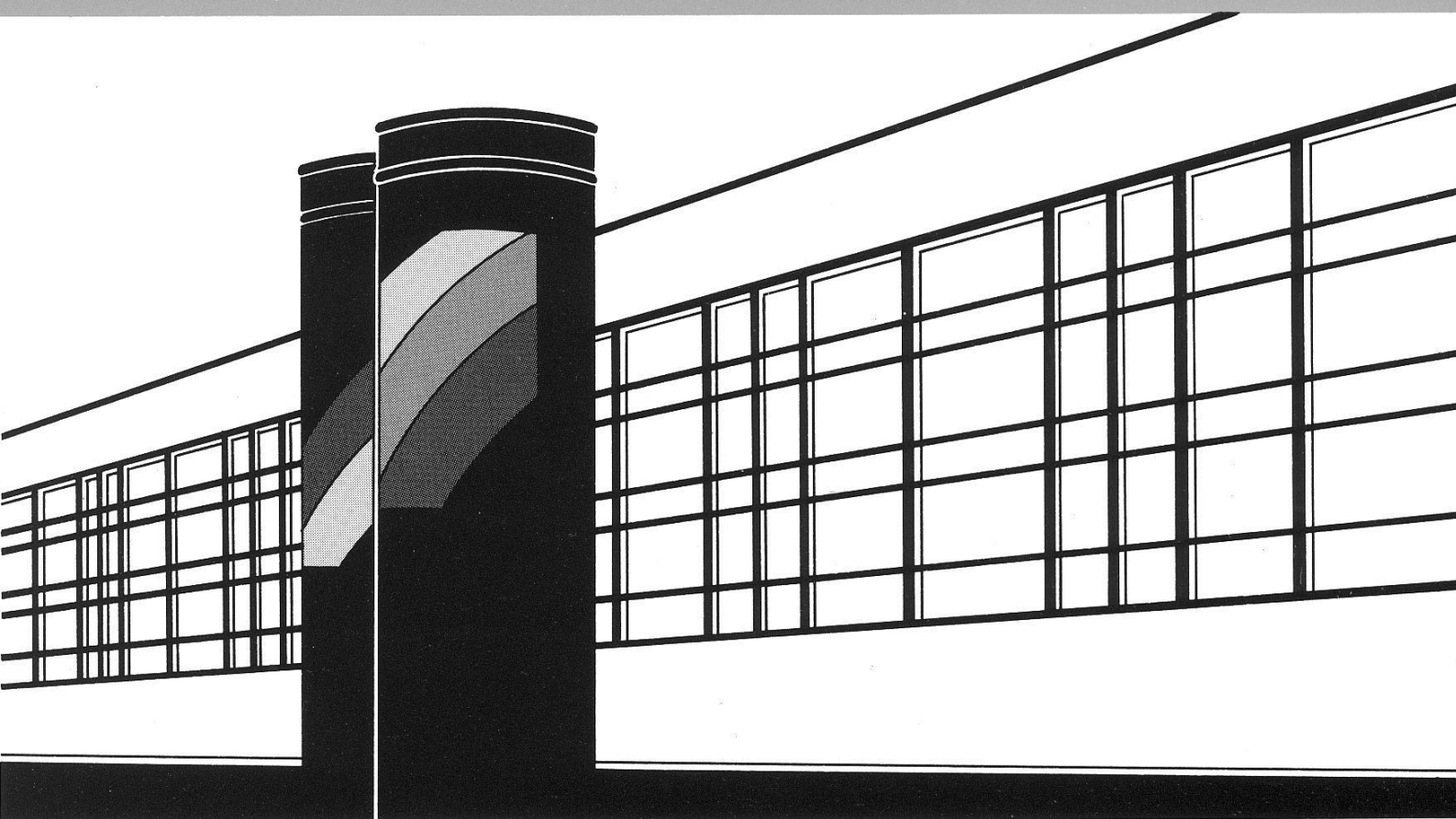


Institut für Wasserbau · Universität Stuttgart

# *Mitteilungen*



Heft 171    Alexandros Papafotiou

Numerical Investigations of the Role of  
Hysteresis in Heterogeneous Two-Phase  
Flow Systems

# **Numerical Investigations of the Role of Hysteresis in Heterogeneous Two-Phase Flow Systems**

Von der Fakultät Bau- und Umweltingenieurwissenschaften der  
Universität Stuttgart zur Erlangung der Würde eines  
Doktor-Ingenieurs (Dr.-Ing.) genehmigte Abhandlung

Vorgelegt von  
**Alexandros Papafotiou**  
aus Heraklion, Griechenland

Hauptberichter: Prof. Dr.-Ing. Rainer Helmig  
Mitberichter: Prof. Dr. Hannes Flühler  
PD Dr. rer.nat Insa Neuweiler

Tag der mündlichen Prüfung: 25. Februar 2008

Institut für Wasserbau der Universität Stuttgart  
2008



Heft 171    Numerical Investigations of the  
Role of Hysteresis in  
Heterogeneous Two-Phase  
Flow Systems

von  
Dr.-Ing.  
Alexandros Papafotiou

**D93 Numerical Investigations of the Role of Hysteresis in Heterogeneous Two-Phase Flow Systems**

Titelaufnahme der Deutschen Bibliothek

Papafotiou, Alexandros:  
Numerical Investigations of the Role of Hysteresis in Heterogeneous Two-Phase Flow Systems / von Alexandros Papafotiou. Institut für Wasserbau, Universität Stuttgart. - Stuttgart: Inst. für Wasserbau, 2008  
  
(Mitteilungen / Institut für Wasserbau, Universität Stuttgart: H. 171)  
Zugl.: Stuttgart, Univ., Diss., 2008)  
ISBN 3-933761-75-1  
NE: Institut für Wasserbau <Stuttgart>: Mitteilungen

Gegen Vervielfältigung und Übersetzung bestehen keine Einwände, es wird lediglich um Quellenangabe gebeten.

Herausgegeben 2008 vom Eigenverlag des Instituts für Wasserbau  
Druck: Document Center S. Kästl, Ostfildern

# Acknowledgement

This dissertation was written during my employment time as a research assistant at the Department of Hydromechanics and Modeling of Hydrosystems of the Institute of Hydraulic Engineering (IWS) at the Universität Stuttgart in Germany. A significant part of the work presented here was carried out within the framework of the project 'First-principle-based Modeling of Transport in Unsaturated Media' (FIMOTUM), financed by the German Research Foundation (DFG).

Firstly, and most importantly, I would like to thank my supervisor and chief examiner Prof. Dr.-Ing. Rainer Helmig, Head of the Department of Hydromechanics and Modeling of Hydrosystems in IWS. I would like to express my sincere and deep gratitude for all the time and energy he devoted to my supervision, the valuable interactions we had and for teaching me how to work in a structured and scientific way. His constant support, ideas and inspiration kept me motivated even during the hardest phases of these last three years.

I would also like to thank Prof. Dr. Hannes Flühler, who as a co-supervisor and my first examiner provided me with valuable feedback both during the course of my research work, as well as on the final dissertation. His vast research experience and scientific insight made our discussions a very important learning experience for me. I am very grateful for the very fruitful collaboration we had these three years.

Last but surely not least I would like to express my sincere thanks to PD Dr. rer.nat. Insa Neuweiler, who contributed not only as my second examiner, but also by very closely supervising my work and providing continuous guidance and consulting. I sincerely thank her for her support, her ideas and her help.

My acknowledgement is also directed at all the partners within the FIMOTUM project. A very special thanks to Peter Lehmann, Jonas Tölke, Benjamin Ahrenholz, Joris Schaap and Andre Peters, who have spent a lot of effort and time on the experiments, measurements and computations that contributed to this work. I would also like to thank Yvonne Lins for her enormous effort on the experiments that formed the basis for the model verification in this work.

I would also like to thank my colleagues from IWS for making my time at the

institute not only pleasant but also a learning experience. Their cooperative spirit, friendly attitude and the fact that they would always volunteer to help are qualities I will remember and take with me as I leave Stuttgart. Naturally, there are some who earn special thanks. Hartmut Eichel and Sabine Manthey were ideal colleagues as we worked close for FIMOTUM. Hussam Sheta spent a lot of hours during my first months at work explaining me aspects of MUFTE-UG and of the implementation of hysteresis. Mia Süß was my first 'colleague' when I still worked for her and I believe nothing would have started without her. A very warm thanks goes of course to Prudence Lawday, our what-would-we-do-without-you English secretary, who welcomed me with her smile even after entering her office endless times with a pile of papers asking for help. Melanie Darcis and Anozie Ebigbo have always been there to help and I owe them a lot. Also, many thanks to Sandra Hölzemann for helping me with the German grammar ;).

My time in Stuttgart doing a PhD would definitely not be the same without the friends I had there and I want to thank them for everything (Mitsos, Kike, Costas, Fiko, Electra, Aco, Irena, Moutas, Alex, Paula..).

Finally, I want to thank my parents, Apostolos and Vasiliki, my brother Giorgos and his wife Theodosia but also all my family from Crete and Thessaloniki for all their love and their constant support all these years I have been away.

*"Ω ΠΑΟΚαρα ειχα δευτρα στα Ζωνιανα.."*

*Θυρα 4.*

# Contents

<b>Notation</b>	<b>XI</b>
<b>Abstract</b>	<b>XV</b>
<b>Zusammenfassung</b>	<b>XVII</b>
<b>1 Introduction</b>	<b>1</b>
1.1 Motivation . . . . .	1
1.2 Spatial scales in porous media . . . . .	7
1.2.1 Definition of spatial scales . . . . .	7
1.2.2 Continuum consideration for porous media on the pore scale	12
1.3 Objective and structure of the thesis . . . . .	13
<b>2 Physical and mathematical model concept</b>	<b>16</b>
2.1 Basic definitions . . . . .	16
2.2 Phase properties . . . . .	17
2.3 Capillary pressure . . . . .	19
2.3.1 Capillary pressure on the pore scale . . . . .	19
2.3.2 Capillary pressure on the local scale . . . . .	23
2.4 The influence of heterogeneities . . . . .	27
2.5 The Darcy law . . . . .	28
2.6 Mathematical description of two-phase flow in porous media . . .	31
<b>3 Capillary hysteresis</b>	<b>33</b>
3.1 Hysteresis on the pore scale . . . . .	34
3.2 Hysteresis on the local scale . . . . .	37
3.2.1 The play-type $p_c$ - $S_w$ hysteresis . . . . .	39
3.2.2 $p_c$ - $S_w$ hysteresis from PARKER AND LENHARD . . . . .	41



<b>4</b>	<b>Numerical model</b>	<b>46</b>
4.1	Spatial and temporal discretization . . . . .	46
4.2	The Interface Condition . . . . .	51
4.3	Numerical implementation of hysteresis . . . . .	53
4.3.1	Implementation in the PPS approach . . . . .	53
4.3.2	Combination of hysteresis with the PPSIC approach . . . . .	55
<b>5</b>	<b>Model verification</b>	<b>58</b>
5.1	Description of the 1-D experiment . . . . .	58
5.2	Numerical simulation . . . . .	60
5.3	Comparison of measurements to simulation results using $p_c-S_w$ measured in the transient state experiment . . . . .	63
5.3.1	Simulation with hysteresis not included . . . . .	64
5.3.2	Simulation with play-type hysteresis included . . . . .	66
5.3.3	Simulation including hysteresis from PARKER AND LENHARD . . . . .	69
5.4	Hysteresis from a simple multistep experiment . . . . .	72
5.5	Synopsis and remarks . . . . .	76
<b>6</b>	<b>From the pore scale to the local scale: numerical simulations of drainage and imbibition in 3-D heterogeneous porous media</b>	<b>78</b>
6.1	Description of experiment . . . . .	80
6.2	Hydraulic properties determined on the local scale . . . . .	84
6.3	Hydraulic properties determined on the pore scale . . . . .	87
6.4	Comparison of hydraulic properties (local scale-pore scale) . . . . .	89
6.4.1	Capillary pressure-saturation . . . . .	90
6.4.2	Permeability . . . . .	93
6.5	Numerical simulation . . . . .	93
6.5.1	Simulation setup . . . . .	94
6.5.2	Influence of hydraulic properties . . . . .	96
6.6	Comparison of simulation results to the experiment . . . . .	100
6.6.1	Simulation A: hydraulic properties determined on the local scale . . . . .	101
6.6.2	Simulation B: hydraulic properties determined on the pore scale . . . . .	104
6.6.3	Simulation C: fitted permeability . . . . .	106
6.7	Synopsis and remarks . . . . .	109
<b>7</b>	<b>Synopsis, conclusions and outlook</b>	<b>113</b>
<b>A</b>	<b>. Comparison of simulation results to the 1-D transient experiment</b>	<b>121</b>

# List of Figures

1	Infiltration and spreading of two hydrophobic substances in a porous medium after MACKAY AND CHERRY (1989) [67]. Non-Aqueous Phase Liquids are distinguished between those lighter than water (LNAPL's) and those heavier than water (DNAPL's). . . . .	2
2	Hysteresis in the capillary pressure-saturation relationship. . . . .	3
3	Consideration of water as a continuum. . . . .	7
4	Definition of density as a continuum property and transition from the molecular to the continuum consideration. . . . .	8
5	Typical spatial scales involved in groundwater flow. . . . .	9
6	Porosity and definition of the REV after BEAR (1972) [9]. . . . .	11
7	Transition from the pore scale to the local and the field scale. . . . .	12
8	Consideration of fluid distribution on the pore scale and on the local scale. . . . .	17
9	Interfacial forces. . . . .	19
10	Surface tensions exerted by the three interfaces. The contact angle $\omega$ adjusts itself such that the three tensions balance each other. . . . .	21
11	Capillary rise $h_c$ in a cylindrical capillary tube with radius $r$ . . . . .	22
12	Distribution of water (wetting phase) and air (non-wetting phase) on the pore scale. . . . .	23
13	Capillary pressure-saturation relationship for a simple bundle of capillary tubes. . . . .	24
14	Different saturations of water (wetting phase) and air (non-wetting phase) on the local scale correspond to different capillary pressures. . . . .	25
15	Capillary pressure-saturation from BROOKS AND COREY (1964) [13] and from VAN GENUCHTEN (1980) [99]. . . . .	26
16	Phase behavior at the boundary between a coarse and a fine sand. . . . .	27
17	Derivation of different saturations across the boundary between a coarse and a fine sand based on the $p_c$ - $S_w$ curves. . . . .	28

18	Relative permeability-saturation from MUALEM/VAN GENUCHTEN. . . . .	30
19	Contact angle for drainage and imbibition. . . . .	35
20	The inkbottle effect. . . . .	35
21	The snap-off effect. . . . .	36
22	The by-passing effect. . . . .	36
23	Hysteresis in the capillary pressure-saturation relationship. . . . .	38
24	Play-type hysteresis in the VAN GENUCHTEN (left) and the BROOKS AND COREY (right) parameterization. . . . .	40
25	Phase entrapment in the $p_c-\bar{S}_w$ curve. . . . .	42
26	Hysteresis in the $p_c-\bar{S}_w$ curve. . . . .	43
27	An example for the formation of a scanning curve using the scaling hysteresis concept from PARKER AND LENHARD. . . . .	45
28	Finite elements and the resulting sub-control volume. . . . .	47
29	Finite elements and the resulting sub-control volume (from JAKOBS (2004) [48]). . . . .	48
30	Node-centered FV method using Full Upwinding [HELMIG (1997) [41]]. . . . .	49
31	Grid consideration in the classical BOX approach and the Interface Condition approach from JAKOBS (2004) [48]. . . . .	52
32	$p_c-S_w$ hysteresis in the PPS and the PPSIC approach. . . . .	56
33	Setup of 1-D transient experiment. . . . .	59
34	Pictures of the tensiometer (left) and the TDR (right) sensors from LINS ET AL. (2007) [66]. . . . .	59
35	Domain and boundary conditions in the numerical simulation. Water outflow and inflow depends only on the Neumann boundary at the bottom. . . . .	61
36	Point 2: saturation (left) and water pressure (right), comparison measurement and simulation with hysteresis not included. . . . .	64
37	Point 3: saturation (left) and water pressure (right), comparison measurement and simulation with hysteresis not included. . . . .	64
38	Point 4: saturation (left) and water pressure (right), comparison measurement and simulation with hysteresis not included. . . . .	65
39	Capillary pressure-saturation at point 2 and point 4: comparison measurement and simulation with hysteresis not included. . . . .	65
40	Point 2: saturation (left) and water pressure (right), comparison measurement and simulation with play-type hysteresis included. . . . .	67

41	Point 3: saturation (left) and water pressure (right), comparison measurement and simulation with play-type hysteresis included. . . . .	67
42	Point 4: saturation (left) and water pressure (right), comparison measurement and simulation with play-type hysteresis included. . . . .	68
43	Capillary pressure-saturation at point 2 and point 4: comparison measurement and simulation with play-type hysteresis included. . . . .	68
44	Point 2: saturation (left) and water pressure (right), comparison measurement and simulation including hysteresis from PARKER AND LENHARD. . . . .	70
45	Point 3: saturation (left) and water pressure (right), comparison measurement and simulation including hysteresis from PARKER AND LENHARD. . . . .	70
46	Point 4: saturation (left) and water pressure (right), comparison measurement and simulation including hysteresis from PARKER AND LENHARD. . . . .	71
47	Capillary pressure-saturation at point 2 and point 4: comparison measurement and simulation including hysteresis from PARKER AND LENHARD. . . . .	71
48	Schematical setup of a pressure/suction cell. . . . .	73
49	Pressure-saturation measurements for drainage and imbibition in the multistep experiments from LINS ET AL. (2007) [66]. The VAN GENUCHTEN fit is also illustrated. . . . .	73
50	Point 2: saturation (left) and water pressure (right), comparison measurement and simulation using the $p_c-S_w$ measured with the multistep experiments. . . . .	74
51	Point 3: saturation (left) and water pressure (right), comparison measurement and simulation using the $p_c-S_w$ measured with the multistep experiments. . . . .	75
52	Point 4: saturation (left) and water pressure (right), comparison measurement and simulation using the $p_c-S_w$ measured with the multistep experiments. . . . .	75
53	Capillary pressure-saturation at point 2 and point 4: comparison measurement and simulation using the $p_c-S_w$ measured with the multistep experiments. . . . .	76
54	Strategy for comparing predictions made in two-phase flow in heterogeneous media with local-scale and pore-scale hydraulic properties. . . . .	79
55	Arrangement of the coarse sand blocks in the column (from SCHAAP (2005) [87]). . . . .	81

56	Tomography images of the first (left) and second (right) drainage step (from SCHAAP (2005) [87]). Dark colors relate to higher water saturations. . . . .	82
57	Measured saturations for 1st and 2nd step (drainage). . . . .	83
58	Measured saturations for 4th and 5th step (imbibition). . . . .	83
59	Schematical setup of the multistep outflow/inflow experiments [from AHRENHOLZ ET AL. (2007) [3]]. . . . .	84
60	Measured and fitted cumulative outflow and pressure head data of the multistep outflow experiment for the coarse and the fine sand from AHRENHOLZ ET AL. (2007) [3]. The lower boundary condition (l.b.) is also indicated. . . . .	85
61	Cross-sections from the coarse and the fine sand 0.44 [cm <sup>3</sup> ] cubes. . . . .	87
62	$p_c$ - $S_w$ calculated with LB for the coarse and fine sand. The fit made with the VAN GENUCHTEN model is provided in the right image. . . . .	88
63	Coarse sand (left) and fine sand (right) hysteretic $p_c$ - $S_w$ relationships determined on the local scale and on the pore scale. . . . .	90
64	Grid considerations (in 2-D projections) for simulating the heterogeneous experiment with the classical BOX approach (left) and using the interface condition (right). . . . .	94
65	Heterogeneous structure and boundary conditions. Black color represents the fine sand and white color the coarse sand. . . . .	95
66	Influence of absolute permeability on the water outflow and inflow during drainage and imbibition in the heterogeneous column. . . . .	98
67	Influence of VAN GENUCHTEN drainage $\alpha$ and $n$ on the water outflow and inflow during drainage and imbibition in the heterogeneous column. . . . .	98
68	Influence of VAN GENUCHTEN imbibition $\alpha$ and $n$ on the water outflow and inflow during drainage and imbibition in the heterogeneous column. . . . .	99
69	Simulation A: simulated outflow and inflow for the entire simulation and outflow rate for the 1st and 2nd step (drainage). . . . .	102
70	Simulation A: measured and simulated saturation profiles for 1st and 2nd step (drainage). . . . .	102
71	Simulation A: measured and simulated saturation profiles for 4th and 5th step (imbibition). . . . .	102
72	Evolution of the fine sand $p_c$ - $S_w$ relationship, as observed on a node near the bottom boundary of the model domain. . . . .	104
73	Simulation B: simulated outflow and inflow for the entire simulation and outflow rate for the 1st and 2nd step (drainage). . . . .	105

---

74	Simulation B: measured and simulated saturation profiles for 1st and 2nd step (drainage). . . . .	105
75	Simulation B: measured and simulated saturation profiles for 4th and 5th step (imbibition). . . . .	105
76	Simulation C: simulated outflow and inflow for the entire simulation and outflow rate for the 1st and 2nd step (drainage). . . . .	107
77	Simulation C: measured and simulated saturation profiles for 1st and 2nd step (drainage). . . . .	107
78	Simulation C: measured and simulated saturation profiles for 4th and 5th step (imbibition). . . . .	107
79	Simulation C: comparison of predicted (left) and measured (right) saturation distribution after the second drainage at layer 7. The simulation with the fitted permeabilities produces variations of the captured saturations at the time of tomography. . . . .	110
80	Simulation C: comparison of predicted (left) and measured (right) saturation distribution after the second drainage at layer 6. The simulation with the fitted permeabilities produces variations of the captured saturations at the time of tomography. . . . .	110
81	Simulated outflow and outflow rate for the 1st and 2nd step (drainage), including low-permeable material interfaces. . . . .	111
82	Saturation and pressure at point 1: comparison measurement and simulation with hysteresis not included. . . . .	122
83	Saturation and pressure at point 1: comparison measurement and simulation with play-type hysteresis included. . . . .	122
84	Saturation and pressure at point 1: comparison measurement and simulation including hysteresis from PARKER AND LENHARD. . .	122

# List of Tables

2	Outflow and inflow rates used to induce drainage and imbibition.	60
3	Phase properties. . . . .	60
4	Hydraulic properties for drainage and imbibition. . . . .	63
5	Hydraulic properties measured with the multistep experiment for drainage and imbibition. . . . .	74
6	Drainage, imbibition and tomography times and measured outflow or inflow during the tomographies. . . . .	81
7	Hydraulic properties determined for the coarse sand (cs) on the local scale with the multistep outflow/inflow experiments. . . . .	86
8	Hydraulic properties determined for the fine sand (fs) on the local scale with the multistep outflow/inflow experiments. . . . .	86
9	Hydraulic properties determined for the coarse sand (cs) on the pore scale with image analysis and lattice Boltzmann numerical simulations. . . . .	89
10	Hydraulic properties determined for the fine sand (fs) on the pore scale with image analysis and lattice Boltzmann numerical simulations. . . . .	89
11	Physical properties of heavy water and air. . . . .	96
12	Variation of hydraulic properties given for the fine sand (fs) and the coarse sand (cs) for demonstrating numerical simulations. . . . .	97

# Notation

The following table shows the significant symbols used in this work. Local notations are explained in the text.

Symbol	Definition	Dimension
<b>Greek Letters:</b>		
$\alpha$	VAN GENUCHTEN parameter	[1/Pa]
$\beta$	slope parameter for linear scanning curves	[-]
$\gamma_{ij}^{FUB}$	transmissivity integral	[-]
$\Gamma$	boundary between two sub-domains	[-]
$\Gamma_{\alpha,D}$	part of a domain comprising Dirichlet boundary conditions	[-]
$\Gamma_{\alpha,N}$	part of a domain comprising Neumann boundary conditions	[-]
$\Gamma_{B_i}$	integration path along the boundary of box $B_i$	[-]
$\delta_{\alpha w}$	<i>Kronecker</i> -delta (with $\alpha \in \{w, n\}$ )	[-]
$\Delta t$	time step	[s]
$\Delta_{start}$	starting time step	[s]
$\Delta_{max}$	maximum time step	[s]
$\Delta_{min}$	minimum time step	[s]
$\Delta x$	element width	[m]
$\epsilon$	measurement error	[m]
$\eta_i$	set of all neighboring nodes of node $i$	[-]
$\theta$	wetting fluid content	[-]
$\lambda$	BROOKS AND COREY parameter	[-]
$\lambda_\alpha$	mobility of phase $\alpha$	[(m s)/kg]
$\lambda_{\alpha ij}^{FUB}$	upwind mobility	[(m s)/kg]
$\mu_\alpha$	dynamic fluid viscosity of phase $\alpha$	[kg/(m s)]



$\rho_\alpha$	fluid density of phase $\alpha$	[kg/m <sup>3</sup> ]
$\sigma$	interfacial tension	[N/m]
$\sigma$	Euclidean norm of interfacial tension	[N/m]
$\tau$	tortuosity	[ - ]
$\phi$	porosity	[ - ]
$\Phi_\alpha$	volume fraction of phase $\alpha$	[ - ]
$\psi_{\alpha i}$	total potential of phase $\alpha$ at node $i$	[ - ]
$\omega$	contact angle	[ ° ]
$\Omega$	objective function	[ - ]

**Latin Letters:**

$B_i$	control volume or box for node $\nu_i$	[ - ]
$ B_i $	area of 2-D control volume	[m <sup>2</sup> ]
$ B_i $	volume of 3-D control volume	[m <sup>3</sup> ]
$\mathbf{b}$	parameter vector	[ - ]
$b_i^k$	sub-control volume for node $\nu_i$ and element $e_k$	[ - ]
$\partial B_i$	boundary of box $B_i$	[ - ]
$cs$	coarse sand	[ - ]
$E$	set of elements in finite element mesh	[ - ]
$E_i$	set of elements connected to node $\nu_i$	[ - ]
$e_k$	element of the finite element mesh	[ - ]
$f$	function	[ - ]
$fs$	fine sand	[ - ]
$\mathbf{g}$	vector of gravitational acceleration $(0, 0, -g)^T$	[m/s <sup>2</sup> ]
$g$	(scalar) gravitational acceleration	[m/s <sup>2</sup> ]
$G$	solution domain	[ - ]
$\partial G$	boundary of solution domain	[ - ]
$h$	piezometric head	[m]
$h_c$	capillary rise	[m]
$Ih$	index for hysteresis	[ - ]
$k_{r\alpha}$	relative permeability for phase $\alpha$	[ - ]
$\mathbf{K}$	tensor of absolute permeability	[m <sup>2</sup> ]
$K$	hydraulic conductivity function	[m/s]
$L$	hysteresis loop index	[ - ]
$LB$	lattice-Boltzmann	[ - ]
$m$	VAN GENUCHTEN parameter	[ - ]
$m_{\alpha i}$	flow of phase $\alpha$ over the Neumann boundary $\partial B_i \cap \Gamma_{\alpha, N}$	[kg / (m <sup>2</sup> s)]

$n$	VAN GENUCHTEN parameter	[ - ]
$\mathbf{n}$	outer normal vector of $\partial G$	[ - ]
$N_i$	basis functions for node $i$	[ - ]
$p_c$	capillary pressure	[Pa]
$p_{c,min}^i$	minimal capillary pressure for node $\nu_i$	[Pa]
$p_{c,1}^i$	starting reversal capillary pressure at node $\nu_i$	[Pa]
$p_{c,2}^i$	ending reversal capillary pressure at node $\nu_i$	[Pa]
$p_e$	entry pressure	[Pa]
$p_d$	displacement pressure	[Pa]
$p_n$	pressure of the non-wetting phase	[Pa]
$p_w$	pressure of the wetting phase	[Pa]
$PPS$	phase pressure saturation	[ - ]
$PPSIC$	phase pressure saturation interface condition	[ - ]
$q_\alpha$	source or sink of phase $\alpha$ in the domain	[m <sup>3</sup> /(m <sup>3</sup> s)]
$r$	radius	[m]
$S_\alpha$	saturation of phase $\alpha$	[ - ]
$S_\alpha^{i,k}$	virtual saturation of phase $\alpha$ at node $\nu_i$ relating to element $e_k$	[ - ]
$S_{\alpha,1}^i$	starting reversal saturation of phase $\alpha$ at node $\nu_i$	[ - ]
$S_{\alpha,2}^i$	ending reversal saturation of phase $\alpha$ at node $\nu_i$	[ - ]
$S_{\alpha,1}^{i,k}$	starting reversal virtual saturation of phase $\alpha$ at node $\nu_i$	[ - ]
$S_{\alpha,2}^{i,k}$	ending reversal virtual saturation of phase $\alpha$ at node $\nu_i$	[ - ]
$S_{\alpha r}$	residual saturation of phase $\alpha$	[ - ]
$\bar{S}_\alpha$	effective saturation	[ - ]
$\bar{\bar{S}}_\alpha$	apparent saturation	[ - ]
$S_{nt}$	trapped non-wetting phase saturation	[ - ]
$S_w^{switch}$	saturation at switches between drainage and imbibition	[ - ]
$t$	time	[s]
$T$	tensiometer	[ - ]
$TDR$	time domain reflectometry sensor	[ - ]
$u$	unknown variable	[ - ]
$\mathbf{u}_\alpha$	Darcy velocity of phase $\alpha$	[m/s]
$\mathbf{v}_\alpha$	average velocity of phase $\alpha$	[m/s]
$\mathbf{v}_i$	node of the finite element mesh	[ - ]
$V$	control volume	[m <sup>3</sup> ]
$w$	weighting factor	[ - ]
$W_i$	weighting function for node $i$	[ - ]

---

$\mathbf{x}^k$	barycenter of the element $e_k$	[ - ]
$z$	elevation head	[m]
$z_i$	geodetic height of node $i$	[m]

**Subscripts:**

$\alpha$	phase
$n$	non-wetting phase
$p$	pressure
$play$	value on play-type scanning curve
$Q$	outflow/inflow
$w$	wetting phase

**Superscripts:**

$di$	switching drainage to imbibition
$dr$	drainage
$id$	switching imbibition to drainage
$im$	imbibition
$int$	value at interface
$MDC$	main drainage curve
$MIC$	main imbibition curve
$n$	time step
$p$	value projected on the main drainage/imbibition curve
$up$	(fully) upwind weighting method

# Abstract

Various groundwater applications often involve the flow of two immiscible fluids in heterogeneous porous media. In problems that involve the assessment of travel times of hazardous substances in the unsaturated zone or monitoring and predicting the fate of groundwater contaminations, efficient tools and approaches need to be developed to achieve accurate predictions of two-phase flow behavior in heterogeneous porous media. However, this is not an easy task, as heterogeneities -observed on different spatial scales- have a strong influence on the distribution of the fluid phases and therefore form a significant source of uncertainty. Moreover, the prediction of two-phase flow in heterogeneous porous media becomes complicated through alternating drainage and imbibition conditions taking place in the complex heterogeneous pore structure that lead to hysteresis effects in the capillary pressure-saturation relationship. Numerical simulations are widely used to predict hysteretic two-phase flow in heterogeneous porous media in lab or field applications. This approach, however, demands good knowledge on the hydraulic properties of the materials that form the heterogeneous structures involved in the application. Traditionally, the hydraulic properties and the hysteretic behavior of porous media are empirically determined on the local scale with lab experiments conducted on material samples. On the other hand, alternative methods suggest the direct determination of hydraulic properties, including hysteretic capillary pressure-saturation relationships, from a pore-scale consideration. This is done using available information on the pore structure of a material. Nevertheless, it remains unclear how accurate predictions can be in problems of hysteretic two-phase flow in porous media, even when advanced state-of-the-art methods are used.

The first part of this thesis deals with the implementation of two hysteresis concepts in a numerical model for the simulation of two-phase flow in heterogeneous porous media. Special attention is given on the combination of the hysteresis concepts with a capillary interface condition for the treatment of material interfaces and the approximation of saturation discontinuities due to heterogeneities. This provides an efficient and consistent approach for the prediction of hysteretic two-phase flow in heterogeneous porous media.

In the second part, predictions made with the numerical implementations of the hysteresis concepts are compared to measurements from a 1-D monitored transient experiment, that involves successive alternating drainage and imbibition conditions. Conclusions related to the importance of hysteresis and the possibilities of the applied hysteresis concepts are drawn. Furthermore, the comparative study presents remarks on the beneficial combination of different approaches – from the modeling and the experimental viewpoint– that lead to reliable predictions on hysteretic two-phase flow.

The third part focuses on the comparison of predictions of two-phase drainage and imbibition in heterogeneous porous media to an experimentally measured hysteretic flow process, using hydraulic properties determined on the one hand on the local scale and on the other hand on the pore scale. In this case, numerical simulations of drainage and imbibition are compared to measurements made in a 3-D heterogeneous structure. The hydraulic properties that are used as input for the numerical simulations are determined with two approaches:

- On the local scale with multistep outflow/inflow experiments.
- On the pore scale with advanced image analysis and pore-scale flow simulations.

The comparative study in this case reveals the possibilities for predictions of hysteretic two-phase flow made with the different approaches for the determination of the hydraulic properties (local-scale and pore-scale approach), indicates sensitivities in the hydraulic properties determined on different scales, reveals the significant influence of material interfaces in heterogeneous structures and finally establishes the apparent temporal- and spatial-scale dependency of non-wetting phase trapping effects during imbibition processes. Conclusions related to the observed hysteresis are drawn considering the assumptions and the conceptual differences involved in the different approaches. Finally the comparison between simulations and experiment triggers a discussion on the potentials of our modeling approaches in the case of heterogeneous structures, shows how one needs to approach applications of hysteretic two-phase flow in heterogeneous porous media and what aspects must be taken into account when dealing with different scales.

# Zusammenfassung

Grundwasser ist weltweit die wichtigste Quelle für Trinkwasser sowie für Wasser für die Landwirtschaft und die Industrie. Gleichzeitig hat Grundwasser eine besondere Funktion im Wasserkreislauf, die es lebenswichtig für verschiedene Natur- und Hydrosysteme macht. Allerdings sind Grundwassersysteme äußerst empfindlich und werden wesentlich von menschlichen Aktivitäten beeinflusst. Vor allem seit der industriellen Revolution verursachen die nicht fachgerechte Entsorgung von zahlreichen schädlichen synthetischen Chemikalien aus der Industrie und der übermäßige Gebrauch von Pestiziden im Ackerbau langanhaltende Kontaminationen im Grundwasser. Diese stellen erhebliche Gesundheitsgefährdungen dar. Infolgedessen reagierten in den letzten Jahren die Öffentlichkeit und die Wirtschaft besorgt über die Konsequenzen der Grundwasserkontaminationen.

Folglich richten sich Forschungsaktivitäten auf die Entwicklung von effizienten Strategien zur Beobachtung und Sanierung von Grundwasserkontaminationen. Solche Fragestellungen behandeln oft Strömungen von zwei nicht-mischbaren Fluiden in heterogenen porösen Medien. Ziel dabei ist es, die Schadstoffe langfristig unterhalb bestimmter gesundheitsgefährdender Grenzen zu halten. Dies erfordert effiziente Ansätze und Werkzeuge, die präzise Prognosen der Zweiphasenströmungen in heterogenen porösen Medien liefern können. Dies ist keine leichte Aufgabe. Heterogenitäten üben einen starken Einfluss auf die Phasenverbreitung im Untergrund aus und stellen daher einen maßgeblichen Unsicherheitsfaktor dar. Außerdem wird die Beschreibung der Zweiphasenströmung in heterogenen porösen Medien dadurch besonders kompliziert, dass die abwechselnde Drainage- und Imbibitionsbedingungen zu Hysterese-Effekten in der Kapillardruck-Sättigungsbeziehung unterworfen sind.

Numerische Simulationen werden zunehmend in Labor- oder Feldanwendungen eingesetzt, um Zweiphasenströmungen in heterogenen porösen Medien unter Berücksichtigung von Hysterese-Effekten zu prognostizieren. Solche Ansätze erfordern jedoch gute Kenntnisse der hydraulischen Eigenschaften der Materialien, die in den betrachteten heterogenen Strukturen zu finden sind.

Es bleibt allerdings unklar, wie genau Prognosen sein können, auch wenn hochentwickelte und präzise Methoden zur Bestimmung der hydraulischen Eigenschaften eingesetzt werden.

Bei der traditionellen Betrachtungsweise werden hydraulische Eigenschaften auf der lokalen Skala durch Labormessungen bestimmt. Die grundlegende Annahme ist, dass ein Material sich genauso in einer Anwendung verhält wie in einer abgetrennten Probe, die zur Messung der hydraulischen Eigenschaften verwendet wird. Die am häufigsten gebrauchte Methode sind die Multistep-Outflow/Inflow-Experimente [LORENTZ ET AL. (1992) [86]; PRIESACK UND DURNER (2006) [80]]. Bei einer alternativen Betrachtungsweise erfolgt die Bestimmung der hydraulischen Eigenschaften auf der Porenskala mit Informationen über die Kornverteilung und die Porenstruktur der Materialien. Auf diesem Konzept basieren verschiedene Methoden. Beim fortgeschrittensten Ansatz werden die genauen Geometrien von Proben mit bildgebenden Verfahren ermittelt und Lattice-Boltzmann-Methoden angewendet, um die Strömung im Porenraum zu simulieren und damit die hydraulischen Eigenschaften, z. B. Kapillardruck-Sättigungsbeziehungen einschließlich Hysterese, zu berechnen [TÖLKE ET AL. (2002) [96]; VOGEL ET AL. (2005) [102]; AHRENHOLZ ET AL. (2007) [3]].

Mittlerweile wurden experimentelle Untersuchungen von Zweiphasenströmungen in porösen Medien mit künstlich erzeugten Heterogenitäten durchgeführt. Es wurden einige Labormethoden zur präzisen Beobachtung der Strömung und Phasenausbreitung bei Drainage- und Imbibitionsverhältnissen in 3-D entwickelt [CULLIGAN ET AL. (2004) [22]; MASSCHAELE ET AL. (2004) [68]; SCHAAP ET AL. (2007) [88]]. Diese Methoden ermöglichen die Validierung der durch numerische Simulationen gemachten Prognosen und den Vergleich mit experimentellen Messungen.

### **Zielsetzung der Arbeit**

Um zusammenzufassen: es gibt fortgeschrittene Methoden zur Abbildung von dreidimensionalen Phasenverteilungen in heterogenen porösen Medien, numerische Ansätze zur Simulation von dreidimensionalen Zweiphasenströmungen unter Berücksichtigung von Hysterese-Effekten, einigermaßen exakte Methoden für Labormessungen von hydraulischen Eigenschaften und hochentwickelte Konzepte zur Berechnung von hydraulischen Eigenschaften auf der Basis von Informationen über die Porenstruktur. Dennoch wurden die oben genannten Betrachtungsweisen noch nicht kombiniert, um ihre Prognosefähigkeit zu prüfen. Dadurch bleiben folgende ungeklärte Fragen:

- Wie genau können Prognosen hinsichtlich Systemen sein, bei denen

Hysterese-Effekte auftreten? Ist in solchen Fällen die Anwendung eines Hysterese-Konzepts erforderlich und, wenn ja, wie einfach kann dieses Konzept sein?

- Sind genaue Prognosen zu Drainage- und Imbibitionsvorgängen in heterogenen porösen Medien bei Anwendung von hydraulischen Eigenschaften, die nur durch Kenntnis der Porenstruktur ermittelt wurden, möglich?
- Welche Möglichkeiten bzw. Einschränkungen gibt es im Vergleich zu der traditionellen Betrachtungsweise, die Multistep-Outflow/Inflow-Experimente einbezieht?
- Bei beiden Betrachtungsweisen müssen bestimmte Annahmen gemacht werden. Wie bestimmen diese Annahmen den beobachteten Hysterese-Effekt und was ist der Einfluss auf das erwartete Zweiphasenströmungsverhalten in heterogenen Strukturen?
- Ist die Anwendung von hydraulischen Eigenschaften, die in lokalen Messungen ermittelt wurden, ausreichend, um die gesamten Drainage- oder Imbibitionsprozesse in heterogenen Strukturen beschreiben zu können?
- Und schließlich: wie können verschiedene Betrachtungsweisen (z. B. Messungen und Simulationen) am effektivsten kombiniert werden, um zuverlässige Vorhersagen zu hysteretischen Zweiphasenströmungen zu erhalten?

Ziel dieser Arbeit ist es, diese ungeklärten Fragen zu diskutieren. Hinsichtlich dieser Zielsetzung ist die erste Aufgabe eine effiziente numerische Implementierung eines Hysterese-Konzepts zur Simulation von Drainage- und Imbibitionsvorgängen in Zweiphasensystemen. Dazu wird das Hysterese-Modell von PARKER UND LENHARD (1987) [78] gewählt. Zudem wird ein sogenanntes Play-Type-Hysterese-Konzept [BELIAEV UND HASSANIZADEH (2001) [11]] implementiert. Die korrekte Approximierung von Sättigungsdiskontinuitäten an Grenzflächen zwischen Heterogenitäten ist eine wichtige Voraussetzung für Zweiphasenströmungssimulationen in heterogenen porösen Medien. Hysteretische Kapillardruck-Sättigungsfunktionen hängen stark vom vorhergehenden Verlauf der Sättigung ab. Dadurch bedarf es einer präzisen Berücksichtigung der Sättigungsdiskontinuitäten in Hysterese-Modellen.

Der nächste Schritt ist die Prüfung der Prognosefähigkeit der numerischen Implementierung dieser Ansätze hinsichtlich des Hystereseverhaltens, das mit eindimensionalen Labormessungen bei Drainage- und Imbibitionsvorgängen beobachtet wurde. Ziel dieses Arbeitsabschnitts ist es, Antworten bezüglich der



Genauigkeit von Vorhersagen in Zweiphasenströmungen, bei denen Hysterese-Effekte auftreten, der Notwendigkeit von Hysterese-Modellen und der erforderlichen Komplexität von Hysterese-Konzepten zu finden.

Anschließend wird das numerische Modell benutzt, um Vorhersagen zu Drainage- und Imbibitionsvorgängen in dreidimensionalen heterogenen Strukturen mit einem experimentell gemessenen Strömungsprozess zu vergleichen. Ziel dabei ist es, die Prognosen zu bewerten und zu vergleichen, die mit hydraulischen Eigenschaften und hysteretische Kapillardruck-Sättigungsbeziehungen gewonnen wurden, die:

- auf der lokalen Skala mit Multistep-Outflow/Inflow-Experimenten gemessen und
- auf der Porenskala durch Bildanalyse und Lattice-Boltzmann-Strömungssimulationen bestimmt wurden.

Mit den Ergebnissen der numerischen Simulationen wird eine Vergleichsstudie durchgeführt, um die Möglichkeiten und die Grenzen der zwei verschiedenen Verfahren zu zeigen.

### **Modellimplementierung**

Die mathematische Beschreibung der Zweiphasenströmung lässt sich aus der Formulierung einer Massenbilanzgleichung der jeweiligen Fluidphasen herleiten. Die Erhaltungsgleichungen werden durch konstitutive Beziehungen ergänzt, die Kapillardruck-Sättigungsbeziehung und die relativen Permeabilität-Sättigungsbeziehungen. Für diese Funktionen werden die Parametrisierungen von VAN GENUCHTEN (1980) [99] und MUALEM (1976) [73] verwendet. In dieser Arbeit werden Hysterese-Effekte in der relativen Permeabilität vernachlässigt. Zwei Konzepte werden für die Beschreibung der Kapillardruck-Sättigungshysterese betrachtet. Das erste Konzept ist die sogenannte Play-Type-Hysterese von BELIAEV UND HASSANIZADEH (2001) [11]. Dabei werden Sekundärkurven durch lineare Funktionen bei konstanter Sättigung beschrieben. Dieser Ansatz setzt voraus, dass die residualen Sättigungen für Drainage und Imbibition nicht variieren. Das zweite Konzept [PARKER UND LENHARD (1987) [78]] basiert auf der Skalierung der scheinbaren Sättigung, die die Sättigung der eingeschlossenen nicht-benetzenden Phase beinhaltet. Damit ermöglicht dieser Ansatz die Bildung von realitätsnahen Sekundärkurven und die Approximation von residualen Sättigungen der nicht-benetzenden Phase in Imbibitionsvorgängen.

Das numerische Modell wird durch eine knotenzentrierte Finite-Volumen-Raumdiskretisierung, die sogenannte BOX-Methode [HELMIG (1997) [41];

BASTIAN (1999) [6]; HUBER UND HELMIG (1999) [47]], und eine implizite Euler-Zeitdiskretisierung gebildet. Die Simulationen werden mit dem numerischen Simulator MUFTE-UG [BASTIAN (1997) [7]; HELMIG ET AL. (1998) [42]] durchgeführt. Um Grenzflächen zwischen Heterogenitäten zu approximieren, wird eine erweiterte kapillare Gleichgewichtsbedingung angewendet [BASTIAN UND HELMIG (1999) [8]; DE NEEF (2000) [75]]. Diese Bedingung berücksichtigt virtuelle Sättigungen an den Knoten, die für alle benachbarten Elemente abhängig von deren Kapillardruck-Sättigungsbeziehungen berechnet werden. Dadurch wird die Beschreibung von Sättigungsdiskontinuitäten an der Grenzfläche von Heterogenitäten möglich. Dieses Verfahren wird durch die oben genannten Hysteresekonzepte erweitert und bietet damit ein konsistentes und vollständiges Vorgehen für Zweiphasenströmungsprognosen in heterogenen porösen Medien unter Berücksichtigung von Hysterese-Effekten.

### Modellverifizierung

Die erste Anwendung des numerischen Modells besteht aus einem Vergleich der Modellprognosen mit einem kontrollierten, eindimensionalen transienten Experiment. Das Experiment umfasst eine Sequenz von Drainage- und Imbibitionsvorgängen in einer homogenen Sandsäule, die mit einer Pumpe geregelt werden. Druck und Wassersättigung werden ständig in verschiedenen Höhen der Säule mit Tensiometern und TDR-Sensoren gemessen. Aus der Modellierungsperspektive werden drei Ansätze mit den experimentellen Messungen verglichen:

- Hysterese wird im numerischen Modell nicht berücksichtigt.
- Die Play-Type-Hysterese wird im numerischen Modell eingesetzt.
- Die Hysterese von PARKER UND LENHARD wird im numerischen Modell eingesetzt.

Dieses Vorgehen zeigt, dass die Einbeziehung von Hysterese in das numerische Modell eine wichtige Voraussetzung für korrekte Zweiphasenströmungsprognosen im Falle von wechselnden Drainage- und Imbibitionsverhältnissen ist. Ohne Betrachtung der Hysterese stimmen die Simulationsergebnisse und die experimentellen Messungen nicht überein, auch wenn die hydraulischen Eigenschaften optimal angepasst werden. Eine Verbesserung der Übereinstimmung erfolgt durch die Einbeziehung des Play-Type-Konzepts. Der Vorteil dieses Konzepts ist, dass es einfach und leicht zu implementieren ist. Auf der anderen Seite besteht damit keine Möglichkeit für die Approximierung des Einschlusses

der nicht-benetzenden Phase bei der Imbibition. Das kann zu Abweichungen von den experimentellen Beobachtungen führen, besonders hinsichtlich der residualen Sättigungen der nicht-benetzenden Phase bei einem Imbibitionsvorgang. Es gibt dennoch eine andere Möglichkeit, bei geringem Rechenaufwand eine bessere Approximation der Hysterese zu erreichen. Tatsächlich liefert die numerische Simulation mit dem Skalierungskonzept von PARKER UND LENHARD eine präzise Strömungsprognose für Drainage und Imbibition, auch bezüglich des Einschlusses der Luftphase. Dieses Hysterese-Konzept ist relativ einfach und stellt hier den aus Modellierungssicht verlässlicheren Ansatz dar. Die vorliegende Arbeit zeigt, dass ein Hysterese-Konzept nicht äußerst kompliziert sein muss, sofern die Möglichkeit für die Prognose des Phaseneinschlusses besteht.

Die vorgestellten Untersuchungen zeigen auch, dass zuverlässige Werte für die hydraulischen Eigenschaften notwendig sind. Die Verwendung einer mit Hilfe eines Multistep-Outflow/Inflow-Experimentes gemessenen Kapillardruck-Sättigungsbeziehung liefert eine unzureichende Prognose der Strömung im transienten Experiment, vor allem hinsichtlich des Lufteinschlusses. Das Multistep-Experiment sowie die Tensiometer- und TDR-Messungen beziehen sich auf die gleiche räumliche Skala und das gleiche Packungsvorgehen, jedoch auf wesentlich unterschiedliche Zeitskalen. Diese Aussage lässt eine Abhängigkeit des Phaseneinschlusses von der Zeitskala gekoppelt an die Methodologie erkennen. Aufgrund dessen sollten Hysterese-Kapillardruck-Sättigungsbeziehungen für Bedingungen und Zeitskalen bestimmt werden, die denjenigen der Zielanwendung entsprechen.

### **Prognosen zur Zweiphasenströmung in heterogenen porösen Medien unter Berücksichtigung von Hysterese-Effekten**

Der letzte Abschnitt dieser Arbeit konzentriert sich auf Prognosen von hysteretischen Zweiphasenströmungen, die mit auf unterschiedlichen räumlichen Skalen bestimmten hydraulischen Eigenschaften erzielt wurden. In diesem Fall werden numerische Simulationen der Drainage und Imbibition mit experimentellen Messungen verglichen, die in einer dreidimensionalen heterogenen Struktur gemacht wurden. Im 3-D-Laborexperiment werden die Äquilibrierungszeiten und Wasserverteilungen bei quasi-stationären Zuständen in einer Struktur mit vordefinierten Würfelheterogenitäten gemessen, die aus einem groben und einem feinen Sand aufgebaut wurden. Sättigungen werden anhand Neutronentomographie nach vier Drainage- und Imbibitionsstufen gemessen, die außen durch Variation des Wasserspiegels geregelt wurden. Bei den numerischen Simulationen wird das Hysterese-Skalierungskonzept von PARKER UND LENHARD

eingesetzt. Als Eingabe werden hydraulische Eigenschaften benutzt, die in zwei Betrachtungsweisen ermittelt wurden:

- Auf der lokalen Skala mit Hilfe von Multistep-Outflow/Inflow-Experimenten und globalen Optimierungsverfahren zur Bestimmung der Porosität, der Permeabilität und der Hysterese  $p_c$ - $S_w$ -Kurven im Rahmen einer einzigen Methode.
- Auf der Porenskala mit Hilfe von präziser Bildanalysetechnik zur Bestimmung der Porosität und zusätzlich durch Lattice-Boltzmann-Ein- und Zweiphasenströmungssimulationen in abgebildeten Sandgeometrien zur Berechnung der Permeabilität und der Hysterese  $p_c$ - $S_w$ -Kurven.

Die Sättigungsmessungen, die durch Neutronentomographie in der heterogenen Säule bei quasi-stationären Zuständen gewonnen wurden, zeigen Schwankungen der Würfel-Sättigungen innerhalb einer Höhe und eines Sandtyps. Teilweise sind diese Schwankungen auf eine zu erwartende Messabweichung sowie auf geringe Verdichtungsunterschiede bei den Sandwürfeln zurückzuführen. Dennoch sind die betrachteten Schwankungen größer als die, die bei vollständig stationären Zuständen gemessen wurden [VASIN ET AL. (2007) [100]]. Die zusätzliche Schwankung in diesem Fall bezieht sich höchstwahrscheinlich auf eine Verteilung, die einem nicht-stationären Zustand entspricht. Dieser Effekt wird auch durch die Ergebnisse einer numerischen Simulation verifiziert, wobei die Permeabilität angepasst wird, um das Zeitskala-Verhalten vom 3-D-Experiment nachzuahmen. Eine weitere wichtige Bemerkung in Bezug auf das 3-D-Experiment ist die Existenz von Übergangsflächen zwischen den gepackten Sandwürfeln. Sättigungsänderungen an den Grenzflächen zwischen den Sandwürfeln können direkt anhand der Tomographie-Abbildungen festgestellt werden. In dieser Arbeit werden die gemessenen Voxel-Sättigungen nur im inneren Teil der Würfel ausgewertet. So werden die vorliegenden Würfel-Sättigungen nicht von den Übergangsflächen beeinflusst. Allerdings können Übergangsflächen-Effekte die Äquilibrierungszeiten beeinflussen, indem diese für die gesamte dreidimensionale Säule gemessen werden.

Die auf der lokalen und der Porenskala bestimmten hydraulischen Eigenschaften werden auf der Basis der Annahmen, die bei den jeweiligen Methodologien getroffen wurden, diskutiert. Die erhaltenen Werte zeigen begründete Abweichungen, wenn man die zwei vom Konzept her unterschiedlichen Betrachtungsweisen bedenkt. Die Abweichungen sind höchstwahrscheinlich auf die unterschiedlichen Verdichtungen zurückzuführen, die in den (kleineren) abgebildeten Sandproben auf der Porenskala und in den (größeren) Sandsäulen auf

der lokalen Skala entstehen. Zusätzlich wird eine potenzielle Abhängigkeit des Phaseneinschluss-Effekts von der räumlichen Skala des betrachteten Volumens festgestellt.

Die numerischen Simulationen zeigen, dass es bei Anwendung der auf der lokalen oder auf der Porenskala ermittelten hydraulischen Eigenschaften nicht zu korrekten Vorhersagen der Äquilibrierungszeiten kommt, die im Labor-experiment gemessen wurden. Durch die Annahme, dass der gesamte Strömungsprozess in der heterogenen Struktur durch die Rekonstruktion der Geometrie und die Zuordnung von lokalen hydraulischen Eigenschaften erfasst werden kann, kann sich die Unstimmigkeit in den Zeitskalen aus der Unsicherheit in den hydraulischen Eigenschaften ergeben.

Daher kommen numerische Simulationen zum Einsatz, um qualitativ zu veranschaulichen, wie Änderungen der hydraulischen Eigenschaften den transienten und quasi-stationären Zustand bei den Drainage- und Imbibitionsstufen beeinflussen können. Die Benutzung der  $p_c$ - $S_w$ -Beziehungen aus der Porenskala mit einer Permeabilitätsanpassung ermöglicht tatsächlich eine qualitative Übereinstimmung bezüglich sowohl der Sättigungsverteilungen als auch der Äquilibrierungszeiten. Das ist bei Verwendung der auf der lokalen Skala gemessenen  $p_c$ - $S_w$ -Kurven nicht möglich, vor allem wegen Unterschieden bei dem Eintrittsdruck und der Steigung der resultierenden Sekundärkurven beim Feinsand. In diesem Sinne zeigt die LB-Methode eine bessere Prognosefähigkeit bezüglich der Form (Eintrittsdruck und Steigung) der Hysterese- $p_c$ - $S_w$ -Beziehungen. Auf der anderen Seite liefert die LB-Methode eine unzureichende Prognose hinsichtlich der Menge der eingeschlossenen Luft, zumindest was die Grobsand-Sättigungen nach der Imbibition betrifft. Die lokale-Skala-Betrachtungsweise prognostiziert eine bedeutende Menge an eingeschlossener Luftphase und bietet damit in diesem Fall die bessere Übereinstimmung mit den Messungen aus der Neutronentomographie.

Die vorliegende Arbeit weist auch auf die äußerste Sensitivität von Permeabilitätswerten hin. Die Permeabilitäten der verwendeten Materialien wurden mit drei verschiedenen Methoden gemessen (LB-Methode, Multistep-Outflow/Inflow-Experimente und zusätzlich in einzelnen Säulen, die mit der gleichen Packungsmethode wie die 3-D-Struktur gepackt wurden). Die drei Vorgehensweisen liefern Werte, die innerhalb von zwei Größenordnungen variieren. Im Allgemeinen kann man keine sicheren Aussagen machen, ob die Schwierigkeiten bei der Prognose der Äquilibrierungszeiten auf die Unsicherheit bei der Permeabilität der Materialien oder auf die dazwischenliegenden Übergangsflächen zurückzuführen sind. Die Permeabilitätswerte, die die bestmögliche Übereinstimmung zwischen Simulation und Experiment liefern, können als Upscaling-Werte betrachtet werden, die repräsentativ für die Mate-

rialen und die Übergangflächen sind. Die numerischen Simulationen in dieser Arbeit zeigen, dass die Äquilibrationszeiten aus dem Experiment prognostiziert werden können. Allerdings müssen dazu entweder die Übergangflächen im Modell explizit berücksichtigt werden, oder es müssen Permeabilitäten verwendet werden, die mit der gleichen Packungsmethode wie die 3-D-Struktur gebaut wurden und somit Übergangflächen-Effekte enthalten.

Aus den abschließenden Bemerkungen wird deutlich, dass auch ein konsistenter und hochentwickelter Modellansatz keine zuverlässige Prognosen ohne die Verknüpfung mit angemessenen Ansätzen zur Bestimmung von hydraulischen Eigenschaften liefern kann. Die Menge an eingeschlossener Luftphase aufgrund von Hysterese-Effekten zeigte große Sensitivität und ist möglicherweise abhängig von den Zeit- und Raumskalen, die an die Methodologie zur Bestimmung der  $p_c$ - $S_w$ -Beziehung gekoppelt sind. Es wird daher empfohlen, hydraulische Eigenschaften unter Bedingungen zu ermitteln, die der Zielanwendung ähnlich sind (z. B. bei einem schnellen oder langsamen Imbibitionsvorgang). Durch die weitere Verbesserung der Rechnerleistung sollte es möglich werden, die Porenraumgeometrie größerer Probenvolumen zu erfassen und auf der Basis von LB-Methoden die Höhe der Residualsättigung der nicht-benetzen Phase für diese Proben zu prognostizieren. Weitere entscheidende Faktoren sind die Methode, die Probe zu packen, und die Verdichtung der Materialien. Die zylindrischen Proben, die im Computertomograph gescannt wurden, wurden mit der gleichen Methode wie die 3-D-Struktur gepackt. Trotzdem lassen die unterschiedlichen Größen keine sicheren Aussagen über den Einfluss der jeweiligen effektiven Spannungen zu. Ein optimales Vorgehen wäre die Abbildung von Geometrien direkt von der gepackten heterogenen Säule. Dadurch ermöglicht die LB-Methode eine einzige, konsistente Untersuchung bezüglich der hydraulischen Eigenschaften der Materialien – genauso verdichtet oder locker wie in der heterogenen Struktur – und gleichzeitig die Betrachtung von eventuellen Effekten an den Übergangflächen.



# 1 Introduction

## 1.1 Motivation

### Problem description

At least since the times of ancient mining, human activities often lead to elevated levels of hazardous substances in the groundwater, referred to as **groundwater contamination**. After the industrial revolution, groundwater contaminations are closely related to the development of the industry. The increasing range of new compounds and hazardous substances used in the industry as well as the inadequate waste disposal during the past decades have dramatically increased the number of contaminated sites in all industrialized countries. At the turn to the new millennium, the European Environment Agency reported that approximately 30,000 contaminated sites have been definitely identified in Western Europe, while a number of 1.36 million waste, industrial and military sites were evaluated as potentially contaminated. At the same time, the consumption-oriented character of modern societies demands the massive use of pesticides in agriculture. These are not necessarily hazardous to the flora, but may infiltrate through the unsaturated zone of the subsurface and reach the aquifers that provide water supply to communities. Hazards in such scenarios commonly include high carcinogenicity and toxicity. A series of incidents in the 1980's and 1990's, combined with the increasing scarcity of freshwater resources in an uncontrollably changing climate, created great public awareness and alarmed the financial markets about the rising environmental problems. The following are only few out of numerous examples of groundwater contaminations that illustrate the scale of the problem:

- At lake Koronia, Greece, long-term extended pesticide use and uncontrolled groundwater withdrawal in the lake basin combined with industrial waste discharge has caused the elimination of the entire fish population as well as large populations of endangered bird species.
- At the Fischer waste site, Austria, a leakage of hazardous substances to



the groundwater was the result of insufficient technology, forming a major threat to the drinking water resources of the area.

- At a fjord near Bergen, Norway, PCB contaminated fjord sediments due to industrial waste water discharges lead to the long term prohibition of fish exploitation.

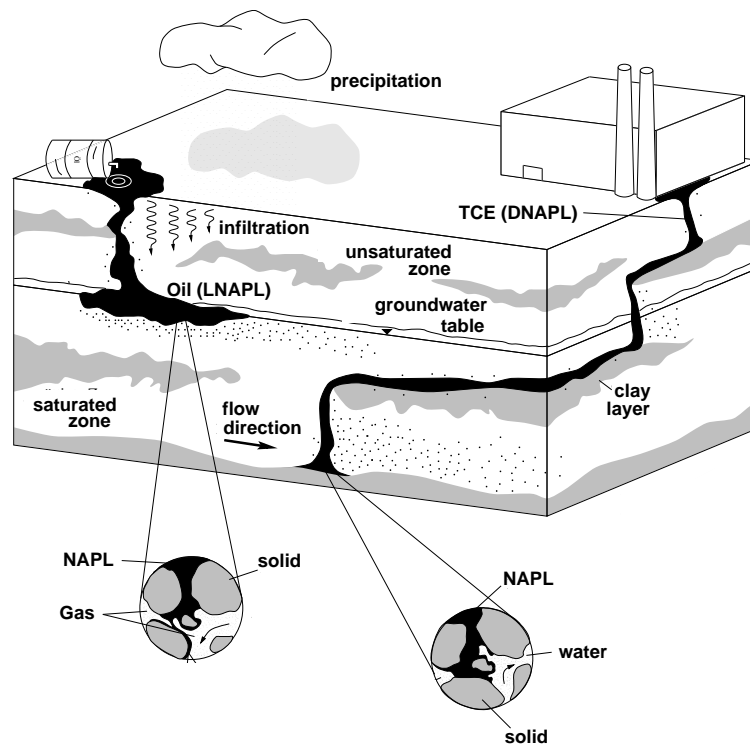


Figure 1: Infiltration and spreading of two hydrophobic substances in a porous medium after MACKAY AND CHERRY (1989) [67]. Non-Aqueous Phase Liquids are distinguished between those lighter than water (LNAPL's) and those heavier than water (DNAPL's).

Research has consequently focused on developing on the one hand monitoring tools to control and observe contaminations in groundwater and on the other hand efficient remediation strategies. As illustrated in Fig. 1, such problems often involve the flow of two immiscible fluids in heterogeneous porous media. As the objective of monitoring and remediation schemes is to maintain contaminants below harmful levels in a long-term basis, it is necessary to have a good understanding of two-phase flow and develop efficient tools that will achieve accuracy in predictions.

Accurate predictions of two-phase flow in the subsurface is a difficult task. The

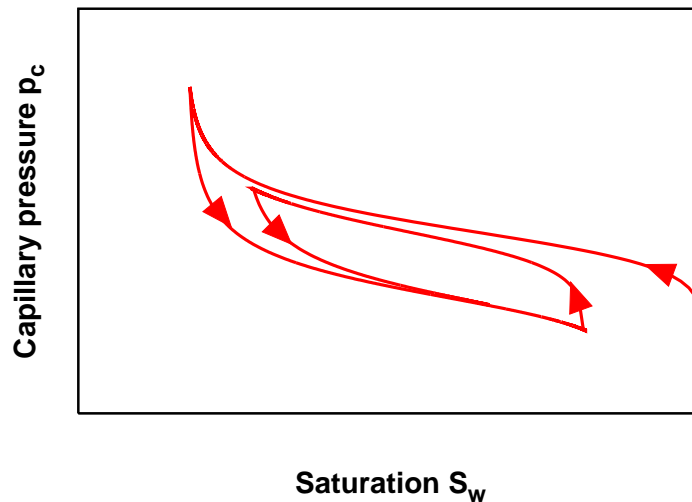


Figure 2: Hysteresis in the capillary pressure-saturation relationship.

processes that take place during two-phase flow in real soils are highly complex due to the heterogeneity of the subsurface. Heterogeneities strongly influence the distribution of the phases and therefore the complex heterogeneous structure of soil forms an important source of uncertainty. The description of two-phase flow in heterogeneous media becomes even more complicated through the dependency of the flow behavior on the type of displacement (drainage or imbibition) and its history. This effect is called **hysteresis**. Hysteresis is commonly observed in the capillary pressure-saturation relationship that differs in drainage and imbibition for the same porous medium, as illustrated in Fig. 2. Alternating drainage and imbibition events take place i.e. during infiltration of precipitation water in the unsaturated zone (meaning the zone between the ground surface and the groundwater table), fluctuations of the groundwater table or during Non-Aqueous Phase Liquids removal during a remediation process.

### Tools for predicting two-phase flow in the subsurface: numerical simulations

Numerical simulations have been increasingly employed to predict two-phase flow in porous media. Several multi-dimensional numerical models based on different approaches for the simulation of multiphase flow processes [ABRIOLA (1989) [1]; HELMIG (1997) [41]; MILLER ET AL. (1998) [70]] have been developed to make predictions of lab or field applications. Most of the numerical studies considering heterogeneities have been carried out for 1-D and 2-D problems [i.e. KUEPER AND FRIND (1991) [60]; ESSAID AND HESS (1993) [27]; DEKKER AND ABRIOLA (2000) [24]], some accounting also for hysteresis effects [GERHARD AND KUEPER (1991) [31]]. Some 3-D simulations have also been applied to predict

multiphase flow in case studies or field applications [PANDAY ET AL. (1994) [77]; HELMIG ET AL. (2006) [44]]. However, it is very difficult to validate results from 3-D simulations due to the complexity of the problems under investigation and the scarcity of good 3-D laboratory or field data. Furthermore, two-phase flow models employ hydraulic properties (porosity, permeability and hysteretic constitutive relationships) to describe the heterogeneous structures of porous media and its interaction with fluids. This concept therefore demands good knowledge related to the hydraulic properties of the porous media involved in the application, for drainage or imbibition conditions. Nevertheless, it is not clear how good predictions can be even if the most accurate methods are used for the determination of hydraulic properties.

### **Classical approach for the determination of hydraulic properties of porous media**

The classical approach to determine hydraulic properties of porous media is to carry out multistep outflow/inflow experiments. In such experiments, a porous medium sample is saturated with water and then drained by decreasing the boundary pressure stepwise [i.e. LORENTZ ET AL. (1992) [86]]. Similarly, it is possible to imbibe a dry sample by increasing the water boundary pressure. Inverse models are then applied to determine the hydraulic properties from the measured outflow/inflow curves [i.e. PRIESACK AND DURNER (2006) [80]]. With this procedure hysteretic drainage and imbibition capillary pressure-saturation curves, permeability and porosity are obtained.

This approach assumes that the same material will behave in the same fashion in an application and a specimen used for a multistep outflow/inflow test, therefore it shall have the same  $p_c-S_w$  relationship. However, it still remains unclear whether this assumption is valid and if this approach can provide reliable hydraulic properties, especially for applications that involve effects of capillary hysteresis.

### **Alternative approaches for the determination of hydraulic properties of porous media**

Another option for the determination of hydraulic properties of porous media is to derive them from knowledge about the pore structure. There are several publications on the determination of the pore structure of porous media. For example, LEHMANN ET AL. (2004) [64] have scanned sand material with a synchrotron light source to determine packing effects on the porosity at the interface between different sand types.

The early alternative methods for determining hydraulic properties aimed to approximate the pore voids of porous media by capillary tubes. Based on the idea that the radii of the capillary tubes should relate to the pore size distribution, ARYA AND PARIS (1981) [4], CAMPBELL AND SHIOZAWA (1989) [18] and JONASSON (1989) [50] have derived capillary pressure-saturation curves using grain size distributions.

Evolving from this concept, *pore network* and *morphological-topological* models have been developed. Pore network models utilize complicated arrangements of capillary tubes in order to resemble porous media, while morphological-topological models describe the geometrical properties of the pore space using statistical parameters.

BRYANT AND BLUNT (1992) [15] and JUANES AND PATZEK (2004) [51] have predicted relative permeabilities in two- and three-phase flow systems while VOGEL AND ROTH (1998) [101] used topological parameters similar to those of natural soil samples in order to determine soil hydraulic functions. Pore network models have also been used to model multiphase flow in porous media [BAKKE AND OREN (1997) [5]] and their predictions have been compared to fluid distributions measured in small samples using synchrotron tomography [COLES ET AL. (1998) [20]].

An advanced technique to determine hydraulic properties of porous media is by means of pore-scale flow simulations utilizing efficient lattice Boltzmann methods. High resolution images of the microstructure of real porous media can provide the base geometry for such simulations [FERREOL AND ROTHMANN (1995) [29]]. Based on this idea, it is possible to apply pore-scale one- and two-phase flow simulations using exact pore space geometries to determine hydraulic properties, including hysteretic capillary pressure-saturation relationships. Such computations have been done by ADLER AND THOVERT (1998) [2], LEHMANN ET AL. (2001) [65], BEKRI AND ADLER (2002) [10], TÖLKE ET AL. (2002) [96] and PAN ET AL. (2004) [76].

A comparison of capillary pressure-saturation curves determined with pore network, morphological and two-phase lattice Boltzmann models is given in VOGEL ET AL. (2005) [102].

### **Experimental investigations of two-phase flow in porous media**

Parallel to modeling techniques, research has focused on investigations of two-phase flow in porous media by means of experimental observations. Various experimental studies can be found in the literature, both for NAPL-water and air-water systems, that address the problem of flow in heterogeneous media and where the movement of the fluids is monitored. Experiments for the

investigation of two-phase flow in 2-D heterogeneous media were carried out i.e. by KUEPER ET AL. (1989) [59], WILDENSCHILD AND JENSEN (1999) [106] and URSINO ET AL. (2001) [98]. Relatively few 3-D experiments have been carried out using X-ray computed tomography (CT) to investigate water distribution in soils [HOPMANS ET AL. (1992) [45]; HEIJS AND DE LANGE (1997) [40]]. Recently, CULLIGAN ET AL. (2004) [22] and CULLIGAN ET AL. (2006) [21] have used CT techniques to measure interfacial areas in 3-D glass bead structures. A quite new method for mapping in 3-D is neutron tomography: an early application was done by SOLYMAR ET AL. (2003) [93], while MASSCHAELE ET AL. (2004) [68] used neutron tomography to qualitatively investigate dynamic processes in limestone and sandstone. In some cases, the monitored distribution of fluids in 2-D or 3-D heterogeneous media has been compared to numerical simulations [i.e. URSINO AND GIMMI (2004) [97]]. However, agreement between measurement and prediction could be found only in a qualitative way. Laboratory experiments commonly involve pre-defined heterogeneities and therefore provide the advantage that the structure is known. However, an uncertainty in such studies remains from the strong influence of the hydraulic properties used as input in the numerical simulations.

### Identification of open questions

To summarize, there are state-of-the-art methods to map 3-D fluid distribution in heterogeneous porous media, numerical tools for the simulation of 3-D hysteretic two-phase flow in heterogeneous media, fairly accurate techniques to determine hydraulic properties of sands in the lab and advanced modeling approaches for the computation of hydraulic properties from knowledge related to the pore structure. However, they have not been combined in order to test the predictive power of these approaches. This gives rise to the following open questions:

- (a) How accurate can predictions be in systems where the hysteresis effect is involved? Is it necessary to use hysteresis models and, if yes, how simple can these models be?
- (b) Is it possible to make correct predictions on drainage and imbibition two-phase flow problems in heterogeneous porous media using hydraulic properties determined with information from the pore structure of the porous media?
- (c) What are the possibilities and limitations compared to the classic approach that uses multistep outflow/inflow experiments to determine hydraulic properties?
- (d) Both approaches have certain assumptions. How does this affect the observed

hysteresis and what is the influence on the predicted two-phase flow behavior in heterogeneous structures?

(e) Is it sufficient to use hydraulic properties from local measurements in order to capture the entire drainage and imbibition process in heterogeneous structures?

(f) Finally, how can different approaches (i.e. measurements and simulations) be combined in order to obtain reliable predictions on hysteretic two-phase flow problems?

## 1.2 Spatial scales in porous media

Two-phase flow in porous media involves several complex processes that are relevant to different spatial and temporal scales. A process that is dominant on one scale may become insignificant if the same system is considered on a different scale. Nevertheless, what is observed under a certain scale consideration, strongly depends or relates to processes that occur in other scales. This dependency makes the description of natural hydrosystems very complicated. Having a clear definition of scales and understanding their role is particularly crucial for the discussion of two-phase flow in porous media.

### 1.2.1 Definition of spatial scales

Water is a chemical substance that consists of molecules that have two hydrogen atoms bonded to a single oxygen atom (in Fig. 3 oxygen atoms are black and hydrogen atoms are white). In general, taking into account the movement of each individual molecule is not suitable for solving problems in fluid mechanics because of the enormous number of molecules that lead to problems of intractable complexity. However, by averaging the effect of the movement of a large number of molecules, they can be replaced by a *continuum*. The transition from the

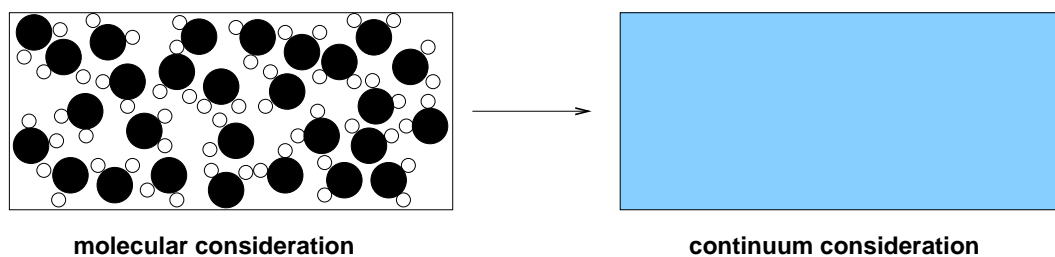


Figure 3: Consideration of water as a continuum.

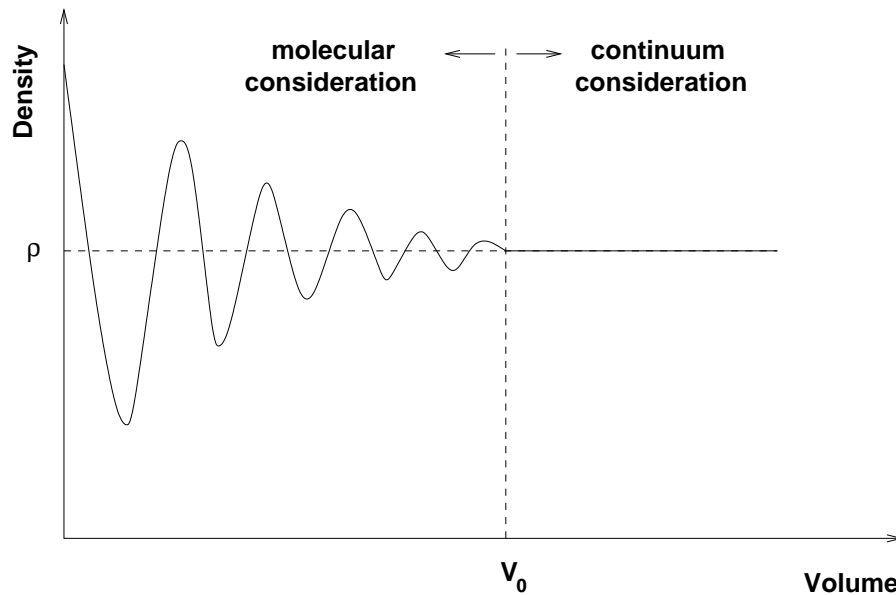


Figure 4: Definition of density as a continuum property and transition from the molecular to the continuum consideration.

molecular consideration to the continuum consideration is based on the kinetic gas theory (see i.e. EINSTEIN (1905) [26]). This is a basic principle of continuum mechanics: it is now possible to define continuum properties such as the density and the viscosity that result from the averaging of a large enough number of molecules or in other words a sufficiently large volume of continuum (see Fig. 4). The transition from the molecular to the continuum consideration also allows for the definition of continuum variables, such as pressure. Based on this concept, pressure is an averaged effect that arises from forces exerted by a large number of molecules. Although the new continuum properties actually depend on the movement and the properties of the molecules, molecular processes are not explicitly considered and fluids are described only by continuum properties. The definition of a spatial scale is not absolute, but relates to the problem under investigation and the model concept that needs to be developed for that purpose. In environmental applications related to groundwater, the typical relevant spatial scales considered are the following:

- pore scale
- local scale
- field scale

These are illustrated in Fig. 5.

Similarly, there are different temporal scales involved in environmental applica-

tions. These may vary from small fractions of a second (i.e. movements of water molecules) to several years (i.e. field-scale geological processes). In the following only the spatial scales will be discussed, as categorized above. For the description of these scales and the transition between them, the example of an unconfined groundwater aquifer in a sedimentary basin is considered (see Fig. 5). Below the groundwater table the porous medium is saturated with water. In the unsaturated zone, meaning the zone between the ground surface and the groundwater table, both water and air can be found.

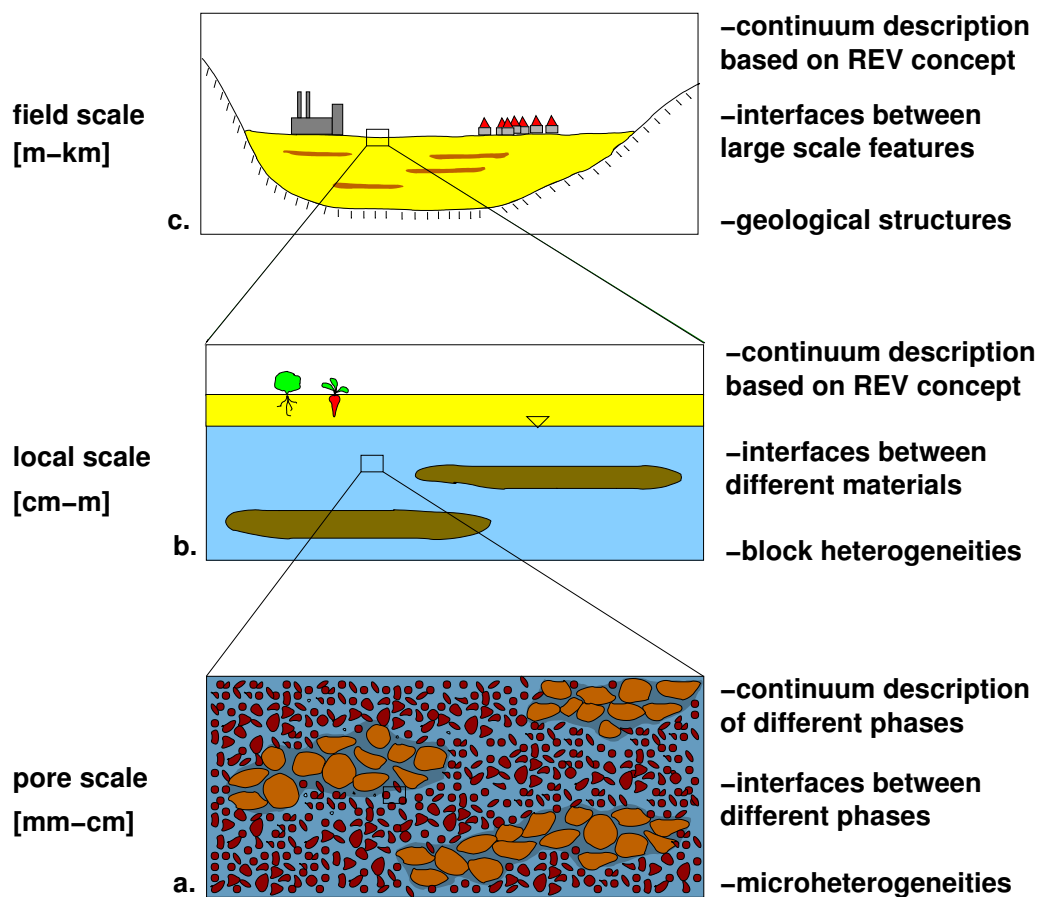


Figure 5: Typical spatial scales involved in groundwater flow.

### The pore scale

On the *pore scale* (see Fig. 5a), one can identify the grains of the porous medium and the void space between them filled with water (in the saturated zone) or water and air (in the unsaturated zone). Fluids that occupy the pore space are considered as continua, which means they can be described with parameters and variables such as density, viscosity and pressure. On the pore scale, one can



identify features of the pore space, such as variable sizes and shapes of the pores that cause spatial microheterogeneities. At each point on this scale, one finds either the solid medium or a fluid that occupies a void (see Fig. 5a). Interfaces are formed between the different fluids and between the fluids and the solid grains of the porous medium. In this consideration, it is possible to directly take the known pore space geometry and –combined with the appropriate boundary conditions– use momentum and mass balance equations in order to describe the flow of fluids in the pore space.

Some important remarks related to the size of the pore scale, as it is considered in this work, are given in Sect. 1.2.2.

### The local scale

On the *local scale* (Fig. 5c), physical and material properties are defined by means of averaging. As an example a typical porous media property is considered, the porosity. Porosity of a porous medium is defined as the ratio of the volume of the pores to the total volume of the considered medium. If a single point is observed on the geometry shown in Fig. 5b, porosity will be either 0 or 1, depending on whether the point lies on a grain or a pore. If the observation volume is enlarged, porosity will fluctuate between 0 and 1, depending on the percentage of grains and pores included in the observation volume. After a certain threshold volume  $V_0$ , further increase of the volume does not cause any further fluctuation in the porosity as it will not depend anymore on the averaging volume (see Fig. 6). Porosity is thus defined by averaging over an appropriate control volume, the *representative elementary volume* or REV [BEAR (1972) [9]]. In general, physical or material properties can be defined averaged over a control volume that is large enough so that no fluctuations of the averaged properties are observed. This way an additional continuum approach is introduced, in this case for porous media.

On the local scale, the pore geometry of a porous medium is not recognizable (see Fig. 5b) and therefore the description of flow can be realized only with averaged properties. At each point on this scale, one finds both the solid and the fluids present. Interfaces in this case exist between different materials that form local-scale block heterogeneities. This consideration is compared to the pore-scale consideration in Fig. 7. On the pore scale, the distribution of the grains and the fluids in an observation volume is known, whereas on the local scale one cannot account for the exact movement of fluids inside the complicated pore geometry of the medium. Governing pore-scale equations, such as the Navier-Stokes equation, are in this consideration not applicable. However, by introducing the REV concept, new equations for flow in porous media can be introduced (i.e. the *Darcy's law*). A significant assumption in this consideration

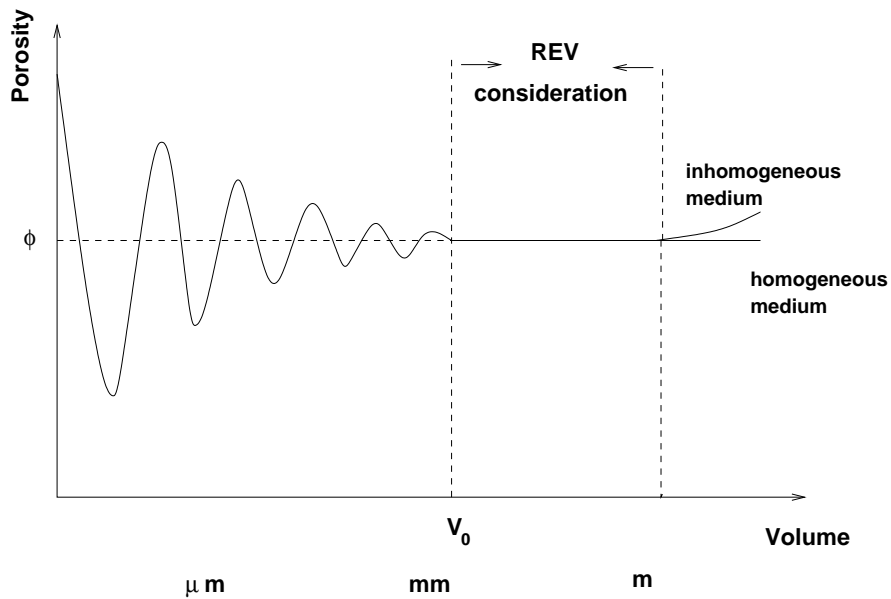


Figure 6: Porosity and definition of the REV after BEAR (1972) [9].

is that effective parameters can be attributed to a REV, i.e. the permeability. This implies that the effects of microheterogeneities averaged over a control volume can be described by assigning effective parameters for that volume.

In models that are based on this concept, each point in a domain represents a REV that has a single value for each variable. Then, effective processes and parameters are assigned and are assumed to correctly represent the pore-scale effects averaged over the REV corresponding to that point. On the local scale, block heterogeneities are observed due to the existence of materials with different averaged properties, or different effective parameters. Hence, heterogeneity can be described by assigning different values of effective parameters to the corresponding coordinates of the point in the domain.

### The field scale

After further zooming out (Fig. 5c), individual local-scale heterogeneities are not recognizable. However, these form patterns at the *field scale*, such as layers and structures of different geological periods. These structures commonly involve several types of materials with different properties. If one tries to characterize porous media for a volume at this scale ([m]-[km]), effective parameters may vary within it. In other words, the concept of the REV has also an upper boundary (see Fig. 6) due to large-scale heterogeneity. The concept is however the same as the one used on the local scale: to build models on the field scale, a field-scale domain is split into several smaller local-scale sub-domains according to

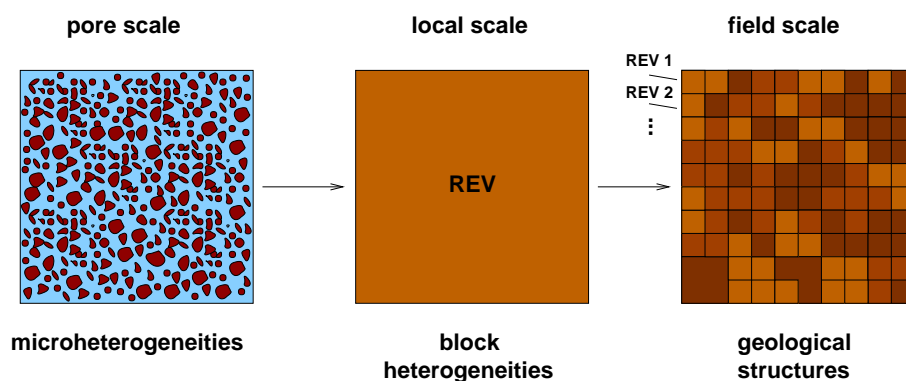


Figure 7: Transition from the pore scale to the local and the field scale.

the geology, assuming that the same equations for flow as in the local scale can be applied. This process is illustrated in Fig. 7. As done before, it is assumed that each of the sub-domains represents a REV and therefore may be described by a single set of effective parameters.

### 1.2.2 Continuum consideration for porous media on the pore scale

As explained above, zooming into a porous medium makes it possible to exactly describe the geometry of the pores, and therefore use appropriate boundary conditions to apply mass and momentum balance equations for modeling the flow of water in the porous medium. The same applies also in the case where more than one fluids occupy the pore space. The detailed distribution of the fluids and the exact positions of the interfaces between different fluids and between fluids and grain walls are available. It is also possible to explicitly track their movements and therefore possible to model the movement and interaction of several fluids in the voids of a porous medium.

On the other hand, at the transition to the local scale the exact distribution of the fluids in the pores is not taken into account, but only an effect averaged over a REV. It is assumed that the complicated geometry of the pore space can be replaced in the REV concept by effective parameters.

The pore scale in this work is considered such that the pore structure can still be identified but also averaged material or physical properties can be defined and do not depend on the averaging volume. According to this definition, on the pore scale one can have a sample of a porous medium that is large enough to be considered as a continuum but at the same time has a known pore space geometry. This means one may define averaged material properties based on the REV con-

cept but can also apply the Navier-Stokes equations to model one- and two-phase flow in the pore space.

In this work, the REV concept applies both to the local and the pore scale. This way, REV-defined hydraulic properties of porous media will be determined on the local and on the pore scale. It must be stated that this is possible because it is here chosen by definition that the pore scale is large enough to form a REV.

## 1.3 Objective and structure of the thesis

The motivation of this thesis is to discuss the identified open questions of Sect. 1.1. Related to this, the following objectives need to be accomplished:

- The first objective is the efficient numerical implementation of a hysteresis model in order to simulate two-phase drainage and imbibition. For that purpose, the scaling concept of PARKER AND LENHARD (1987) [78] is chosen. Also, a play-type hysteresis concept [BELIAEV AND HASSANIZADEH (2001) [11]] is implemented. The first goal is to test the ability of the numerical implementation of these concepts to predict the hysteretic behavior observed in 1-D laboratory measurements in drainage and imbibition. This part provides answers related to the accuracy of predictions on hysteretic two-phase flow, the necessity of hysteresis models and the complexity required in a hysteresis concept. Also, light is shed to the crucial open question (f) concerning beneficial combinations of different approaches.
- In simulations of two-phase flow in heterogeneous media, it is important to correctly predict discontinuities of saturation at the boundaries of heterogeneities. Hysteretic capillary pressure-saturation functions strongly depend on the history of the saturation evolution. Thus, a crucial point is to precisely observe saturation discontinuities at material interfaces in the hysteresis model.
- The numerically implemented hysteresis model is used to discuss the open questions (b) to (f). By means of numerical simulations, it is possible to compare predictions of two-phase flow drainage and imbibition in 3-D heterogeneous structures to an experimentally measured flow process. The aim is to evaluate and compare predictions made with hydraulic properties and hysteretic capillary pressure-saturation relationships:
  - measured on the local scale with multistep outflow/inflow experiments,

- determined on the pore scale with image analysis and lattice-Boltzmann flow simulations.
- A comparative study using the results from the numerical simulations is carried out in order to reveal possibilities and limitations of the different approaches and provide knowledge related to the potential for reliable predictions of hysteretic two-phase flow in heterogeneous structures.

The thesis is structured as follows: In Ch. 2 the physical and mathematical model concept of two-phase flow in heterogeneous porous media is described. Definitions of the hydraulic properties involved in this model concept are given.

Chapter 3 focuses on the effect of capillary hysteresis on the pore scale and the local scale. The functional concepts used in this thesis for the description of hysteretic capillary pressure-saturation relationships are also explained.

In Ch. 4, a description of the discretization techniques applied in the numerical model is given. Secondly, the model extension for capillary pressure-saturation hysteresis including a capillary interface condition for heterogeneous porous media is analyzed.

Before using the model to simulate two-phase drainage and imbibition in 3-D heterogeneous structures, it is necessary to evaluate its predictive ability for a simple one dimensional setup. For that purpose, numerical simulations are compared to a 1-D transient drainage and imbibition experiment performed by Yvonne Lins and Tom Schanz in the Department for Soil Mechanics at the Bauhaus University of Weimar. This is described in Ch. 5. In the numerical simulations, the hysteresis model from PARKER AND LENHARD (1987) [78] as well as the concept of vertical scanning curves proposed by BELIAEV AND HASSANIZADEH (2001) [11] are tested.

The comparison of predictions on two-phase hysteretic flow in heterogeneous media using hydraulic properties from the pore scale and local scale is presented in Ch. 6. To monitor hysteresis effects in heterogeneous media, a well-controlled 3-D drainage and imbibition experiment is conducted in the facility of the Paul Scherrer Institute (PSI), Switzerland. This work is carried out by Joris Schaap, Peter Lehmann, Anders Kaestner and Hannes Flühler from the Institute for Terrestrial Ecology at the ETH Zürich, in collaboration with Rene Hassanein and Eberhard Lehmann from PSI. Equilibration times and water distributions in the 3-D heterogeneous structure are measured after drainage and imbibition steps. In the same chapter, the hydraulic properties of the sands are discussed. In the classic local-scale approach, a set of properties is determined by means of multi-step outflow/inflow experiments and global optimization techniques. This work is done by Andre Peters and Wolfgang Durner at the Department of Soil Science

and Soil Physics, Institute of Geoecology of the Braunschweig Technical University. In the pore-scale approach, the hydraulic properties are determined with advanced image analysis of mapped samples (performed by Peter Lehmann and Anders Kaestner) and pore-scale simulations of one- and two-phase flow in the obtained geometries. These simulations are carried out by Benjamin Ahrenholz, Jonas Tölke and Manfred Krafczyk at the Institute for Computer Applications in Civil Engineering of the Braunschweig Technical University.

The structure and boundary conditions from the 3-D experiment are used to set up 3-D two-phase flow numerical simulations. The results from the numerical simulations are compared to the measurements from the experiment. As input for the numerical simulations, hydraulic properties from both approaches (from the pore scale and from the local scale) are used. The comparison of numerical simulations to the 3-D experiment triggers a discussion related to the predictive ability, the limitations and the improvements necessary in the different approaches.

A synopsis of the work, the drawn conclusions and some closing remarks are given in Ch. 7.

## 2 Physical and mathematical model concept

This thesis deals with the flow process of two immiscible fluids in a rigid porous medium. The REV consideration, as introduced in Sect. 1.2, forms the conceptual basis for the development of a mathematical model for the description of such problems. In the following, basic definitions of variables and hydraulic properties included in the model formation are introduced. Moreover, physical underlying principles behind the mathematical model will be discussed.

### 2.1 Basic definitions

The pore scale and the local scale considerations were introduced in Sect. 1.2. Figure 8 illustrates the two considerations for the case that two fluids occupy the pore space of a porous medium. The grains of the porous medium are considered as a non-deforming solid matrix. Furthermore, the pore scale consideration provides information about the exact distribution of the fluids in the pore space and the positions of fluid-fluid and fluid-solid interfaces. On the local scale, interfaces are no longer resolved and therefore it is necessary to consider subvolumes inside a REV occupied by the solid grains and the fluids, assuming their distribution inside the REV is homogeneous and continuous (see Fig. 8). This concept allows the introduction of a new variable, the *Saturation*  $S_\alpha$  of the fluid  $\alpha$ . It is defined as the ratio of pore space volume occupied by the fluid to the total pore space volume

$$S_\alpha = \frac{\text{Volume of the fluid in REV}}{\text{Volume of the pore space in REV}}. \quad (1)$$

According to the definition, it is further valid that

$$\sum_{\alpha=1}^{n_{fluids}} S_\alpha = 1. \quad (2)$$

Similarly, the *fluid content*  $\theta_\alpha$  can be defined as

$$\theta_\alpha = \frac{\text{Volume of the fluid in REV}}{\text{Volume of REV}}. \quad (3)$$

In this consideration pressures of fluids are assumed to be evenly distributed inside a REV. In other words, a single pressure value is assigned to each fluid within a REV, which implies that, theoretically, the pressure of the fluid  $\alpha$  in a REV should be equal to the pressure one would obtain by averaging all the individual pressure values from the pore space inside the REV.

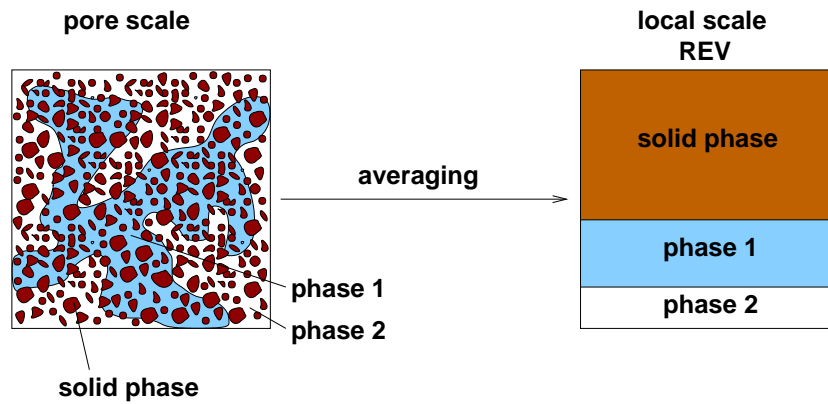


Figure 8: Consideration of fluid distribution on the pore scale and on the local scale.

## 2.2 Phase properties

As explained in Sect. 1.1, separate phases might exist in porous media in several natural or technical problems, such as the movement of a NAPL in a groundwater aquifer. Here some important remarks are given, related to the properties of phases as they are considered for the development of the model concept used in this thesis.

The term *phase* describes a matter that has homogeneous chemical composition and physical state, and one can further distinguish solid, liquid and gas phases. In this work the last two are referred to as *fluid phases*. Although air in reality consists of different chemical compounds (i.e.  $N_2$ ,  $O_2$ ,  $CO_2$ ), it is assumed that one can neglect its heterogeneous chemical composition and therefore consider it as a single phase.

On the molecular scale, one can distinguish a transition layer between different phases, where molecules from both phases can be found. In the model concept



applied in this thesis, fluids are only considered as immiscible continua and thus the transitions between them is approximated as sharp fluid interfaces. Moreover, any kind of mass transfer between different phases is not accounted for. Under these assumptions, the existence of a phase on the local scale is sufficiently described with the phase saturation.

The *density*  $\rho$  of a phase is defined by the ratio of its mass to the volume it occupies. Incompressibility is a reasonable assumption for liquid phases, however the density of gas phases may change with temperature and pressure. In this work only isothermal conditions are considered and the dependency of air density on pressure is not taken into account.

The *dynamic viscosity*  $\mu$  of a fluid is defined as the ratio of the shear stress divided by the velocity gradient. It results from intermolecular attractive forces that oppose to any change in the shape form of the phase. The dynamic viscosity of fluids depends on temperature, therefore in this work it can be considered as a time and space invariant fluid phase property.

The grains of a porous medium form a non-deforming solid phase. The ratio of the pore volume to the total volume of a porous medium is expressed with a material property very commonly used in hydrogeology, the *porosity*  $\phi$

$$\phi = \frac{\text{Volume of the pores in REV}}{\text{Total volume of REV}}. \quad (4)$$

A basic assumption in the definition of porosity is that the entire volume of the pores inside the matrix of a material is accessible to the fluid phases. This is a reasonable assumption for environmental applications, as the proportion of isolated pores is small related to the total number of pores in sands and natural soils. Porosity in conventional methods can be measured with instruments called *porosimeters* or by successively completely drying and wetting a given volume of a porous medium while measuring the weight of the water stored in the volume. A more delicate, non-destructive method is to scan a porous medium with a synchrotron light source to capture high-resolution 2-D images [LEHMANN ET AL. (2004) [64]]. By means of advanced image analysis, it is then possible to split the scanned image in pore and grain parts and thus determine the porosity.

Porosity may also change with time. This effect may have a significant influence in the behavior of flow in deforming porous media, shrinking-swelling clays, formations with unstable and dissolvable minerals, or in cases where organic material forms in the pore space of a porous medium. In this work however we restrict to porous media where the porosity can be considered as a time-invariant medium property.

## 2.3 Capillary pressure

As this thesis aims to discuss hysteresis effects in the capillary pressure-saturation relationship, the basic principles of capillarity in two-phase flow in porous media need to be analyzed. This is done starting from the pore scale and then proceeding to the local scale, as this sequence gives a better insight in the role of capillary pressure.

### 2.3.1 Capillary pressure on the pore scale

#### Interfacial tension

Between the molecules of a fluid act forces that originate in the electrical field of the molecules. These forces may be attractive or repulsive. Here two typical fluid phases involved in environmental applications are considered: gas and water. Gases are characterized by low density and large distances between the molecules. Therefore, intermolecular forces only act in small fractions of time during collisions between molecules. This results also to the ability of gases to fill the entire space that is available. On the other hand, the density of water is much higher and molecules have smaller distances. In this case, the equilibrium between molecular forces determines the arrangement of the molecules.

As a consequence, molecular forces at the interface between water and gas do not balance out, but result to a force  $F_{w,a}^{int}$  normal to the interface (see Fig. 9). This causes the familiar curvature of fluid interfaces: if a molecule moves from the interface to the interior, an amount of interfacial energy is released while the area of the interface is reduced. If other external forces are absent, this

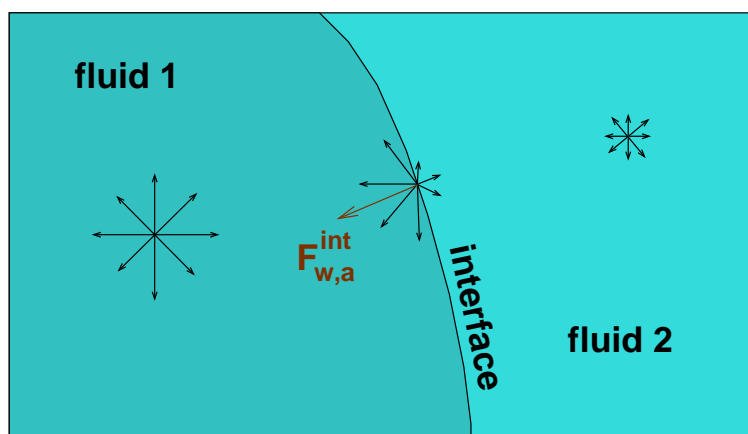


Figure 9: Interfacial forces.

means that the interface will form the minimal area for the given volume of fluid. At equilibrium, this area cannot be further decreased because any further movement of molecules to the interior would increase the density and thus cause counteracting forces. The tendency to minimize the area results in tangential forces at an interface. The tangential force per unit length is called *interfacial tension*  $\sigma$ . This force is also equal to the areal density of the interfacial energy and an equivalent definition of interfacial tension is work done per unit area. In order to increase the interfacial area of a mass of liquid by  $\delta A$ , a quantity of work  $\sigma\delta A$  is required. This work is stored as potential energy. Consequently surface tension can be measured in force per unit length or energy per unit area. For a water-air interface at 20°C, the Euclidean norm of the interfacial tension is  $\sigma_{wa} = 0.0725$  [N/m].

Since mechanical systems try to reach a state of minimum potential energy, free droplets of fluids have naturally a spherical shape (i.e. the free-floating blobs that water forms in air in the absence of gravity). The existence of interfacial tension also explains, if external forces are assumed to be absent, why one liquid forms perfect spheres inside another. As an example one can think the spherical bubbles that air forms inside honey.

### Contact angle

Two immiscible fluids in contact with a flat solid surface are considered (see Fig. 10). An example is a drop of water on a solid surface. The *contact angle*  $\omega$  is defined as the angle between the fluid-fluid interface and the solid surface. There are in total three interfaces in the system and therefore three interfacial tensions  $\sigma_{sn}$ ,  $\sigma_{sw}$  and  $\sigma_{nw}$ . For the drop to be stable, the horizontal components of the interfacial tensions have to balance. This gives for the lengths of the vectors  $\sigma_{sn}$ ,  $\sigma_{sw}$ ,  $\sigma_{nw}$

$$\cos\omega = \frac{\sigma_{sn} - \sigma_{sw}}{\sigma_{nw}}. \quad (5)$$

This is known as *Young's Equation* and it has a solution only if  $\sigma_{nw} > |\sigma_{sn} - \sigma_{sw}|$ . In Fig. 10 the contact angle for the water is smaller than 90°, thus water is notated as the *wetting phase* (w). The contact angle for the gas is larger than 90°, therefore gas is in this case the *non-wetting phase* (n).

If we consider in general the fluid phases 1 and 2 instead of gas and water with  $\sigma_{12} < |\sigma_{s1} - \sigma_{s2}|$ , there are two cases: the first case occurs when the attractive forces between the solid and the molecules of the phase 2 dominate. Then phase 2 will completely spread on the solid (i.e. water on very smooth glass). In the second case, the attractive forces between the solid and the molecules of phase 1

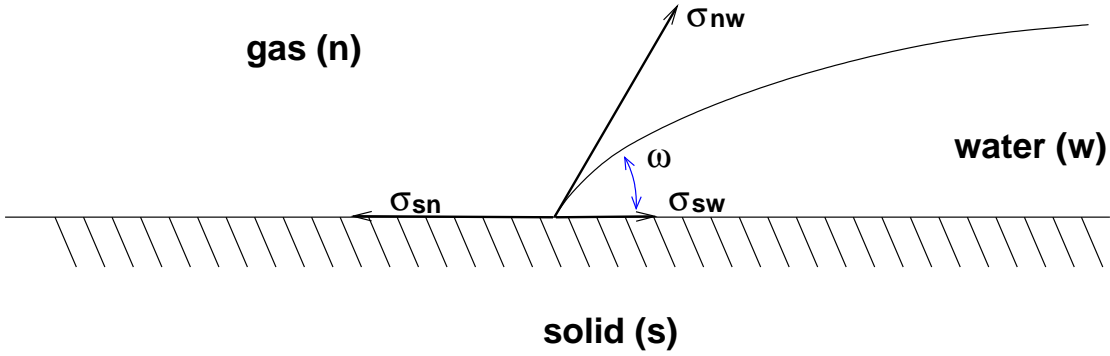


Figure 10: Surface tensions exerted by the three interfaces. The contact angle  $\omega$  adjusts itself such that the three tensions balance each other.

dominate, forming a spherical blob (i.e. water on an oiled surface).

### Capillary pressure

If a capillary tube is brought in contact with a fluid surface, the attraction between the two fluids and the solid walls of the capillary tube results to different interfacial tensions. This causes the familiar capillary rise of the fluid surface inside the capillary tube. If the fluid is the wetting phase, the rise will be positive and if the fluid is non-wetting the rise will be negative.

For simplicity, let us consider an example for the first case: water rises from a free surface in a capillary tube (see Fig. 11). The interfacial tension between water and air  $\sigma_{nw}$  and the contact angle  $\omega$  are also indicated. The only force counteracting to  $\cos\omega \cdot \sigma_{nw}$  is the weight of the water inside the tube. Thus, the water surface inside the tube will stop rising at  $h_c$  when these two forces balance. For an equilibrium to be established it is necessary that pressure at the water-air interface inside the tube is discontinuous. The difference between the non-wetting (air) and the wetting (water) phase pressures at the interface is called *capillary pressure*  $p_c$

$$p_c^{int} = p_n^{int} - p_w^{int}. \quad (6)$$

Capillary pressure in the case of a cylindrical capillary tube with radius  $r$  is formulated in LAPLACE (1806) [62] with

$$p_c^{int} = \frac{2\sigma_{nw}\cos\omega}{r}. \quad (7)$$

As can be easily recognized in Eq. 7, capillary pressure depends on the one hand on the geometry of the tube (radius  $r$ ) and on the other hand on the physical prop-

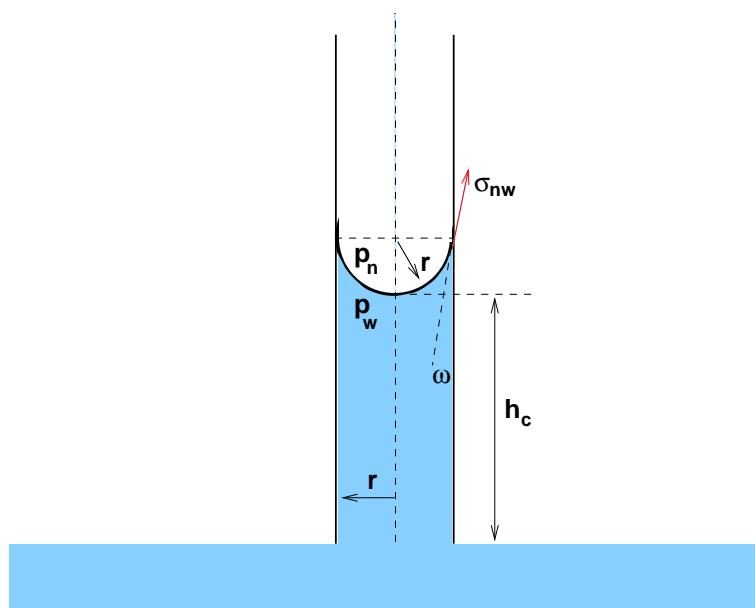


Figure 11: Capillary rise  $h_c$  in a cylindrical capillary tube with radius  $r$ .

erties of the fluids and the solid surface (interfacial tension  $\sigma_{nw}$  and contact angle  $\omega$ ). The same principles apply for any combination of fluid phases. SCHIEGG (1979) [89] gives an overview of the capillary behavior using various combinations of fluids.

On the pore scale, a porous medium can be conceptualized as a complex arrangement of interconnected capillaries with variable lengths and radii. This is illustrated in Fig. 12. If water and air co-exist in a porous medium, water is attracted by the solid phase and fills narrow passages between the grains and pores with smaller diameters, while air occupies the larger pores. The interface between water and air has the typical curved shape of a meniscus and is characterized by a pressure jump across the interface (see Fig. 12a). This pressure difference is equal to the capillary pressure which, as discussed above, is bound to the radius of the respective capillary. It is now assumed that due to some externally applied pressures (i.e. a boundary condition) the pressure of water decreases, the meniscus will move to a new position in favor of air occupying the pore, until pressure equilibrium is established again (see Fig. 12b). In this case, air will enter the larger capillaries previously occupied by water, while the smallest capillaries will remain as before filled with water. Obviously, the configuration of Fig. 12b corresponds to less volume of water in the pores and larger capillary pressure at the menisci compared to Fig. 12a.

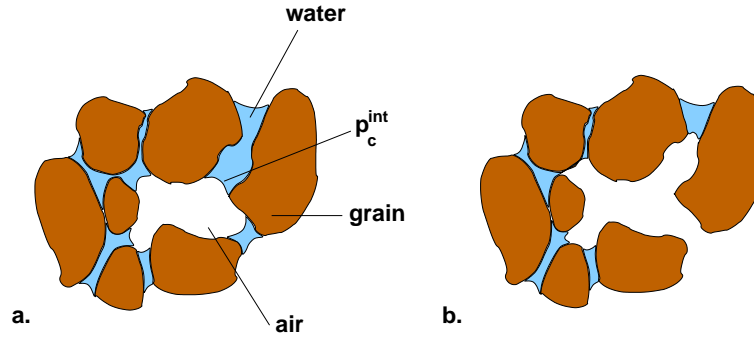


Figure 12: Distribution of water (wetting phase) and air (non-wetting phase) on the pore scale.

### 2.3.2 Capillary pressure on the local scale

Consider a bundle of parallel, vertical capillary tubes in contact with a free surface of a wetting fluid. Depending on the radii, various capillary rises are observed in the tubes and, consequently, various values of capillary pressure at the fluid-fluid interfaces. One can plot the different fluid contents in the bundle of tubes versus the corresponding values of capillary rise or, in other words, capillary pressure (Fig. 13). The wetting fluid content  $\theta_w$  becomes smaller than 1.0 for the minimal capillary pressure (or rise), that relates to the tube with the largest radius. Beyond that point,  $\theta$  decreases with capillary pressure monotonically. The largest capillary pressure is observed at the tube with the smallest radius, as at this rise the fraction of wetting fluid in the bundle reaches the minimum value.

In real porous media, however, the pore geometry is much more complex than that of Fig. 13. On the local scale, the exact distribution of the phases in the pore space is replaced with volumetric water contents. This was analyzed in Sect. 2.1. Similarly, the phase pressures  $p_n$  and  $p_w$  are considered on the local scale averaged over a REV. The same principle is applied for capillary pressure and a value of capillary pressure is assigned for a REV. On the pore scale, capillary pressure is by definition equal to the difference of the pressures of the two phases at the interface. It is assumed that also on the local scale the capillary pressure is the difference of the phase pressures

$$p_c = p_n - p_w. \quad (8)$$

This is a significant assumption that is often discussed in the literature. HASSANIZADEH AND GRAY (1993) [39] and BELIAEV AND HASSANIZADEH (2001) [11] have proposed an alternative relationship incorporating a dynamic term that includes the rate of change of saturation. To examine the validity of Eq. 8, several studies have been carried out by means of pore-network models [DAHLE ET

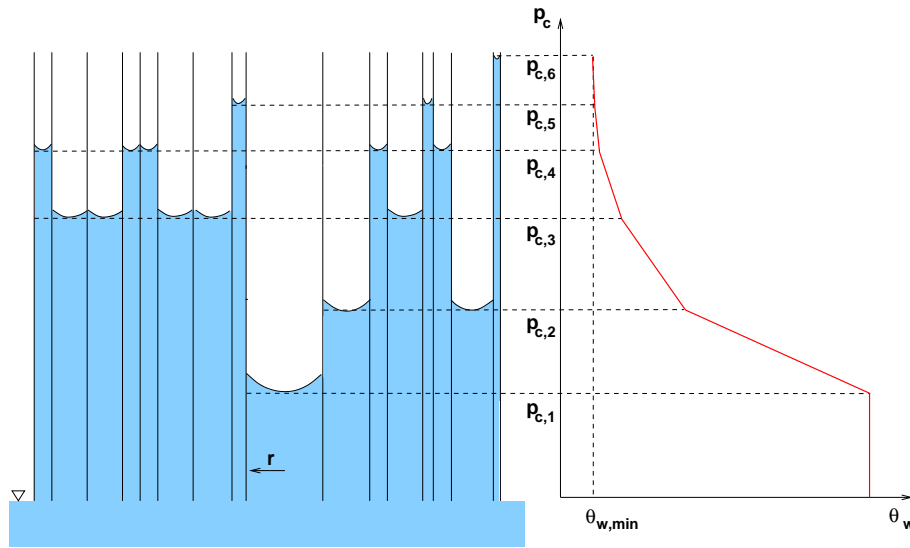


Figure 13: Capillary pressure-saturation relationship for a simple bundle of capillary tubes.

AL. (2002) [23]; GIELEN ET AL. (2002) [33]; HASSANIZADEH ET AL. (2002) [38]] and experimental investigations [HASSANIZADEH (2003) [37]; HASSANIZADEH ET AL. (2004) [36]] However, the ongoing research in this field is still at early stage and in this work it is assumed that Eq. 8 is valid.

Capillary pressure dimensionally corresponds to energy per unit volume and in soil physics refers to the matric potential of the water phase. Water flow in porous media occurs from a higher to a lower potential, which implies that capillary pressure should be negative (otherwise flow from lower to higher saturations would occur). However, in this work the consideration of capillary pressure is based on the approach described in Sect. 2.3.1 and therefore it is taken as a positive quantity.

Having defined a capillary pressure also for the local scale, it is possible to relate it to saturation. As demonstrated for the pore scale in the previous section, increased capillary pressure at the water-air interfaces relates to less volume of water occupying the pores of the porous medium. This can be transferred to the local scale as illustrated in Fig. 14: different values of local-scale capillary pressure correspond to different saturations of water and air in the same REV. Hence, it is expected that capillary pressure on the local scale can be formulated as a function of saturation

$$p_c = p_c(S_w). \quad (9)$$

The relationship between capillary pressure and saturation plays an important

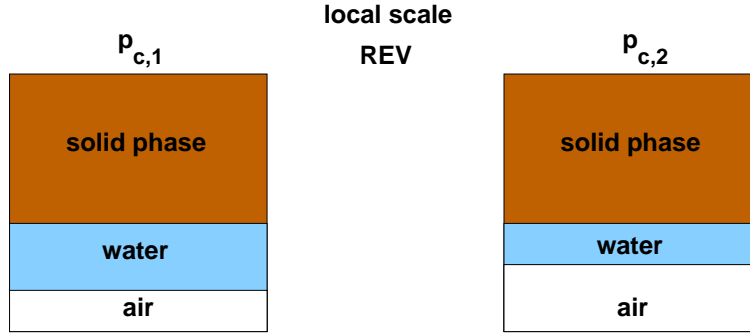


Figure 14: Different saturations of water (wetting phase) and air (non-wetting phase) on the local scale correspond to different capillary pressures.

role in two-phase flow in porous media, as it relates saturation to the difference of phase pressures (Eq. 8 and 9). Capillary pressure-saturation curves for real porous media are commonly measured with experimental methods. Until today, there is no functional relationship between capillary pressure and saturation rigorously derived for porous media.

Several empirical models for the parameterization of a general capillary pressure-saturation functional relationship have been proposed [i.e. BROOKS AND COREY (1964) [13]; CAMPBELL (1974) [17]; BRUTSAERT (1967) [14]; VAN GENUCHTEN (1980) [99], for an overview see SHETA (1999) [92]]. These models in general employ shape parameters to fit measured resp. calculated capillary pressure-saturation data. BROOKS AND COREY (1964) [13] have formulated the following empirical function to describe the  $p_c$ - $S_w$  relationship:

$$p_c = p_e \cdot (\bar{S}_w)^{-\frac{1}{\lambda}} \quad \text{for } p_c \geq p_e, S_w \geq S_{wr}, \quad (10)$$

where  $\bar{S}_w$  is the *effective* saturation defined as

$$\bar{S}_w = \frac{S_w - S_{wr}}{1 - S_{wr}}. \quad (11)$$

In the latter,  $S_{wr}$  [-] is the *residual* saturation of the wetting phase defined as the minimum wetting phase saturation that can be achieved if a saturated porous medium is fully drained. This is typically not zero. For instance, in a water-air system, small pores surrounded by large pores will hold water while the large pores are dry. Also, water forms thin films that cover the grains of the porous medium and, even if it is entirely drained, the smallest pores and cracks keep the water attached due to capillary forces (see Sect. 2.3.1). This residual water can be extracted by evaporation but not by gravity or pressure gradients.

The *entry* pressure  $p_e$  [Pa] is the capillary pressure at which the reduction of the wetting phase saturation begins (see Fig. 15). A similar shape was observed in the



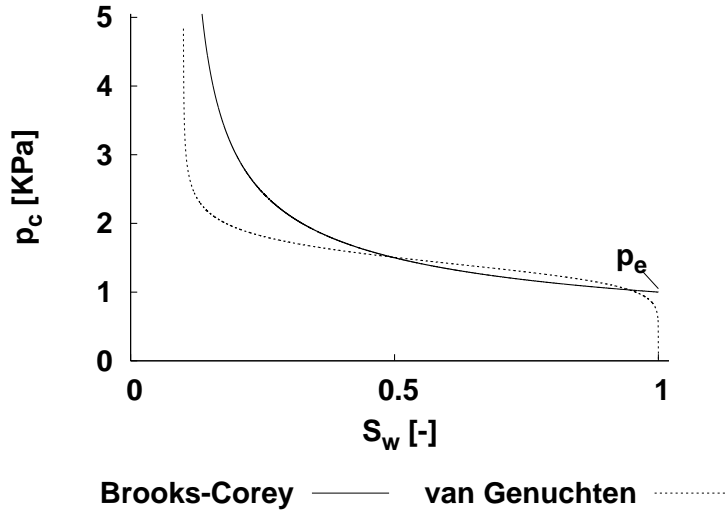


Figure 15: Capillary pressure-saturation from BROOKS AND COREY (1964) [13] and from VAN GENUCHTEN (1980) [99].

simple bundle of capillary tubes example (see Fig. 13): after a certain capillary pressure value that relates to the tube with the largest radius, the saturation of water decreases. Similarly, in a porous medium the entry pressure theoretically relates to the pore with the largest diameter at a non-wetting phase front. In this pore-scale context, it is referred to as the *displacement* pressure  $p_d$ .

The parameter  $\lambda$  [-] in Eq. 10 is a shape parameter that determines the inclination of a  $p_c$ - $S_w$  curve. Large  $\lambda$  values produce flat curves. A decrease in  $\lambda$  results to steeper curves. The reason for different inclinations of  $p_c$ - $S_w$  curves can also be explained with the bundle of capillary tubes example: if the bundle consists only of tubes with a large and a small radius, the  $p_c$ - $S_w$  relationship will be a flat line for a large range of saturation (saturation will decrease dramatically in one step due to the tubes with the large radius) and consequently a very steep one because of the tubes with the smaller radius. On the other hand, a larger distribution of tube radii results to a steeper  $p_c$ - $S_w$  relationship (Fig. 13). The same applies for porous media: a wide distribution of pore sizes gives  $p_c$ - $S_w$  curves with larger inclination. Therefore,  $\lambda$  can be related to the grain size distribution of a porous medium.

The parameterization from VAN GENUCHTEN (1980) [99] is formulated as

$$p_c = \frac{1}{\alpha} [(\bar{S}_w)^{-\frac{1}{m}} - 1]^{\frac{1}{n}} \quad \text{for } p_c \geq 0. \quad (12)$$

This model considers also capillary pressure values that are smaller than  $p_e$  and larger than zero (see Fig. 15). The parameter  $\alpha$  [1/Pa] relates to the inverse of the entry pressure. The parameter  $n$  [-] is a shape parameters similar to the  $\lambda$  parameter of the BROOKS AND COREY function. Large  $n$  values relate to poorly

distributed porous media (flat  $p_c-S_w$  curves). The parameter  $m$  [-] can be defined according to MUALEM (1976) [73]

$$m = 1 - \frac{1}{n}. \quad (13)$$

## 2.4 The influence of heterogeneities

In the following an example is used to discuss the influence of heterogeneities on the two-phase flow system behavior. A domain that is initially saturated with water is considered. The domain is open to the atmosphere, so that air can enter into it from the top. The left and the right side are closed so that no flow occurs. The domain consists of two sub-domains: sub-domain I (coarse sand) and sub-domain II (fine sand). The pressure of water is then externally reduced at the bottom gradually. Air will infiltrate from the top and will reach the material interface between the coarse and the fine sand (see Fig. 16).

From the pore scale consideration, each pore radius at the material interface relates to a certain capillary pressure. In the configuration of Fig. 16 (left), the capillary pressure is smaller than the pressure that is needed for the pore to be entered by air, the pore displacement pressure. To move an interface into the pore, the pressure of water has to be further decreased so that the capillary pressure can exceed the pore displacement pressure.

At the boundary between coarse and fine sand, the pore with the largest radius will be the first infiltrated by air. Theoretically, this effect is captured on the local scale with the entry pressure in the  $p_c-S_w$  curves. Based on Eq. 8, the entry

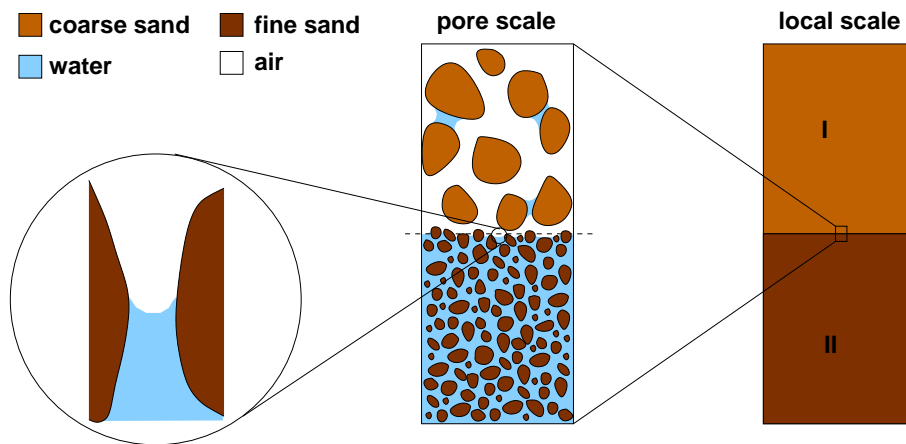


Figure 16: Phase behavior at the boundary between a coarse and a fine sand.

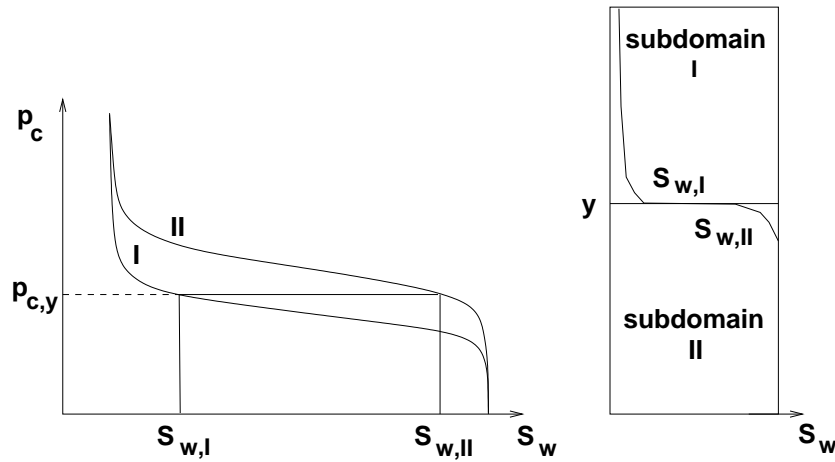


Figure 17: Derivation of different saturations across the boundary between a coarse and a fine sand based on the  $p_c$ - $S_w$  curves.

pressure corresponds to the phase pressure difference required so that the non-wetting phase can displace the wetting phase. In this example, the water pressure has to decrease so that the pressure difference exceeds the entry pressure of the fine sand and air can enter the fine sand sub-domain. In the VAN GENUCHTEN model entry pressure is approximated with a very steep increase in capillary pressure for maximum saturation (see Fig. 15). In this case, the  $p_c$ - $S_w$  relationship at full saturation remains a continuous function.

Once the entry pressure is exceeded, air infiltrates the fine sand and thus water saturation in sub-domain II has to increase (Fig. 17, right). The coarse and fine sand are characterized by different  $p_c$ - $S_w$  curves. At the boundary between coarse and fine sand, pressure has to be continuous. As Fig. 17 (left) shows, this pressure relates to two different saturation values on each side. This results, in general, to discontinuities of saturation at material interfaces. In Fig. 17 (left) this is shown with the unique capillary pressure  $p_{c,y}$  at the material interface that corresponds to two saturations  $S_{w,I}$  and  $S_{w,II}$  across it.

## 2.5 The Darcy law

The flow velocity  $\mathbf{u}$  of water in a porous medium is given from Darcy's law

$$\mathbf{u} = -\mathbf{K} \frac{\rho g}{\mu} \nabla h. \quad (14)$$

$h$  [m] is the hydraulic head,  $\mathbf{K}$  [ $\text{m}^2$ ] the *absolute permeability* tensor,  $\mu$  [Pa s] the dynamic viscosity of water,  $\rho$  [ $\text{kg}/\text{m}^3$ ] the density of water and  $g$  [ $\text{m}/\text{s}^2$ ] the gravity.

This relationship was found experimentally for 1-D from DARCY (1856), however it has been derived based on a momentum conservation using averaging [see i.e. WHITAKER (1986) [105]; QUINTARD AND WHITAKER (1994) [81, 82, 83]] or homogenization [HORNUNG (1997) [46]] techniques.

The absolute permeability is a material property that depends only on the porous medium. Therefore, it only depends on position in space in case of heterogeneous porous media (and not on fluid properties). The absolute permeability is defined as a symmetric tensor:

$$\mathbf{K} = \begin{bmatrix} \kappa_{xx} & \kappa_{xy} & \kappa_{xz} \\ \kappa_{xy} & \kappa_{yy} & \kappa_{yz} \\ \kappa_{xz} & \kappa_{yz} & \kappa_{zz} \end{bmatrix} \quad (15)$$

As a tensorial quantity, permeability may vary in direction. Anisotropic permeability can be used for porous media that have a preferable flow direction. This work restricts to isotropic porous media so that the absolute permeability in a x-y-z coordinate system reads:

$$\mathbf{K} = \begin{bmatrix} \kappa & 0 & 0 \\ 0 & \kappa & 0 \\ 0 & 0 & \kappa \end{bmatrix} \quad (16)$$

The absolute permeability is commonly measured in experiments conducted in saturated columns of porous media, by applying different pressure gradients while measuring the outflow (see i.e. JURY (1991) [52]).

The Darcy's law is extended for two-phase flow:

$$\mathbf{u}_\alpha = -\frac{k_{r\alpha}(S_\alpha)\mathbf{K}}{\mu_\alpha} (\nabla p_\alpha - \rho_\alpha \mathbf{g}). \quad (17)$$

$p$  [Pa] is the pressure, the index  $\alpha$  denotes the fluid phases,  $\mathbf{g}$  [m/s<sup>2</sup>] the gravity vector while the non-dimensional scalar  $k_{r\alpha}$  [-] is called *relative permeability*.

When two phases are present in the pore space, the one phase reduces the flow path of the other phase and thus the permeability. The relative permeability captures the effect of the reduced flow paths of a phase and can be considered as a scaling factor

$$0 \leq k_{r\alpha}(S_\alpha) \leq 1. \quad (18)$$

The value of the relative permeability depends on the phase effective saturation. For  $\bar{S}_\alpha = 0.0$  [-], the relative permeability  $k_{r\alpha}$  also has to be zero as a continuous

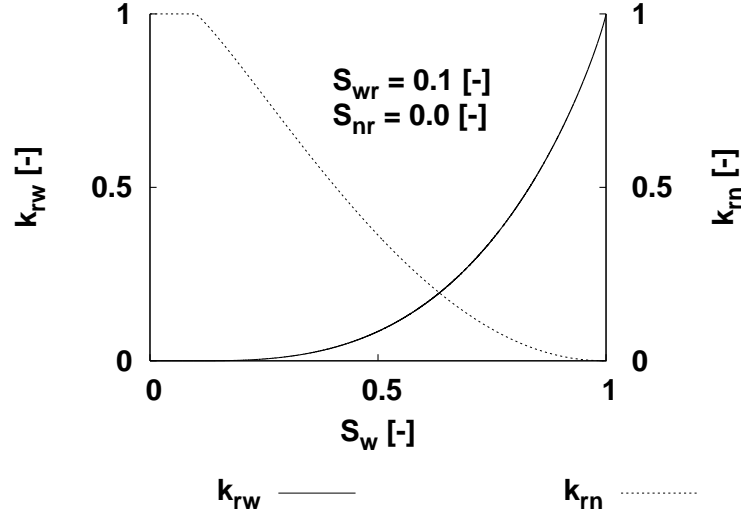


Figure 18: Relative permeability-saturation from MUALEM/VAN GENUCHTEN.

phase is not present. Similarly, for  $\bar{S}_\alpha = 1.0$  [-] it is valid that  $k_{r\alpha} = 1.0$  [-]. Between these extreme values the relative permeability has to increase monotonically with the phase saturation.

The relative permeability-saturation relationship can either be derived empirically with experimental methods or semi-empirically with pore network models and analytical solutions based on capillary bundle models [BURDINE (1953) [16], MUALEM (1976) [73], BROOKS AND COREY (1964) [13], VAN GENUCHTEN (1980) [99]]. A literature review and an analytical description of the most widely used relative permeability-saturation conceptual models is given in SHETA (1999) [92]. In this work, the MUALEM/VAN GENUCHTEN concept is used that relates relative permeability of the wetting and the non-wetting phase to the effective phase saturation according to the relationships

$$k_{rw} = \bar{S}_w^\tau [1 - (1 - \bar{S}_w^{1/m})^m]^2, \quad (19)$$

$$k_{rn} = (1 - \bar{S}_w)^\tau (1 - \bar{S}_w^{1/m})^{2m}. \quad (20)$$

The indices  $w$  and  $n$  stand for the wetting and the non-wetting phase,  $m$  is the VAN GENUCHTEN shape parameter (see Sect. 2.3.2) and  $\tau$  [-] is the tortuosity. For the analytical derivation of the MUALEM/VAN GENUCHTEN concept it is commonly introduced that  $\tau = 0.5$  [-]. Fig. 18 illustrates an example of  $k_r$ - $S_w$  curves using the MUALEM/VAN GENUCHTEN model.

## 2.6 Mathematical description of two-phase flow in porous media

To formulate a model for two-phase flow in porous media, mass balance equations are accounted for the individual phases in a control volume  $V$ . Based on an Eulerian approach, a mass balance can be formulated for each phase  $\alpha$  in a non-deforming control volume with the *Reynold's* transport theorem. The storage and sources/sinks terms are described with volume integrals over  $V$ , while the flux term is described with an areal integral of fluxes over the boundaries  $\Gamma$  of the control volume:

$$\frac{\partial}{\partial t} \int_V \phi S_\alpha \varrho_\alpha dV + \int_\Gamma \phi \varrho_\alpha \mathbf{v}_\alpha d\Gamma - \int_V \varrho_\alpha q_\alpha dV = 0. \quad (21)$$

$\phi$  [-] is the porosity,  $S_\alpha$  [-] the saturation,  $\mathbf{v}_\alpha$  [m/s] the average velocity and  $q_\alpha$  [ $\text{m}^3/(\text{m}^3 \text{ s})$ ] sources or sinks for phase  $\alpha$ . Here, only the convective flux in the flux term is considered. Using the Gaussian integral theorem, the flux term can be reformulated to obtain

$$\frac{\partial}{\partial t} \int_V \phi S_\alpha \varrho_\alpha dV + \int_V \nabla(\phi \varrho_\alpha \mathbf{v}_\alpha) dV - \int_V \varrho_\alpha q_\alpha dV = 0. \quad (22)$$

It is also valid that

$$\mathbf{u}_\alpha = \phi \mathbf{v}_\alpha, \quad (23)$$

where  $\mathbf{u}_\alpha$  [m/s] is the Darcy velocity. Inserting Eq. 23 into Eq. 22 and assuming continuous integrands yields the differential form of the balance equation,

$$\frac{\partial(\phi S_\alpha \varrho_\alpha)}{\partial t} + \nabla(\varrho_\alpha \mathbf{u}_\alpha) - q_\alpha \varrho_\alpha = 0. \quad (24)$$

The transition from the integral form (Eq. 22) to the differential form (Eq. 24) of the balance equations requires continuity of the functions  $\frac{\partial(\phi S_\alpha \varrho_\alpha)}{\partial t}$ ,  $\nabla(\varrho_\alpha \mathbf{u}_\alpha)$  and  $q_\alpha \varrho_\alpha$ . This condition can be violated i.e. through changes of material properties formed with jumps in permeability. In such cases,  $V$  is divided into subdomains where certain jump conditions satisfy the continuity requirements (see Sect. 4.1). The extended Darcy's law (Eq. 17) is inserted into the mass balance Eq. 24 to obtain the continuity equation for phase  $\alpha$

$$\frac{\partial(\phi S_\alpha \varrho_\alpha)}{\partial t} + \nabla \cdot \left[ -\varrho_\alpha \frac{k_{r\alpha}}{\mu_\alpha} \mathbf{K} (\nabla p_\alpha - \varrho_\alpha g) \right] - q_\alpha \varrho_\alpha = 0. \quad (25)$$

As introduced in Sect. 2.2, in this work fluids are considered to be incompressible and porosity time-invariant. With the supplementary constraints

$$p_n = p_c + p_w \quad (26)$$

and

$$S_w + S_n = 1, \quad (27)$$

one obtains for the wetting and the non-wetting phase

$$-\phi \varrho_w \frac{\partial S_n}{\partial t} + \nabla \cdot \left[ -\varrho_w \frac{k_{rw}}{\mu_w} \mathbf{K} (\nabla p_w - \varrho_w g) \right] - q_w \varrho_w = 0, \quad (28)$$

$$\phi \varrho_n \frac{\partial S_n}{\partial t} + \nabla \cdot \left[ -\varrho_n \frac{k_{rn}}{\mu_n} \mathbf{K} (\nabla p_w + \nabla p_c - \varrho_n g) \right] - q_n \varrho_n = 0. \quad (29)$$

Additionally, the capillary pressure  $p_c$  [Pa] and the relative permeabilities  $k_{rw}$  [-] and  $k_{rn}$  [-] are functions of saturation (see Sect. 2.3.2 and 2.5). Thus, the unknowns in Eqs. 28 and 29 are reduced to two and the system is closed.

### 3 Capillary hysteresis

Two types of fluid displacement are distinguished in two-phase flow in porous media: *drainage* takes place when the wetting phase is displaced by the non-wetting phase and *imbibition* when the wetting phase displaces the non-wetting phase. The interaction between the two phases and their distribution in a porous medium strongly depend on the type of displacement that takes place. It is also influenced from the state at which a change of displacement type took place, hence a two-phase flow system also depends on its history. The dependency of two-phase flow behavior on the type and the history of phase displacement is called *hysteresis*. The term originates from the Greek word *υστέρηση* meaning 'deficiency' and was first introduced for magnetism by EWING (1895) [28] as:

*When there are two quantities  $M$  and  $N$ , such that cyclic variations of  $N$  cause cyclic variation of  $M$ , then if the changes of  $M$  lag behind those of  $N$ , we may say that there is hysteresis in the relation of  $M$  and  $N$ .*

The term hysteresis can be found in several scientific fields (i.e. physics, mechanics, economics, biology) and is generally used to describe history- and direction-dependent processes [KRASNOSELSKII AND POKROVSKII (1989) [57]; FRANZ (1990) [30]; MAYERGOYZ (1991) [69]; BROKATE AND SPREKELS (1996) [12]; SETTERFIELD (1997) [91]; KREJCI AND SPREKELS (1999) [58]; POMERENING ET AL. (2003) [79]].

Hysteretic effects make the investigation of two-phase flow in porous media complicated and require special attention. From the local-scale viewpoint, hysteresis appears in the capillary pressure-saturation relationship. Hysteretic  $p_c$ - $S_w$  relationships can be observed in natural hydrosystems, for instance during water infiltration in the unsaturated zone or fluctuations of a groundwater table [STAUFFER AND DRACOS (1986) [94]]. They also play a significant role in several technical applications that involve reversals of the direction of fluid displacement. A few examples are the water-oil displacement during oil recovery, the wetting and drying of paper in the paper industry, the development of fuel cells and several more. A typical environmental application is the infiltration of a DNAPL in a heterogeneous aquifer and then the removal of the contamination



with pump-and-treat methods.

In Sect. 2.3.2, the capillary pressure-saturation relationship was qualitatively derived for a bundle of parallel, vertical capillary tubes. In such an idealized case, both drainage and imbibition are fully reversible. In real soils, however, the high irregularity of pore sizes and their complex arrangement generate hysteresis. Therefore, the causes of hysteresis can be understood only by looking at processes occurring on the pore scale of a porous medium. Although these processes cannot be resolved on the local scale, their effect is depicted in the  $p_c$ - $S_w$  relationship.

In the following, hysteresis effects will be first discussed on the pore scale (Sect. 3.1), focusing on the mechanisms that generate local-scale hysteresis. The form of hysteretic  $p_c$ - $S_w$  relationships on the local scale as well as concepts used for their approximation are then discussed in Sect. 3.2.

### 3.1 Hysteresis on the pore scale

Hysteresis on the pore scale can be observed with three effects: the hysteresis related to the contact angle, the inkbottle effect and the entrapment of non-wetting phase.

#### Contact angle hysteresis

If the non-wetting phase displaces the wetting phase (drainage), the contact angle is smaller than that observed in the reversed process (imbibition). This is qualitatively illustrated in Fig. 19. An example of contact angle hysteresis is the shape of a raindrop: the advancing (water displaces air) contact angle is larger compared to the retreating (air re-displaces water) contact angle.

Additionally, the fluid displacement process and consequently the contact angle are influenced by microstructures of the solid surface (see Fig. 19) and therefore might differ for drainage and imbibition.

#### Inkbottle effect

Consider a single pore that is wider in the middle and narrow at the two throats (see Fig. 20). It is assumed that the pore is initially filled with the wetting phase  $w$  and the interface to the non-wetting phase  $n$  is positioned at the left opening as shown in Fig. 20,I. This fluid distribution of situation I relates to an interfacial capillary pressure  $p_{c,1}$ . Reducing the pressure of the wetting phase at the right opening will force the interface to move into the pore and reach the

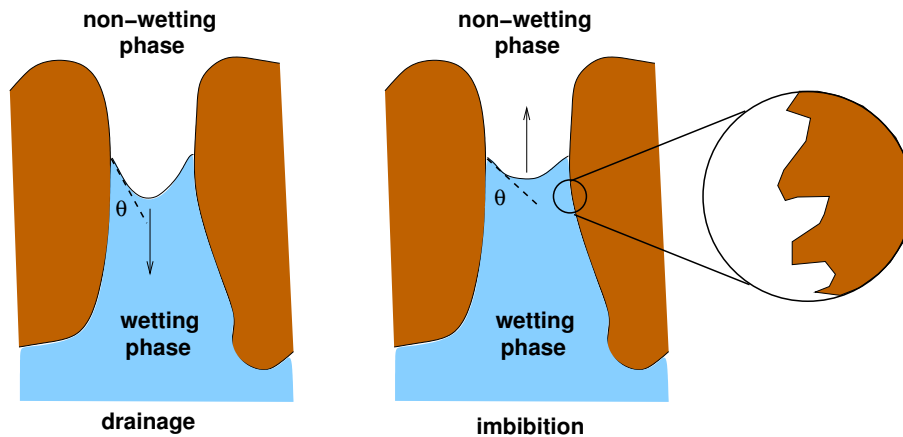


Figure 19: Contact angle for drainage and imbibition.

minimal pore radius at the left opening (Fig. 20,II). In this case, the capillary pressure  $p_{c,2}$  is smaller than the pore displacement pressure. Once the capillary pressure exceeds the displacement pressure, the entire cavity will be emptied leading to the fluid distribution of situation III (drainage), because the pore radius in the cavity is too large to sustain the interface with capillary pressure  $p_{c,3}$ . If now the process is reverted (imbibition) by increasing the pressure of the wetting phase at the right opening (same pressure as in situation II), the fluid distribution will not be the same as in situation II. Instead, the wetting phase will enter the pore only until the radius of the interface corresponds to  $p_{c,2}$  (situation IV). Similarly, in order to fill again the entire cavity with the wetting phase, the wetting phase pressure has to become larger than that of configuration I and increase until the interface reaches the largest radius of the cavity. This situation would correspond to a capillary pressure  $p_{c,0}$ . After that

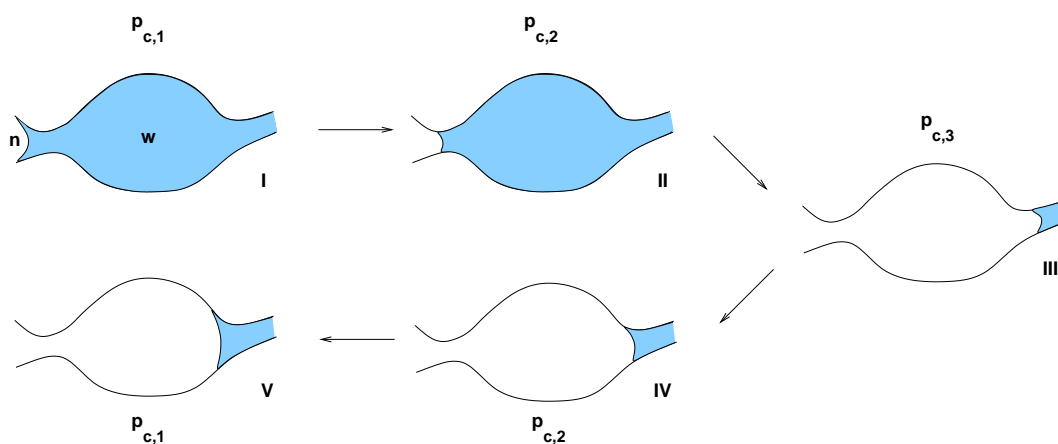


Figure 20: The inkbottle effect.

point, the radius decreases again and thus the wetting fluid will occupy the entire cavity and the left pore throat. Such discontinuous changes of fluid content observed in capillaries are referred to as *Haines jumps* [HAINES (1930) [34]]. As described above, Haines jumps occur in drainage when the interface passes the smallest radius and in imbibition when the interface passes the largest radius.

### Phase trapping

When an imbibition process takes place in a porous medium, the displacement of the non-wetting phase from a wetting phase may cause the trapping of non-wetting phase inside the pores. This way, the non-wetting phase can form disconnected ganglia and blobs that remain immobile as they are surrounded by the connected wetting phase. There are two mechanisms responsible for the trapping of a non-wetting phase during an imbibition event: the *snap-off* and the *by-passing* effect [CHATZIS AND DULLIEN (1983) [19]].

The snap-off effect is illustrated in Fig. 21. Blobs of the displaced non-wetting phase can be held back, depending on the one hand on the contact angle and on the other hand on the relationship between diameters of pore cavities and pore throats [WARDLAW (1982) [103]]. The by-passing effect occurs in pathways that are connected but have different diameters. As shown in Fig. 22, two capillaries with different radii surrounding a grain can lead to the entrapment of the non-wetting phase in the capillary with the largest radius. MOORE AND SLOBOD (1956) [71] have shown that the amount of trapped fluid depends on the ratio between viscous (due to pressure gradients) and capillary forces and on the ratio of the two diameters. Dominating capillary forces and large diameter ratios lead to

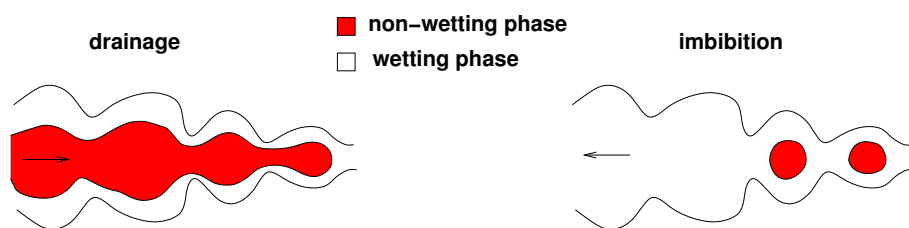


Figure 21: The snap-off effect.

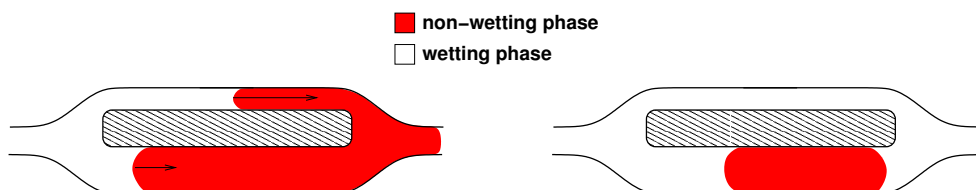


Figure 22: The by-passing effect.

larger amount of phase trapping.

In a groundwater contamination scenario, where the non-wetting phase is a DNAPL and the wetting phase is water, this effect has a significant impact on the efficiency of a remediation scheme. Isolated parts of DNAPL are difficult to be removed and form a source of long-term contamination. In such applications, it is therefore crucial to predict correctly the amount of trapped phase from a local-scale consideration.

## 3.2 Hysteresis on the local scale

The pore-scale effects of contact angle hysteresis, inkbottle behavior and phase trapping are not individually recognizable on the local scale, yet have a significant influence on the behavior of a two-phase flow system. On the local scale, the averaged effect of these phenomena is observed as a hysteretic behavior in the capillary pressure-saturation curves. The first experimental evidence of hysteretic effects in porous media was reported in HAINES (1930) [34] and RICHARDS (1931) [85].

Hysteresis may also appear in the relative permeability-saturation relationship. However,  $k_r$ - $S_w$  hysteresis is normally regarded insignificant compared to  $p_c$ - $S_w$  hysteresis and in this work it will be neglected. Apart from this, there is little information found in the literature related to experimental investigations of  $k_r$ - $S_w$  hysteresis [GERHARD AND KUEPER (2003) [32], MILLER ET AL. (1998) [70]].

Consider a porous medium initially fully saturated with a wetting phase. The monotonic increase of capillary pressure during the drainage of the porous medium can be described i.e. with the VAN GENUCHTEN parameterization (see Eq. 12). The curve 1  $\rightarrow$  2 in Fig. 23 is called *main drainage curve* (MDC). When the porous medium is entirely drained, the wetting phase saturation reaches a residual value. With this situation as the initial state one may observe now the reversed process: the evolution of the  $p_c$ - $S_w$  curve during imbibition. The *main imbibition curve* (MIC) is illustrated in Fig. 23 with the curve 2  $\rightarrow$  3. For a given capillary pressure, less wetting phase saturation is observed in imbibition compared to drainage. This behavior is similar to the inkbottle effect described above. Apart from this, it is also observed that the MIC ends to a smaller wetting phase saturation than the MDC. This occurs due to the non-wetting phase entrapment during the imbibition.

If the starting state for imbibition does not correspond to a drained medium but any intermediate situation, a *primary imbibition scanning curve* (PISC) is obtained. The PISC corresponds to the curve 4  $\rightarrow$  5 in Fig. 23. In this case, the maximum wetting phase saturation lies somewhere between the maximum saturations of

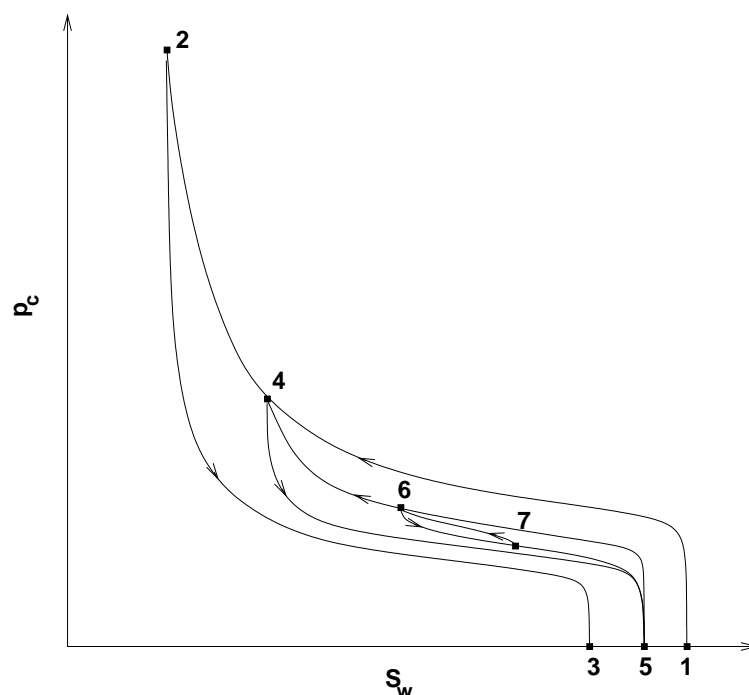


Figure 23: Hysteresis in the capillary pressure-saturation relationship.

the MIC and the MDC (point 5 has to lie somewhere between points 3 and 1). If this saturation is reached and then a new drainage takes place, a *primary drainage scanning curve* (PDSC) is obtained. This is indicated with the curve  $5 \rightarrow 4$  in Fig. 23. The loop formed through drainage and imbibition  $4 \rightarrow 5 \rightarrow 4$  is called a *hysteresis loop*.

Similarly, any further switch from drainage to imbibition (and vice versa) starting from a scanning curve, will generate hysteresis loops of *secondary* scanning drainage or imbibition curves (i.e. curve  $7 \rightarrow 6$  in Fig. 23). It becomes obvious that there is an infinite number of possible  $p_c$ - $S_w$  configurations, depending on the type of displacement process and the initial states (i.e. points 1 to 7 in Fig. 23). One can also observe that all possible combinations of  $p_c$ - $S_w$  on primary or secondary scanning paths have to lie somewhere between the main drainage and the main imbibition curve.

The existence of the dependency of  $p_c$ - $S_w$  hysteresis on the pore-scale effects described in Sect. 3.1 is –at least theoretically– understood and well-established. Still, the quantitative description of this dependency –by means of a theoretical derivation of  $p_c$ - $S_w$  hysteresis from pore-scale effects– is not possible due to the enormous complexity of the processes taking place in the pore-scale structure of real porous media.

There are, however, several formulations and concepts found in the literature that

approximate  $p_c$ - $S_w$  hysteresis for two-phase flow in porous media. These include empirical approaches based on scaling [SCOTT ET AL. (1983) [90]; KOOL AND PARKER (1987) [56]; PARKER AND LENHARD (1987) [78]; GERHARD AND KUEPER (2003) [31]], dependent domain models [MUALEM (1974) [72]; MUALEM (1984) [74]], while new approaches aim to consider additional variables (other than saturation) in order to quantify capillary pressure on the local scale [REEVES AND CELIA (1996) [84]; WEI AND DEWOOLKAR (2006) [104]; JOEKAR-NIASAR ET AL. (2007) [49]].

In the following, the two hysteresis concepts used in this thesis will be analyzed. The first is a *play-type* concept proposed from BELIAEV AND HASSANIZADEH (2001) [11] where saturation on a scanning curve does not change and thus scanning curves are always considered to be vertical. The second is the scaling concept from PARKER AND LENHARD that can reproduce, in general, realistic scanning curves of variable saturation.

### 3.2.1 The play-type $p_c$ - $S_w$ hysteresis

The play-type form of hysteresis is a general concept used in many fields as a first approximation of hysteretic behaviors. In the case of two-phase flow in porous media, it was first incorporated by BELIAEV AND HASSANIZADEH in the framework of an extended dynamic capillary pressure relationship. However, play-type hysteresis can also be applied in the classic  $p_c$ - $S_w$  approach that is used in this work.

The play-type hysteresis concept can be formulated with the relationship

$$S_w = \begin{cases} {}^{MDC} f(p_c) & \text{for } p_c = p_c^{MDC} \\ S_w^{switch} & \text{for } p_c^{MDC} > p_c > p_c^{MIC} \\ {}^{MIC} f(p_c) & \text{for } p_c = p_c^{MIC}. \end{cases} \quad (30)$$

Here,  ${}^{MDC} f$  and  ${}^{MIC} f$  denote the functions that describe the main drainage and the main imbibition  $p_c$ - $S_w$  curve.  $p_c^{MDC}$  and  $p_c^{MIC}$  is the capillary pressure from the main drainage and main imbibition curve, respectively. With  $S_w^{switch}$  is notated the saturation at which a switch from drainage to imbibition or vice versa takes place. As seen in Fig. 24, it is only necessary to keep track of the saturation and use  $S_w^{switch}$  to represent hysteresis. Scanning curves are approximated by vertical lines where the saturation remains constant (lines 4  $\rightarrow$  5 and 6  $\rightarrow$  7 in Fig. 24).

In the play-type approach, saturation after a switch from drainage to imbibition does not change until the capillary pressure reaches the value on the main imbibition curve  $p_c^{MIC}$ . Once capillary pressure reaches the value  $p_c^{MIC}$ , the slope

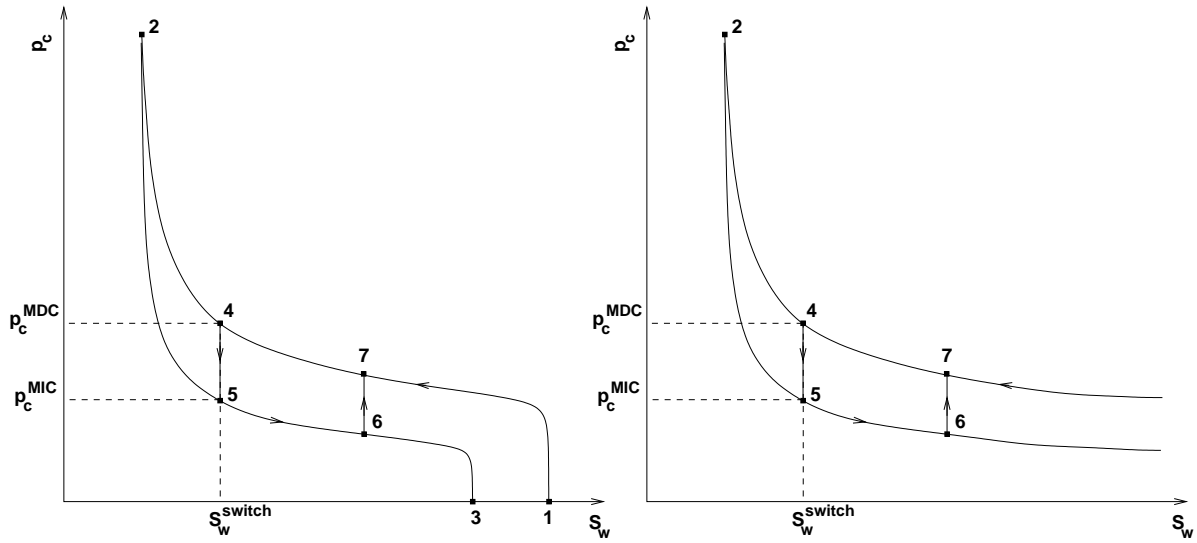


Figure 24: Play-type hysteresis in the VAN GENUCHTEN (left) and the BROOKS AND COREY (right) parameterization.

changes instantly and saturation decreases following the main imbibition curve. This behavior resembles the Haines jumps observed on the pore scale (see Sect. 3.1). On the pore scale, once the wetting phase reaches the maximum radius, it instantly occupies the rest of the pore as well due to the capillary forces. On the local scale, the gradient of the capillary pressure-saturation curve changes instantly when capillary pressure reaches the value  $p_c^{MIC}$ . Therefore, during imbibition in the play-type hysteresis concept the capillary pressure  $p_c^{MIC}$  can be theoretically linked to the maximum pore radii.

However, vertical scanning curves are only an approximation. On the pore scale, there is a slow increase of the wetting phase saturation also before the maximum pore radius is reached. That means that the inclination of the scanning curve should actually be larger compared to the main imbibition curve, but not vertical. Also, scanning curves must depend on the pore size distribution of the porous medium and therefore cannot be always vertical. The variation of the pore sizes causes different inclinations of scanning curves.

Nevertheless, the main disadvantage of the play-type hysteresis is the lack of a firm concept that accounts for the trapped non-wetting phase saturation. Scanning curves starting from the main drainage curve at saturations that lie between the maximum wetting phase saturation in imbibition and drainage (points 3 and 1 on Fig. 24, left) have to be treated separately and form a source of instability in a numerical model. On the other hand, the play-type concept offers the advantage that, once implemented, it can be easily applied to other capillary pressure-saturation parameterizations by simply switching the functional rela-

tionship that describes the main drainage and the main imbibition curve (i.e. VAN GENUCHTEN or BROOKS AND COREY, see Fig. 24).

Play-type hysteresis is in general a good approximation for porous media with a narrow pore-size distribution. Such porous media are characterized by flat  $p_c$ - $S_w$  curves and steep scanning curves. To summarize, this hysteresis concept cannot describe the entrapment of non-wetting phase, yet has the advantage that it is simple and it can be applied in different  $p_c$ - $S_w$  functions as long as the main drainage and the main imbibition curve are available.

### 3.2.2 $p_c$ - $S_w$ hysteresis from PARKER AND LENHARD

PARKER AND LENHARD (1987) [78] have developed an empirical scaling hysteresis concept that can produce a more realistic representation of scanning curves and hysteresis loops. Their concept introduces an *apparent* saturation in order to mimic the effect of residual trapped non-wetting phase saturation.

#### Entrapment of the non-wetting phase

This concept distinguishes between the mobile and the trapped part of the non-wetting phase. To account for the entrapment of the non-wetting phase, the effective saturation  $\bar{S}_{nt}$  of the non-mobile non-wetting phase that is trapped in the wetting phase is defined as

$$\bar{S}_{nt} = \frac{S_{nt}}{1 - S_{wr}}. \quad (31)$$

Here,  $S_{nt}$  stands for the saturation of the trapped non-wetting phase. Practically, this saturation is a proportion of the non-wetting phase saturation that corresponds to isolated ganglia and blobs surrounded by the wetting phase.

Similarly, the effective residual non-wetting phase saturation  $\bar{S}_{nr}$  reads

$$\bar{S}_{nr} = \frac{S_{nr}}{1 - S_{wr}}. \quad (32)$$

In the latter,  $1 - \bar{S}_{nr}$  is the maximum wetting phase saturation reached when the imbibition process began at residual wetting phase saturation (see Fig. 25). LAND (1968) [61] experimentally observed that the amount of trapped non-wetting phase after an imbibition process ( $\bar{S}_{nr(i)}$ , see Fig. 25) increases with the effective non-wetting phase saturation at the beginning of the imbibition ( $1 - \bar{S}_{w(i)}$ ). In the same work, the following empirical relationship is proposed



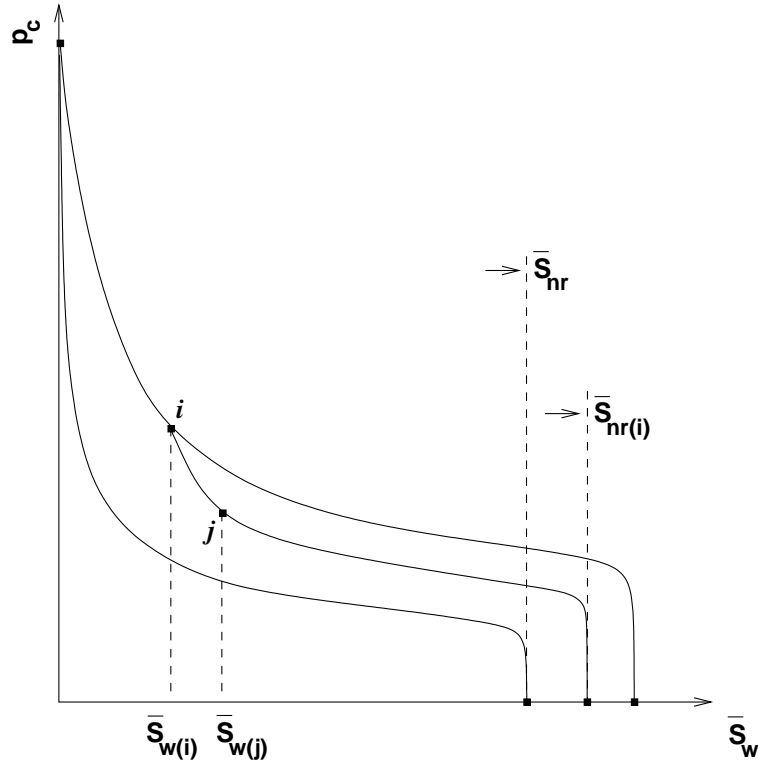


Figure 25: Phase entrapment in the  $p_c$ - $\bar{S}_w$  curve.

$$\bar{S}_{nr(i)} = \frac{1 - \bar{S}_{w(i)}}{1 + R(1 - \bar{S}_{w(i)})}, \quad (33)$$

with

$$R = \frac{1}{\bar{S}_{nr}} - 1. \quad (34)$$

PARKER AND LENHARD distinguish between the effective and the apparent wetting phase saturation. The effective saturation  $\bar{S}_w$  is considered as the mobile part of the phase. The apparent saturation  $\bar{\bar{S}}_w$  is the sum of the effective saturation  $\bar{S}_w$  and trapped effective saturation  $\bar{S}_{nt}$

$$\bar{\bar{S}}_w = \bar{S}_w + \bar{S}_{nt}. \quad (35)$$

The apparent saturation, as explained later, is the variable used in this hysteresis concept for the derivation of the  $p_c$ - $S_w$  relationship (instead of the effective saturation as done in the common VAN GENUCHTEN function).

The effective trapped saturation of the non-wetting phase  $\bar{S}_{nt(ij)}$  at any point  $j$  on an imbibition curve (that started from point  $i$ ) is obtained with linear interpolation

$$\bar{S}_{nt(ij)} = \bar{S}_{nr(i)} \cdot \frac{\bar{S}_w(j) - \bar{S}_w(i)}{1 - \bar{S}_w(i)}. \quad (36)$$

### Formation of hysteresis

When using the effective saturation  $\bar{S}_w$ , it is only possible to describe hysteresis that accounts for the contact angle hysteresis and the inkbottle effect. If there is non-wetting phase entrapment (existence of  $\bar{S}_{nr(i)}$ ), the  $p_c$ - $\bar{S}_w$  curves for drainage and imbibition do not form closed loops. The formation of closed loops is possible by substitution of the effective by the apparent saturation (see Fig. 26), that also accounts for fluid entrapment. This way, a MDC and a MIC described i.e. with the VAN GENUCHTEN model

$${}^{MDC}\bar{S}_w = [1 + ({}^{MDC}\alpha p_c)^n]^{-m}, \quad (37)$$

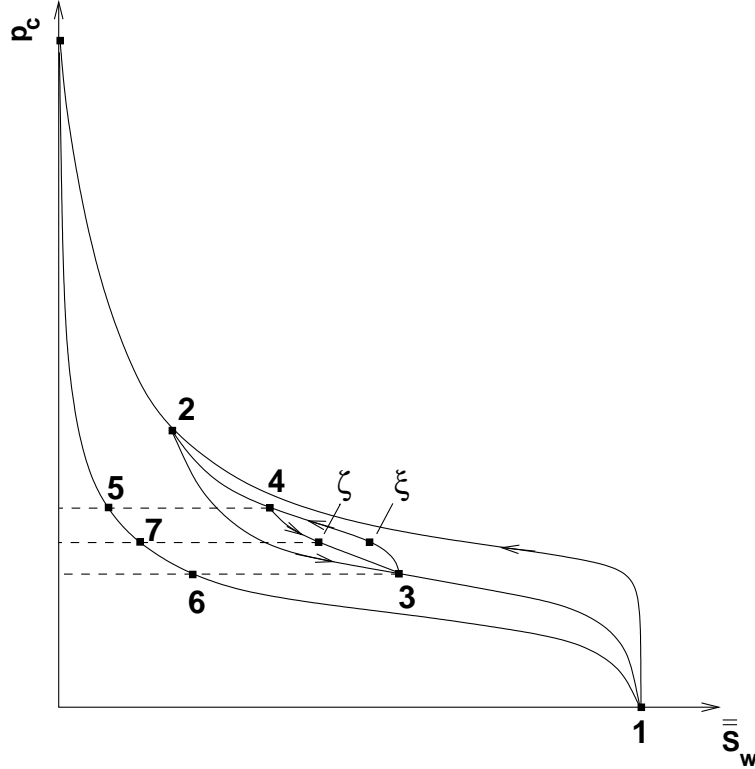


Figure 26: Hysteresis in the  $p_c$ - $\bar{S}_w$  curve.

$${}^{MIC}\bar{S}_w = [1 + ({}^{MIC}\alpha p_c)^n]^{-m} \quad (38)$$

will form a closed hysteresis loop, while trapped non-wetting phase is accounted for. Here, it is assumed for simplicity that  $n$  is the same for drainage and imbibition.

With the main drainage and imbibition curves and using the saturations at which a switch from drainage to imbibition (or vice versa) takes place, it is possible to scale the apparent saturation. The scaling relationship reads for imbibition

$$\bar{S}_{w(\zeta)}(p_c) = \frac{{}^{MIC}\bar{S}_w(p_c) - {}^{MIC}\bar{S}_w(id p_c)}{{}^{MIC}\bar{S}_w(di p_c) - {}^{MIC}\bar{S}_w(id p_c)} \cdot ({}^{di}\bar{S}_w - {}^{id}\bar{S}_w) + {}^{id}\bar{S}_w. \quad (39)$$

In the latter,  $\zeta$  denotes a point on a secondary imbibition scanning curve (see Fig. 26).  ${}^{MIC}\bar{S}_w(p_c)$  is the apparent saturation that corresponds to the main imbibition curve. The indices  $di$  and  $id$  stand for switching points (imbibition to drainage and vice versa). For example, Eq. 39 can be expressed based on the points given in Fig. 26 as

$$\bar{S}_{w(\zeta)} = \frac{\bar{S}_7 - \bar{S}_6}{\bar{S}_5 - \bar{S}_6} \cdot (\bar{S}_4 - \bar{S}_3) + \bar{S}_3. \quad (40)$$

Similarly, the scaling relationship can be formulated for drainage

$$\bar{S}_{w(\xi)}(p_c) = \frac{{}^{MDC}\bar{S}_w(p_c) - {}^{MDC}\bar{S}_w(di p_c)}{{}^{MDC}\bar{S}_w(id p_c) - {}^{MDC}\bar{S}_w(di p_c)} \cdot ({}^{id}\bar{S}_w - {}^{di}\bar{S}_w) + {}^{di}\bar{S}_w. \quad (41)$$

Practically, Eq. 39-41 imply that a scanning curve is scaled between the starting and the ending point using the main drainage or the main imbibition curve, depending on the type of the current displacement event. The starting point of the current scanning curve is known from the history of saturation while the end point coincides with the starting point of the previous scanning curve. For example, the value  $\bar{S}_{w(\zeta)}$  has a direct dependency only on points 4 (starting point) and 3 (starting point of the preceding drainage scanning curve), as far as the history of displacement is concerned (see Fig. 26).

### Example

To illustrate the hysteresis concept described above, an example is used to derive a point on an imbibition scanning curve as shown in Fig. 27. Following initially

the main drainage path, a reversal from drainage to imbibition at point  $i$  is considered, with  $S_{w(i)} = 0.368$  [-] and  $p_{c(i)} = 2798$  [Pa]. Here it is assumed that saturation acts as the primary variable (input), while scanning curves are formed through the calculation of capillary pressure (output). In this example, it is aimed to find the capillary pressure value that corresponds to a point  $j$  positioned on the scanning curve with  $S_{w(j)} = 0.457$  [-].

First of all it is given that  $S_{wr} = 0.15$  and  $S_{nr} = 0.2$  [-], meaning that for imbibition the effective residual non-wetting phase saturation is  $\bar{S}_{nr} = 0.235$  [-] according to Eq. 32. Consequently, it is found from Eq. 34 that  $R = 3.25$  [-]. The reversal point  $i$  has a saturation  $S_{w(i)} = 0.368$  [-] (see Fig. 27) that corresponds to  $\bar{S}_{w(i)} = 0.257$  [-]. Equation 33 yields the value  $\bar{S}_{nr(i)} = 0.217$  [-] or  $S_{nr(i)} = 0.185$  [-].

After the switch from drainage to imbibition, in order to find the apparent saturation that corresponds to a saturation  $S_{w(j)} = 0.457$  [-] (or  $\bar{S}_{w(j)} = 0.361$  [-]) it is first necessary to calculate the effective trapped non-wetting phase saturation  $\bar{S}_{nt(ij)}$ . This is done by linear interpolation using Eq. 36 that yields the value  $\bar{S}_{nt(ij)} = 0.03$  [-]. Thus, based on Eq. 35 the apparent saturation for point  $j$  is  $\bar{S}_{w(j)}(p_c) = 0.391$  [-]. Finally, this apparent saturation can be used in Eq. 39 to calculate the scaled apparent saturation on the main curve  $^{MIC}\bar{S}_w(p_c)$ , that is equal to 0.189 [-]. From this saturation value the corresponding capillary pressure is then found  $p_{c(j)} = 1775$  [Pa].

*Input for main drainage and main imbibition*

$$\begin{aligned} S_{wr} \text{ (dr.)} &= 0.15 \text{ [-]} \\ S_{wr} \text{ (im.)} &= 0.15 \text{ [-]} \\ S_{nr} \text{ (dr.)} &= 0.0 \text{ [-]} \\ S_{nr} \text{ (im.)} &= 0.2 \text{ [-]} \\ \alpha \text{ (dr.)} &= 0.0004 \text{ [1/Pa]} \\ \alpha \text{ (im.)} &= 0.0007 \text{ [1/Pa]} \\ n \text{ (dr.)} &= 11.0 \text{ [-]} \\ n \text{ (im.)} &= 11.0 \text{ [-]} \end{aligned}$$

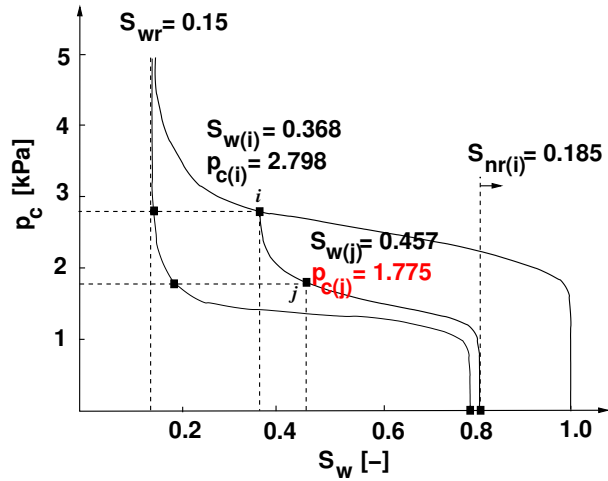


Figure 27: An example for the formation of a scanning curve using the scaling hysteresis concept from PARKER AND LENHARD.

## 4 Numerical model

In Sect. 2.6 the mathematical model for the description of flow of two incompressible, immiscible fluid phases in rigid, non-deformable porous media was introduced. The continuity equations 28 and 29 form a strongly coupled non-linear system of equations through the inclusion of the constitutive relationships of capillary pressure-saturation and relative permeability-saturation. In the following, the discretization techniques applied in this thesis for the approximation of these equations will be explained.

### 4.1 Spatial and temporal discretization

The numerical simulations in this work are carried out with the numerical simulator MUFTE-UG (Multiphase Flow Transport and Energy model on Unstructured Grids). The simulator consists of a part that deals with the physical and mathematical problem description as well as the discretization (HELMIG ET AL. (1998) [42]) and a part that contains numerical tools and solvers that can handle multigrid data structures, grid generation, parallelization techniques and visualization [BASTIAN (1997) [7]]. In the framework of this thesis, only two- and three-dimensional structured grids are applied.

The balance equations for the two phases (Eqs. 28, 29) are solved fully coupled based on a vertex-centered Finite-Volume discretization in space, the BOX-scheme [BASTIAN (1999) [6]; HELMIG (1997) [41]; HUBER AND HELMIG (1999) [47]].

A domain  $G$  is discretized with an initial finite element (FE) mesh that consists of  $n$  nodes  $V = v_1, \dots, v_n$  and  $m$  elements  $E = e_1, \dots, e_m$ . Dirichlet or Neumann boundary conditions can be assigned at the boundary  $\Gamma$  of the domain. The BOX-scheme requires the construction of a second grid. This is done by linking the barycenter of each element from the FE mesh with the midpoints of the edges of this element (see Fig. 28). This way, a control volume  $B_i$  is constructed around each node  $v_i$  of the FE mesh. The intersection of a control volume with an element  $e_\kappa$  is called a sub-control volume  $b_i^\kappa$ .

In Fig. 29 the continuous lines represent the FE mesh and the dashed lines the

control volumes. In this case, the boundary  $\Gamma_{1,2}$  between two sub-domains  $G_1$  and  $G_2$  is determined by the control volumes and not the finite elements.

A weighting function  $W$  is defined equal to 1 inside the control volume and 0

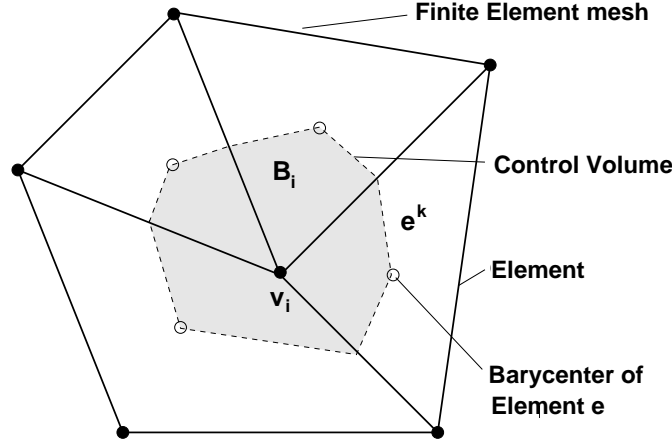


Figure 28: Finite elements and the resulting sub-control volume.

outside the control volume

$$W_i(x) = \begin{cases} 1 & \text{if } x \in B_i \\ 0 & \text{if } x \notin B_i. \end{cases} \quad (42)$$

Furthermore, a linear basis (or shape) function  $N_i$  is considered such that it is 1 at the node  $i$  and 0 at all other nodes. A graphical representation of the weighting and the base functions for 1-D is given in Fig. 30.

Multiplying the two-phase flow equations (Eqs. 28-29) by the weighting function  $W_i$  and integrating over the whole domain  $G$  results in integrals over the control volumes

$$\int_{B_i} \frac{\partial S_\alpha}{\partial t} \phi dB_i - \int_{B_i} \nabla \cdot (\lambda_\alpha K (\nabla p_\alpha - \rho_\alpha \mathbf{g})) dB_i - \int_{B_i} q_\alpha dB_i = 0, \quad (43)$$

where  $\lambda_\alpha = \frac{k_{r\alpha}}{\mu_\alpha}$  is the *mobility* of phase  $\alpha$ . Applying the Gaussian integral theorem with  $\Gamma_{B_i}$  as the boundary of  $B_i$  gives

$$\int_{B_i} \frac{\partial S_\alpha}{\partial t} \phi dB_i + \oint_{\Gamma_{B_i}} (\lambda_\alpha K (\nabla p_\alpha - \rho_\alpha \mathbf{g})) \cdot \mathbf{n} d\Gamma_{B_i} - \int_{B_i} q_\alpha dB_i = 0. \quad (44)$$

The integral over  $\Gamma_{B_i}$  describes the discrete fluxes between the control volumes and forms the basis for a mass-conservative scheme. A midpoint approximation is used for the evaluation of the integral. That is, the value at the middle of the

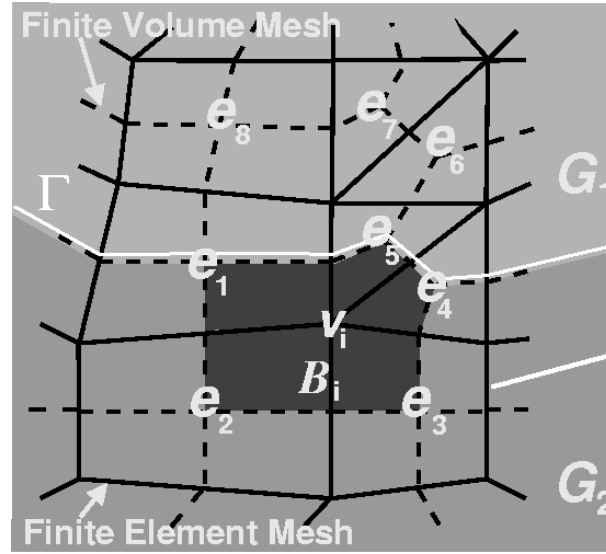


Figure 29: Finite elements and the resulting sub-control volume (from JAKOBS (2004) [48]).

sub-control volume edge (*integration point*) is multiplied with the length of the edge (in 3-D edges are replaced by faces).

In general, for a time-dependent variable  $u$  the temporal discretization is formulated as

$$\frac{\partial u}{\partial t} \approx \frac{u^{n+1} - u^n}{t^{n+1} - t^n}. \quad (45)$$

Taking the shape functions into account

$$p_w \approx \sum_{i \in V} p_{wi} N_i, \quad (46)$$

$$p_c \approx \sum_{i \in V} p_{ci} N_i, \quad (47)$$

$$S_n \approx \sum_{i \in V} S_{ni} N_i, \quad (48)$$

yields the discretized two-phase flow equations

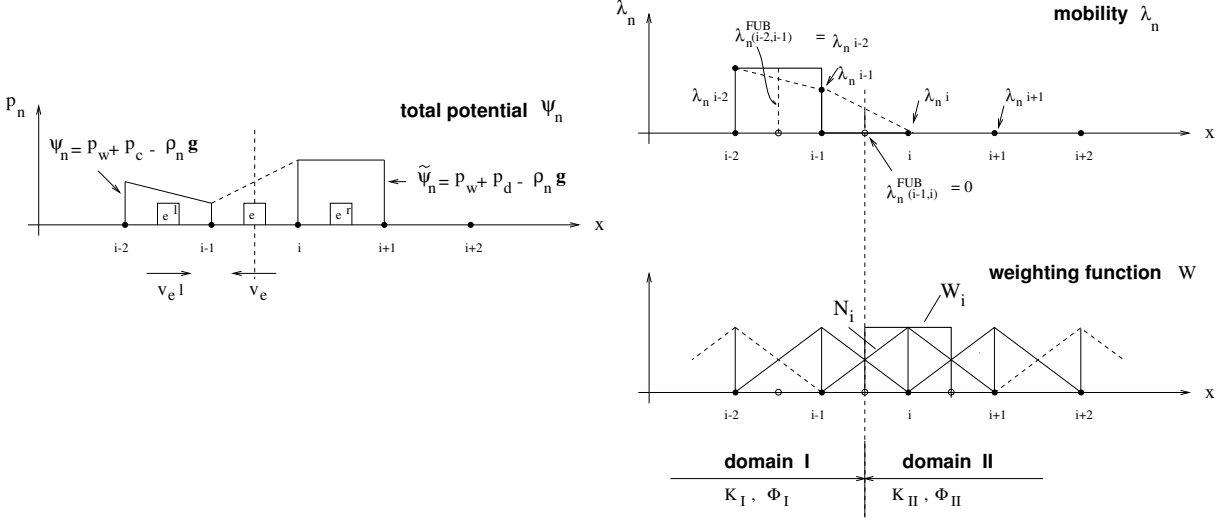


Figure 30: Node-centered FV method using Full Upwinding [HELMIG (1997) [41]].

$$\begin{aligned}
g_{\alpha i}(S_{ni}^{n+1}; S_{ni}^n; p_{wi}^{n+1}; p_{wj}^{n+1}) &:= \\
&- \underbrace{(-1)^{\delta_{\alpha w}} \{ [S_n \varrho_{\alpha}]_i^{n+1} - [S_n \varrho_{\alpha}]_i^n \} \frac{\phi}{\Delta t} |B_i|}_{M_{\alpha}} \\
&- \underbrace{\sum_{j \in \eta_i} \gamma_{ij}^{FUB} \lambda_{\alpha ij}^{FUB} \varrho_{\alpha ij} \gamma_{\alpha ij}^{FUB} (\psi_{\alpha j}^{n+1} - \psi_{\alpha i}^{n+1})}_{A_{\alpha}} \\
&- \underbrace{\varrho_{\alpha i} q_{\alpha i}^{n+1} |B_i| - m_{\alpha i}}_{Q_{\alpha}} = 0, \\
&\alpha \in \{w, n\}, \tag{49}
\end{aligned}$$

which forms a fully implicit Euler scheme that is unconditionally stable for arbitrary timesteps [HELMIG (1997) [41]]. Here,  $\eta_i$  is the set of neighboring nodes whose control volumes share sub-control volume edges/faces with  $B_i$  and  $E_i$  is the set of elements which have node  $v_i$  as a corner, for example  $\{e_1, e_2, e_3, e_4, e_5\}$  for node  $v_i$  in Fig. 29.  $|B_i|$  represents the area (in 2-D) respectively the volume (in 3-D) of the control volume, the indices  $n$  and  $n+1$  stand for the time step and  $j$  is a neighboring node of  $i$ .  $M_{\alpha}$  denotes the discretized accumulation term,  $A_{\alpha}$  the discretized flux term and  $Q_{\alpha}$  the sources/sinks term and the flow term over  $\partial B_i \cap \Gamma_{\alpha N}$  where  $\Gamma_{\alpha N}$  is a Neumann type boundary for phase  $\alpha$ .



It is further considered that

$$\gamma_{\alpha ij}^{FUB} = \oint_{\partial B_i \setminus \Gamma_{N\alpha}} \mathbf{K} \mathbf{grad} N_j \mathbf{n} d\Gamma, \quad (50)$$

$$\psi_{\alpha i}^{n+1} = p_{wi} + \delta_{\alpha n} p_{ci}^{n+1} - \varrho_{\alpha i} g_i. \quad (51)$$

The sign of  $\psi_{\alpha m} - \psi_{\alpha i}$  gives the direction of the flow of phase  $\alpha$  across the interface between two control volumes.  $\mathbf{n}$  is the outer normal vector with respect to  $B_i$ . The mobilities are defined using a fully upwind method

$$\lambda_{\alpha ij}^{FUB} = \begin{cases} \lambda_{\alpha i} & \text{if } (\psi_{\alpha j} - \psi_{\alpha i}) \geq 0 \\ \lambda_{\alpha j} & \text{if } (\psi_{\alpha j} - \psi_{\alpha i}) \leq 0, \end{cases} \quad (52)$$

which means that the mobility of the node with the higher potential is chosen (upstream mobility, see Fig. 30).

The vertex-centered FV method is locally mass conservative, as the boundary integral over  $\partial B_i \cap \partial B_j$  is equal for the two neighboring control volumes  $B_i$  and  $B_j$ . HELMIG AND HUBER (1998) [43] have shown that weighting the mobilities between two neighboring nodes would lead to a non-physical flux from the domain of lower to the domain of higher permeability. Using the upwind mobility sets this flux to zero. For example, in Fig. 30 the node  $i$  is the upwind node due to the higher potential. As the mobility at the node  $i$  is zero, there can be no flow of non-wetting phase from domain II to domain I. If the mobility was weighted between nodes  $i$  and  $i - 1$ , a flow from domain II to domain I would result to a negative saturation value at node  $i$ .

The non-linear system of equations is solved with a damped, inexact NEWTON scheme that utilizes a *line search* to determine a damping factor. This scheme achieves global convergence and automatically adapts the time step. The maximum number of line search steps lies between 4 and 6. If the damping factor can be calculated after the first line search, the time step is increased by a factor  $dt_{scale}$ . In case that after 6 line search steps the damping factor cannot be determined, the time step is decreased, reducing the numerical diffusion introduced by the temporal discretization. For this algorithm, the following information has to be defined:

- The size of the starting timestep  $\Delta_{start}$ .
- The size of the maximum timestep  $\Delta_{max}$ .

- The minimum allowed timestep size  $\Delta_{min}$ , that functions as an abortion criterium if convergence is not achieved for this time step size.

At the beginning of each time step, the NEWTON solver requires starting values of the unknowns for the iteration. In case of mesh refinements, multigrid methods can be applied. For that purpose, the solution of the previous time step on the coarsest level serves as an initial guess. The resulting solution on the coarsest grid is then interpolated to be used as an initial guess for the next level and the procedure is repeated until the finest level is reached. The evolving linear system of equations is handled with a stabilized bi-conjugate gradient algorithm (BiCGStab) for the multigrid method.

## 4.2 The Interface Condition

Although the fully upwind method describes better the flow of non-wetting phase across the boundary of two sub-domains, compared to a weighting of the mobility, it is not possible to model discontinuities of saturation at material interfaces, as described in Sect. 2.4.

However, it is possible to achieve a sharp discontinuity in saturation at interfaces between different materials using an interface condition. In the vertex-centered FV method described above, the interface between two subdomains with different properties coincides with the edge/face between control volumes. This introduces an error that depends on the grid width. In other words, the solution is dependent on the discretization length at the interfaces. For the implementation of the interface condition, the grid is shifted so that the interface lies on the FE grid (see Fig. 31). In this case, a sharp discontinuity of saturation can lie on the nodes of the FE mesh (in other words at the boundary between two elements).

In the consideration of the interface condition, capillary pressure of the nodes at the material interface acts as a quasi-primary variable. First, a minimum capillary pressure  $p_{c,min}^i$  is assigned for each node  $v_i$ . This is equal to  $p_c(S_n^i)$  if  $v_i$  lies in the interior of a domain. If  $v_i$  lies on the interface,  $p_{c,min}^i$  will be the minimum capillary pressure for  $S_n^i$ , with respect to the domains  $G_j$  having  $v_i$  on its boundary of  $p_c|_{G_j}(S_n^i)$

$$p_{c,min}^i = \min_{k \in E(i)} p_c(\mathbf{x}^k, S_n^i), \quad (53)$$

where  $\mathbf{x}^k$  is the barycenter of the element  $e_k$  and  $p_c(\mathbf{x}^k, \cdot)$  is the capillary pressure function  $p_c|_{G_j}$  for which  $\mathbf{x}^k \in G_j$ .

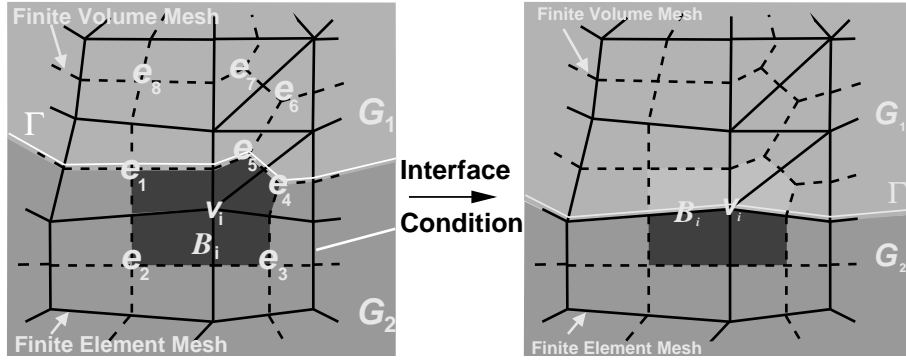


Figure 31: Grid consideration in the classical BOX approach and the Interface Condition approach from JAKOBS (2004) [48].

An example is illustrated in Fig. 31, where a subdomain  $G_1$  with low entry pressure and high permeability lies next to a subdomain  $G_2$  with higher entry pressure and smaller permeability. In this case  $p_{c,min}^i$  will be equal to the capillary pressure from the function  $p_c|_{G_1}$ .

Furthermore, a virtual saturation  $S_n^{i,k}$  is defined at each node  $v_i$ . This virtual saturation relates to the elements  $e_k$  having  $v_i$  as a node and is used for the computation of the entries of the local stiffness matrices. If  $v_i$  is not on an interface,  $S_n^{i,k} = S_n^i$ . If  $v_i$  lies on an interface, there are three possibilities:

- $e_k$  belongs to the domain  $G_j$  with the minimum capillary pressure  $p_{c,min}^i$  for  $S_n^i$ , i.e. is the material with the lowest entry pressure. In this case  $S_n^{i,k} = S_n^i$ .
- $e_k$  belongs to a domain  $G_j$  that has entry pressure  $p_c|_{G_j}(S_n = 0)$  larger than the minimum capillary pressure  $p_{c,min}^i$ . In this case,  $S_n^{i,k} = 0$ .
- $e_k$  belongs to a domain  $G_j$  that is not the one with the minimum capillary pressure, but  $p_{c,min}^i$  is greater than the entry pressure of  $G_j$ . This case yields  $S_n^{i,k} = p_c|_{G_j}(p_{c,min}^i)$ .

This can be in general formulated [BASTIAN AND HELMIG (1999) [8]; DE NEEF (2000) [75]] as

$$S_n^{i,k} = \begin{cases} \tilde{S}_n^i & \text{if } p_c(x^k, 1 - \tilde{S}_n^i) = p_{c,min}^i \\ 0 & \text{if } p_{c,min}^i < p_c(x^k, 1) \\ \tilde{S}_n^i & \text{where } \tilde{S}_n^i \text{ solves } p_c(x^k, \tilde{S}_n^i) = p_{c,min}^i. \end{cases} \quad (54)$$

In the following, the classical BOX-scheme will be referred to as the *PPS* approach (Phase Pressure Saturation), whereas the extension by the interface condition as the *PPSIC* approach (Phase Pressure Saturation Interface Condition).

In the PPS approach all quantities are evaluated at the mesh nodes. This is not possible in the PPSIC approach, as saturation (and thus all quantities derived from it) can be discontinuous across element boundaries. The evaluation in this case is done element-wise (at element barycenters). To ensure a consistent approach for dealing with heterogeneities, it is assumed that spatially-variant properties, such as porosity and absolute permeability, may also be discontinuous across element boundaries and they are evaluated at element barycenters as well.

## 4.3 Numerical implementation of hysteresis

In Sect. 3.2, the hysteresis concepts from BELIAEV AND HASSANIZADEH (2001) [11] and from PARKER AND LENHARD (1987) [78] were introduced. In the following, the implementation of these concepts in the BOX-scheme will be discussed. First this is done for the classic PPS approach. Secondly, since a main objective of this thesis is to model drainage and imbibition processes in heterogeneous structures, hysteresis has to be incorporated in the PPSIC approach.

### 4.3.1 Implementation in the PPS approach

The methodology for the numerical implementation of hysteresis in the PPS approach is the same as in SHETA (1999) [92]. After each timestep, the following procedure is carried out at each node:

- First the type of displacement that takes place (drainage or imbibition) is determined, as well as possible reversals (i.e. if there was a switch from drainage to imbibition in the last timestep). This is achieved by comparing after each timestep the calculated saturation  $S_n^i$  at each node  $v_i$  to the saturation of the previous timestep. A threshold value (i.e.  $1.0e-5$ ) is used for the comparison to avoid oscillations.
- Consequently, the value +1 is assigned to an index  $Ih^i$  for drainage and -1 for imbibition. This value is compared to the previous  $Ih^i$  index value at this node.
- If the old and new index value are not equal, it means that a reversal took place. A counter  $L^i$  is used to keep track of the reversals. It is now possible to form the hysteresis models analyzed in Sect. 3.2.

- In the play-type hysteresis, the use of vertical scanning curves practically implies an infinite number of  $p_c$ - $S_w$  solutions for a single saturation value. Therefore, scanning curves have to be approximated as linear functions with large inclination:

$$p_{play}^i = p_{c,1}^i - \beta \cdot (S_w^i - S_{w,1}^i). \quad (55)$$

Here,  $p_{c,1}^i$  and  $S_{w,1}^i$  are the reversal capillary pressure and saturation of node  $v_i$ ,  $S_w^i$  is the saturation of node  $v_i$  and  $\beta$  determines the inclination of the scanning curve. The capillary pressures  $^{dr}p_c^i$  and  $^{imb}p_c^i$  that correspond to the current saturation  $S_w^i$  on the main drainage resp. imbibition curve are computed with the VAN GENUCHTEN model (Eq. 12). We formulate Eq. 30 as:

$$p_c^i = \begin{cases} ^{dr}p_c^i & \text{if } p_{play}^i > ^{dr}p_c^i \\ p_{play}^i & \text{if } ^{imb}p_c^i < p_{play}^i < ^{dr}p_c^i \\ ^{imb}p_c^i & \text{if } p_{play}^i < ^{imb}p_c^i. \end{cases} \quad (56)$$

The history of previous reversals is in this case not required, thus  $S_{w,1}^i$  and  $p_{c,1}^i$  can be overwritten after each reversal. In total, 4 parameters have to be stored at each node:

- The hysteresis index from the current timestep  $Ih_{new}^i$ .
  - The hysteresis index from the previous timestep  $Ih_{old}^i$ .
  - The saturation of the last reversal point  $S_{w,1}^i$ .
  - The capillary pressure of the last reversal point  $p_{c,1}^i$ .
- Equations 39 and 41 that describe the hysteresis model from PARKER AND LENHARD can be re-written in a general form as

$$\bar{\bar{S}}_w(i)(p_c) = \frac{p \bar{\bar{S}}_w(p_c) - p \bar{\bar{S}}_{w,2}}{p \bar{\bar{S}}_{w,1} - p \bar{\bar{S}}_{w,2}} \cdot (\bar{\bar{S}}_{w,1} - \bar{\bar{S}}_{w,2}) + \bar{\bar{S}}_{w,2}. \quad (57)$$

The indices 1 and 2 stand for the reversal point and the endpoint of the current  $p_c$ - $S_w$  curve. The index  $p$  denotes the main drainage resp. imbibition curve. In this case, the previous reversal point (endpoint) has to be known, therefore values have to be stored dynamically using the counter  $L^i$  (loop index). To compute the required apparent saturations (Eq. 57), it is necessary to store the saturations  $S_{w,1}^i$ ,  $S_{w,2}^i$  and capillary pressures  $p_{c,1}^i$ ,  $p_{c,2}^i$  of the current drainage or imbibition  $p_c$ - $S_w$  curve. In total, 7 parameters are needed at each node:

- The hysteresis index from the current timestep  $Ih_{new}^i$ .
- The hysteresis index from the previous timestep  $Ih_{old}^i$ .
- The loop index  $L^i$ .
- The saturation of the last reversal point  $S_{w,1}^i$ .
- The saturation  $S_{w,2}^i$  of the endpoint of the  $p_c$ - $S_w$  curve that will be reached at the end of the current drainage or imbibition event.
- The capillary pressure  $p_{c,1}^i$  of the last reversal point. This value is required in order to find the corresponding apparent saturation on the main drainage or imbibition curve (the projected value  ${}^p\bar{S}_{w,1}$ ).
- The capillary pressure  $p_{c,2}^i$  of the endpoint, also necessary to calculate the respective apparent saturation on the main curve.

### 4.3.2 Combination of hysteresis with the PPSIC approach

As explained in Sect. 4.2, the interface condition allows a better approximation of sharp saturation discontinuities at the nodes of the FE mesh. In this case, material interfaces lie on the edges of the finite elements. For the development of a hysteresis concept that accounts for such interfaces, it is necessary to include discontinuities in saturation in the history of the displacement. Thus, the saturation used in the hysteresis models must be the virtual saturation defined at each node, that relates to the neighboring elements (see Sect. 4.2). On the other hand, reversal saturations and capillary pressures have to be accounted for in the interface condition.

The reversal saturations at node  $v_i$  relevant to the neighboring elements  $e_k$  will be denoted with  $S_{w,1}^{i,k}$  and  $S_{w,2}^{i,k}$ . Pressure is continuous also at heterogeneities and therefore single nodal values are sufficient (see Fig. 32). The combination of hysteresis with the interface condition can be summarized in the following points:

- It is considered that at each node  $v_i$  either drainage or imbibition takes place, thus the hysteresis index at interfaces does not relate to the neighbouring elements but has a unique value for  $v_i$ . As done for the PPS approach, after each timestep the computed node saturation  $S_n^i$  is compared to the old saturation to determine the indices  $Ih^i$  and  $L^i$ . The loop index  $L^i$  is not necessary for the formation of the play-type hysteresis.
- If there is a reversal (determined by  $Ih_{new}^i \neq Ih_{old}^i$ ), the minimum capillary pressure of the node  $v_i$  with respect to the neighbouring elements is found

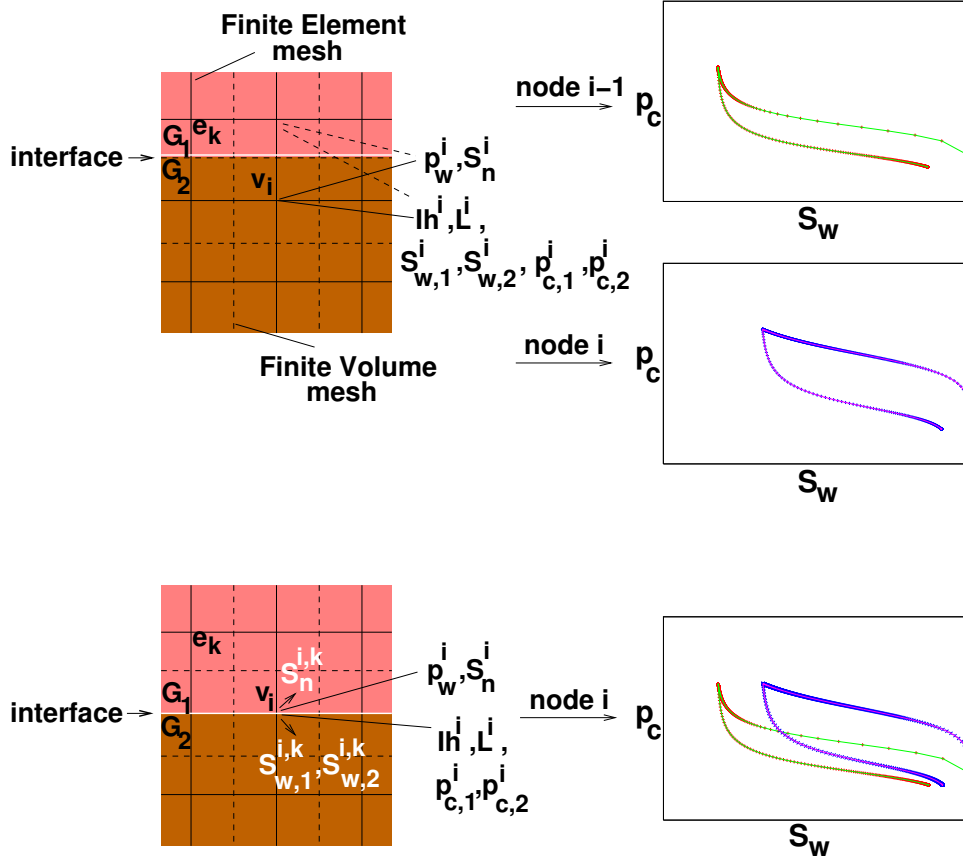


Figure 32:  $p_c$ - $S_w$  hysteresis in the PPS and the PPSIC approach.

using the node saturation  $S_n^i$ . Since the capillary pressure-saturation relationship is hysteretic, the history of the current displacement process (which now corresponds to  $L^i-1$ ) is required.

- Using Eq. 54, the virtual saturations  $S_n^{i,k}$  related to the elements  $e_k$  having  $v_i$  as a node are computed, based on the current displacement history (which corresponds to  $L^i-1$ ).
- The computed virtual saturations are dynamically assigned to  $S_{w,1}^{i,k}$ ,  $S_{w,2}^{i,k}$ . That means each node may have several  $S_{w,1}$  and  $S_{w,2}$  reversal saturations, depending on the amount of elements related to that node (see Fig. 32). For example, the application of play-type hysteresis in 2-D with a rectangular mesh requires the storage of 4  $S_{w,1}$  values, while the model from PARKER AND LENHARD needs for a 3-D rectangular mesh 8  $S_{w,1}$  and 8  $S_{w,2}$  values.
- The capillary pressures  $p_{c,1}^i, p_{c,2}^i$  of reversals are only considered at nodes, as done for the PPS approach.

- The stored reversal values  $S_{w,1}^{i,k}$ ,  $S_{w,2}^{i,k}$ ,  $p_{c,1}^i$  and  $p_{c,2}^i$  (corresponding to  $L^i$ ) are consequently used for the calculation of the minimum capillary pressure  $p_{c,min}^i$  (see Sect. 4.2) and the virtual saturation  $S_n^{i,k}$  with the interface condition (Eq. 54), based on the hysteretic  $p_c$ - $S_w$  relationship.



# 5 Model verification

The following work aims to discuss issues such as the necessity of hysteresis models in predictions of two-phase flow, the evaluation of the predictive ability of the numerical model developed in Sect. 4.3, the amount of complexity required in hysteresis models and the reliability of different approaches from the numerical and the experimental point of view. For that purpose, results from numerical simulations are compared to data measured in a well-controlled 1-D transient experiment performed by Yvonne Lins and Tom Schanz in the Faculty of Civil Engineering at the Bauhaus University of Weimar, Germany [LINS ET AL. (2007) [66]]. The experiment includes four successive steps of alternating drainage and imbibition in a homogeneous sand column. This is described in Sect. 5.1. The setup used in the numerical simulations is described in Sect. 5.2, while the comparison between numerical and experimental results is presented in Sects. 5.3 and 5.4. A discussion is finally given in Sect. 5.5.

## 5.1 Description of the 1-D experiment

The experiment is conducted with a quartz sand with grain size diameters ranging from 0.1 to 1.0 [mm]. The sand is packed in a cylindrical tube 54 [cm] high with a diameter of 30.5 [cm]. The experimental setup is given in Fig. 33. The top of the sand column is in contact to the atmosphere. The bottom of the sand column is connected to a water reservoir. The water reservoir and the sand column are connected through a perforated plexiglass plate that allows the flow of water from the reservoir to the column and vice versa. A highly permeable geotextile is placed between the sand and the perforated plexiglass plate to prevent sand grains from flushing into the reservoir. Several openings along the tube allow the connection of sensors to the sand column. Four miniature tensiometers (T1-T4) and four miniature Time Domain Reflectometry probes (TDR1-TDR4) are placed along the height of the column with a distance of approximately 10 [cm]. Point 1 (T1 and TDR1) refers to the measurement position closest to the bottom of the column, while point 4 to the position near the top. The sensors are shown in Fig. 34. The exact heights of the sensors are indicated in Fig. 33.

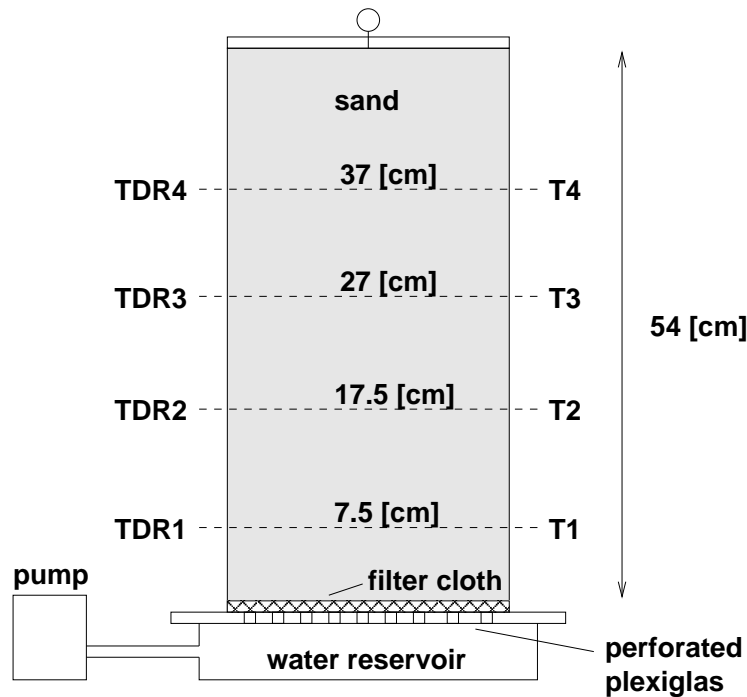


Figure 33: Setup of 1-D transient experiment.

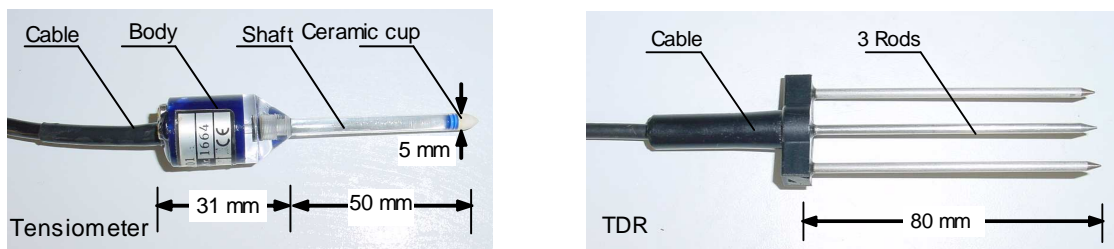


Figure 34: Pictures of the tensiometer (left) and the TDR (right) sensors from LINS ET AL. (2007) [66].

Under saturated conditions tensiometers measure the hydrostatic pressure of water. Under unsaturated conditions they measure negative water pressure. When present, the air phase is assumed to form continuous paths to the top of the sand column that is in contact with the atmosphere. Therefore, air pressure in this experiment is considered to be always zero. In this case, in unsaturated conditions tensiometers indicate the capillary pressure (equal to the negative pressure of water). On the other hand, TDR sensors measure the saturation of water. It is thus possible to monitor the change of water pressure and saturation over time at different heights of the column and also obtain the evolution of the capillary pressure-saturation relationship on the course of the successive drainage and imbibition events.

The sand column is initially saturated with water. This is done by packing the sand in water. The reservoir beneath the column always remains filled with water. The drainage process of the column is introduced by pumping water out with an electronic pump attached to the reservoir. Air enters the sand column from the top. Water is pumped out of the sand column until air reaches the bottom of the column. Similarly, imbibition is induced by pumping water back into the reservoir. This continues until water reaches the top of the sand column. In total, two drainage and two imbibition steps are carried out. The applied outflow and inflow rates and the corresponding times are given in Table 2.

Time [min]	Outflow (+) or inflow (-) [kg/min]	Process
0-430	+0.02673	Drainage
430-775	-0.02889	Imbibition
775-1315	+0.018126	Drainage
1315-1612	-0.03642	Imbibition

Table 2: Outflow and inflow rates used to induce drainage and imbibition.

## 5.2 Numerical simulation

Property	Symbol	Value	Unit
Density of water	$\rho_w$	1000	[kg/m <sup>3</sup> ]
Density of air	$\rho_n$	1.19	[kg/m <sup>3</sup> ]
Viscosity of water	$\mu_w$	$1.124 \times 10^{-3}$	[kg/(m s)]
Viscosity of air	$\mu_n$	$1.65 \times 10^{-5}$	[kg/(m s)]

Table 3: Phase properties.

For the numerical simulation, a regular rectangular mesh is used. Along the  $z$  direction (direction of gravity), the spacing of the grid is 0.5 [cm]. The width of the finite elements on the  $x$  direction is chosen such that the bottom area of the discretized model domain corresponds to the bottom area of the cylindrical sand column described in the previous section. In the numerical simulation, although the problem is one-dimensional, the model domain has a depth of 100 [cm]. Thus, the width of the domain in the numerical model is set to 7.3062 [cm] (see Fig. 35). A timestep of 4 [s] is chosen.

As shown in Eq. 28 and 29, fluid phases in the two-phase flow model are described by the density and the dynamic viscosity. The density and viscosity values given for water and air in the numerical simulation are listed in Table 3.

### Initial and boundary conditions

The initial and boundary conditions in the numerical simulation mimic those of the experiment. The primary variables are the water pressure  $p_w$  and the air saturation  $S_n$ . Initially, the saturation of water in the model domain is equal to 1.0 [-] and hydrostatic distribution is given for the pressure of water. At the top boundary, a Dirichlet boundary condition is applied for the water and the air phase. This boundary condition prescribes directly a pressure value equal to -3400 [Pa] for water at the top of the column. This value is equal to the maximum value of capillary pressure. Combined with the Dirichlet boundary value 1.0 [-] for the air saturation, the definition of phase pressure difference ( $p_c = p_n - p_w$ ) delivers that the pressure of air at the top boundary is equal to zero (atmospheric).

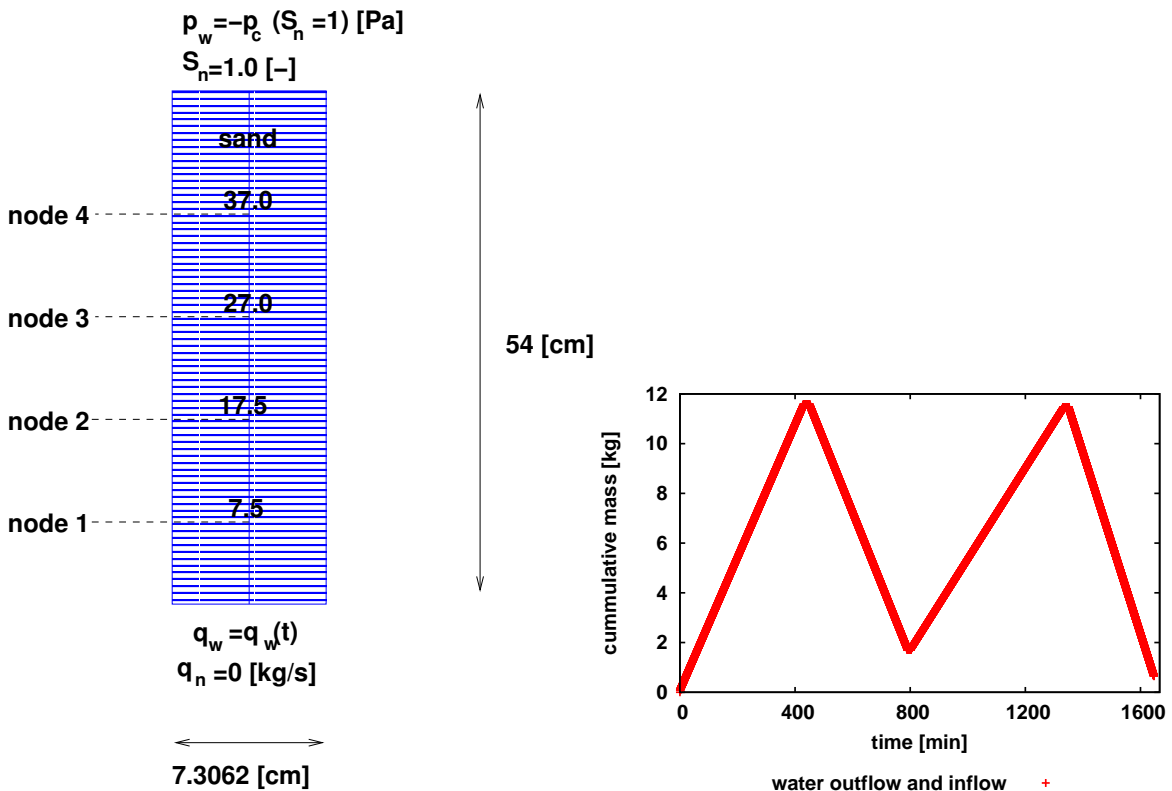


Figure 35: Domain and boundary conditions in the numerical simulation. Water outflow and inflow depends only on the Neumann boundary at the bottom.

As water phase infiltrates the domain from the bottom, it is possible to obtain non-physical water flux out of the domain through the top boundary, because of the Dirichlet boundary condition. This effect might introduce an error in the mass balance. To prevent any mass of water from leaving the domain through the top boundary, the upwind wetting phase mobility at the finite elements of the upper layer is explicitly set to zero.

At the bottom boundary, a Neumann no-flow boundary condition is assigned to air. Practically, in the experiment and also in the numerical simulations air does not reach the bottom of the sand column resp. of the model domain. However, this boundary condition ensures that no mass of air flows through the bottom. For the water phase, also a Neumann boundary condition is applied. In this case, the amount of water flux in or out of the model domain is a predefined function of time as shown in Table 2.

### Hydraulic properties

The fixed flux of water phase introduced by the Neumann boundary condition implies that at a certain time a certain mass of water has entered the model domain. For instance, during imbibition the total mass of water in the domain does not depend on the hysteresis model, or even on whether hysteresis is taken into account at all, but only on the value of water influx at the bottom boundary. The same is true for the hydraulic properties of the sand that are used as input in the numerical simulation. Permeability, porosity and capillary pressure-saturation relationship do not relate to the amount of water mass in the domain, but strongly influence how this mass distributes in it. The water mass outflow and inflow is shown in Fig. 35.

The capillary pressure-saturation relationship used as input for the numerical simulation is determined here with two different approaches.

In the first approach, the drainage and imbibition  $p_c$ - $S_w$  curve is obtained from the sensor measurements taken at point 4 (TDR4 and T4) during the transient experiment. This point is closest to the top boundary and thus reaches during drainage the lowest saturation value compared to the other measurement points. It is therefore the most appropriate point to determine the main drainage and the main imbibition curve. To achieve that, the measured data are fitted to the VAN GENUCHTEN capillary pressure-saturation function. The residual phase saturations and also the fitted  $\alpha$  and  $n$  shape parameters for the main drainage and main imbibition curve are given in Table 4. The numerical simulations based on this approach are presented in Sect. 5.3.

In the second approach, the capillary pressure-saturation relationship is determined with separate multistep outflow/inflow experiments. This procedure and

Property	Symbol	Value drainage	Value imbibition	Unit
Water residual saturation	$S_{wr}$	0.13	0.13	[-]
Air residual saturation	$S_{nr}$	0.0	0.18	[-]
VAN GENUCHTEN $\alpha$	$\alpha$	0.0005	0.001	[1/Pa]
VAN GENUCHTEN n	$n$	8.0	6.5	[-]
Absolute permeability	K	1.0e-10	1.0e-10	[m <sup>2</sup> ]
Porosity	$\phi$	0.5	0.5	[-]

Table 4: Hydraulic properties for drainage and imbibition.

a comparison between an additional numerical simulation and the measurements from the transient state experiment is presented in Sect. 5.4.

Purpose here is to investigate whether and how capillary hysteresis models can improve predictions, compare the implementation of the hysteresis concepts described in Sect. 3.2 to experimental measurements and draw conclusions related to which modeling and experimental approaches are suitable for correct predictions of hysteretic two-phase flow. It is therefore beneficial and sufficient to reduce any uncertainty in permeability and porosity by taking the values from the best fit to the temporal change of saturation and water pressure at the four measurement points. The values of porosity and permeability determined in this way are given in Table 4.

### **5.3 Comparison of measurements to simulation results using $p_c$ - $S_w$ measured in the transient state experiment**

In the following, the measurements from the experiment will be compared to three numerical simulations. All simulations are based on the setup and the boundary conditions described above. The hydraulic properties of Table 4 also remain unchanged. In the first simulation, hysteresis is not taken into account. In the second simulation, the play-type hysteresis is used while the third simulation employs the scaling concept for hysteresis from PARKER AND LENHARD.

For the comparison of the results of the numerical simulations to the measured data, water pressure and saturation are obtained over time at four nodes of the rectangular grid. The nodes are at the same height as the four measurement points in the experiment (see Fig. 35). Furthermore, capillary pressure is plot-

ted with saturation at each timestep, allowing the visual comparison between simulated and measured scanning curves.

### 5.3.1 Simulation with hysteresis not included

In this first simulation, hysteresis is not accounted for in the capillary pressure-saturation relationship. All drainage and imbibition events are described with a single  $p_c-S_w$  curve that corresponds to the main drainage.

In the following, results will be discussed based on points 2,3 and 4. The results at point 1 are also given in Appendix A. The predicted water saturation at points 2, 3 and 4 during the entire drainage and imbibition sequence is plotted together with the saturation measured in the experiment in Figs. 36-38 (left). Some discontinu-

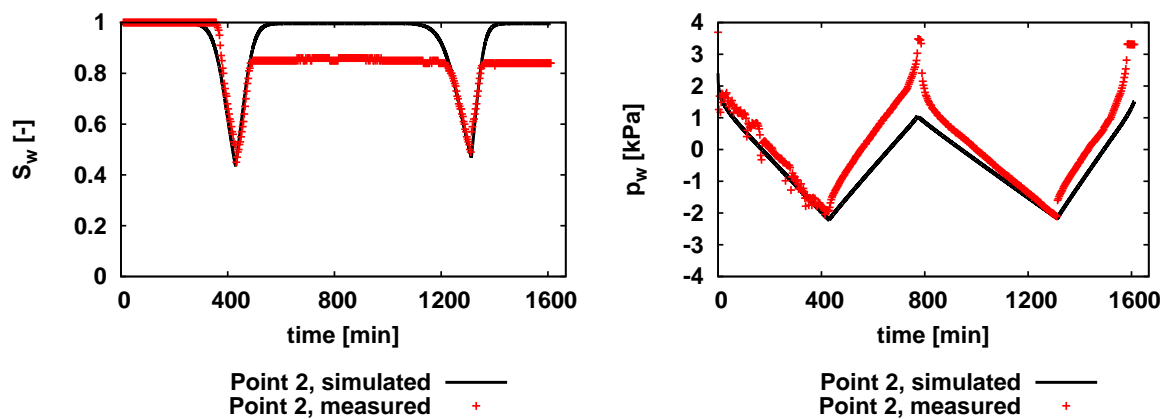


Figure 36: Point 2: saturation (left) and water pressure (right), comparison measurement and simulation with hysteresis not included.

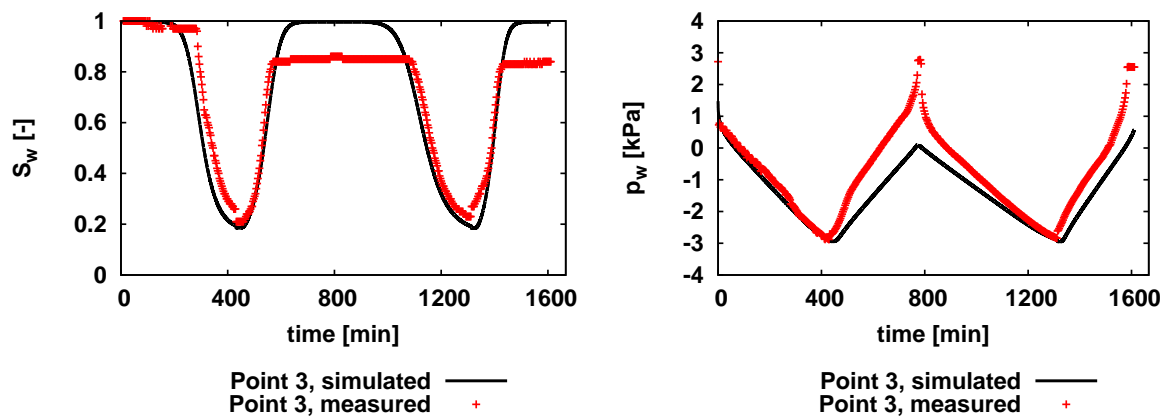


Figure 37: Point 3: saturation (left) and water pressure (right), comparison measurement and simulation with hysteresis not included.

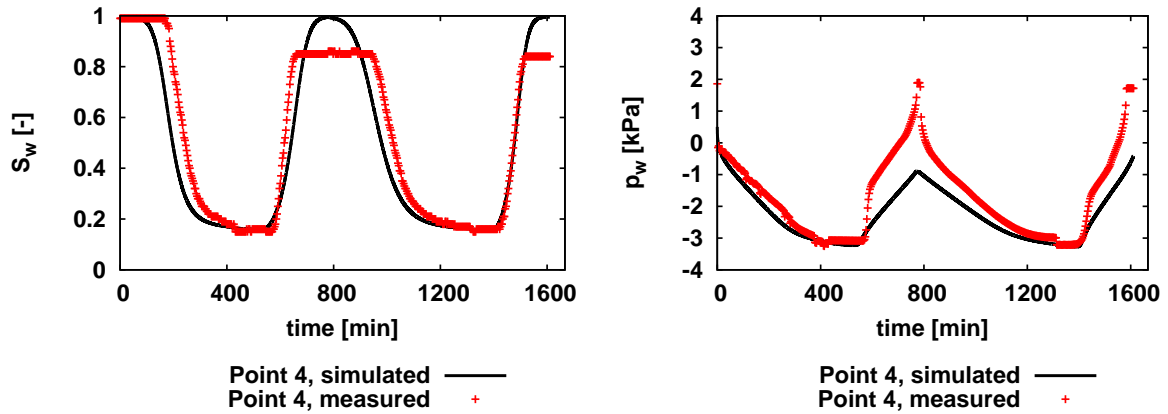


Figure 38: Point 4: saturation (left) and water pressure (right), comparison measurement and simulation with hysteresis not included.

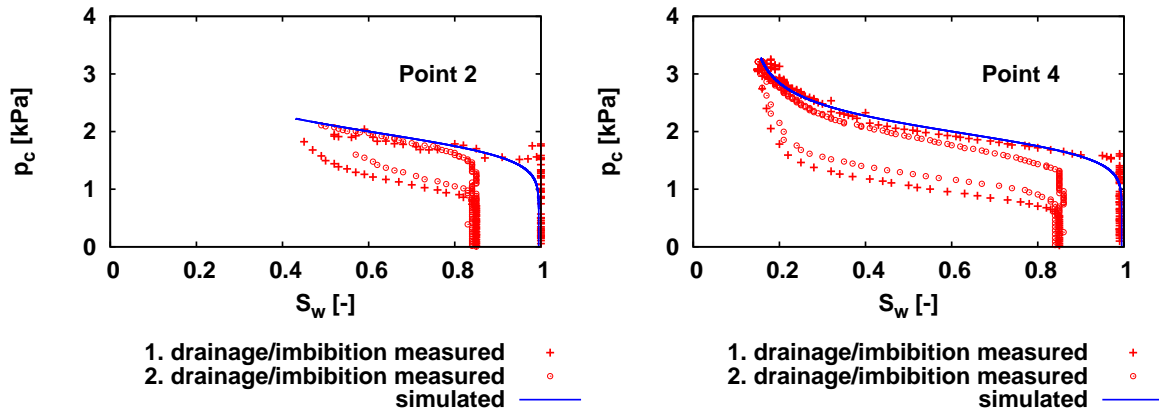


Figure 39: Capillary pressure-saturation at point 2 and point 4: comparison measurement and simulation with hysteresis not included.

ities observed in the measurements when switches from drainage to imbibition or vice versa take place (i.e. at the time 430 [min], see Fig. 37) result from the fact that the pump is turned off after each drainage/imbibition event and the column is left to rest for several hours. This procedure has also been simulated, however the influence of these relaxation periods on the obtained pressure and saturation is negligible. Therefore, results from the simulations and the experiment are presented here leaving out the relaxation periods (that would correspond to the times 430, 775 and 1315 [min]).

Water saturation at point 4 reaches at the end of drainage values close to 0.15 [-] while point 2 is positioned lower and therefore the minimum water saturation observed is approximately 0.42 [-]. In the experiment, water saturation at the end of imbibition (at time 775 [min]) does not reach the maximum value 1.0 [-] that was the initial condition, but a lower value equal to 0.85 [-]. This indicates that



there is a trapping of air that results to a residual air saturation for imbibition. On the other hand, the numerical simulation does not consider phase entrapment and therefore cannot capture this effect. Water saturation after imbibition reaches back to the maximum value 1.0 [-]. This difference between simulated and measured saturation is observed at all points 2, 3 and 4 for the first imbibition (times 430-775 [min]) and the second imbibition (times 1315-1612 [min]).

Figures 36-38 also illustrate the measured and the simulated values of water pressure at points 2, 3 and 4. Water pressure at point 2 is higher due to the hydrostatic distribution of pressure. Negative water pressures dominate at point 4 as the largest capillary pressure is observed near the top. The predicted water pressure however shows deviation from the measurements, especially during imbibition. The steep increase of water pressure observed in the experiment at the end of the first and the second imbibition (at times 775 and 1612 [min]) relates to the steep decrease of capillary pressure when the maximum water saturation 0.85 [-] is reached. In the numerical simulation, the maximum water saturation at imbibition remains equal to 1.0 [-] and thus the water influx from the bottom boundary can be stored in the domain without reaching the steep decrease of capillary pressure on the  $p_c-S_w$  curve.

On the other hand, at the end of the second drainage (at time 1315 [min]) predicted and measured water pressure agree (the same applies for saturation). This occurs because the scanning curves observed in the experiment during drainage end at the main drainage curve, that is also used in the simulation (see Fig. 39).

### 5.3.2 Simulation with play-type hysteresis included

In this case, the measurements from the 1-D transient experiment are compared to the predicted saturations and water pressures from a simulation incorporating the play-type hysteresis concept. Here the main imbibition curve is also given as input for the model (see Table 4). However, the play-type concept does not account for phase entrapment at the end of the imbibition process as the effective saturation must form closed loops (see Sect. 3.2.1). Therefore, the residual saturation of air in drainage and in imbibition is equal to 0.0 [-].

Figures 40-42 (left) show the predicted saturation at points 2, 3 and 4 plotted with the measurements. The predicted saturation is almost identical as in the previous simulation where hysteresis was not taken into account. At the end of the first and the second imbibition, the numerical simulation predicts smaller values of air saturation compared to the experiment, because phase trapping is not accounted for. However, the use of the play-type concept improves the agreement between the predicted water pressure and the tensiometer measurements. This

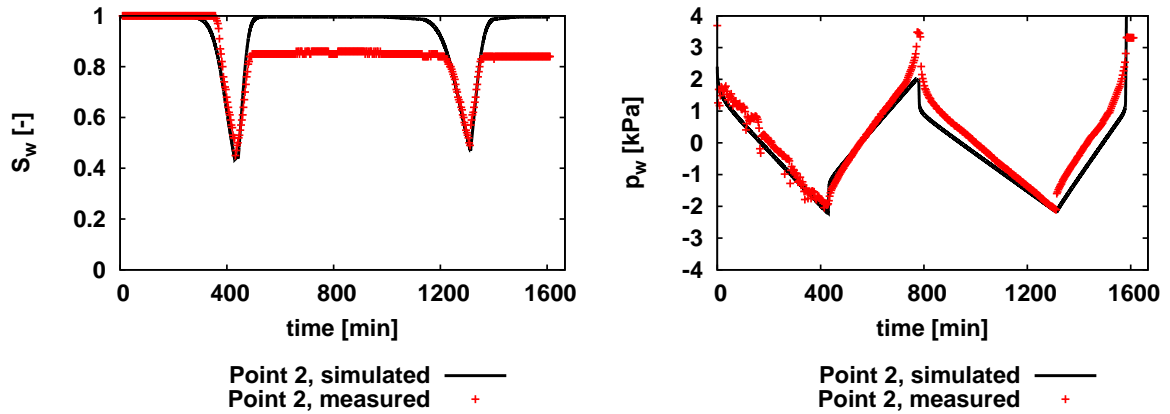


Figure 40: Point 2: saturation (left) and water pressure (right), comparison measurement and simulation with play-type hysteresis included.

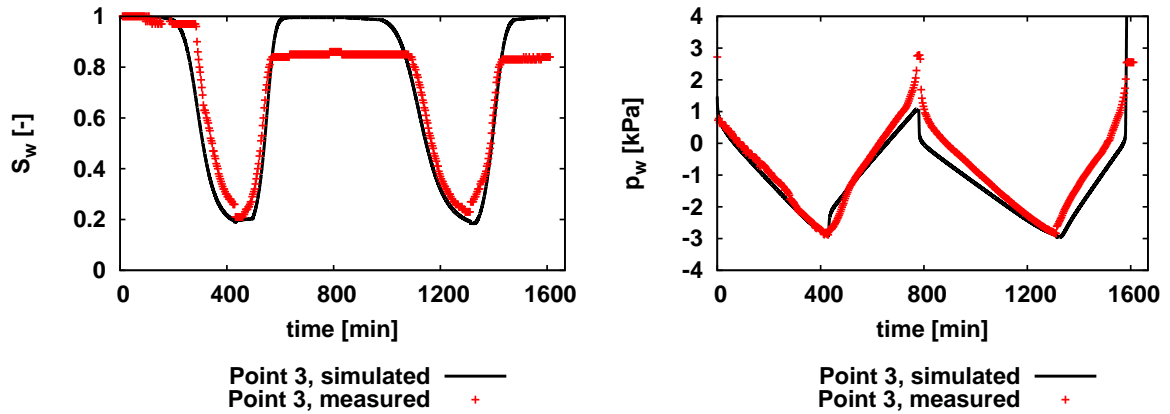


Figure 41: Point 3: saturation (left) and water pressure (right), comparison measurement and simulation with play-type hysteresis included.

is shown in Figs. 40-42 (right). The play-type hysteresis produces a step drop in capillary pressure when imbibition starts. This results to an increase of water pressure that gives a better prediction of the pressure distribution. Introducing the play-type hysteresis in the numerical simulation only affects the predicted pressure and not the saturation. This behavior relates to the Neumann boundary condition given for water at the bottom, that has a pronounced influence on the saturation. As the water flux is fixed, at each timestep the water mass in the domain and thus the saturation has to increase or decrease by a certain amount. Given that permeability and porosity are kept the same in the simulation without hysteresis and the simulation with the play-type hysteresis, it is reasonable to obtain similar saturation distributions from both simulations. On the other hand, water pressure is only restricted by the initial hydrostatic condition and it is therefore more sensitive to changes in the capillary pressure-saturation

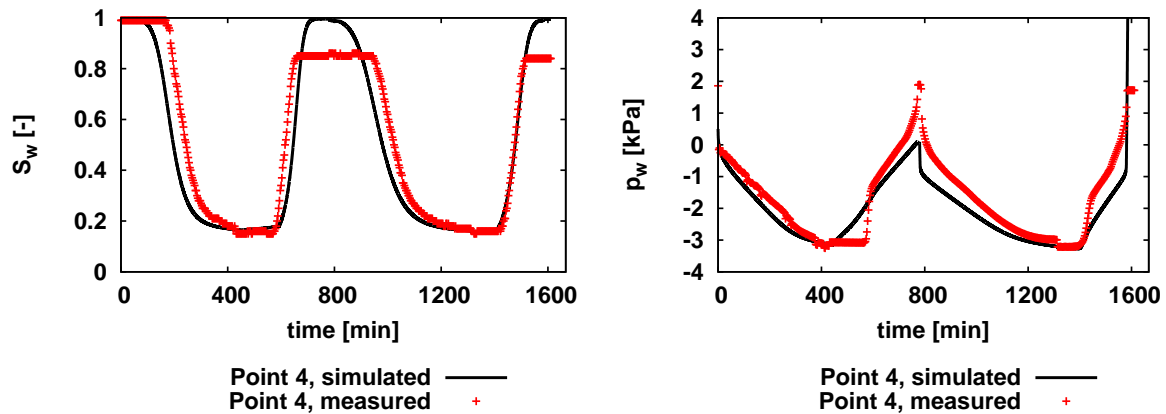


Figure 42: Point 4: saturation (left) and water pressure (right), comparison measurement and simulation with play-type hysteresis included.

relationship.

Figure 43 illustrates a comparison between the capillary pressure-saturation relationship from the numerical model and the one derived from the saturation and water pressure measurements. In the model, the vertical scanning curves from the first and the second imbibition coincide. Furthermore, the vertical scanning curve from the second drainage practically coincides with the main drainage curve. In the experiment, this does not occur due to the different values of residual air saturation observed in drainage and imbibition. Nevertheless, scanning curves at point 4 appear to be almost vertical at the beginning and then approach the main curves. Figure 43 presents what is observed in the results of Figs. 40 and 42 from a different angle. The play-type model can be a reasonable approximation for hysteretic effects if there is no significant trapping of non-wetting phase.

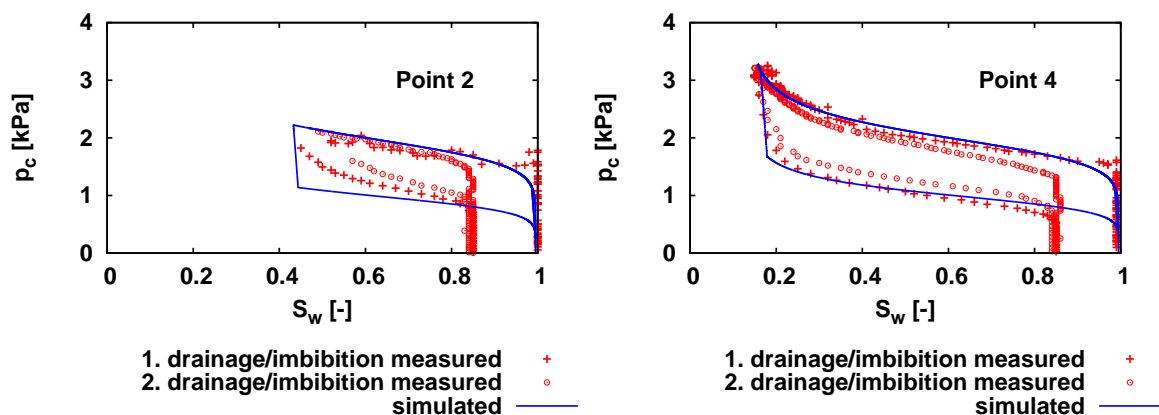


Figure 43: Capillary pressure-saturation at point 2 and point 4: comparison measurement and simulation with play-type hysteresis included.

### 5.3.3 Simulation including hysteresis from PARKER AND LENHARD

In the following, the scaling hysteresis concept from PARKER AND LENHARD (see Sect. 3.2.2) is used to describe the capillary pressure-saturation relationship in the numerical simulation. The necessary input for this approach are the parameters for the main drainage and the main imbibition curve as given in Table 4.

As described in Sect. 3.2.2, this hysteresis model accounts for trapped non-wetting phase. The predicted saturations at points 2, 3 and 4 is given in Figs. 44-46 (left) together with the values obtained from the TDR sensors. In this case, the numerical simulation has the ability to predict correctly the residual saturation of air at the end of each imbibition event. Furthermore, this model improves the agreement in saturation also at transient state (i.e. first imbibition at point 4, see Figs. 46, 42 and 38). The agreement between numerical simulation and experiment is also good in terms of water pressure as shown in Figs. 44-46 (right). The simulation can reproduce the development of water pressure at transient state and also the peaks observed in the experiment when the maximum water saturation is reached in imbibition (at times 775 and 1612 [min]).

The evolution of the capillary pressure-saturation relationship during the numerical simulation is plotted in Fig. 47 together with the derived data pairs from the sensor measurements for points 2 and 4. The following remarks are given related to the individual events:

#### First imbibition

For the first imbibition, modeled and measured scanning curves show good qualitative agreement. At the end of the first imbibition, a deviation is observed in the maximum water saturation reached. In the hysteresis model, this value is scaled between the maximum water saturation of the main imbibition and the main drainage curve, depending on the starting point of the current imbibition  $p_c-S_w$  curve (value  $S_{w,1}^i$ , see Sect. 4.3). At point 2, the starting saturation value on the  $p_c-S_w$  curve is approximately 0.42 [-] and the maximum water saturation on this scanning curve will be a value interpolated between 0.82 and 1.0 [-]. Point 4 reaches a lower water saturation before imbibition starts and therefore the maximum water saturation will lie closer to the value 0.82 [-] that corresponds to the main imbibition curve. The TDR sensors, on the other hand, measured at points 2,3 and 4 a maximum water saturation of 0.85 [-].

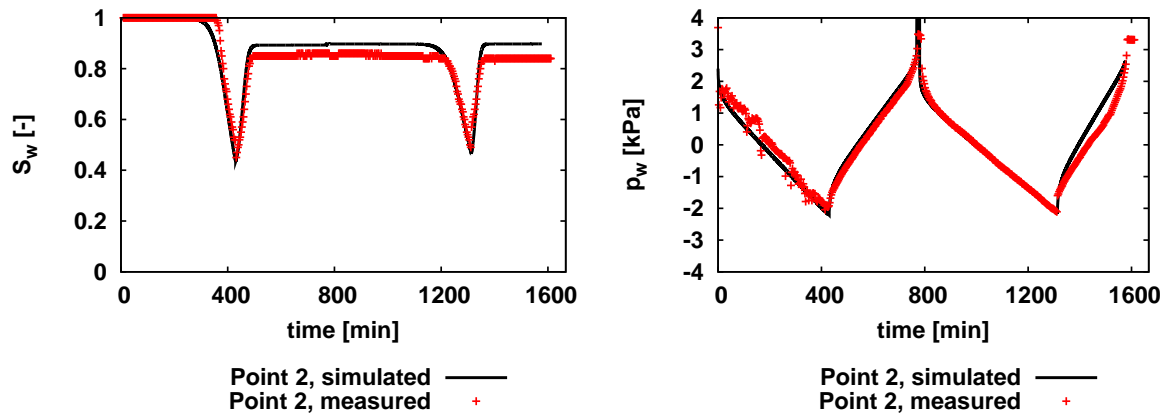


Figure 44: Point 2: saturation (left) and water pressure (right), comparison measurement and simulation including hysteresis from PARKER AND LENHARD.

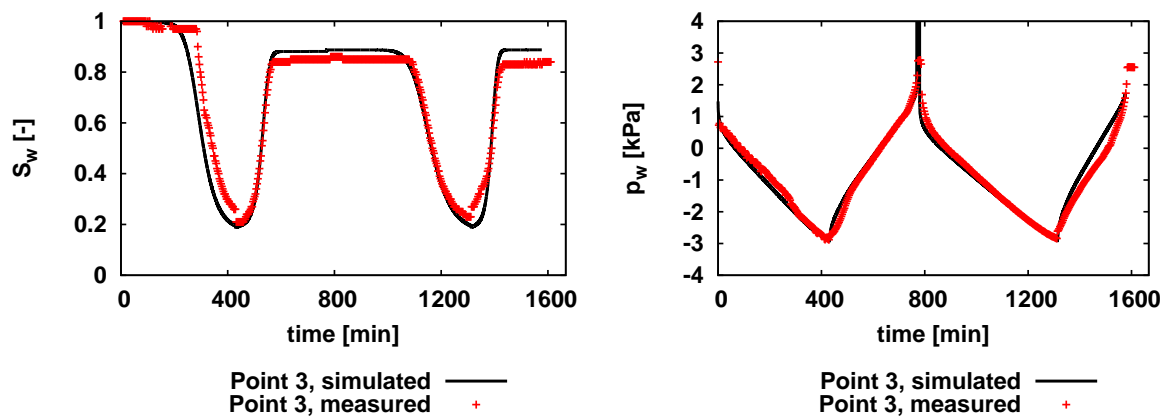


Figure 45: Point 3: saturation (left) and water pressure (right), comparison measurement and simulation including hysteresis from PARKER AND LENHARD.

## Second drainage

In the second drainage, scanning curves on the  $p_c$ - $S_w$  plane start where the first imbibition has ended. The scanning curves produced by the model show good qualitative agreement to those from the measurements. At the beginning of the second drainage there is a steep increase in the capillary pressure. In the model, this is influenced by the steep part of the main drainage curve and relates to the entry pressure. After a certain value, that is observed to be the same in the model and in the experiment, the  $p_c$ - $S_w$  scanning curve starts to approach the main drainage curve (see Fig. 47). Although the starting position of the modeled and the measured scanning curve differ, the shape of the curve is in both cases the same.

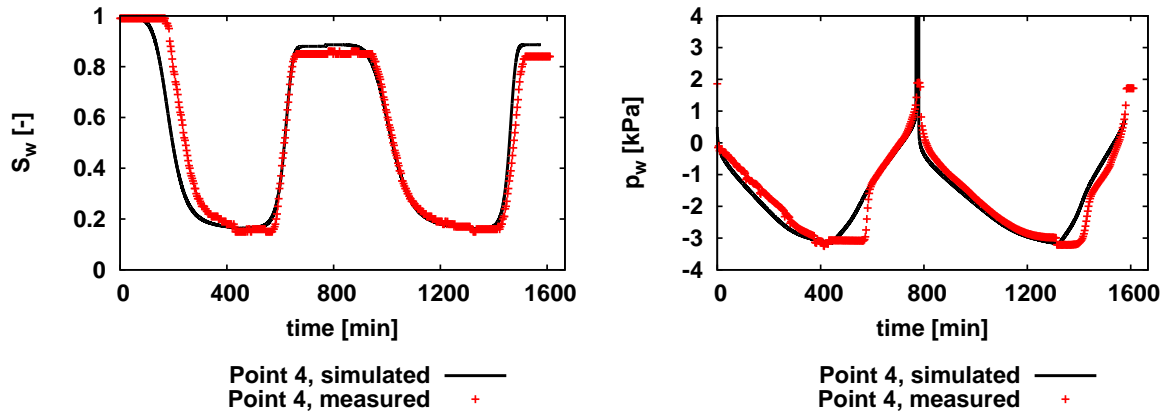


Figure 46: Point 4: saturation (left) and water pressure (right), comparison measurement and simulation including hysteresis from PARKER AND LENHARD.

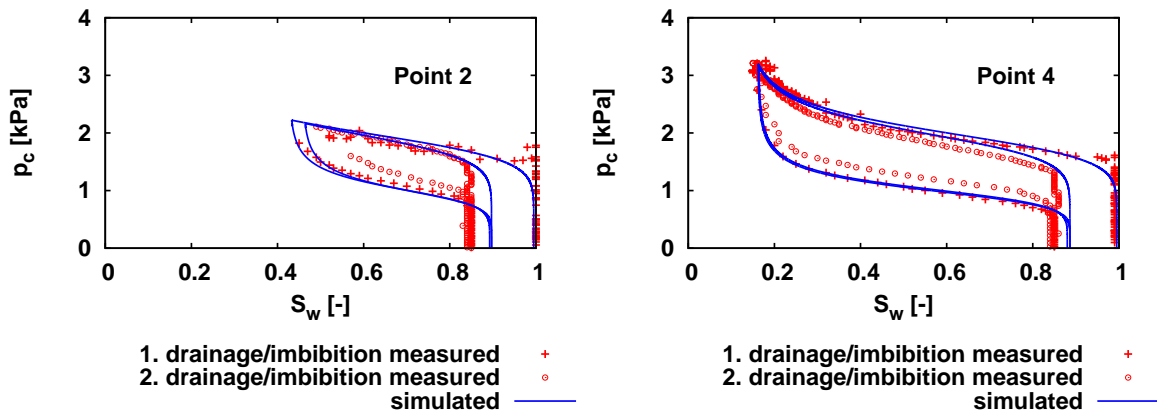


Figure 47: Capillary pressure-saturation at point 2 and point 4: comparison measurement and simulation including hysteresis from PARKER AND LENHARD.

### Second imbibition

In the numerical simulation and the experiment, the second drainage at point 4 ends approximately at the same saturation values as the first drainage did (see Fig. 47, value is approximately 0.15 [-]). In the model, this means that the starting saturation for the second imbibition curve is similar to that of the first imbibition curve. Furthermore, the ending saturation of the second imbibition curve will be the saturation at which the previous event started. That is, the value 0.88 [-] that was observed at the beginning of the second drainage. Practically, this implies that the modeled first and second imbibition scanning curves will be approximately the same. A similar effect is observed also at point 2 (see Fig. 47).

In the experiment, however, the scanning curves of the second imbibition event do not coincide with these of the first imbibition but follow a parallel course. According to the measurements, in the second imbibition capillary pressure relates to larger water saturation compared to the first imbibition, despite the fact that the two events start and end at the same saturation. This might be an indication that history dependence in secondary scanning curves (i.e. the second imbibition in this experiment) does not restrict to the previous event and the main drainage/imbibition curves but may also relate to the course of other intermediate events (i.e. the first imbibition in this experiment). In general, such an effect would require a large computational effort in order to keep track of the entire displacement history.

As explained above, it is not possible to capture this behavior in the second imbibition scanning curves with the PARKER AND LENHARD hysteresis concept. However, the numerical simulation shows a good agreement to the measurements in terms of saturation and pressure for all drainage and imbibition events, using a rather simple (from the mathematical and computational point of view) scaling concept for hysteresis. In praxis, measuring several scanning  $p_c$ - $S_w$  curves is a complicated and painstaking procedure. Here it is shown that it is sufficient to measure a main drainage and a main imbibition curve and use only this information to correctly predict -using the scaling concept- any scanning curve between the two main curves. However, as explained in the following section, the main drainage and imbibition curve must be properly determined depending on the application they are purposed for.

## 5.4 Hysteresis from a simple multistep experiment

A method very commonly used for the determination of the capillary pressure-saturation relationship in air-water systems is the *controlled outflow/inflow cell technique*, described for instance by LORENTZ ET AL. (1992) [86].

In the controlled outflow/inflow cell technique, a sample of a sand that is fully saturated with water is placed on a hydrophilic membrane or a ceramic porous plate that allows only water to flow through. The sample with the porous plate are positioned in a *pressure/suction cell* (see Fig. 48). By increasing the air pressure in the chamber (pressure cell) or by decreasing the pressure of water in the sand (suction cell), water leaves the sand sample through the porous plate while air enters from the top. The phase pressures during the experiment are controlled and changed incrementally. At each pressure step, water flows out and once steady-state is reached the corresponding saturation in the sample is determined. This way measured data pairs of pressure and saturation are obtained.

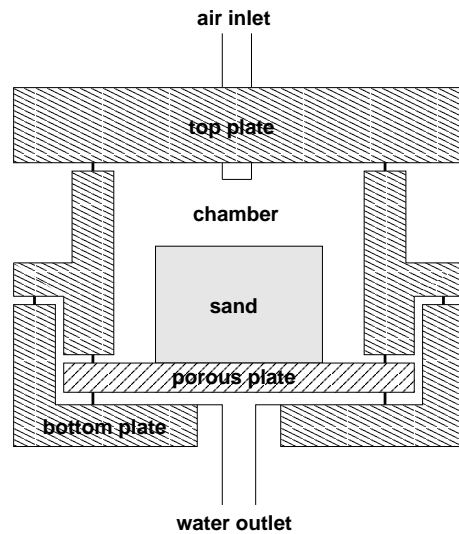


Figure 48: Schematical setup of a pressure/suction cell.

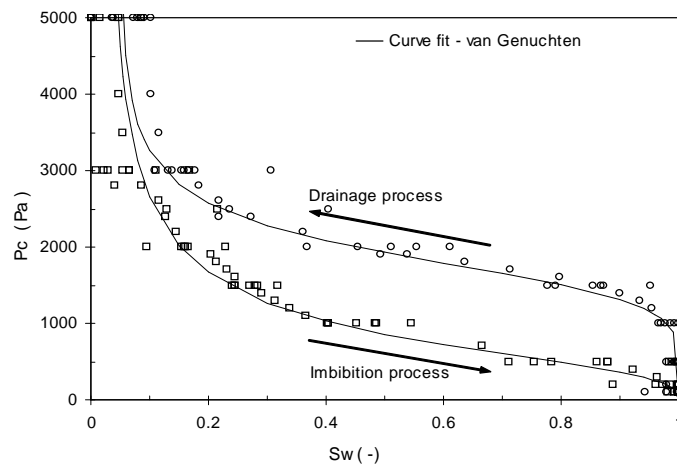


Figure 49: Pressure-saturation measurements for drainage and imbibition in the multistep experiments from LINS ET AL. (2007) [66]. The VAN GENUCHTEN fit is also illustrated.

This procedure is commonly referred to as a multistep experiment. Although multistep experiments can involve more complex setups and inverse modeling algorithms for the determination of hydraulic properties, the procedure explained here is the simplest and also one frequently used.

Numerical investigations of unsaturated flow often employ  $p_c$ - $S_w$  curves for porous media that have been determined with simple multistep experiments. As explained in Sect. 1.1, it remains unclear whether this methodology is appropriate to provide reliable predictions, especially if hysteresis effects are involved in



Property	Symbol	Value drainage	Value imbibition	Unit
Water residual saturation	$S_{wr}$	0.05	0.02	[-]
Air residual saturation	$S_{nr}$	0.01	0.01	[-]
VAN GENUCHTEN $\alpha$	$\alpha$	0.00055	0.0015	[1/Pa]
VAN GENUCHTEN $n$	$n$	6.0	2.8	[-]

Table 5: Hydraulic properties measured with the multistep experiment for drainage and imbibition.

the application. The problem here lies on the one hand on the disturbances in the porous medium introduced during the preparation of the separate sample for the multistep experiment and, on the other hand, on the different boundary conditions, flow and time regimes involved in the multistep experiment and the application.

In this section, it is assumed that the TDR and tensiometer measurements are not available for the determination of the  $p_c$ - $S_w$  relationship. In other words, what happens if the only information available about the  $p_c$ - $S_w$  curves comes from a classic multistep experiment? Would it then be possible to correctly predict the flow behavior during the successive drainage and imbibition events in the column?

For that purpose, multistep experiments using the same sand from the 1-D transient experiment are carried out. The cylindrical sand samples used are 2 [cm] high with a diameter of 7.1 [cm]. This sample size is similar to the size of the area captured by the sensors within the column in the transient experiment (see Sect.

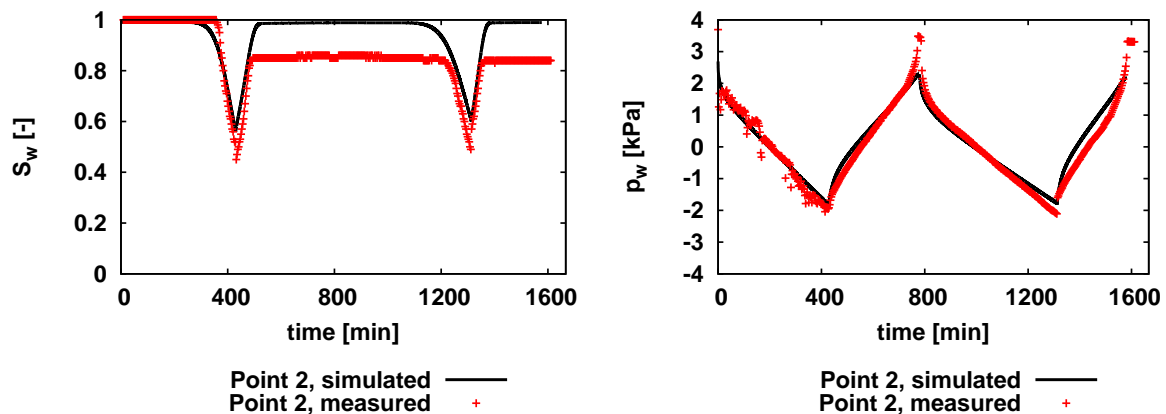


Figure 50: Point 2: saturation (left) and water pressure (right), comparison measurement and simulation using the  $p_c$ - $S_w$  measured with the multistep experiments.

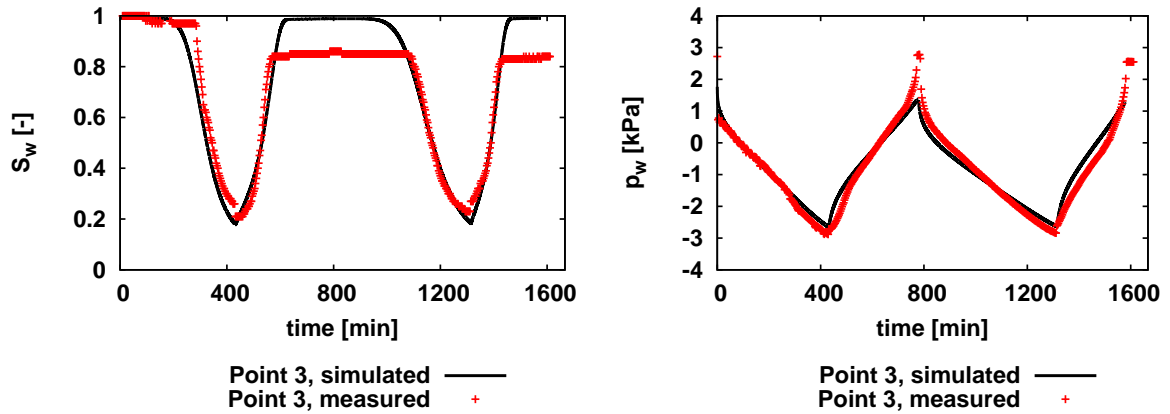


Figure 51: Point 3: saturation (left) and water pressure (right), comparison measurement and simulation using the  $p_c$ - $S_w$  measured with the multistep experiments.

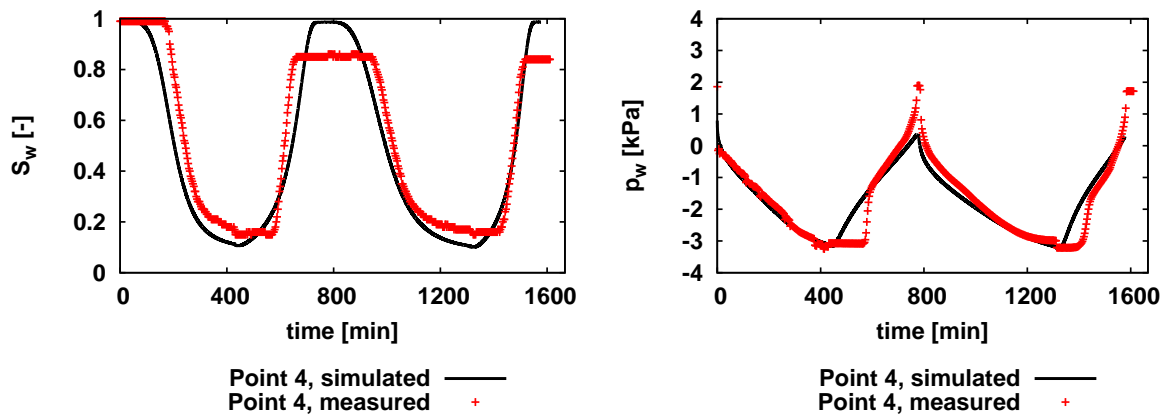


Figure 52: Point 4: saturation (left) and water pressure (right), comparison measurement and simulation using the  $p_c$ - $S_w$  measured with the multistep experiments.

5.1). In this sense, the approach described here determines the  $p_c$ - $S_w$  relationship on the same spatial scale as before, but with a different methodology. Water pressure is changed in increments of 100 [Pa]. The experiment is repeated seven times with different specimens of the sand. The time scale is similar in all seven tests. As an example, the full drainage in one of the tests lasts approximately 25 days whereas imbibition is completed after 30 days. During the experiments measures to prevent evaporation have been taken. The pressure and saturation pairs obtained are given in Fig. 49. The VAN GENUCHTEN parameters fitted to the results from the multistep experiments are given in Table 5. Directly from the values of the residual saturations one observes that at the end of imbibition no air trapping takes place. This contradiction to the transient experiment is also demonstrated

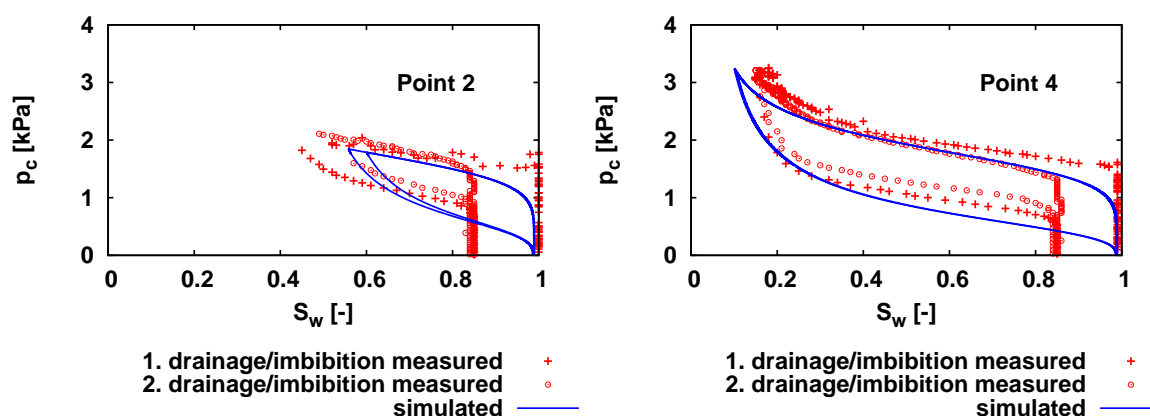


Figure 53: Capillary pressure-saturation at point 2 and point 4: comparison measurement and simulation using the  $p_c$ - $S_w$  measured with the multistep experiments.

with an additional numerical simulation that includes the hysteresis concept from PARKER AND LENHARD with the VAN GENUCHTEN parameters given in Table 5. The results from this numerical simulation are illustrated in Figs. 50-52. As in the multistep experiments no residual saturation of air is measured in imbibition, the prediction one would get with this approach is poor with respect to air trapping. This difference is also visualized in Fig. 53. The qualitative agreement in the  $p_c$ - $S_w$  curves in terms of entry pressure and inclination provides a good prediction of saturation and pressure in the transient state (see Figs. 50-52). On the other hand, the deviation in the residual trapped air saturation leads to an overestimation of the maximum water saturations.

## 5.5 Synopsis and remarks

In Sect. 5.3, a comparison between a monitored drainage and imbibition flow and the predictions made with different approaches is analyzed. This process shows that it is necessary to include a hysteresis concept in the numerical simulation, when flow during drainage and imbibition conditions needs to be predicted. The first modeling approach does not account for hysteresis and it is not possible to predict correctly the distribution of pressure and saturation in the transient experiment, even if the best fit of permeability and porosity is used.

The second modeling approach includes the play-type hysteresis that is conceptually simple but lacks a firm basis for the approximation of residual saturations in imbibition. Indeed, the simulation including the play-type hysteresis provides an approximation of the flow process in the transient experiment, however does

not predict the trapping of air. This concept would be suitable, for example, for modeling the multistep experiment of Sect. 5.4, where the imbibition process takes place with several increments and at the end water saturation returns to 1.0 [-].

In the third modeling approach, the scaling concept from PARKER AND LENHARD is used for hysteresis. This simulation provides a very good agreement to the measurements from the transient experiment. The hysteresis concept used in this case is an empirical scaling approach that is not very demanding with respect to computational effort. It is shown that in order to obtain a reliable prediction it is not necessary to use (infinite) scanning curves as input for the model, but only a main drainage and a main imbibition curve combined with the scaling concept. Still, the goodness of the results does not depend only on the model concept, but also on the input given to it. It is shown that a single pair of a TDR and a tensiometer (used to measure only the main drainage and the main imbibition curve), combined with the model from PARKER AND LENHARD, can provide a fairly accurate prediction of hysteretic flow in the entire 54 [cm] high column. On the other hand, using only the information available from the multistep experiments would not be enough for a correct prediction, independently from the modeling approach. Related to this, a remarkable deviation is observed in the amount of trapped air measured after imbibition in the transient and in the multistep experiments. Although the measurements correspond to samples of the same spatial scale, the time scales in the two approaches differ. In the transient experiment, the imbibition caused by the fixed water inflow is completed at point 4 within approximately 80 [min] (i.e. for the first imbibition saturation at point 4 changes from the minimum to the maximum value from 580 to 657 [min]). On the other hand, imbibition in the multistep experiments occurs stepwise and in several equilibria within larger time periods (several days). This suggests that the amount of trapped air, and thus the resulting  $p_c$ - $S_w$  relationship, depends on the methodology and the time scales linked to it. Practically, these observations imply that the input that is necessary for a correct model prediction are the two main curves -that correspond, however, to the time regimes that are relevant to the application under investigation.

## **6 From the pore scale to the local scale: numerical simulations of drainage and imbibition in 3-D heterogeneous porous media**

As explained in Sect. 1.1, there are different approaches and possibilities involved in the broad and complex problem of making predictions of hysteretic two-phase flow in heterogeneous porous media. Hydraulic properties of materials can be determined, as done traditionally, on the local scale with lab experiments or with alternative approaches that are based on a pore-scale consideration. Nevertheless, even when high-end methods are used, it is not clear how good predictions can one achieve. Related to the open questions identified in Sect. 1.1, an objective of this thesis is to compare predictions of two-phase drainage and imbibition in heterogeneous porous media to an experimentally measured hysteretic flow process, using hydraulic properties determined on the one hand on the pore scale and on the other hand on the local scale. The concept that is followed for that purpose is given in Fig. 54.

The connecting link of the applied strategy is a well-controlled 3-D drainage and imbibition experiment. To construct the heterogeneous column for the experiment, a pre-defined arrangement of two different sands is used. The equilibration times and the 3-D water distributions in the column are measured using neutron tomography after successive drainage and imbibition steps. This work is described in detail in SCHAAP ET AL. (2007) [88], a brief overview is given in Sect. 6.1.

The hydraulic properties of the sands are determined separately from the experiment with two different approaches.

In the first approach, a set of properties is determined as done in the classic way: multistep outflow/inflow experiments are conducted and global optimization techniques are used to determine the best fit parameter vector for a given model (in this case the porosity, the absolute permeability and the capillary pressure-saturation relationship for drainage and for imbibition). Details about

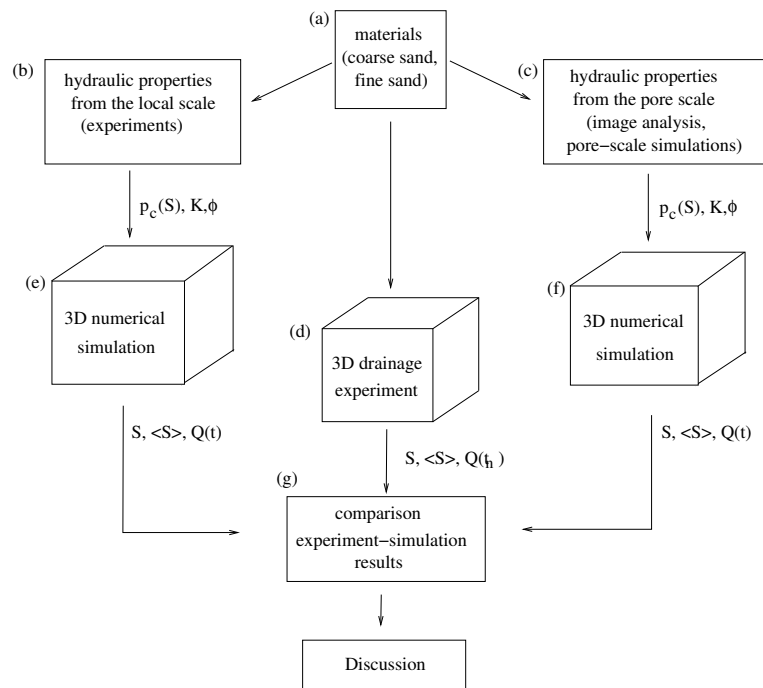


Figure 54: Strategy for comparing predictions made in two-phase flow in heterogeneous media with local-scale and pore-scale hydraulic properties.

the methodology and the experiments are given in AHRENHOLZ ET AL. (2007) [3], a short description is given in Sect. 6.2.

In the second approach, the pore structure of the sands is captured using tomography with synchrotron light. The pore geometry of the sands is mapped by means of high resolution advanced image analysis of the synchrotron tomography data. The hydraulic properties are then determined with the simulation of two-phase flow in the pore space described by the Navier-Stokes equations utilizing lattice Boltzmann methods. These simulations provide permeabilities and drainage/imbibition capillary pressure-saturation relationships for the two sands. This work is described in AHRENHOLZ ET AL. (2007) [3], here it is introduced in Sect. 6.3.

A comparison between the hydraulic properties obtained with these two approaches is provided in Sect. 6.4.

In the next part (Sect. 6.5), the structure and the boundary conditions from the 3-D experiment is approximated with 3-D two-phase flow numerical simulations. The equilibration times and measured water distributions from the experiment are compared to results from the numerical simulations. As input for the numerical simulations, hydraulic properties from the local-scale and from the pore-scale approach are used.

A synopsis and some related remarks are given in Sect. 6.7.

## 6.1 Description of experiment

The experiment was performed by Joris Schaap, Peter Lehmann, Anders Kaestner and Hannes Flühler from the Soil Physics group of the Institute for Terrestrial Ecology at the ETH Zürich, in collaboration with Rene Hassanein and Eberhard Lehmann from the Paul Scherrer Institute in Switzerland. The measurements of the saturation distribution were carried out at the NEUTRA beam line of the spallation neutron source SINQ at the PSI. A detailed description of the applied methods can be found in SCHAAP ET AL. (2007) [88].

The heterogeneous structure ( $10.2 \cdot 10.2 \cdot 12.8$  [cm<sup>3</sup>]) consists of an arrangement of sand blocks (each  $1.7 \cdot 1.7 \cdot 1.6$  [cm<sup>3</sup>]) containing either fine (grain diameter between 0.1 and 0.5 [mm]) or coarse (grain diameter between 0.3 and 0.9 [mm]) sand. The packing technique is the same as described in SCHAAP ET AL. (2007) [88]. The coarse sand blocks (33% of the total number of blocks) form a continuous pathway from top to bottom in the fine sand (67% of the total number of blocks). Figure 55 shows a graphical representation of the block arrangement. The structure rests on a bottom layer of fine sand with thickness 3.2 [cm] and is covered with a layer of coarse sand (of the same thickness) on top to protect it. A bronze filter plate of 0.2 [cm] thickness with an air entry value of -85 [cm] and an absolute permeability  $4.71e-13$  [m<sup>2</sup>] is placed at the bottom.

Heavy water (D<sub>2</sub>O) is water in which the hydrogen is replaced by its heavier isotope, deuterium. As it attenuates neutrons seven times less than normal water (H<sub>2</sub>O), heavy water is used for the experiment. Besides the attenuation coefficient, D<sub>2</sub>O has practically the same physical properties as water [KIRSCHENBAUM (1951) [55]] which makes it ideal for mapping water flow in porous media with neutron transmission.

The bottom outlet of the column is hydraulically connected to a large reservoir filled with water. The top of the column is open to air. The water table in the reservoir is assumed to be constant. Initially, the structure has maximum water saturation, reached by slowly elevating the water table from the bottom. This 'natural' wetting procedure practically results to some air trapping effects and thus the initial water saturation is not equal to 1.0 [-]. The reservoir can be moved vertically in order to apply different pressure heads at the bottom of the column. Three successive drainage steps and two imbibition steps are applied (see Table 6). Strictly speaking, these steps do not correspond to main drainage and main imbibition processes, as the column is not initially 100% saturated with water.

First, the water table is lowered to -2.2 [cm] from the bottom of the column (first drainage step). During the first drainage step, the fine sand is still saturated. Once quasi steady-state is reached (outflow  $<0.2$  [g/min]), the column is scanned (first tomography). After that, the water table is further lowered to -14.2 [cm] (second

Pressure at the bottom [cm]	Equilibration time [min]	Tomography time [min]	Flow during tomography [g]
-2.2 (dr.)	45	75	2.32
-14.2 (dr.)	160	80	10.05
-40.7	175	-	-
-14.2 (imb.)	71	79	11.27
-2.2 (imb.)	94	77	14.80

Table 6: Drainage, imbibition and tomography times and measured outflow or inflow during the tomographies.

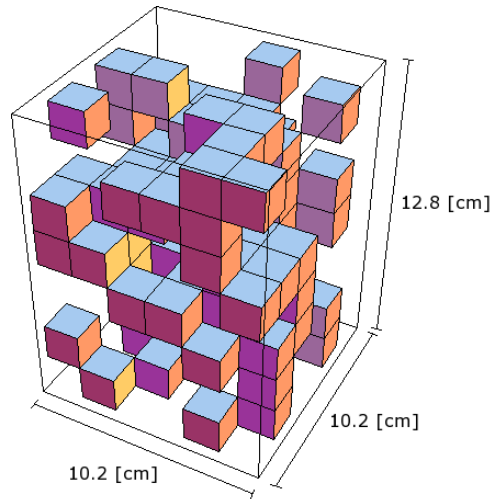


Figure 55: Arrangement of the coarse sand blocks in the column (from SCHAAP (2005) [87]).

drainage step) and when quasi steady-state is again established, the second tomography takes place. After the second drainage step, the coarse sand is entirely drained (residual water saturation). For the third drainage step the water table is set to -40.7 [cm] and no tomography takes place. Imbibition is then introduced by rising the water table back to -14.2 [cm] (first imbibition step) and at quasi steady-state (inflow  $< 0.2$  [g/min]) the third tomography is carried out. Finally, the water table is set to -2.2 [cm] for the second imbibition step and the fourth tomography.

The resulting neutron tomography images for drainage are shown in Fig. 56. Gray values (quantifying neutron attenuation) obtained from the tomography are related to the water content using a physically-based linear relationship between the water saturation and the logarithm of the gray level of the image (Beer-



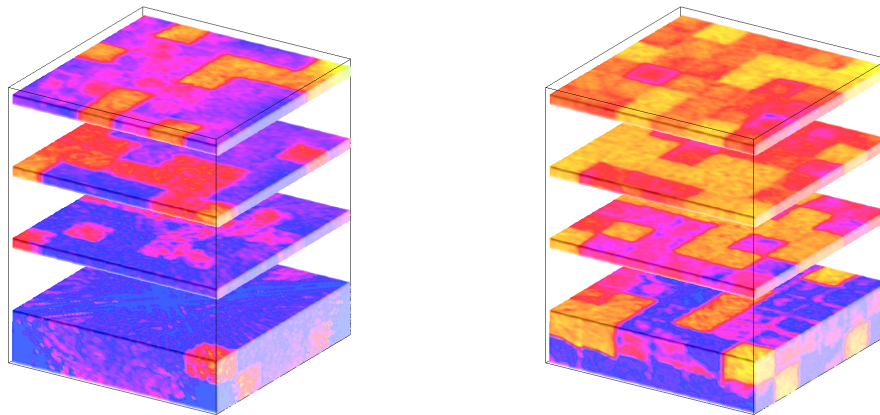


Figure 56: Tomography images of the first (left) and second (right) drainage step (from SCHAAP (2005) [87]). Dark colors relate to higher water saturations.

Lambert law, see i.e. KAESTNER ET AL. (2007) [53]). The linear relation is calculated by assigning the total water mass, that is measured with a balance, to the logarithm of the average gray level in the column. To find the mean gray level, only the inner 90% of the column is accounted for to avoid an error due to scattering effects at the edges. This might introduce an error in the mass balance that is, however, empirically corrected. For a more detailed description see HASSANEIN ET AL. (2005) [35] and SCHAAP ET AL. (2007) [88].

From the gray level, an averaged water saturation value is obtained for each sand block of the structure. In order to minimize the measurement error and avoid variations of saturation near the sensitive boundaries of the sand cubes (see Fig. 56), only the inner  $1.1 \cdot 1.1 \cdot 1.1$  [cm<sup>3</sup>] of the cubes is used for the evaluation of the average cube saturation. Due to the uncertainty of the tomography data at very dry and very wet regions, focus is given on the coarse sand saturation in the first drainage and the second imbibition step (water table at -2.2 [cm]) and the fine sand saturation in the second drainage and the first imbibition step (water table at -14.2 [cm]).

The resulting cube saturations are given for each layer in Figs. 57 and 58. The measurement error in the voxel saturation is determined to be 5% [VASIN ET AL. (2007) [100]; HASSANEIN ET AL. (2005) [35]]. This error is small compared to the variations observed in the cube saturation for each layer. Therefore, in order to estimate the uncertainty in the saturation measurements from the 3-D experiment, the error in the voxel saturation is here replaced by the (larger) variation of the cube saturations per sand type and per horizontal layer.

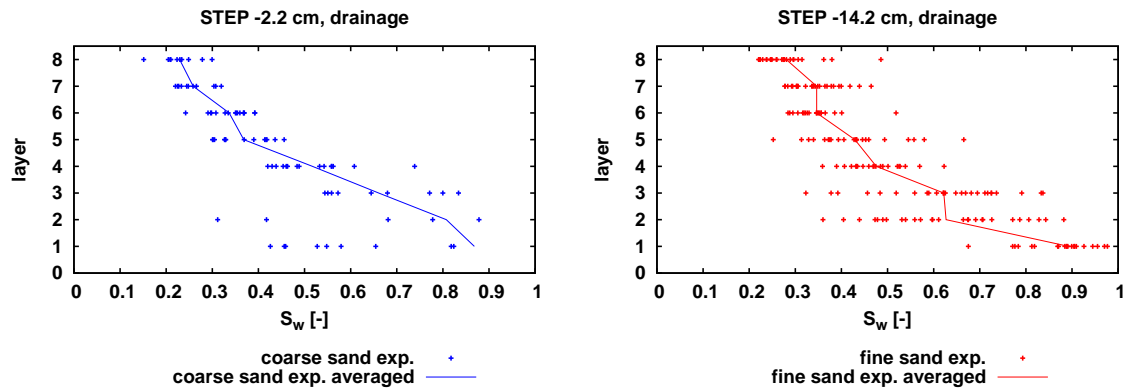


Figure 57: Measured saturations for 1st and 2nd step (drainage).

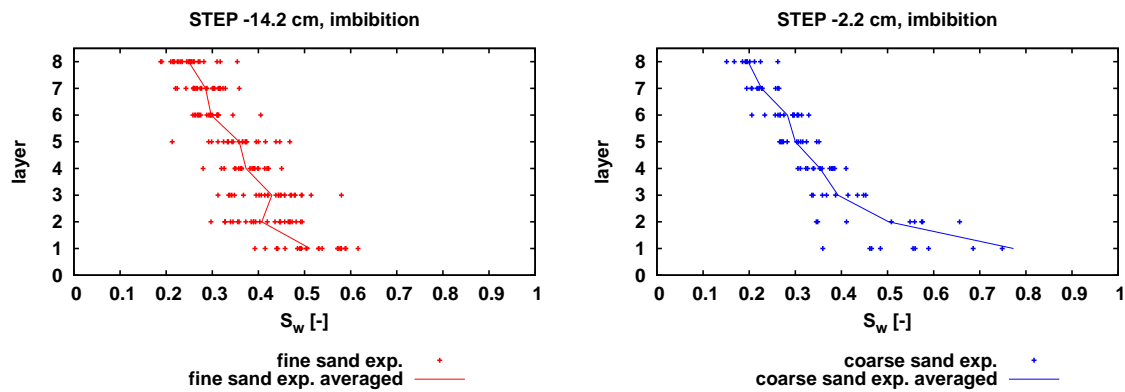


Figure 58: Measured saturations for 4th and 5th step (imbibition).

The large variations in cube saturations observed at the lower three layers result from the scattering of neutrons at the bronze porous plate. This effect can also be identified directly on the tomography images shown in Fig. 56. Although it is established that a large error is included in these values, they are presented here in order to provide useful knowledge for future work.

Apart from that, variations in cube saturations appear also in the other layers. A part of this variation (up to 10%, see VASIN ET AL. (2007) [100]) in the measured cube saturations comes from small differences in the packing of the individual cubes as well as due to the measurement error in the voxel saturation. However, the variations in cube saturations at the upper layers that exceed this value relate to the fact that the tomography took place at quasi steady-state (meaning steady-state was not yet reached). Measurements of saturation taken at full steady-state are presented in VASIN ET AL. (2007) [100] and only variations up to 10% are observed. The effect of the quasi steady-state condition on the saturation distribution is investigated with the numerical simulations and is discussed further in

Sects. 6.6 and 6.7.

Additionally, each horizontal layer in the structure is divided in a coarse and a fine sand part based on the arrangement design. The average saturation per sand type is calculated (see Figs. 57 and 58). In this way, average saturation data are obtained per sand type and per horizontal layer. Besides the water distribution at quasi steady-state, the equilibration times of the whole column are measured (see Table 6).

## 6.2 Hydraulic properties determined on the local scale

In the first approach, the hydraulic properties of the sands are determined by inverse modeling of multistep outflow/inflow experiments. The experiments were carried out by Andre Peters and Wolfgang Durner from the Institute of Geocology at the Braunschweig Technical University, Germany. The methodology is

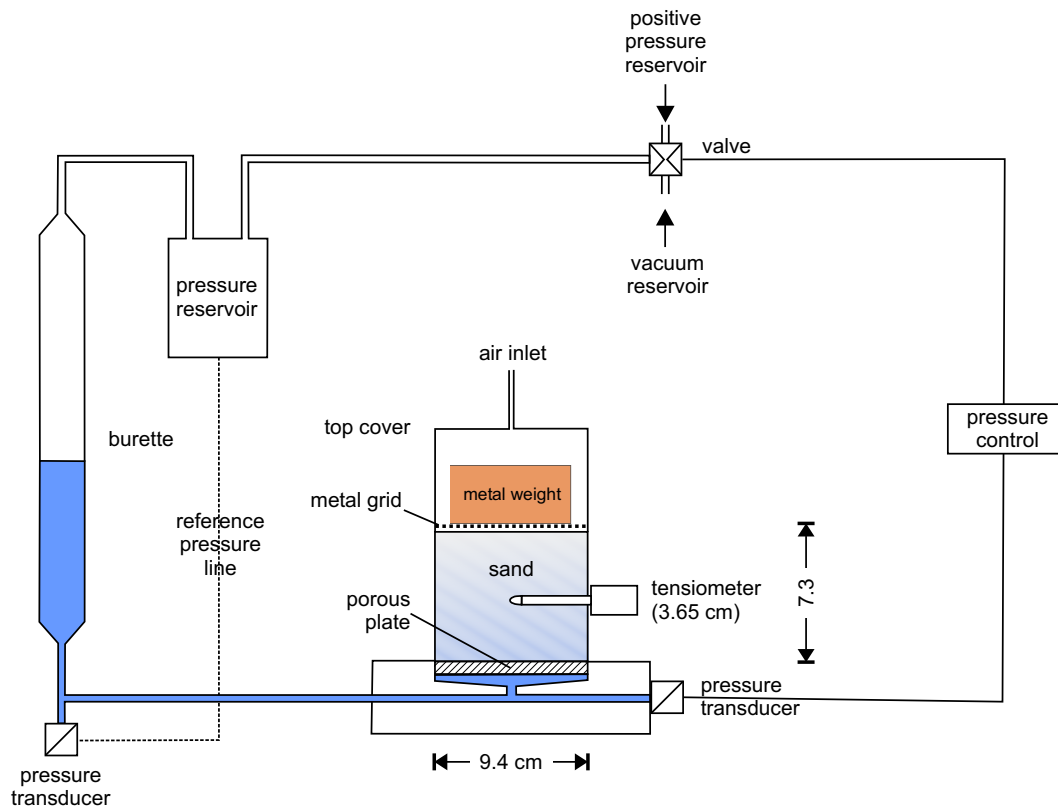


Figure 59: Schematical setup of the multistep outflow/inflow experiments [from AHRENHOLZ ET AL. (2007) [3]].

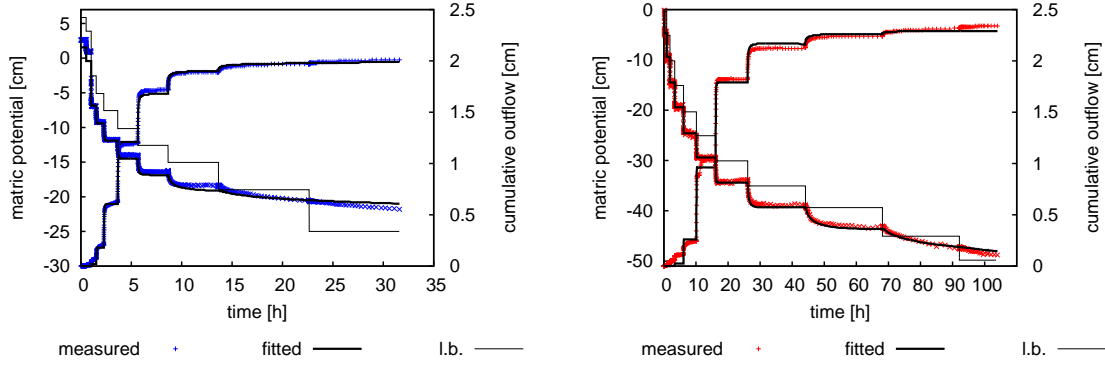


Figure 60: Measured and fitted cumulative outflow and pressure head data of the multistep outflow experiment for the coarse and the fine sand from AHRENHOLZ ET AL. (2007) [3]. The lower boundary condition (l.b.) is also indicated.

described in detail in AHRENHOLZ ET AL. (2007) [3].

The setup used in the multistep outflow/inflow experiments is given in Fig. 59. The fine and coarse sand columns used are 7.3 [cm] high and have a diameter of 9.4 [cm]. The sand columns are positioned on a ceramic plate while the top is covered with a metal grid and loaded with 1.5 [kg]. During drainage, the water table at the bottom of the plate is lowered stepwise from 6.0 to -25 [cm] in the coarse sand multistep experiment and from 7.5 to -50 [cm] in the fine sand multistep experiment. For the imbibition, the pressure at the bottom is increased back to the starting value with the same number of steps. The cumulative outflow/inflow and the pressure in the center of the column are measured during the experiments.

For the estimation of the hydraulic properties from the measured data, the 1-D Richards equation [RICHARDS (1931) [85]] is used

$$\frac{d\theta}{dp} \frac{\partial p}{\partial t} - \frac{\partial}{\partial z} \left[ K(p) \left( \frac{\partial p}{\partial z} - \rho_w g \right) \right] = 0, \quad (58)$$

where  $p$  [Pa] is the pressure,  $\theta$  [-] is the volumetric water content,  $z$  [m] is the vertical length unit,  $t$  [s] is the time,  $K(p)$  [m/s] is the hydraulic conductivity function,  $\rho_w$  [kg/m<sup>3</sup>] is the water density and  $g$  [m/s<sup>2</sup>] represents the gravitational acceleration. The constitutive relationships  $\theta(p)$  and the hydraulic conductivity function,  $K(p)$ , are described by the MUALEM/VAN GENUCHTEN model. Equation 58 including the constitutive functions is fitted to the measured pressure and cumulative outflow/inflow data by minimizing an objective function  $\Omega$ , which is here the sum of weighted squared residuals between predicted and measured data:

Property	Symbol	cs (dr.)	cs (im.)	Unit
VAN GENUCHTEN $\alpha$	$\alpha$	0.000763	0.001353	[1/Pa]
VAN GENUCHTEN $n$	$n$	10.06	3.87	[-]
Water residual saturation	$S_{wr}$	0.1	0.074	[-]
Air residual saturation	$S_{nr}$	0.182	0.223	[-]
Absolute permeability	$\mathbf{K}$	1.18e-10	1.18e-10	[m <sup>2</sup> ]
Porosity	$\phi$	0.39	0.39	[-]

Table 7: Hydraulic properties determined for the coarse sand (cs) on the local scale with the multistep outflow/inflow experiments.

Property	Symbol	fs (dr.)	fs (im.)	Unit
VAN GENUCHTEN $\alpha$	$\alpha$	0.000346	0.000655	[1/Pa]
VAN GENUCHTEN $n$	$n$	11.42	14.45	[-]
Water residual saturation	$S_{wr}$	0.185	0.29	[-]
Air residual saturation	$S_{nr}$	0.034	0.142	[-]
Absolute permeability	$\mathbf{K}$	4.0e-11	4.0e-11	[m <sup>2</sup> ]
Porosity	$\phi$	0.41	0.41	[-]

Table 8: Hydraulic properties determined for the fine sand (fs) on the local scale with the multistep outflow/inflow experiments.

$$\Omega(\mathbf{b}) = w_p \sum_{i=1}^{r_p} [p_i - \hat{p}_i(\mathbf{b})]^2 + w_Q \sum_{i=1}^{r_Q} [Q_i - \hat{Q}_i(\mathbf{b})]^2, \quad (59)$$

where  $\mathbf{b}$  is the parameter vector,  $r_p$  and  $r_Q$  stand for the number of measurements for pressure and cumulative outflow/inflow while  $w_p$  and  $w_Q$  are the weighting factors for the different data types.  $p_i$  and  $Q_i$  represent the measured values and  $\hat{p}_i(\mathbf{b})$  and  $\hat{Q}_i(\mathbf{b})$  the model prediction values. The vector  $\mathbf{b}$  contains the residual water content  $\theta_r$  (relates to the residual water saturation  $S_{wr}$ ), the VAN GENUCHTEN parameters  $\alpha$ ,  $n$  and the tortuosity  $\tau$ . The maximum water content  $\theta_s$  (relates to the residual air saturation  $S_{nr}$ ) and  $\mathbf{K}$  are treated as known. The factors  $w_p$  and  $w_Q$  are chosen to be the inverse of the squared a priori assumed measurement errors,  $\epsilon_p$  and  $\epsilon_Q$ . These are assumed to be 20 [Pa] and 1.0e-4 [m], respectively. The fitting procedure is carried out with the shuffled complex evolution algorithm [DUAN ET AL. (1992) [25]] which is a global optimizer [AHRENHOLZ

ET AL. (2007) [3]].

The cumulative outflow and pressure head data and model fits for drainage are shown in Fig. 60. The fitted hydraulic properties for drainage and imbibition are listed in Tables 7 and 8.

### 6.3 Hydraulic properties determined on the pore scale

In this approach, the hydraulic properties of the sands are determined from microscans of the pore space and pore-scale flow simulations using lattice Boltzmann (LB) methods. The simulations were performed by Benjamin Ahrenholz, Jonas Tölke and Manfred Krafczyk at the Institute for Computer Applications in Civil Engineering, Braunschweig Technical University, Germany.

X-rays from a synchrotron light source are used to map the 3-D pore-space structure of the sands with a resolution of 11 microns. By means of advanced image analysis, the images are segmented and divided into pore space and space occupied by sand grains. The method is described in detail in KAESTNER ET AL. (2007) [54]. The cylindrical scanned samples of the coarse and fine sand are 1 [cm] high and have a diameter of 1.5 [cm]. The porosity of the sands can be determined directly from the pictures. Cross-sections of the structures obtained for the coarse and the fine sand are shown in Fig. 61. In order to determine the permeability and the capillary pressure-saturation curves for the two sands, the scanned structures are used as base geometries in a 3-D nineteen velocity lattice

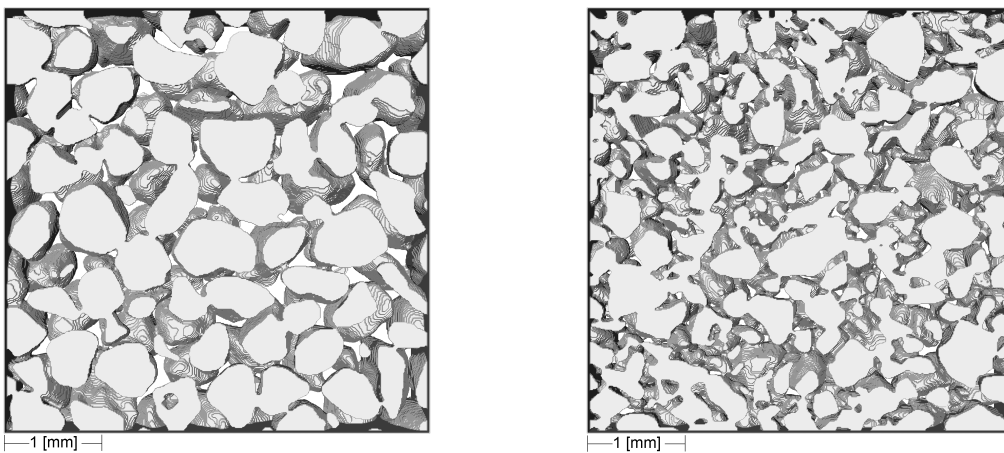


Figure 61: Cross-sections from the coarse and the fine sand  $0.44 \text{ [cm}^3\text{]}$  cubes.

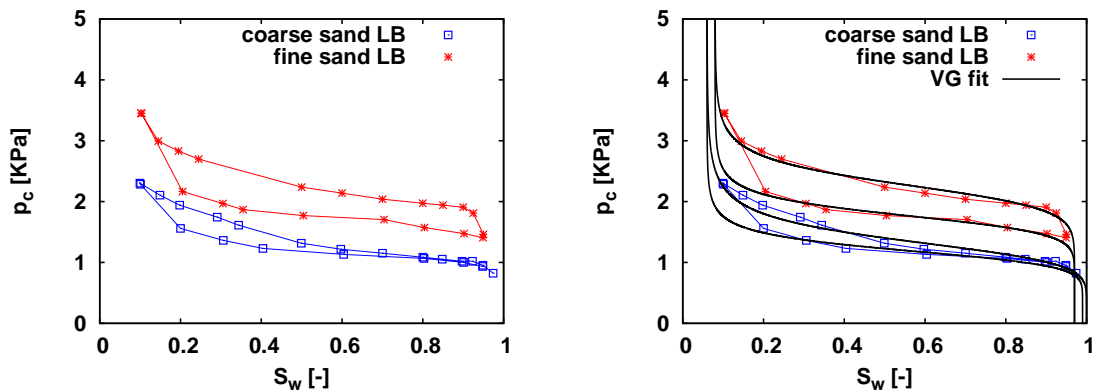


Figure 62:  $p_c$ - $S_w$  calculated with LB for the coarse and fine sand. The fit made with the VAN GENUCHTEN model is provided in the right image.

Boltzmann model (D3Q19) for immiscible binary fluids developed in TÖLKE ET AL. (2006) [95].

Details about the lattice Boltzmann simulations are given in AHRENHOLZ ET AL. (2007) [3]. For the determination of the permeability, single phase flow simulations are carried out in  $0.88 \text{ [cm}^3\text{]}$  cubes of the scanned structures.

AHRENHOLZ ET AL. (2007) [3] have carried out a comparative study on the ability of the method to predict  $p_c$ - $S_w$  curves and also investigated the influence of pore throat distributions and boundary effects on the predicted  $p_c$ - $S_w$  relationship using  $0.22 \text{ [cm}^3\text{]}$  cubic samples. Based on those observations, the samples here are chosen to be  $0.44 \text{ [cm}^3\text{]}$  cubes in order to minimize fluctuations in the calculated  $p_c$ - $S_w$  curves. In this case, the computational effort does not allow an error analysis. However, the  $0.44 \text{ [cm}^3\text{]}$  structures used here are chosen among several samples as the most representative, with respect to the pore throat distribution at the boundaries and the inner of the sample.

The pore space is initially filled with the wetting phase (water) and the capillary pressure is zero. The drainage process is simulated by decreasing the wetting phase pressure at the bottom in several pressure steps. The simulation for each pressure step is run until the system reaches a static equilibrium. The obtained capillary pressure-saturation pairs represent points on the  $p_c$ - $S_w$  curve. Starting from the situation that corresponds to the point with the minimum saturation, the water pressure is again stepwise increased to obtain the imbibition  $p_c$ - $S_w$  curve. In Fig. 62 the calculated capillary pressure-saturation pairs for the coarse and fine sand are shown. In the dry range, the LB method is not able to reproduce the strong increase in capillary pressure due to resolution problems of the wetting phase (films of wetting phase cannot be resolved with the given resolution). Therefore, the exact determination of the residual water saturation is not possible. However, it can be estimated from the last points in the dry region of the

calculated  $p_c-S_w$  curves. The results for the hydraulic properties from the pore scale are given in Tables 9 and 10. The  $\alpha$  and  $n$  parameters correspond to the fitted curves of the VAN GENUCHTEN function to the calculated  $p_c-S_w$  pairs.

Property	Symbol	cs (dr.)	cs (im.)	Unit
VAN GENUCHTEN $\alpha$	$\alpha$	0.00075	0.00084	[1/Pa]
VAN GENUCHTEN $n$	$n$	7.0	9.0	[-]
Water residual saturation	$S_{wr}$	0.06	0.06	[-]
Air residual saturation	$S_{nr}$	0.0	0.01	[-]
Absolute permeability	$\mathbf{K}$	$3.38 \times 10^{-10}$	$3.38 \times 10^{-10}$	[m <sup>2</sup> ]
Porosity	$\phi$	0.41	0.41	[-]

Table 9: Hydraulic properties determined for the coarse sand (cs) on the pore scale with image analysis and lattice Boltzmann numerical simulations.

Property	Symbol	fs (dr.)	fs (im.)	Unit
VAN GENUCHTEN $\alpha$	$\alpha$	0.00044	0.000565	[1/Pa]
VAN GENUCHTEN $n$	$n$	11.0	11.5	[-]
Water residual saturation	$S_{wr}$	0.08	0.08	[-]
Air residual saturation	$S_{nr}$	0.03	0.03	[-]
Absolute permeability	$\mathbf{K}$	$1.49 \times 10^{-10}$	$1.49 \times 10^{-10}$	[m <sup>2</sup> ]
Porosity	$\phi$	0.41	0.41	[-]

Table 10: Hydraulic properties determined for the fine sand (fs) on the pore scale with image analysis and lattice Boltzmann numerical simulations.

## 6.4 Comparison of hydraulic properties (local scale-pore scale)

In Tables 7, 8, 9 and 10, deviations between the hydraulic properties obtained with multistep outflow/inflow experiments and with the lattice Boltzmann simulations are observed. The differences are discussed in the following.



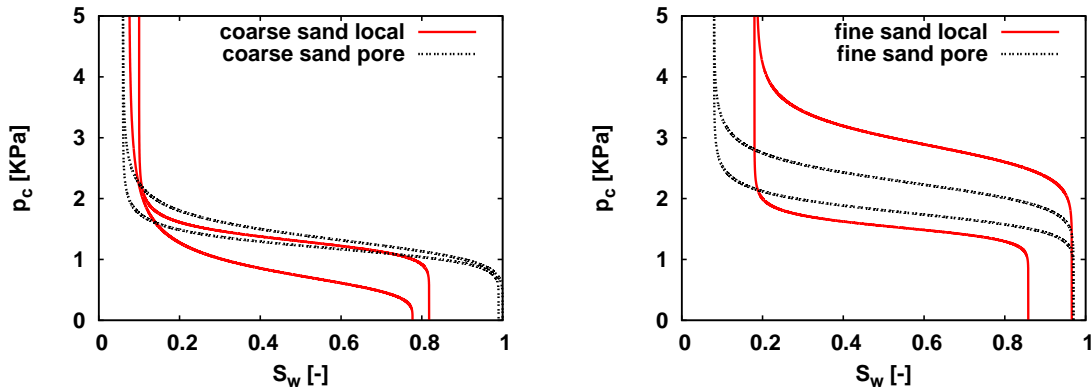


Figure 63: Coarse sand (left) and fine sand (right) hysteric  $p_c$ - $S_w$  relationships determined on the local scale and on the pore scale.

### 6.4.1 Capillary pressure-saturation

As explained in Sect. 2.3.2, the shape of a capillary pressure-saturation curve in the VAN GENUCHTEN model is described with the parameters  $\alpha$ ,  $n$ ,  $S_{wr}$  and  $S_{nr}$ . The parameter  $n$  determines the slope of the curve,  $\alpha$  relates to the inverse of entry pressure,  $S_{wr}$  and  $S_{nr}$  are the minimum and maximum water saturations.

#### Drainage

Although the drainage  $p_c$ - $S_w$  curves illustrated in Fig. 63 correspond to the primary drainage, the maximum water saturation is not  $S_w = 1.0$  [-]. In the local-scale approach, this is due to the trapped air saturation that develops during the packing of the sand columns. The columns are not flushed with  $\text{CO}_2$  in order to have a consistent approach with the packing of the 3-D heterogeneous column and similar conditions with the experiment described in Sect. 6.1.

In general, the slope of the  $p_c$ - $S_w$  curve depends on the pore throat distribution of the material. On the local scale the entry pressure is defined as the pressure that has to be exceeded so that the non-wetting phase can infiltrate a material. On the pore scale, large pores at the boundary of the sample will allow the non-wetting phase to penetrate, resulting to a low displacement pressure. Smaller pores on the other hand result to larger displacement pressure values.

The  $p_c$ - $S_w$  curves of the fine sand measured in the lab and calculated on the pore scale are plotted together in Fig. 63. Both curves have a flat slope ( $n=11.42$  and  $n=11.0$  [-]). The agreement in the inclination of the curves shows that saturation changes in a similar fashion for a given change in pressure. That means that the lattice Boltzmann numerical simulation reproduces correctly the redistribution of the phases in the pore space for a given pressure change.

However, the entry pressure of the curve measured on the local scale is larger compared to the displacement pressure calculated on the pore scale. The origin of the deviation in the entry pressure can be understood by looking at the experimental and the numerical setup: the sand columns in the multistep outflow experiments are covered with a metal grid and then a load is applied. This may cause a compaction of the column. In this case, it is expected to have a larger entry pressure. The application of a load on top of the sand column is a basic requirement in the multistep outflow experiments methodology. The influence of compaction on the estimated entry pressure was investigated i.e. by WINKLER (2002) [107]. One should also consider that the displacement pressure computed with the LB method may be influenced by the selected geometry we sample from the same sand. This is analyzed in detail in AHRENHOLZ ET AL. (2007) [3]. However, this dependence is here minimized, given the available computational resources, and in any case cannot cause the deviation from the local-scale  $p_c-S_w$  curves.

The  $p_c-S_w$  curves of the coarse sand are given in Fig. 63. In this case the two curves agree in terms of entry pressure. A reasonable explanation for the fact that differences in entry pressure are observed for the fine sand but not for the coarse sand is the potential difference in the bulk density of the two materials. Bulk density is defined as mass per unit volume (including the pore space) and is generally considered in soil science as a measure of the compactness of a material. Its value can also be influenced by the presence of water. Here it is possible that the fine sand has a larger bulk density during the drainage process and thus is more compact. Moreover, both curves (pore/local scale) for the coarse sand are flat ( $n=10.06$  and  $n=8.0$  [-]). They differ in the residual air saturation value ( $S_{nr}=0.182$  and  $S_{nr}=0.08$  [-]). This comes from the different methodologies: In the LB simulation, the pore space is saturated in the initial condition and then the saturation is calculated by stepwise changing the pressure. On the other hand, on the local scale the coarse sand column is first slowly saturated by elevating the water table before conducting the experiment. As described for the heterogeneous 3-D experiment (see Sect. 6.1), this methodology naturally results to an initial condition that does not correspond to a 100% saturated pore space.

### Imbibition

As observed for drainage, the imbibition  $p_c-S_w$  curves of the fine sand are characterized by a low slope ( $n=11.50$  for the pore scale and  $n=14.45$  [-] for the local-scale approach). Additionally, the two approaches show a qualitative agreement in terms of entry pressure. In both approaches, a strong hysteretic effect is observed in the fine sand  $p_c-S_w$  relationship that translates into different saturations

for a given pressure value at drainage and imbibition. However, significant differences are observed in the estimated residual saturations. The saturation at the beginning of the imbibition curves corresponds to the residual water saturation that was reached at the end of drainage. On the other hand, the saturation at the end of imbibition depends on the amount of the entrapped air phase (see Sect. 3.2). While a residual trapped saturation of air  $S_{nr}=0.142$  [-] is measured in imbibition for the fine sand with the multistep inflow experiment, the pore scale simulations predict that trapping of air does not occur and thus water saturation reaches back to the original maximum value.

Similarly, the lattice Boltzmann simulation does not predict any trapping of air in the imbibition  $p_c$ - $S_w$  curve for the coarse sand. The hysteresis effect is in this case less pronounced and restricts only to water saturations below the value  $S_w \approx 0.7$  [-]. On the other hand, the multistep inflow experiment produces a significant hysteresis effect also for the coarse sand as well as additional trapping of air at the end of imbibition. The measured coarse sand  $p_c$ - $S_w$  relationship for imbibition strongly differs from drainage not only in the entry pressure but also in the inclination.

As discussed in Sect. 5.5, even samples of the same size may demonstrate deviations in the trapped air saturation depending on the methodology. Here the pore-scale approach deals with 0.44 [cm<sup>3</sup>] cubes whereas the local-scale approach with 7.3 [cm] high and 9.4 [cm] thick columns. Both approaches are based on the same methodology: imbibition takes place as a sequence of equilibria introduced by the stepwise increase of water pressure. The fact that a significant amount of air trapping takes place on the local scale but not on the pore scale, possibly suggests that the pore scale sample is not large enough to have pronounced trapping effects. This could be explained, for instance, through the different degrees of pores connected to the boundaries (in the 0.44 [cm<sup>3</sup>] cubes it is more likely that the majority of pores forms connected pathways to the top or the bottom boundary), the different force ratios relevant to each scale consideration or the different influence of the boundaries in each case. This translates to a scale dependency of the observed amount of phase trapping. In this sense, the considerable difference in the sizes involved in the two approaches inevitably leads to differences in the predicted trapped air saturation. The same principle and explanation applies for the deviation in the residual water saturation observed for drainage in the fine sand  $p_c$ - $S_w$  relationship (see Fig. 63).

### 6.4.2 Permeability

For the fine sand, the absolute permeability calculated from the pore scale is approximately 3.72 times larger than the permeability measured in the lab. The ratio for the coarse sand is 2.86. The absolute permeability from the pore-scale simulations is larger because it is calculated strictly for a one-phase system (medium fully saturated with water). On the other hand, as explained above full saturation is not obtained in the real column. LEHMANN ET AL. (2007) [63] show that a change of 0.1% in water content can cause 10% deviations in permeability.

However, the differences in the permeabilities are within an order of magnitude and this may be viewed as a satisfactory agreement, considering that these values come from approaches from two different scales. Furthermore, it is likely that the differences in the permeability values are also due to the different packing of the columns in the lab and of the small samples scanned with synchrotron light. Permeability measurements can also be carried out in homogeneous sand columns packed and saturated in the same way as in the 3-D heterogeneous experiment. In this case, the columns have a saturation degree of approximately 80-90% water. The permeability of the fine sand found in this case is equal to  $2.9 \times 10^{-12}$  [m<sup>2</sup>] (51 times smaller than the permeability from the pore-scale simulations). The permeability of the coarse sand is  $1.3 \times 10^{-11}$  [m<sup>2</sup>] (26 times smaller than the permeability from the pore-scale simulations). These large deviations in the permeability values found with these additional lab measurements possibly relate to the formation of trapped air bubbles during the initial packing and wetting procedure (that is the same as in the 3-D experiment). The presence of air bubbles reduces the flow path available for water and therefore the measured absolute permeability.

## 6.5 Numerical simulation

In this section, the model setup and some demonstrative numerical simulations of the 3-D heterogeneous drainage and imbibition experiment are presented. At first, the different approaches concerning the meshing of the model domain are discussed and the boundary conditions are explained (Sect. 6.5.1). In Sect. 6.5.2 the geometry and the boundary conditions from the 3-D experiment are applied in a theoretical study. Variations of the hydraulic properties that are given as input in the numerical model are presented, in order to demonstrate qualitatively their influence on the two-phase flow behavior during drainage and imbibition in the 3-D simulation.

### 6.5.1 Simulation setup

As explained in Sects. 4.1 and 4.2, there are different ways to approximate heterogeneities in the numerical simulation, depending on the discretization concept. With the classic PPS approach in the BOX discretization (see Sect. 4.1), heterogeneities are represented by allocating different hydraulic properties to nodes. This way the boundary between two materials lies between two nodes, introducing an error that depends on the discretization length. Practically that means that in order to simulate two-phase flow in the 3-D heterogeneous structure described in Sect. 6.1, one needs elements with significantly smaller width compared to the width of the sand cubes (for a regular rectangular grid). This can be achieved, i.e. by refining a rectangular grid. The smaller the width of the elements, the more precise becomes the approximation of the material boundary (assuming that the ideal approximation is that of a sharp interface). In this way, each sand cube contains several finite elements. Accordingly, saturation is evaluated at each node, hence a mean saturation value can be obtained for each sand cube. However, this approach is disadvantageous due to the increasing computational effort after each refinement.

It is therefore more efficient to reduce the total number of elements in the grid by using the PPS approach combined with a local refinement as shown in Fig. 64 (left). Here, elements with smaller width are placed only across the material boundaries, while larger elements represent the sand cubes. In this case, saturation for each sand cube is obtained by averaging the eight nodal values from the larger elements.

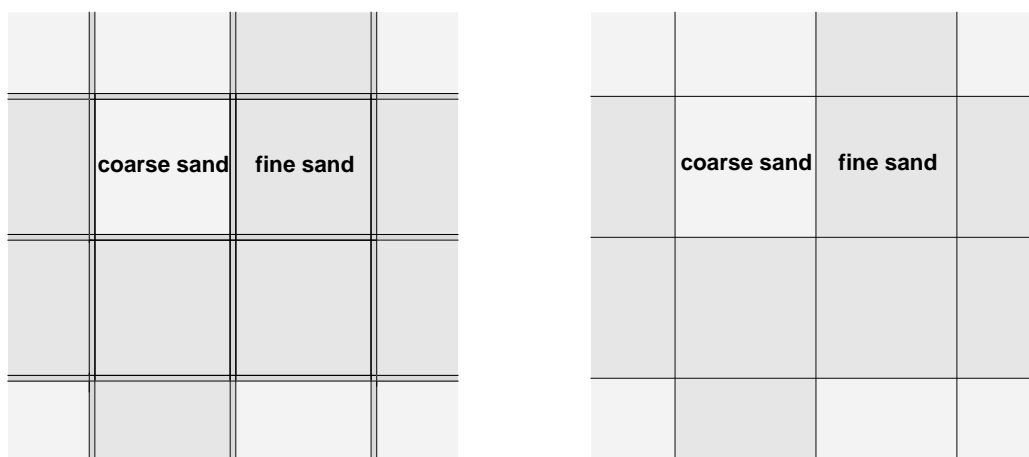


Figure 64: Grid considerations (in 2-D projections) for simulating the heterogeneous experiment with the classical BOX approach (left) and using the interface condition (right).

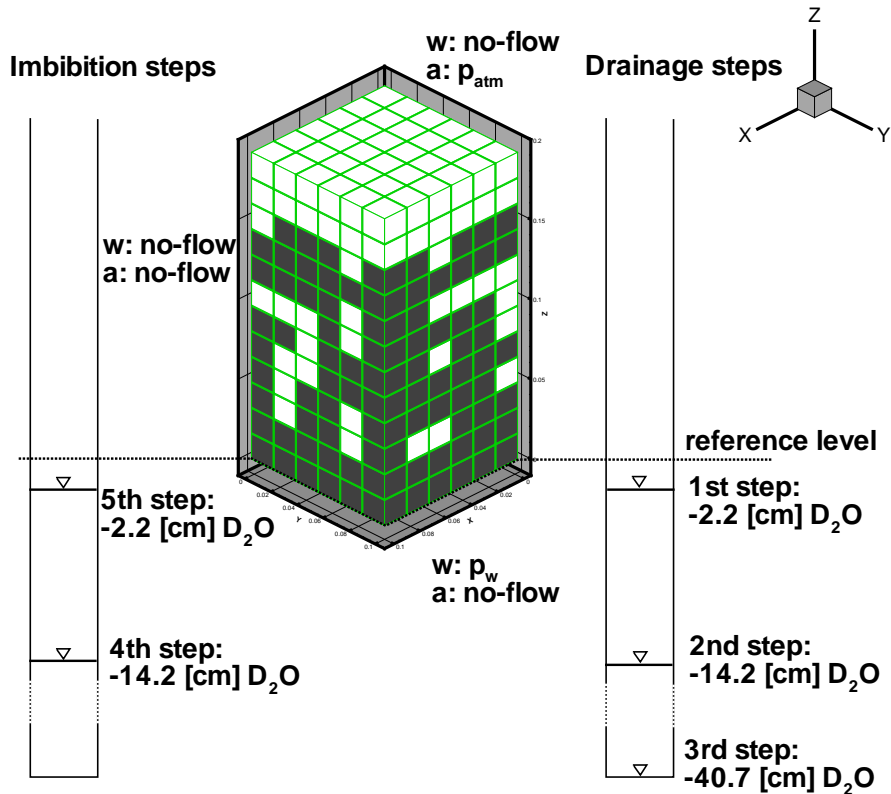


Figure 65: Heterogeneous structure and boundary conditions. Black color represents the fine sand and white color the coarse sand.

The third and more advantageous option is to use the interface condition explained in Sect. 4.2. In the PPSIC approach, material boundaries lie on the edges of the elements and saturation can be discontinuous across these boundaries. Each sand cube can be represented with a single element (see Fig. 64, right) and therefore it is beneficial to simulate two-phase flow in the heterogeneous structure using the coarsest mesh possible. In this case, the virtual saturation is used for the evaluation of the predicted mean sand cube saturation.

The use of the PPSIC approach for the entire drainage and imbibition process in the 3-D heterogeneous column greatly improves the ability for thorough numerical investigations: using the PPS approach combined with three refinements (element width 0.2 [cm]) results to a grid with 0.22 million elements. A complete numerical simulation of the drainage and imbibition experiment on this grid requires a large amount of resources and may last several weeks on parallel computing. Applying a local refinement (see Fig. 64, left) with 0.1 [cm] elements only at the boundaries between the sand cubes reduces the computation time to few days up to one week, even when using a single processor. The same simulation on a single processor using a coarse mesh and the PPSIC approach is completed

within approximately 5 hours.

Figure 65 shows an illustration of the 3-D mesh with the pre-defined arrangement of the heterogeneities together with the boundary conditions. The model domain includes the homogeneous layers above and below the heterogeneous structure as well as the porous plate that was placed under the column during the experiment. Initially, the saturation of air is equal to the residual value and a hydrostatic pressure distribution is given for water. The boundary conditions are shown in Fig. 65: at the top boundary, a Dirichlet boundary condition is assigned for air. This sets the air pressure at the top equal to atmospheric. For water, a Neumann no-flow boundary condition is given.

The air phase in the numerical simulation does not reach the bottom boundary due to the high entry pressure of the lower elements that represent the porous plate. This entry pressure is approximately 8000 [Pa]. Nevertheless, at the bottom boundary a no-flow boundary condition is given for air. The pressure of water at the bottom is variable over time as in the lab experiment (see Table 6) using a time-dependent Dirichlet boundary condition. That is, from  $t=0$  to  $t=120$  [min] (first drainage and tomography) the water pressure at the bottom is set to -238.48 [Pa] (or -2.2 [cm]  $D_2O$ ). From  $t=120$  to  $t=360$  [min] (second drainage and tomography) the water pressure given is -1539.28 [Pa] (or -14.2 [cm]  $D_2O$ ). For the third drainage, the water pressure at the bottom is -4411.9 [Pa] (or -40.7 [cm]  $D_2O$ ) from  $t=360$  to  $t=535$  [min]. The water pressure is then increased back to -1539.28 [Pa] from  $t=535$  to  $t=685$  [min] (first imbibition and third tomography) and is finally set to -238.48 [Pa] from  $t=685$  to 856 [min] (second imbibition and fourth tomography).

The physical properties for heavy water and air are given in Table 11.

Property	Symbol	Value	Unit
Density of heavy water	$\rho_w$	1105	[kg/m <sup>3</sup> ]
Density of air	$\rho_n$	1.19	[kg/m <sup>3</sup> ]
Viscosity of heavy water	$\mu_w$	$1.22 \times 10^{-3}$	[kg/(ms)]
Viscosity of air	$\mu_n$	$1.65 \times 10^{-5}$	[kg/(ms)]

Table 11: Physical properties of heavy water and air.

### 6.5.2 Influence of hydraulic properties

Before using the available sets of hydraulic properties in the numerical simulations, it is necessary to demonstrate the influence of the absolute permeability

parameter	ref.	sim. <i>i</i>	sim. <i>ii</i>	sim. <i>iii</i>	sim. <i>iv</i>	sim. <i>v</i>
fs $K$ [m <sup>2</sup> ]	$8.0 \times 10^{-12}$	<b><math>2.0 \times 10^{-12}</math></b>	$8.0 \times 10^{-12}$	$8.0 \times 10^{-12}$	$8.0 \times 10^{-12}$	$8.0 \times 10^{-12}$
cs $K$ [m <sup>2</sup> ]	$4.0 \times 10^{-11}$	<b><math>5.0 \times 10^{-12}</math></b>	$4.0 \times 10^{-11}$	$4.0 \times 10^{-11}$	$4.0 \times 10^{-11}$	$4.0 \times 10^{-11}$
fs (dr.) $\alpha$ [1/Pa]	0.0004	0.0004	<b>0.0005</b>	0.0004	0.0004	0.0004
cs (dr.) $\alpha$ [1/Pa]	0.0007	0.0007	<b>0.0008</b>	0.0007	0.0007	0.0007
fs (dr.) $n$ [-]	9.0	9.0	9.0	<b>11.0</b>	9.0	9.0
cs (dr.) $n$ [-]	8.0	8.0	8.0	<b>10.0</b>	8.0	8.0
fs (im.) $\alpha$ [1/Pa]	0.00065	0.00065	0.00065	0.00065	<b>0.0008</b>	0.00065
cs (im.) $\alpha$ [1/Pa]	0.0009	0.0009	0.0009	0.0009	<b>0.0011</b>	0.0009
fs (im.) $n$ [-]	5.0	5.0	5.0	5.0	5.0	<b>9.0</b>
cs (im.) $n$ [-]	5.0	5.0	5.0	5.0	5.0	<b>8.0</b>

Table 12: Variation of hydraulic properties given for the fine sand (fs) and the coarse sand (cs) for demonstrating numerical simulations.

$K$  and the VAN GENUCHTEN parameters  $\alpha$  and  $n$  on the flow behavior during drainage and imbibition in the heterogeneous column. For that purpose, a simulation with a reference set of hydraulic properties is compared to simulations where each time a single parameter is changed. The input parameters  $\alpha$  and  $n$  are tested separately for drainage and imbibition. The geometry, the discretization and the boundary conditions remain the same for all simulations and are those described in Sect. 6.5.1. The water mass leaving or entering the 3-D model domain through the bottom boundary during the drainage and imbibition events is depicted in Figs. 66-68. The times that correspond to the tomography scanings during the experiment are also illustrated with green-colored intervals in the same figures. In total, six simulations are demonstrated using the following notation (see also Table 12):

- Reference simulation.
- Simulation *i*: decreased absolute permeability.
- Simulation *ii*: increased  $\alpha$  for drainage.
- Simulation *iii*: increased  $n$  for drainage.
- Simulation *iv*: increased  $\alpha$  for imbibition.
- Simulation *v*: increased  $n$  for imbibition.

As seen on the outflow and inflow curve from the reference simulation (see i.e. Fig. 66), after each pressure decrease at the bottom boundary introduced by the



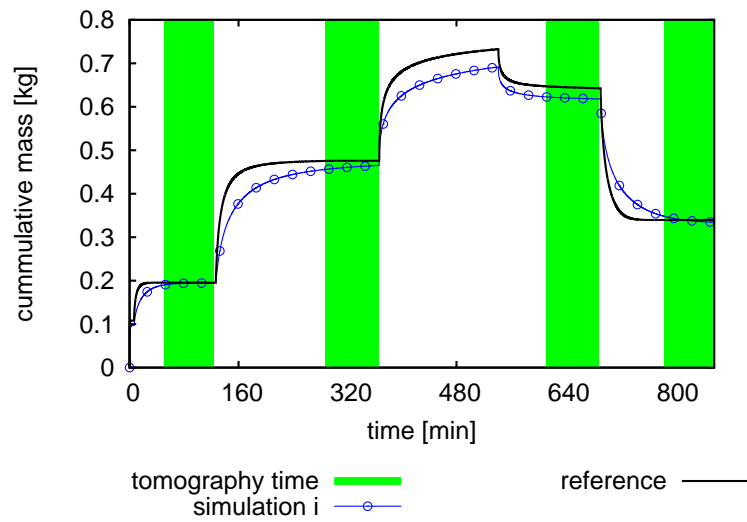


Figure 66: Influence of absolute permeability on the water outflow and inflow during drainage and imbibition in the heterogeneous column.

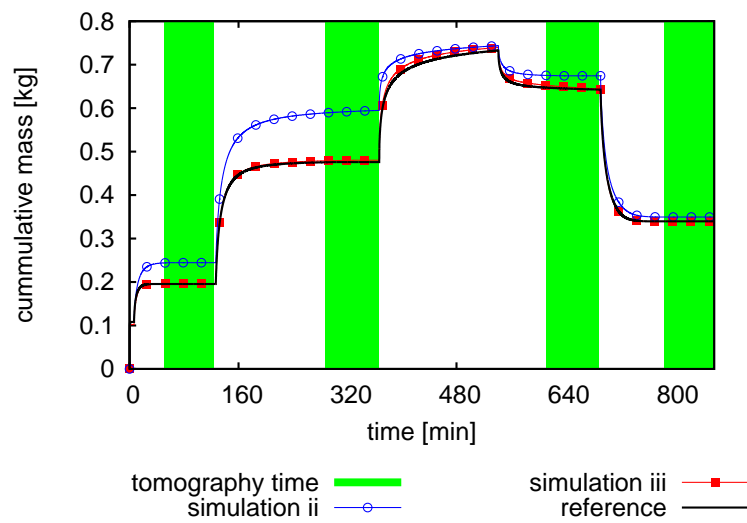


Figure 67: Influence of VAN GENUCHTEN drainage  $\alpha$  and  $n$  on the water outflow and inflow during drainage and imbibition in the heterogeneous column.

Dirichlet boundary condition, a transient state is observed during which the water mass in the model domain decreases. This continues until an equilibrium is reached between the saturations at the grid nodes and the pressure distribution. The resulting steady-state configuration depends on the capillary pressure-saturation relationship given for the materials. The same behavior is observed during imbibition. However, in this case the same boundary pressure values correspond to a lesser water mass in the domain at equilibrium. This difference in

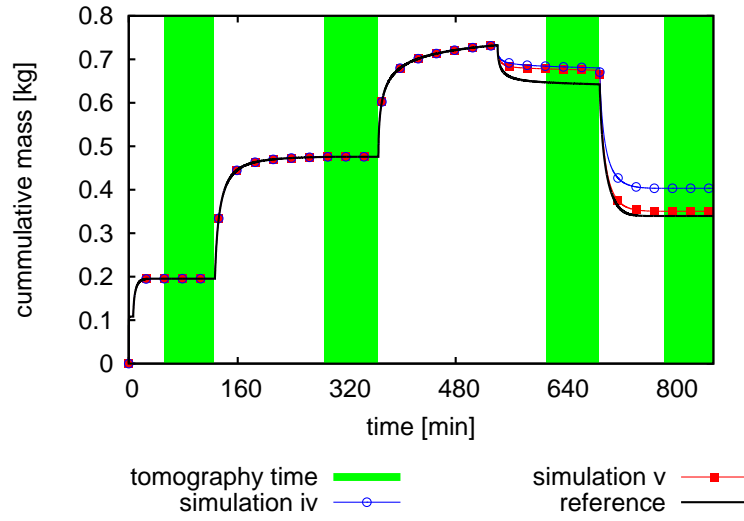


Figure 68: Influence of VAN GENUCHTEN imbibition  $\alpha$  and  $n$  on the water out-flow and inflow during drainage and imbibition in the heterogeneous column.

the steady-state configuration in the heterogeneous domain results from the hysteresis effect in the  $p_c$ - $S_w$  relationship.

The cumulative mass from simulation  $i$  is plotted together with that from the reference case in Fig. 66. As seen on this figure, the time that is required for equilibrium to be reached after each pressure step is different in the two simulations. Changing the permeability of the materials has a significant effect on the flow behavior during the transient state and hence influences the time at which steady-state is established. Nevertheless, the amount of water mass that is found in the system at steady-state does not depend on the permeability.

The value given for the  $\alpha$  parameter has a direct impact on the capillary pressure-saturation curve and thus on the relationship between pressure and saturation that is established at steady-state. In other words, changing the  $\alpha$  parameter of the drainage  $p_c$ - $S_w$  curves affects the steady-state distribution of the phases after each decrease in the boundary pressure. This is demonstrated in Fig. 67, where less water is observed at steady-state after each drainage step in simulation  $ii$  compared to the reference case. Furthermore, the flow behavior during the 4th step depends on the distribution of saturation at the beginning of the imbibition. This starting distribution for the 4th step coincides with the distribution at the end of the previous drainage event (3rd step). Numerically, this is realized through the values of the reversal saturations stored for the computation of the hysteretic  $p_c$ - $S_w$  curves, that come from the virtual saturations assigned element-wise to each node.

A similar effect is also observed in simulation  $i$ . Through the decrease of perme-

ability, the initial water mass at the beginning of imbibition changed and therefore also the amount of water mass observed at the steady-state of the 4th step. These observations in general indicate that the hydraulic properties assigned for drainage have an indirect influence on the behavior of flow during imbibition.

As it is valid for the  $\alpha$  parameter, the  $n$  parameter has a direct effect on the shape of the capillary pressure-saturation relationship. However, the results of the numerical simulation are less sensitive to changes in the  $n$  parameter.

Variations of the VAN GENUCHTEN parameters associated to the imbibition  $p_c-S_w$  curves have an influence only on the 4th and 5th step and not on the drainage steps. This is shown in the outflow and inflow curve from simulation *iv* (see Fig. 68), that differs from the reference case only during imbibition. An increase in the  $\alpha$  parameter given for the main imbibition curve means smaller water saturations at the same capillary pressures, and therefore produces a stronger hysteresis effect. This results to the reduced amount of water inflow during the 4th and 5th step in simulation *iv*.

Changing the  $n$  parameter assigned for the imbibition curve again influences only the imbibition events. In simulation *v* the increase in the  $n$  parameter translates to a flatter main imbibition  $p_c-S_w$  curve, compared to the reference case. This produces steeper scanning curves at the transition from drainage to imbibition. The effect on the inflow curve is given in Fig. 68. Steeper scanning curves relate to a lesser increase of water saturation for a given decrease of capillary pressure, or in other words to less water inflow. On the other hand, during the 5th step this effect is less pronounced. This is due to the fact that in the second imbibition less nodes have saturations close to the reversal values (area of steep transition) and more nodes already have saturations on the main imbibition  $p_c-S_w$  curve.

## 6.6 Comparison of simulation results to the experiment

In this section, results from numerical simulations employing hydraulic properties from the different approaches are compared to the measurements from the 3-D experiment. The numerical simulations using the hydraulic properties determined on the local scale and on the pore scale are presented in Sects. 6.6.1 and 6.6.2, respectively. An additional simulation is presented in Sect. 6.6.3 while a discussion on the results is given in Sect. 6.7.

### 6.6.1 Simulation A: hydraulic properties determined on the local scale

In this first case, the hydraulic parameters measured on the local scale with the multistep outflow/inflow experiments (see Tables 7 and 8) are used as input for the 3-D numerical simulation. This case is notated as *simulation A*. Saturation is captured in the simulation for each drainage and imbibition step after half of the tomography time (at the times 82.5, 320, 645.5 and 817.5 [min]). The saturations and profiles obtained are given in Fig. 70 for the drainage steps and in Fig. 71 for the imbibition steps. In the same graph the averaged profiles from the experiment are plotted together with the variation of saturations at each layer. The simulated water outflow and inflow is shown in Fig. 69, left. Additionally, using a simple backward difference at each timestep, the water outflow rate during drainage is plotted (see Fig. 69, right). The corresponding time intervals where the tomography scannings took place are also illustrated in the same figures.

#### Equilibration times

From the simulated water outflow and inflow and the outflow rate it becomes clear that steady-state is already established in the simulation when saturation is captured. During drainage, quasi steady-state is reached at  $t=19$  [min] (first drainage step) and at  $t=156$  [min] (second drainage step). These times are much smaller compared to the times measured in the experiment (45 and 280 [min], respectively). The same applies for the two imbibition steps. In the simulation, quasi steady-state is reached for the first and second imbibition at  $t=553$  and  $t=738$  [min], while in the experiment the observed times are 606 and 779 [min]. Based on those deviations, it may be stated that the numerical simulation cannot predict the time scale behavior observed in the experiment.

#### Saturations

Since steady-state is fully reached at the tomography times, the saturation values presented for the two drainage steps from simulation A (Fig. 70) depend only on the drainage  $p_c-S_w$  curves of the materials, as permeability and porosity have an effect only on the transient state. Also, due to the steady-state condition the predicted saturations for each sand type do not vary within a single layer (see Fig. 70).

At the first drainage step (coarse sand saturations), there is agreement between the averaged measured (3-D experiment) and simulated saturation (that corresponds to the  $p_c-S_w$  curve from the multistep outflow experiment). The inclina-

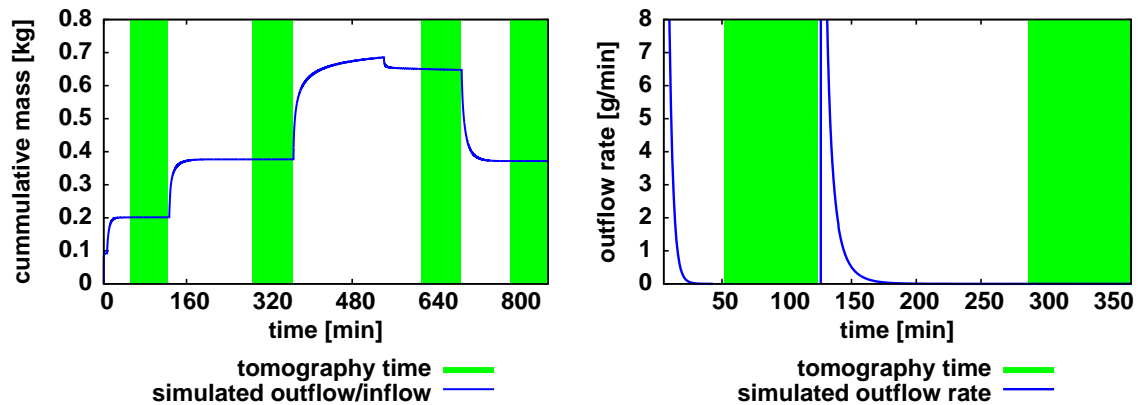


Figure 69: Simulation A: simulated outflow and inflow for the entire simulation and outflow rate for the 1st and 2nd step (drainage).

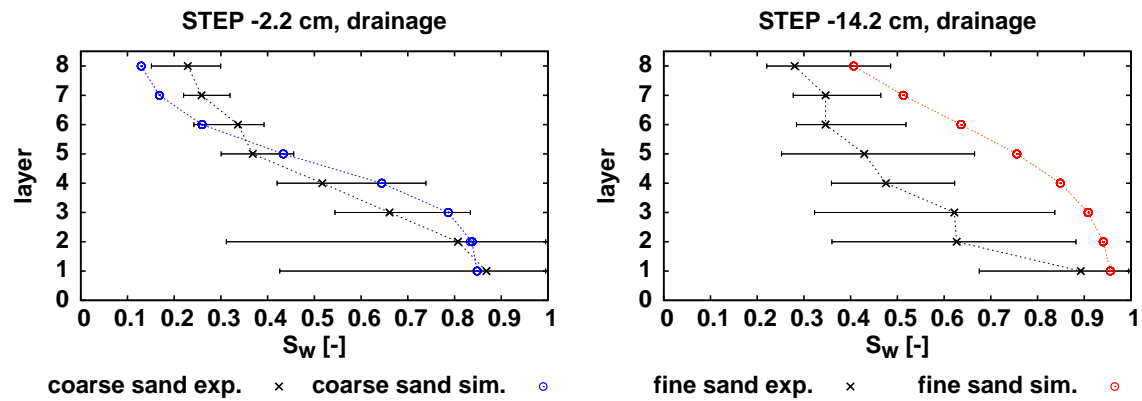


Figure 70: Simulation A: measured and simulated saturation profiles for 1st and 2nd step (drainage).

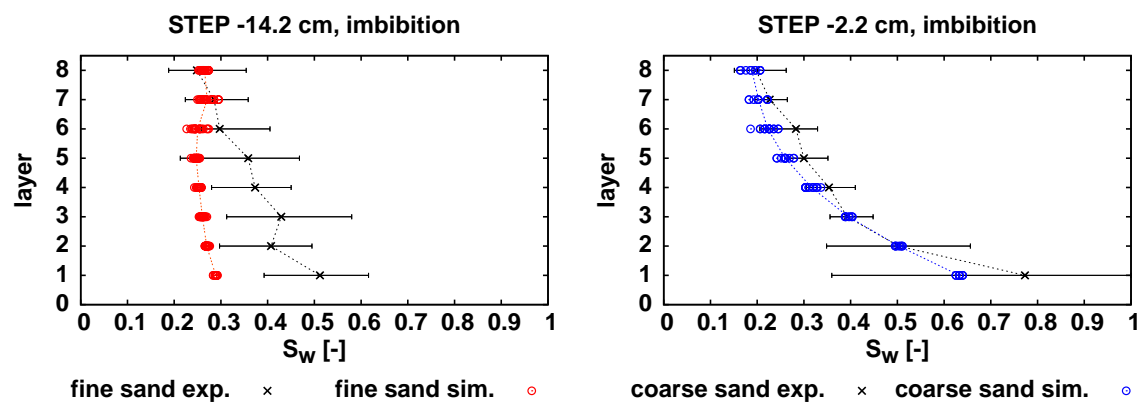


Figure 71: Simulation A: measured and simulated saturation profiles for 4th and 5th step (imbibition).

tion of the measured saturation is, however, smaller. It is reasonable to assume that the difference between the inclinations (multistep outflow experiment and 3-D heterogeneous experiment) results from the different packings. The technique used to pack the pre-defined 3-D structure is described in SCHAAP ET AL. (2007) [88]. Despite the painstaking and thorough packing procedure, discontinuities and small gaps in the microstructure of the sand grains are observed, so that the packing results to a larger distribution of the pore diameters. On the other hand, the same sand is easier to pack homogeneously for the multistep outflow experiment. In this case, the narrow distribution of the pore diameters produces a flat capillary pressure-saturation curve.

At the second drainage step, the fine sand capillary pressure-saturation relationship determined in the lab cannot reproduce the saturation profile of the experiment. In general, it would be necessary to reduce the entry pressure in order to achieve agreement. The difference in the entry pressure is presumably also due to the packing technique. The sand columns used for the multistep outflow experiments show more compaction compared to the column used in the 3-D heterogeneous experiment.

Also for the imbibition, steady-state condition is established at the tomography times. However, in this case there are variations of the predicted saturations within each layer (see Fig. 71). These variations relate to the transient state condition at the end of the third drainage step. The increase of the bottom boundary pressure back to -14.2 [cm], that initiates the first imbibition event, takes place before reaching the steady-state configuration for the -40.7 [cm] pressure. As explained in Sect. 6.5.2, this has an influence on the starting saturation distribution of the first imbibition step. Therefore, hysteretic  $p_c$ - $S_w$  curves at the same height in the model domain are initiated at different saturations and consequently different saturations for the same height and material are predicted even for steady-state. For the first imbibition step, the predicted saturations (see Fig. 71) are characterized by a steeper distribution compared to the neutron tomography measurements. The saturation profile from the simulation depends on the input drainage and imbibition curves shown in Fig. 63. In the local-scale approach, the transition from drainage to imbibition occurs with steep scanning curves on the  $p_c$ - $S_w$  relationship (see Fig. 72). As demonstrated also in Sect. 6.5.2, this shape relates to the small amount of water inflow during the first imbibition step (see Fig. 69, left). On the other hand, the predicted and measured coarse sand saturation profiles for the second imbibition step show good agreement.

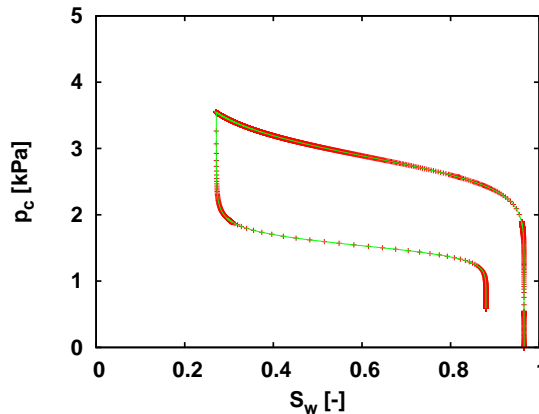


Figure 72: Evolution of the fine sand  $p_c$ - $S_w$  relationship, as observed on a node near the bottom boundary of the model domain.

### 6.6.2 Simulation B: hydraulic properties determined on the pore scale

As analyzed in Sect. 6.3, porosity, permeability and capillary pressure-saturation curves for the two materials (*fs* and *cs*) are also determined on the pore scale. These properties are used as input in *simulation B*. As done for simulation A, the calculated saturations captured after half of the tomography time are compared to the saturations measured with the neutron tomography. Figure 73 illustrates the predicted outflow and inflow for the entire simulation as well as the outflow rate for the two drainage steps. Additionally, the saturations and profiles from the simulation using the hydraulic properties from the pore scale are shown in Figs. 74 and 75.

#### Equilibration times

In this case, the permeabilities of the materials given as input for the numerical simulation are larger compared to simulation A. As shown in Fig. 73, steady-state in simulation B is once more established much earlier before the tomography times are reached. The numerical simulation also in this case reaches steady-state too fast and therefore does not provide agreement to the experimental observations in terms of equilibration times.

#### Saturations

The drainage saturation profiles of simulation B also depend only on the capillary pressure-saturation relationship. Once more, the saturation variations measured

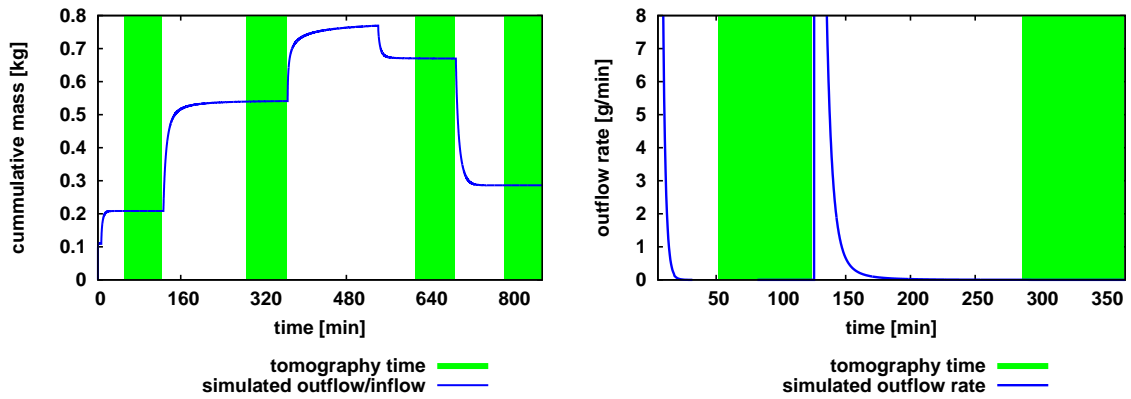


Figure 73: Simulation B: simulated outflow and inflow for the entire simulation and outflow rate for the 1st and 2nd step (drainage).

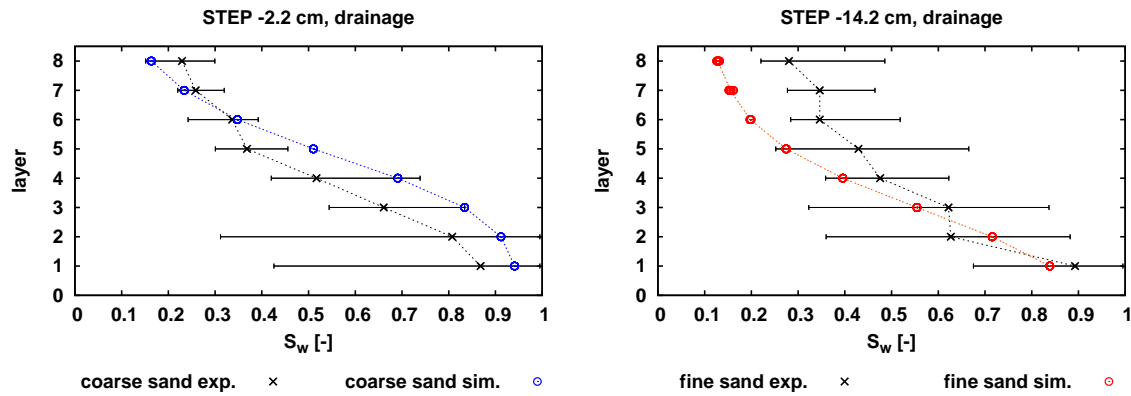


Figure 74: Simulation B: measured and simulated saturation profiles for 1st and 2nd step (drainage).

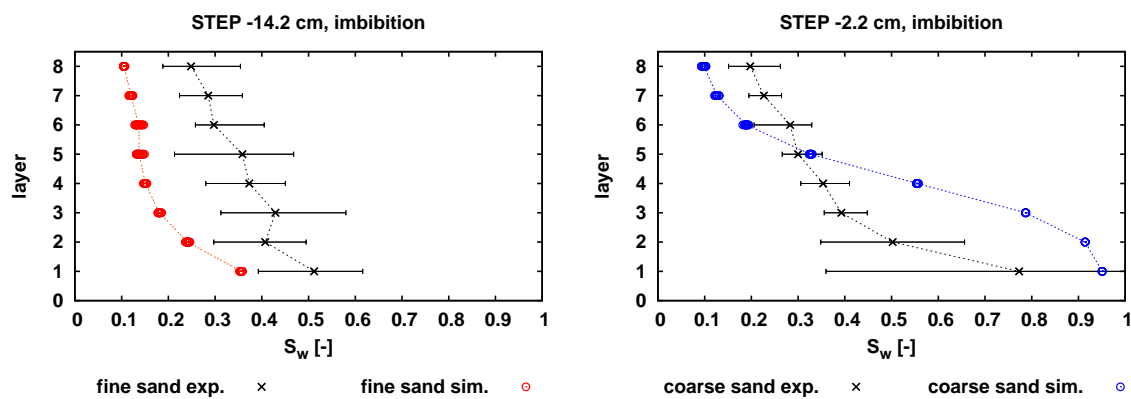


Figure 75: Simulation B: measured and simulated saturation profiles for 4th and 5th step (imbibition).



in drainage in the experiment are not observed in the saturations predicted with the numerical simulation. For the first drainage step (coarse sand saturation) an effect similar to that of simulation A is observed. The coarse sand  $p_c$ - $S_w$  curve calculated on the pore scale agrees to the averaged saturation profile from the 3-D experiment, although the later shows a steeper slope at the upper layers.

Nevertheless, simulation B can also reproduce better the saturations of the fine sand in the second drainage step. Due to the lower entry pressure given for the fine sand in simulation B, the saturation values are closer to the experimental values, compared to simulation A. As explained in Sect. 6.4, the smaller displacement pressure of the calculated  $p_c$ - $S_w$  curve for the fine sand presumably relates to the smaller amount of compaction in the scanned samples.

For imbibition, the variations of saturation observed for the same sand type and pressure relate to the non steady-state condition at the beginning of the first imbibition step, as elaborated in Sect. 6.6.1. In the first imbibition step, the predicted fine sand saturations show a vertical distribution similar to that measured in the experiment. However, the predicted values are shifted by a difference of  $\Delta S_w \approx 0.1-0.2$  [-]. The agreement in the inclination of the saturation profiles at the first imbibition step, though with shifted values, translates to an agreement in the shape of the  $p_c$ - $S_w$  relationship at the transition from drainage to imbibition, however with a deviation in the reversal saturations. As the values of the reversal saturations originate from the non steady-state condition at the end of the third drainage step, the predicted profiles shown in Fig. 75 depend indirectly also on the permeability.

In the second imbibition step (coarse sand saturations), the  $p_c$ - $S_w$  relationship calculated for imbibition on the pore scale does not provide the saturation values found in the experiment with the neutron tomography measurements. As explained in Sect. 6.3, hysteresis in the LB coarse sand  $p_c$ - $S_w$  relationship is found only in the dry region and without any air trapping. Therefore, the saturation profile predicted for imbibition (see Fig. 75, right) is similar to that for drainage (see 74, left). On the other hand, the 3-D saturations measured in the coarse sand cubes demonstrate hysteretic effects also in the wet region, potentially indicating the existence of trapped air at the end of the experiment.

### 6.6.3 Simulation C: fitted permeability

In fact, in the experiment tomography is carried out when steady-state is approached, but not yet fully established. As mentioned in Sect. 6.1, there is still a small outflow or inflow of water during the four scannings (for the outflow and inflow values see Table 6). Simulations A and B reveal that this is clearly not the

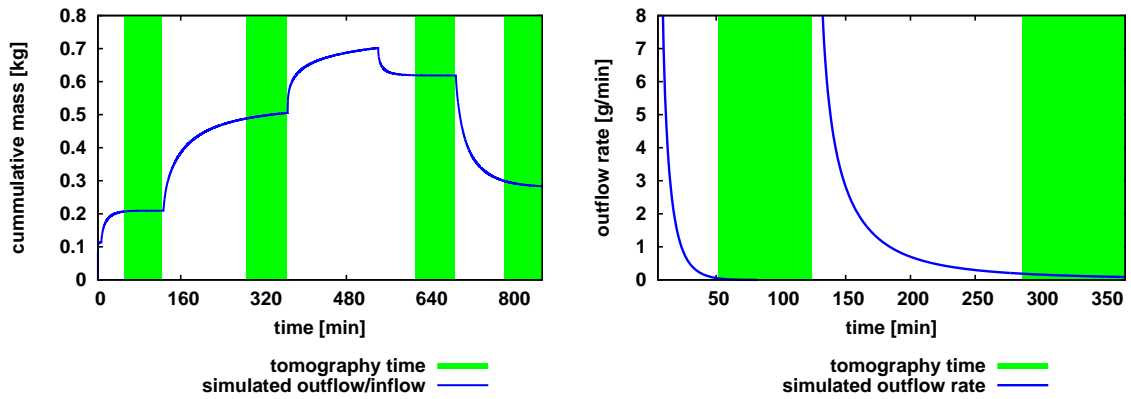


Figure 76: Simulation C: simulated outflow and inflow for the entire simulation and outflow rate for the 1st and 2nd step (drainage).

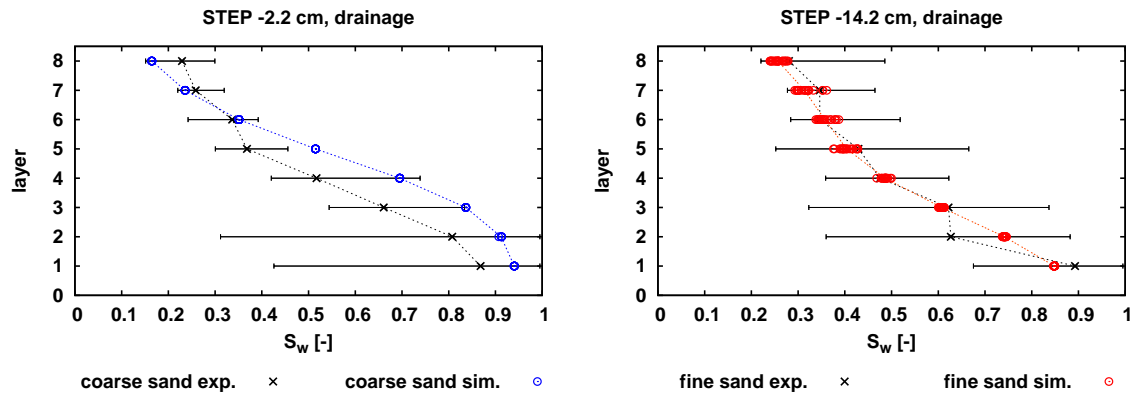


Figure 77: Simulation C: measured and simulated saturation profiles for 1st and 2nd step (drainage).

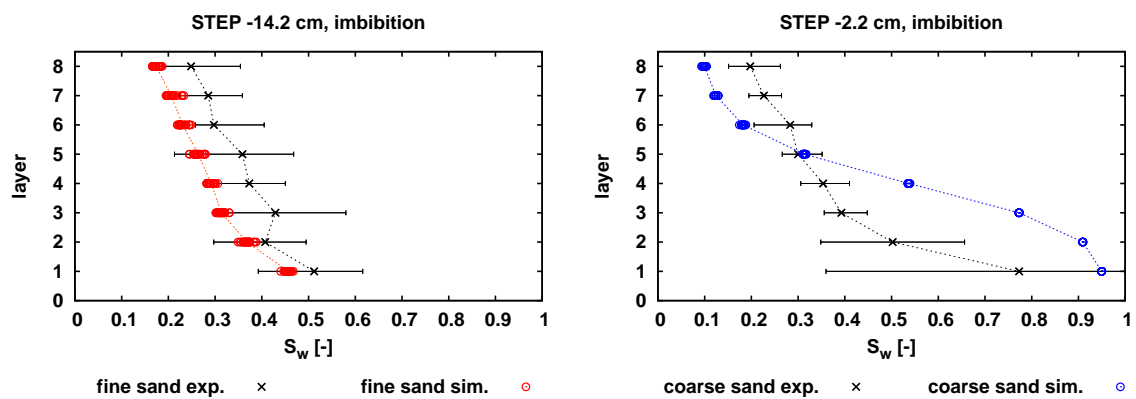


Figure 78: Simulation C: measured and simulated saturation profiles for 4th and 5th step (imbibition).

case if one takes the permeabilities measured with the multistep outflow/inflow experiments or calculated by means of pore-scale LB simulations (see i.e. Fig. 73). In other words, the time scale in the simulation and the experiment is different, as the simulations reach steady-state too fast. In general, the difference of the equilibration time could be an effect of the ratio between permeability and porosity. Equilibration times are also influenced by the  $p_c$ - $S_w$  relationship, but not at the magnitude of the differences observed in simulations A and B.

In the third simulation presented here, the porosity and the capillary pressure-saturation relationships determined on the pore scale are used, while the permeabilities of the two materials are fitted in order to get the best possible agreement to the experimental measurements of saturation. The permeability values found with this approach are  $K = 1.5 \times 10^{-12} \text{ [m}^2\text{]}$  for the fine sand and  $K = 2.0 \times 10^{-11} \text{ [m}^2\text{]}$  for the coarse sand. This simulation is referred to as *simulation C*.

### Equilibration times

In simulation C, drainage reaches quasi steady-state at  $t=40 \text{ [min]}$  (first drainage step) and  $t=279.2 \text{ [min]}$  (second drainage step). For imbibition the corresponding times are  $t=577 \text{ [min]}$  (first imbibition step) and  $t=808 \text{ [min]}$  (second imbibition step). These values of equilibration times qualitatively agree to those measured in the experiment (45, 280, 606 and 779 [min]).

The outflow and inflow from the entire simulation is given in Fig. 76. In the same figure, the outflow rate for the two drainage steps is illustrated. In simulations A and B, the system reached steady-state much earlier than observed in the experiment. There was no outflow or inflow during the tomography times. In simulation C, there is still an amount of water mass leaving/entering the system (1.2 [g] for the first tomography, 12.5 [g] for the second, 0.6 [g] for the third and 15.9 [g] for the fourth). The latter qualitatively agrees also with the experimental values 2.32, 10.05, 11.27 and 14.80 [g] of water outflow or inflow during the four tomography scans, respectively (see Table 6).

### Saturations

The saturations and averaged profiles from simulation C are presented in Figs. 77 and 78. For the two drainage steps, the experimental and simulated profiles of the coarse and fine sand agree. It is observed that in this case the averaged saturation profile of the fine sand is not the same as in steady-state (simulation B). That means that the 10.05 [g] of water outflow during the second tomography have an influence on the fine sand saturation profile and lead to agreement to the measured profile. Furthermore, the predicted fine sand saturations from simula-

tion C correspond to a quasi steady-state and therefore show variations of 3-7% within the upper 6 layers (see Figs. 77, 79 and 80).

Similarly, the predicted fine sand profile for imbibition is strongly influenced by the change in permeability. A shift of the fine sand profile to larger saturations is produced. In this case, the difference from the profile of simulation B (see Fig. 75) does not result from a non steady-state condition at the time when saturation is captured, but from the non steady-state condition at the beginning of imbibition. In simulation C, there is more water mass in the model domain at the beginning of imbibition, compared to simulation B, giving larger reversal saturation values. On the other hand, the predicted coarse sand saturations are not influenced by the change in permeability. As in simulation B, the coarse sand saturations reach the steady-state configuration in imbibition, which directly translates to an underestimation of the hysteretic effect.

## 6.7 Synopsis and remarks

For the coarse sand, the drainage  $p_c-S_w$  curves measured in the lab and calculated with pore-scale simulations both agree with the saturation profile that was measured with neutron tomography in the 3-D experiment. The different packings of the coarse sand only influence the slope of the  $p_c-S_w$  relationship and not the entry pressure. In principle, the saturation distribution found in the coarse sand in the 3-D experiment can be viewed as a steady-state  $p_c-S_w$  relationship and therefore can be directly compared to the calculated or measured  $p_c-S_w$  curves. For the fine sand, the drainage  $p_c-S_w$  curve measured in the lab has a larger entry pressure compared to the displacement pressure calculated with the pore-scale simulations and to that observed in the 3-D experiment. In simulation B the lower entry pressure produces a fine sand saturation profile similar to the one measured in the 3-D experiment (see Fig. 74). As explained above, it is reasonable to assume that this relates to the different compaction of the fine sand in the multistep outflow experiments, the mapped samples and the heterogeneous 3-D structure.

Simulation C shows that it would be necessary to decrease the permeabilities in order to shift the times when steady-state is approached approximately to the tomography times. Simulation C further shows that a qualitatively good prediction of the flow process in the experiment is achieved if the saturation is evaluated at a non-steady state condition.

For the two drainage steps, the  $p_c-S_w$  curves from the pore scale combined with fitted permeability can provide agreement in saturation distribution and qualitatively in terms of simulation and experiment time scale. This agreement, nevertheless, is achieved only with a decrease in the permeabilities by an order of

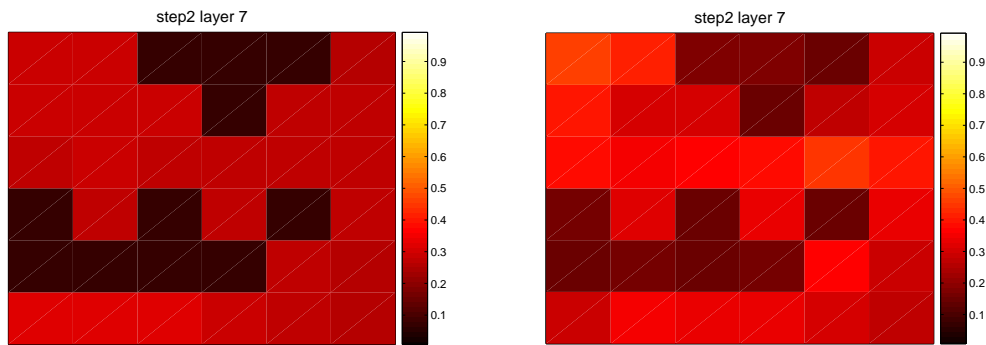


Figure 79: Simulation C: comparison of predicted (left) and measured (right) saturation distribution after the second drainage at layer 7. The simulation with the fitted permeabilities produces variations of the captured saturations at the time of tomography.

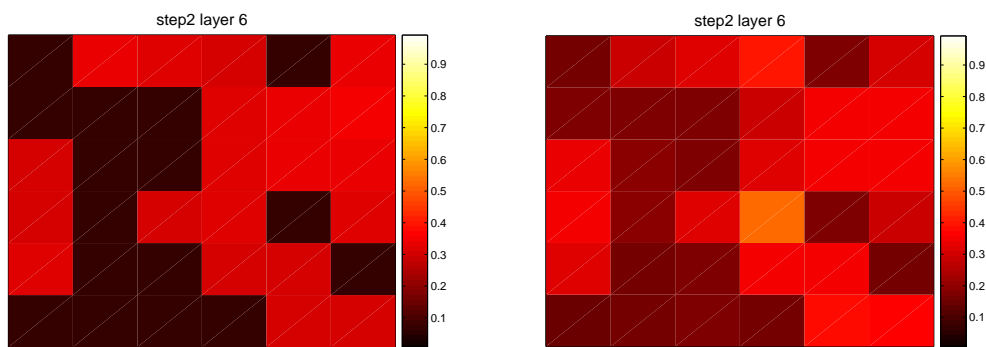


Figure 80: Simulation C: comparison of predicted (left) and measured (right) saturation distribution after the second drainage at layer 6. The simulation with the fitted permeabilities produces variations of the captured saturations at the time of tomography.

magnitude. This is not possible using the  $p_c-S_w$  curves obtained from the multistep outflow experiments. In this case in quasi steady-state after drainage the water saturation would be higher and thus the deviation from the experimental values would be larger.

Additionally, the predicted saturation values of simulation C (see Fig. 77) show that having quasi steady-state at the end of a drainage event can cause variations in the fine sand saturations at the tomography time up to 7% for a single layer. This behavior is also observed in the experiment, however it is possible that in this case it results from hysteresis phenomena -during the first and second drainage- that relate to different starting saturations formed during the initial wetting of the 3-D structure. As the modeling approach considers the first and

second drainage as main drainage processes, at steady-state (simulations A and B) a single saturation value per material corresponds to each layer.

With respect to imbibition, a significant difference is observed in the amount of air trapping in the hysteretic  $p_c-S_w$  curves determined on the pore and the local scale, as discussed in Sect. 6.4. This most likely indicates a scale dependency of the effect of phase trapping.

Simulation C shows that decreasing the permeability, in order to obtain a realistic representation of the time scale behavior in the numerical simulation, has a significant influence on the imbibition fine sand saturation profile as well. This relates to the amount of water mass in the system when imbibition is initiated and thus to the reversal saturations that determine the steady-state saturation configuration. This way, the fine sand saturations in imbibition are higher and the agreement with the experimental values improves, compared to simulation B.

The imbibition coarse sand  $p_c-S_w$  curve determined on the local scale (simulation A) provides a better prediction of saturation, compared to the pore scale approach. As in the multistep outflow/inflow experiment, the coarse sand demonstrates a considerable hysteresis effect also in the 3-D heterogeneous experiment. On the other hand, the imbibition coarse sand  $p_c-S_w$  from the pore scale shows a less pronounced hysteresis effect and no air trapping.

In simulation C, the change of permeability does not influence the predicted coarse sand saturation values. The continuous path of the coarse sand reaches steady-state after each drainage and imbibition event, even with a decreased permeability. Therefore, the first drainage and second imbibition step profiles remain unchanged in simulations B and C.

The fact that time scales between experiment and simulations A and B differ is an indication of the importance of microstructures and shows how sensitive hy-

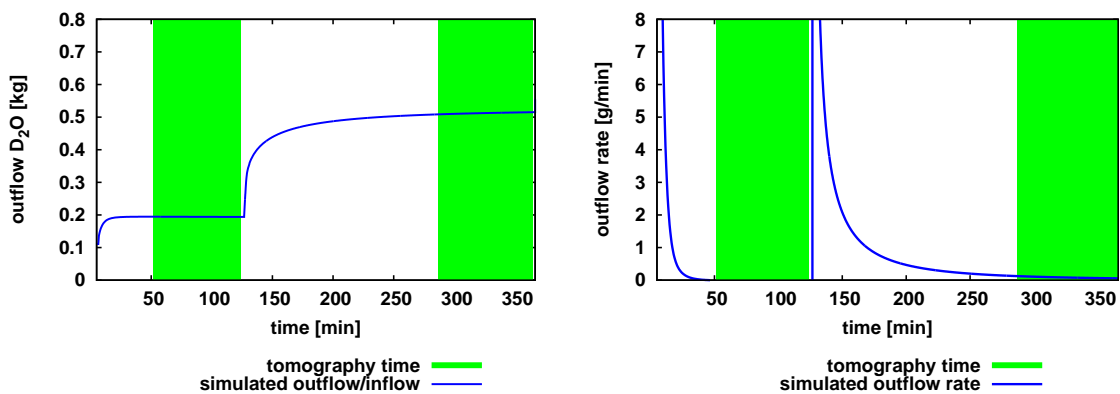


Figure 81: Simulated outflow and outflow rate for the 1st and 2nd step (drainage), including low-permeable material interfaces.

draulic properties (such as the permeability) are to pore space properties. For instance, both the pore-scale calculation and the multistep outflow/inflow experiments are done for each sand separately and obviously do not take into account the influence of material interfaces (between two sand cubes). Due to the packing procedure, the porosity at the interface between two sand cubes is affected and changes between 0.28 and 0.41 [-] have been observed [LEHMANN ET AL. (2004) [64]; KAESTNER ET AL. (2007) [54]]. The decrease in the porosity could, in general, indicate that the interfaces between the sands might slow down the drainage/imbibition process or act as capillary barriers.

In order to qualitatively demonstrate the effect of such interfaces on the time scale behavior during drainage in the heterogeneous column, an additional numerical simulation only for the first two drainage steps is presented here. This simulation incorporates the hydraulic properties determined on the pore scale (same as simulation B). In this case, however, low-permeable transition interfaces are implemented between the finite elements that represent the sand cubes. The interfaces have a width of 0.1 [cm], according to observations made with synchrotron light, while a permeability equal to  $1.0 \times 10^{-12}$  [m<sup>2</sup>] is used. This value is chosen only as an estimation. The outflow and the outflow rate from this simulation is given in Fig. 81. As seen by comparison to simulation B, the existence of low-permeable interfaces can slow down the drainage process and shift the equilibration times. This issue however needs to be investigated in detail in order to draw safe conclusions concerning the interfaces (i.e. values of hydraulic properties at interfaces between coarse-fine sand or fine-fine sand).

## 7 Synopsis, conclusions and outlook

In the last decades, the problem of groundwater contaminations has become severe. Combined with the increasing scarcity of freshwater resources and the uncontrolled world climate change, this has alarmed the public opinion, the financial markets and the scientific community about the upcoming consequences. When dealing with the assessment of travel times of hazardous substances in the unsaturated zone or problems of monitoring and predicting the fate of groundwater contaminations, it is important to have the ability for reliable and accurate predictions of two-phase flow behavior in heterogeneous porous media. This is a difficult task, on the one hand due to the uncertainty related to the hydraulic properties of porous media and on the other hand due to the alternating drainage and imbibition conditions that cause hysteresis effects in the  $p_c$ - $S_w$  relationship. Hysteresis is observed in many aspects of groundwater-related problems, i.e. during the infiltration of precipitation water in the unsaturated zone, fluctuations of the groundwater table or during the migration/removal of contaminants that have infiltrated the subsurface.

Traditionally, the hydraulic properties and the hysteretic behavior of porous media are empirically determined by means of lab experiments conducted on the local scale with material specimens. Nevertheless, alternative methods suggest that this can be done on the pore scale, by using directly the exact pore structure of the porous medium. In any case, it remains unclear how good predictions can be in applications of hysteretic two-phase flow in heterogeneous porous media, even when high-end methods are used.

Purpose of this work is to investigate the potential for making accurate predictions of hysteretic two-phase flow with numerical simulations, combine different approaches from different scales (pore scale and local scale) and test their predictive abilities, discuss the qualities of these approaches when it comes to heterogeneous structures and provide overall in-depth knowledge related to the possibilities of combined approaches to predict hysteretic two-phase flow.

In order to perform the numerical investigations related to the motivation and the objectives of this work, two hysteresis concepts are implemented in a numer-



ical model for the simulation of two-phase flow in heterogeneous porous media. The first concept is the play-type hysteresis from BELIAEV AND HASSANIZADEH (2001) [11], that approximates scanning curves as linear functions at a constant saturation. This approach assumes that the same starting and ending saturations apply for drainage and imbibition. The second concept [PARKER AND LENHARD (1987) [78]] is based on the scaling of an apparent saturation that includes a trapped non-wetting phase saturation. This approach therewith enables the formation of more realistic scanning curves and the approximation of non-wetting phase residual saturations in imbibition. The numerical model incorporates an interface condition [BASTIAN AND HELMIG (1999) [8]; DE NEEF (2000) [75]] for the approximation of material interfaces. The interface condition accounts for virtual saturations at nodes that relate to the neighboring elements, depending on the capillary pressure-saturation relationship. This allows the prediction of discontinuities of saturation at heterogeneities. This procedure is extended with the above mentioned capillary pressure-saturation hysteresis concepts, providing a firm and consistent approach for the prediction of hysteretic two-phase flow in heterogeneous porous media.

The first application of the numerical model is presented in Ch. 5. Predictions from numerical simulations are compared to a monitored 1-D transient experiment. The experiment involves a sequence of drainage and imbibition events using a homogeneous sand column. Pressure and saturation are obtained continuously over time at different heights on the column using tensiometers and TDR sensors. From the numerical point of view, three approaches are applied in the comparison to the experimental measurements:

- Hysteresis is not accounted for in the numerical model.
- Play-type hysteresis is included in the numerical model.
- Hysteresis from PARKER AND LENHARD is included in the numerical model.

This procedure shows that including a hysteresis concept in the two-phase flow numerical model significantly improves the predictions made with the simulations. Without hysteresis, the numerical simulation cannot reproduce the experimental observations even when using the best possible fit for the hydraulic properties given as input. Inclusion of the play-type concept improves the agreement between predictions and measurements. The play-type hysteresis concept has the advantage that it is conceptually simple and easy to implement. On the other hand, it does not have the ability to predict non-wetting phase trapping in imbibition. That may lead to a disagreement to experimental observations, as described

in Sect. 5.3.2. Still, it is possible to maintain low computational demands and at the same time achieve a more delicate approximation of capillary hysteresis. As shown in Sect. 5.3.3, the numerical simulation including the scaling concept for hysteresis provides an accurate prediction of flow during drainage and imbibition, also with respect to phase trapping. Although this hysteresis concept is relatively simple, it forms a reliable approach from the modeling viewpoint.

The work presented in Ch. 5 also points out the necessity for reliable hydraulic properties used as input for the numerical simulation. As explained in Sect. 5.4, the drainage and imbibition capillary pressure-saturation relationship can be determined in separate multistep outflow/inflow experiments using samples of the sand and by directly assigning applied pressures to resulting saturations. Nevertheless, this traditional approach results to a poor prediction of the transient experiment, especially with respect to air trapping (see Sect. 5.4). The multistep experiments and the tensiometer-TDR measurements relate to the same spatial scale and the same packing procedure of the sand. However, the time scales involved in the two approaches are considerably different (see Sect. 5.5). This is evidence that phase trapping relates to the time scales connected to the imbibition process. From this aspect, hysteretic capillary pressure-saturation relationships should be determined under conditions and time scales similar to the application they are purposed for.

The next part, described in Ch. 6, focuses on predictions of hysteretic two-phase flow made with hydraulic properties determined on different spatial scales. In this case, numerical simulations of drainage and imbibition are compared to experimental measurements in a 3-D heterogeneous structure. In the 3-D experiment equilibration times and water distributions are measured at quasi steady-state in a structure with pre-defined cube heterogeneities made of a coarse and a fine sand. Saturation measurements are taken by means of thermal neutron tomography after four drainage and imbibition steps that are externally introduced by variations of the water table. The numerical simulations include the scaling hysteresis concept from PARKER AND LENHARD, as it has proven the ability for reliable predictions of hysteretic behavior in two-phase flow. The hydraulic properties used as input are obtained from two approaches:

- On the local scale with multistep outflow/inflow experiments and global optimization techniques for the determination of sand porosities, permeabilities and hysteretic  $p_c-S_w$  curves within a single framework.
- On the pore scale with advanced image analysis for the determination of porosities and additionally with one- and two-phase flow lattice Boltzmann simulations in mapped geometries of the sands for the calculation of permeabilities and hysteretic  $p_c-S_w$  curves.

The saturation measurements done with the neutron tomography on the heterogeneous column at quasi steady-state show variations of cube saturations at the same height and for the same sand type. As explained in Sect. 6.1, a part of this variation comes from the expected measurement error and minor packing differences among the sand cubes. However, the variations observed here are larger compared to variations observed in similar measurements done at full steady-state [VASIN ET AL. (2007) [100]]. This additional variation most likely relates to a non steady-state configuration. This statement is also supported by the results of simulation C, presented in Sect. 6.6.3, that show variations of cube saturations at a quasi steady-state condition. In this simulation, permeability is fitted in order to obtain the time scale behavior observed in the 3-D experiment. Another important remark related to the 3-D experiment is the existence of interfaces between the packed sand cubes. Changes in saturation at the boundaries between sand cubes can be observed directly on the tomography images (see Fig. 56). In this work, the measured voxel saturations are evaluated only in the inner part of the cubes. This means that the presented cube saturations do not include saturations at the interfaces. However, interfacial effects can influence the times necessary for reaching steady-state that are measured for the entire column.

The hydraulic properties determined on the local scale and on the pore scale are discussed based on the assumptions made in the individual methodologies. As explained in Sect. 6.4, the values obtained from the local scale and the pore scale show reasonable deviations, considering that they come from two approaches with basic conceptual differences. Concerning the drainage capillary pressure-saturation curves, the main difference lies in the higher entry pressure measured with the multistep outflow experiment for the fine sand. This effect is most likely due to the different degrees of compaction in the (smaller) mapped sand sample on the pore scale and the (larger) sand column on the local scale (see Sect. 6.4). In imbibition, the LB simulations predict that no trapping of air occurs, in contrary to the measurements from the multistep inflow experiments. This difference resembles the difference described above in the predicted values of trapped air from the tensiometer-TDR measurements and the multistep experiment presented in Sect. 5.4. Here, however, the local and the pore scale approach apply the same methodology (a sequence of several static equilibria for the determination of  $p_c$ - $S_w$  curves) and only differ in the size of the sand samples. This observation suggests that the effect of phase trapping potentially also depends on the spatial scale of the volume under consideration.

The numerical simulations (see Sect. 6.6) reveal that it is not possible to correctly predict the equilibration times measured in the experiment, by using the hydraulic properties measured either on the local scale or on the pore scale. Assuming that the entire flow process in the heterogeneous structure can be cap-

tured by reconstructing the geometry and locally assigning hydraulic properties, this disagreement in time scales may be due to the uncertainty in the hydraulic properties of the sands.

As demonstrated in Sects. 6.5.2 and 6.6.3, changes in permeability influence the transient and quasi steady-state in the drainage steps, but also the steady-state observed in a subsequent imbibition step. Indeed, using the  $p_c$ - $S_w$  relationships measured on the pore scale and fitting the permeability makes it possible to obtain qualitative agreement both in terms of saturation and of equilibration times. This is not possible to achieve when using the  $p_c$ - $S_w$  curves measured on the local scale, mostly due to deviations in the entry pressure and the inclination of the resulting scanning curves for the fine sand. In this sense, the LB method shows a better predictive ability with respect to the form (entry pressure and inclination) of the hysteretic  $p_c$ - $S_w$  relationships. On the other hand, the LB method does not predict any trapping of air which does not seem to be the case at least for the 3-D measured saturations in the coarse sand after imbibition. The local scale approach in this case predicts a significant amount of air trapping and thus provides a better agreement to the neutron tomography measurements.

Nevertheless, permeabilities have to be changed up to two orders of magnitude in order to get agreement. These observations also reveal how sensitive the values of permeability can be. For the materials used in this work, the permeabilities are measured with three different approaches (LB method, multistep outflow/inflow experiments and additionally in separate columns using similar packing as in the 3-D experiment, see Sect. 6.4). All approaches give different values that range within two orders of magnitude. In general, it cannot be certain whether the difficulty in the prediction of the equilibration times results from the uncertainty in the permeability of the materials or from the interfaces that lie between them. The values of permeability ( $2.0 \times 10^{-11}$  and  $1.5 \times 10^{-12}$  [m<sup>2</sup>]) used in simulation C, that provide the best possible agreement to the experiment, can be viewed as upscaled values that represent the materials and any interfacial effects in the column. Indeed, these values are very close to those measured in 1-D columns packed with the same methodology as the 3-D column (see Sect. 6.4). The same time-scale behavior can also be demonstrated by including the material interfaces in the numerical simulations. This is shown with the last simulation presented in Sect. 6.7 only as a qualitative demonstration.

These statements do not simply indicate possibilities and limitations when using the experimental or computational methods presented in this work, but show in general how one needs to approach applications of hysteretic two-phase flow in heterogeneous media and what aspects must be taken into account when dealing with different scales. Based on all the information provided above, the following closing remarks and suggestions are given for future work on hysteretic

two-phase flow problems:

- Consideration of hysteresis is a necessary prerequisite for correct predictions of two-phase flow problems that involve alternating drainage and imbibition conditions.
- A hysteresis model does not need to be extremely sophisticated, as long as it offers some possibility for the prediction of phase trapping. In this work, the implementation of a fairly simple (from the mathematical and computational viewpoint) scaling model for hysteresis including phase trapping enabled a fairly accurate prediction of an experimentally controlled and monitored hysteretic two-phase flow system.
- The LB method provides good predictions of  $p_c$ - $S_w$  relationships from the pore scale with respect to entry pressure and inclination, but underestimates the effect of air trapping in imbibition. Combined with a fitted permeability, the hysteretic  $p_c$ - $S_w$  from the pore scale provided a qualitatively good agreement between simulation and experiment, with the exception of the imbibition distribution in the coarse sand due to the underestimation of air trapping.
- The  $p_c$ - $S_w$  relationship determined with the multistep outflow/inflow experiments agreed to the neutron tomography measurements for the coarse sand distribution but not for the fine sand. This presumably relates to the different compactions of the material resulting from the loose packing of the heterogeneous column.
- Neither the LB method nor the multistep outflow/inflow experiments could provide permeability values that predict (with simulations) the equilibration times measured in the experiment. In general, the permeabilities values depended on the approach used for their determination and showed strong sensitivity to the packing procedure. The simulation that captured the time scale behavior of the experiment involved permeability values similar to those measured in separate 1-D experiments on columns packed in the same way as the 3-D column.
- The differences in time scales most likely relate to the interfacial effects. Variations in saturation at the boundaries between sand cubes were observed directly on the tomography images. Relevant investigations on such interfacial effects resulting from packings of similar heterogeneous structures showed a major influence on the porosity. This evidence suggests that a modeling approach based on the reconstruction of the geometry and the

assignment of local hydraulic properties can be insufficient. An alternative would be to have a detailed description of the properties of the material interfaces or use an upscaled value of permeability that captures all these effects. Indeed, the numerical simulations in this work qualitatively demonstrate that the equilibration times from the experiment can be correctly predicted either by explicitly accounting for material interfaces in the model or by using permeabilities that come from measurements on columns packed with the same methodology as the 3-D structure and therefore a priori include any interfacial effects.

- The 3-D water distribution in the heterogeneous structure at quasi steady-state can differ significantly from the actual steady-state configuration. When dealing with hysteresis, this difference can have an important influence on the steady-state configurations in imbibition. In this work, switching to a quasi steady-state in the numerical simulation produced 15% differences in the predicted saturations in imbibition.
- Even the most consistent modeling approach cannot provide reliable predictions if it is not combined with a correct approach for the determination of the hydraulic properties. The amount of air trapping in materials due to hysteresis showed large sensitivity and potentially a dependency on time and spatial scales involved in the methodologies for the determination of the  $p_c$ - $S_w$  relationship. It is therefore advisable to determine hydraulic properties under conditions similar to the application they are purposed for (i.e. for fast or slow imbibition).

Additionally, an important factor appeared to be the packing technique and the compaction of the materials. The scanned cylindrical samples used for the pore-scale sand geometries were packed in the same fashion as the sand blocks in the 3-D experiment. However, the different sizes do not allow any safe conclusions regarding the influence of the effective stress in each case.

Finally, related to the conclusions of this work, the following topics arise for future scientific research:

- A systematic, thorough experimental investigation on the dependency of  $p_c$ - $S_w$  hysteresis on different time and spatial scales can provide in-depth knowledge and better understanding related to hysteresis effects. This could be done, for instance, with different sample sizes of a single material, tested for drainage and imbibition under different boundary conditions (i.e. fast or slow imbibition, produced with many/few equilibria after smaller/larger pressure steps).

- The impact of time and spatial scales can also be investigated on the pore-scale. For example, testing larger geometries in the pore-scale approach –when possible from the computational point of view– should shed more light on the problem of the amount of air trapping calculated with the LB method in imbibition.
- The influence of material interfaces can also be investigated by means of experiments and simulations. High-resolution neutron tomography can provide valuable information related to the actual behavior of the fluid phases in these interfaces. Consequently, this information can be combined with the LB method. An optimal approach would be to obtain mapped geometries directly from the constructed heterogeneous column. This way, the LB method would enable a unique, consistent investigation with respect to the hydraulic properties of the sands, as compacted or loose as they are in the heterogeneous structure, while observing at the same time any effects due to material interfaces. This strategy is not meant to be applied each time a prediction of two-phase flow in heterogeneous media is needed, but can give understanding of the underlying processes, provide knowledge necessary for future applications and reveal patterns that determine the behavior of such systems.

# **A . Comparison of simulation results to the 1-D transient experiment**

In Ch. 5, the comparison between the numerical simulation and the transient experiment was based on the predicted and the measured values at points 2, 3 and 4. In Figs. 82-84, the same comparison is presented for the values at point 1. As point 1 is located very close to the bottom of the column, it remains saturated during the entire sequence of the drainage and imbibition events. Saturation remains equal to 1.0 [-] both in simulation and experiment. Regarding the pressure values, the same remarks and conclusions as for the other measurement points can be drawn. The inclusion of the play-type hysteresis improves the prediction, however a good agreement between predicted and measured values is achieved using the scaling concept for hysteresis.



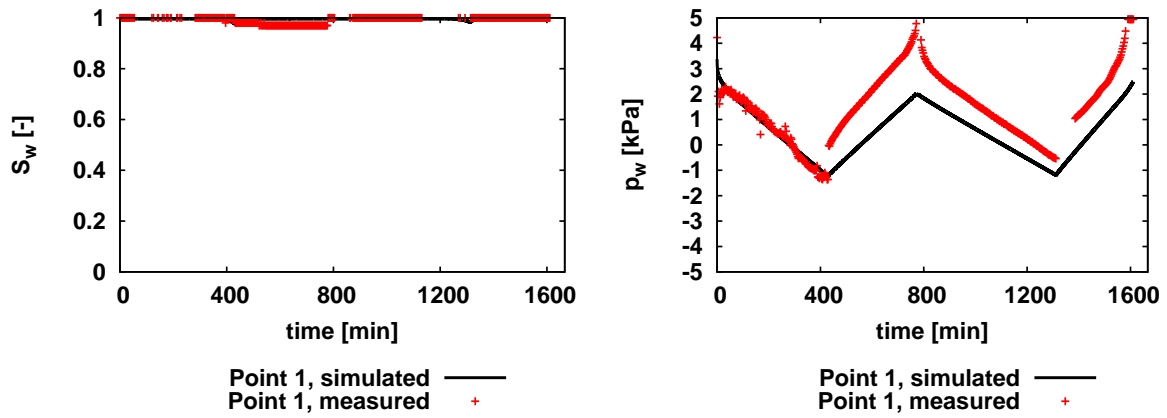


Figure 82: Saturation and pressure at point 1: comparison measurement and simulation with hysteresis not included.

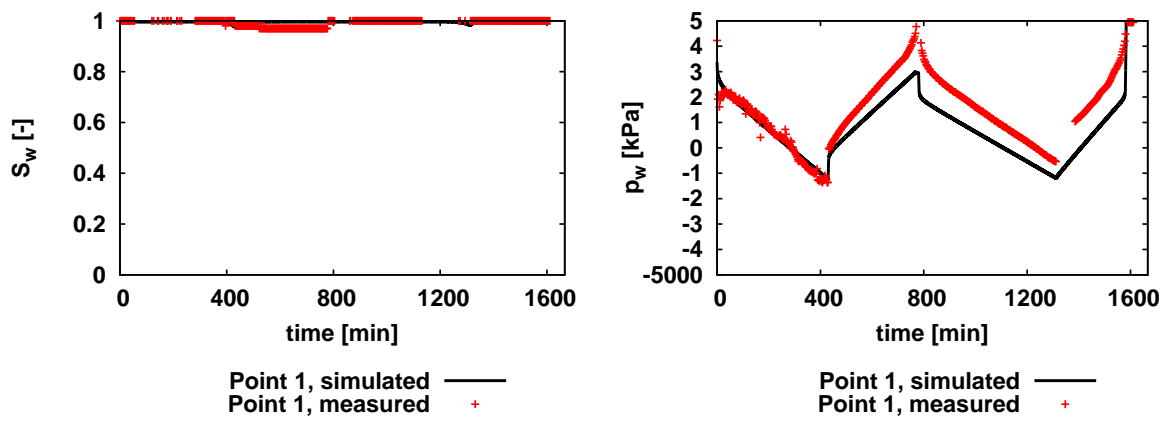


Figure 83: Saturation and pressure at point 1: comparison measurement and simulation with play-type hysteresis included.

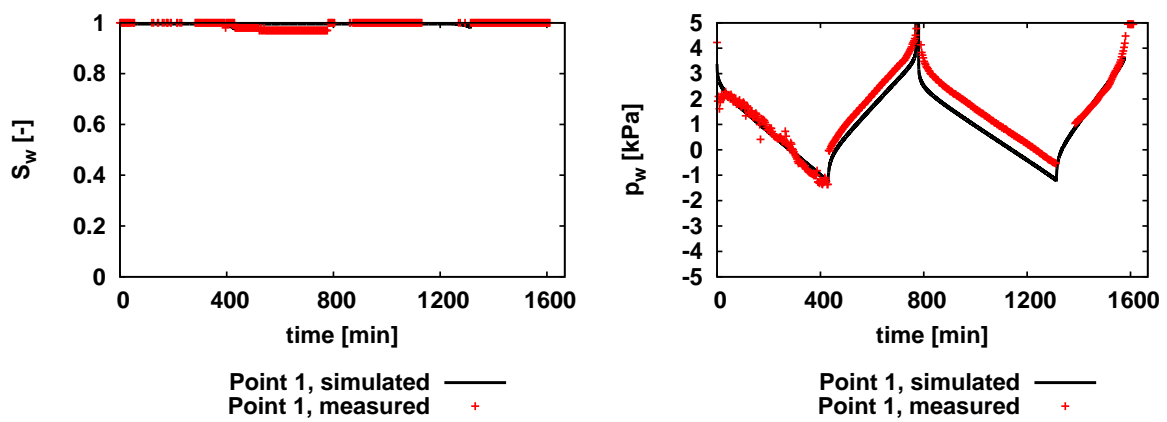


Figure 84: Saturation and pressure at point 1: comparison measurement and simulation including hysteresis from PARKER AND LENHARD.

# Bibliography

- [1] Abriola, L. M. Modeling multiphase migration of organic chemicals in groundwater systems—A review and assessment. *Environ. Health Perspect.*, 83:117–143, 1989.
- [2] Adler, P. M. and Thovert, F. F. Real porous media: Local geometry and macroscopic properties. *Appl. Mech. Rev.*, 51(9):537–585, 1998.
- [3] Ahrenholz, B., Tölke, J., Lehmann, P., Peters, A., Kaestner, A., Krafczyk, M., and Durner, W. Prediction of capillary hysteresis in porous material using lattice boltzmann methods and comparison to experimental data and a morphological pore network model. *Advances in Water Resources*, preprint submitted, 2007.
- [4] Arya, L. M. and Paris, J. F. A Physicoempirical Model to Predict the Soil Moisture Characteristic from Particle–Size Distribution and Bulk Density Data. *Soil Sci. Soc. Am. J.*, 45:1023–1030, 1981.
- [5] Bakke, S. and Oren, P. E. 3-d pore-scale modelling of sandstones and flow simulations in the pore networks. *Society of Petroleum Engineers Journal*, 2(2):136–149, 1997.
- [6] Bastian, P. Numerical computation of multiphase flows in porous media, 1999. Habilitation thesis, Christian-Albrechts-Universität Kiel.
- [7] Bastian, P., Birken, K., Johannsen, K., Lang, S., Eckstein, K., Neuss, N., Reichert, H. R., and Wieners, C. UG – A Flexible Software Toolbox for Solving Partial Differential Equations. *Computing and Visualization in Science*, 1:27–40, 1997.
- [8] Bastian, P. and Helmig, R. Efficient Fully-Coupled Solution Techniques for Two Phase Flow in Porous Media. Parallel Multigrid Solution and Large Scale Computations. *Adv. Water Resour.*, 23:199–216, 1999.

- [9] Bear, J. *Dynamics of Fluids in Porous Media*. Dover Publications, Inc, New York, 1972.
- [10] Bekri, S. and Adler, P. M. Dispersion in multiphase flow through porous media. *Int. Journal of Multiphase flow*, 28:665–697, 2002.
- [11] Beliaev, A. Y. and Hassanizadeh, S. M. A Theoretical Model of Hysteresis and Dynamic Effects in the Capillary Relation for Two-phase Flow in Porous Media. *Transport in Porous Media*, 43:487–510, 2001.
- [12] Brokate, M. and Sprekels, J. *Hysteresis and Phase Transitions*. Springer-Verlag Berlin, 1996.
- [13] Brooks, R. H. and Corey, A. T. Hydraulic properties of porous media. In *Hydrol. Pap.*, Band Band 3. Colorado State University, Fort Collins, 1964.
- [14] Brutsaert, W. Some methods of calculating unsaturated permeability. *Trans. ASAE*, 10:400–404, 1967.
- [15] Bryant, S. L. and Blunt, M. J. Prediction of relative permeability in simple porous media. *Physical Review A*, 46(4):2004–2011, 1992.
- [16] Burdine, N. T. Relative permeability calculations from pore – size distribution data. Forschungsbericht, Reseach Report, Petroleum Transactions, AIME, 1953.
- [17] Campbell, G. A simple model for determining unsaturated hydraulic conductivity from moisture retention data. *Soil Sci.*, 117:311–314, 1974.
- [18] Campbell, G. and Shiozawa, S. Prediction of hydraulic properties of soils using particle size density data. In *Indirect methods for estimating the hydraulic properties of unsaturated soils*. Riverside, California, Oct. 11–13, 1989.
- [19] Chatzis, I. and Dullien, F. A. Dynamic immiscible displacement mechanisms in pore doublets: theory versus experiment. *Journal of Colloid and Interface Science*, 91:199–222, 1983.
- [20] Coles, M., Hazlett, R., Spanne, P., Sole, W., Muegge, E., and Jones, K. Pore level imaging of fluid transport using synchrotron X-ray microtomography. *Journal of the Society of petroleum Engineers*, 19:55 – 63, 1998.
- [21] Culligan, K., Wildenschild, D., Christensen, B., Gray, W., and Rivers, M. Pore-scale characteristics of multiphase flow in porous media: a comparison of air-water and oil-water experiments. *Advances in Water Resources*, 29:227–238, 2006.

- [22] Culligan, K., Wildenschild, D., Christensen, B., Gray, W., Rivers, M., and Tompson, A. Interfacial area measurements for unsaturated flow through a porous medium. *Water Resources Research*, 40:W12413, doi:10.1029/2004WR003278, 2004.
- [23] Dahle, H. K., Celia, M. A., Hassanizadeh, S. M., and Karlsen, K. H. A total pressure-saturation formulation of two-phase flow incorporating dynamic effects in the capillary-pressure-saturation relationship. In Hassanizadeh, S. M., Schotting, R. J., Gray, W. G., Pinder, G. F., and Brebbia, C. A., Hrsg., *Proceedings of the XIV International Conference on Computational Methods in Water Resources held in Delft, The Netherlands*, S. 1067–1074. Technical University of Delft, The Netherlands, June 23-28, 2002.
- [24] Dekker, T. J. and Abriola, L. M. The influence of field-scale heterogeneity on the infiltration and entrapment of dense nonaqueous liquids in saturated formations. *J. Contam. Hydrol.*, 42:187–218, 2000.
- [25] Duan, Q., Sorooshian, S., and Gupta, V. Effective and efficient global optimization for conceptual rainfall-runoff models. *Water Resources Research*, 28:1015–1031, 1992.
- [26] Einstein, A. On the motion -required by the molecular kinetic theory of heat- of small particles suspended in a stationary liquid. *Annalen der Physik*, 17:549 – 560, 1905.
- [27] Essaid, H. I. and Hess, K. M. Monte Carlo Simulations of Multiphase Flow Incorporating Spatial Variability of Hydraulic Properties. *Ground Water*, 31(1):123–134, 1993.
- [28] Ewing, J. A. Experimental Research in Magnetism. *Phil. Trans. R. Soc. Lond.*, 176(II), 1895.
- [29] Ferreol, B. and Rothmann, D. Lattice-Boltzmann simulations of flow through Fontainebleu sandstone. *Transport in Porous Media*, 20:3–20, 1995.
- [30] Franz, W. *Hysteresis Effects in Economic Models*. Physica-Verlag Heidelberg, 1990.
- [31] Gerhard, J. and Kueper, B. H. Capillary pressure characteristics necessary for simulating DNAPL infiltration, redistribution and immobilization in saturated porous media. *Water Resources Research*, 39(8):1212, doi:10.1029/2002WR001270, 2003.

- [32] Gerhard, J. and Kueper, B. H. Relative permeability characteristics necessary for simulating DNAPL infiltration, redistribution and immobilization in saturated porous media. *Water Resources Research*, 39(8):1213, doi:10.1029/2002WR001490, 2003.
- [33] Gielen, T., Hassanizadeh, S. M., Celia, M. A., and Dahle, H. K. Study of  $P^c - S^w$  relationships using a dynamic pore-scale network model. In Hassanizadeh, S. M., Schotting, R. J., Gray, W. G., Pinder, G. F., and Brebbia, C. A., Hrsg., *Proceedings of the XIV International Conference on Computational Methods in Water Resources held in Delft, The Netherlands*, S. 1099–1106. Technical University of Delft, The Netherlands, June 23–28, 2002.
- [34] Haines, W. B. Studies in the physical properties of soils: V. The hysteresis effect in capillary properties and the modes of moisture distribution associated therewith. *J. Agric. Sci.*, 20:97–116, 1930.
- [35] Hassanein, R., Lehmann, E., and Vontobel, P. Methods of scattering corrections for quantitative neutron radiography. *Nuclear Instruments and Methods in Physics Research*, A 542:353–360, 2005.
- [36] Hassanizadeh, M., Oung, O., and Manthey, S. Laboratory experiments and simulations on the significance of non-equilibrium effect in the capillary pressure–saturation relationship. In Schanz, T., Hrsg., *Int. Conf. From experimental evidence towards numerical modelling of unsaturated soils*, Weimar, Lecture Notes in Applied Mechanics. Springer, 2004.
- [37] Hassanizadeh, S. M. Experimental evidence of dynamic capillary pressure effects in two-phase flow. In *Recent Advances in Multiphase Flow and Transport in Porous Media*, European Science Foundation Exploratory Workshop, Delft University of Technology, Delft, The Netherlands, June 23-25, 2003. European Science Foundation (ESF), 2003.
- [38] Hassanizadeh, S. M., Celia, M. A., and Dahle, H. K. Dynamic effect in the capillary pressure - saturation relationship and its impact on unsaturated flow. *Vadose Zone Hydrology*, 1:38–57, 2002.
- [39] Hassanizadeh, S. M. and Gray, W. G. Thermodynamic Basis of Capillary Pressure in Porous Media. *Water Resources Research*, 29(10):3389–3405, 1993.
- [40] Heijs, A. W. J. and Lange, J. D. Determination of pore networks and water content distributions from 3–D computed tomography images. *Bioimaging*, 5:194–204, 1997.

- [41] Helmig, R. *Multiphase Flow and Transport Processes in the Subsurface*. Springer, 1997.
- [42] Helmig, R., Class, H., Huber, R., Sheta, H., Ewing, J., Hinkelmann, R., Jakobs, H., and Bastian, P. Architecture of the Modular Program System MUFTE\_UG for Simulating Multiphase Flow and Transport Processes in Heterogeneous Porous Media. *Mathematische Geologie*, 2, 1998.
- [43] Helmig, R. and Huber, R. Comparison of galerkin-type discretization techniques for two-phase flow in heterogeneous porous media. *Advances in Water Resources*, 21(8):697–711, 1998.
- [44] Helmig, R., Sheta, H., Meiners, H., and Kunz, E. Numerische Simulation von Gasströmen im Grubengebäude und im Gebirge. *Glückauf*, 142:37–44, 2006.
- [45] Hopmans, J. W., Vogel, T., and Koblik, P. D. X-ray Tomography of Soil Water Distribution in One-Step Outflow Experiments. *Soil Sci. Am. J.*, 56:355–362, 1992.
- [46] Hornung, U. *Homogenization and Porous Media*. Springer-Verlag, 1997.
- [47] Huber, R. and Helmig, R. Multiphase flow in heterogeneous porous media: A classical finite element method versus an implicit pressure-explicit saturation-based mixed finite element-finite volume approach. *International Journal for Numerical Methods in Fluids*, 29:899–920, 1999.
- [48] Jakobs, H. *Simulation nicht-isothermer Gas-Wasser-Prozesse in komplexen Kluft-Matrix-Systemen*. Dissertation, University of Stuttgart, Institute of Hydraulic Engineering, 2004.
- [49] Joekar, V., Hassanizadeh, S. M., and Leijnse, A. Insights into the relationships among capillary pressure, saturation, interfacial area and relative permeability using pore-scale network modeling. *Transport in Porous Media*, preprint submitted, 2007.
- [50] Jonasson, S. Estimation of the van genuchten parameters from grain-size distribution. In *Indirect methods for estimating the hydraulic properties of unsaturated soils*. Riverside, California, Oct. 11–13, 1989.
- [51] Juanes, R. and Patzek, T. W. Relative permeabilities for strictly hyperbolic models of three-phase flow in porous media. *Transport in Porous Media*, 57:125–152, 2004.

- [52] Jury, W. A., Gardner, W. R., and Gardner, W. H. *Soil Physics*. John Wiley & Sons, Inc., New York, 1991.
- [53] Kaestner, A., Hassanein, R., Vontobel, P., Lehmann, P., Schaap, J., Lehmann, E., and Flühler, H. Mapping the 3d water dynamics in heterogeneous sands using thermal neutrons. *Chemical Engineering Journal*, 130:79–85, 2007.
- [54] Kaestner, A., Lehmann, P., and Stampanoni, M. Imaging and image processing in porous media research. *Advances in Water Resources*, preprint submitted, 2007.
- [55] Kirschenbaum, I. *Physical properties and analysis of heavy water*. McGraw-Hill, New York, 1951.
- [56] Kool, J. and Parker, J. Development and evaluation of closed-form expressions for hysteretic soil hydraulic properties. *Water Resources Research*, 23(1):105–114, 1987.
- [57] Krasnoselskii, M. and Pokrovskii, A. *Systems with Hysteresis*. Springer-Verlag New York, 1989.
- [58] Krejci, P. and Sprekels, J. Variations of domain and free-boundary problems in solid mechanics. *Kluwer Acad. Publ.*, Dordrecht:237 – 244, 1999.
- [59] Kueper, B. H., Abbott, W., and Farquhar, G. Experimental Observations of Multiphase Flow in Heterogeneous Porous Media. *Journal of Contaminant Hydrology*, 5:83–95, 1989.
- [60] Kueper, B. H. and Frind, E. O. Two-Phase Flow in Heterogeneous Porous Media, 2. Model Application. *Water Resources Research*, 27(6):1059–1070, 1991.
- [61] Land, C. S. Calculation of imbibition relative permeability for two- and three phase flow from rock properties. *Trans. Am. Inst. Min. Metall. Pet. Eng.*, 243, 1968.
- [62] Laplace, P. S. *Traité de Mécanique Céleste; Supplement au Dixième Livre, Sur l'Action Capillaire*. Courcier, Paris, 1806.
- [63] Lehmann, P., Berchtold, M., Ahrenholz, B., Tölke, J., Kaestner, A., Krafczyk, M., Flühler, H., and Künsch, H. Impact of geometrical properties on permeability and fluid phase distribution in porous media. *Advances in Water Resources*, preprint submitted, 2007.

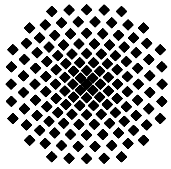
- [64] Lehmann, P., Kaestner, A., Beckmann, F., and Fluehler, H. Geometric properties of layered sands and their relevance for water distribution. Forschungsbericht, Hamburger Synchrotronstrahlungslabor HASY-LAB, 2004.
- [65] Lehmann, P., Krafczyk, M., Gygi, A., Flisch, A., Wyss, P., and Flühler, H. Modelling flow of water and air in reconstructed structures of porous media. In *Proceedings of the 2nd world congress on industrial tomography, Hannover*, S. 628–635, 2001.
- [66] Lins, Y., Papafotiou, A., Helmig, R., and Schanz, T. Experimental and numerical investigations for the prediction of hysteretic unsaturated flow including air entrapment. *Advances in Water Resources*, preprint submitted, 2007.
- [67] Mackay, D. M. and Cherry, J. A. Groundwater contamination: Pump and treat remediation. *Environmental Science Technology*, 23:630–636, 1989.
- [68] Masschaele, B., Dierick, M., Hoorebeeke, L. V., Cnudde, V., and Jacobs, P. The use of neutrons and monochromatic X-rays for non-destructive testing in geological materials. *Environmental Geology*, 46:486–492, 2004.
- [69] Mayergoyz, I. *Mathematical Models of Hysteresis*. Springer-Verlag, 1991.
- [70] Miller, C. T., Christakos, G., P.T.Imhoff, J.F.McBride, J.A.Pedit, and J.A.Trangenstein. Multiphase flow and transport modeling in heterogeneous porous media: challenges and approaches. *Advances in Water Resources*, 21:77–120, 1998.
- [71] Moore, T. F. and L.Slobod, R. The effect of viscosity and capillarity on the displacement of oil by water. *Producers Monthly*, 20, 1956.
- [72] Mualem, Y. A conceptual model of hysteresis. *Water Resources Research*, 10:514–520, 1974.
- [73] Mualem, Y. A new model for predicting the hydraulic conductivity of unsaturated porous media. *Water Resources Research*, 12(3):513–522, 1976.
- [74] Mualem, Y. A modified dependent-domain theory of hysteresis. *Soil Science*, 137(5):283–291, 1984.
- [75] de Neef, M. J. *Modeling Capillary Effects in Heterogeneous Porous Media*. Dissertation, Technische Universiteit Delft, 2000.



- [76] Pan, C., Hilpert, M., and Miller, C. T. Lattice-Boltzmann simulation of two-phase flow in porous media. *Water Resources Research*, 40:W01501 doi:10.1029/2003WR002120, 2004.
- [77] Panday, S., Wu, Y. S., Huyakom, P. S., and Springer, E. P. A three-dimensional multiphase flow model for assessing DNAPL contamination in porous and fractured media: 2.Porous medium simulation examples. *J. Contam. Hydrol.*, S. 131–156, 1994.
- [78] Parker, J. C. and Lenhard, R. J. A model for hysteretic constitutive relations governing multiphase flow 1. saturation pressure relations. *Water Resources Research*, 23(4):618–624, 1987.
- [79] Pomeroy, J. R., Sontag, E. D., and Ferrell, J. E. J. Building a cell cycle oscillator: hysteresis and bistability in the activation of Cdc2. *Nature Cell Biology*, 5:346–351, 2003.
- [80] Priesack, E. and Durner, W. Closed-form expression for the multi-modal unsaturated conductivity function. *Vadose Zone J.*, 5:121–124, 2006.
- [81] Quintard, M. and Whitaker, S. Transport in ordered and disordered porous media: I. The cellular average and the use of weighting functions. *Transport in Porous Media*, 14:163 – 177, 1994.
- [82] Quintard, M. and Whitaker, S. Transport in ordered and disordered porous media: II. Generalized volume averaging. *Transport in Porous Media*, 14:179 – 206, 1994.
- [83] Quintard, M. and Whitaker, S. Transport in ordered and disordered porous media: III. Closure and comparison between theory and experiment. *Transport in Porous Media*, 15:31 – 49, 1994.
- [84] Reeves, P. C. and Celia, M. A. A functional relationship between capillary pressure, saturation, and interfacial area as revealed by a pore-scale network model. *Water Resources Research*, 32(8):2345–2358, 1996.
- [85] Richards, L. A. Capillary Conduction of Liquids through Porous Medium. *Physics*, S. 318–333, 1931.
- [86] S.A. Lorentz, D. D. and Corey, A. Liquid retention measurement in porous media using a controlled outflow cell. Forschungsbericht, Dept. of Chemical and Bioresource Engineering, Colorado State University, Fort Collins, Co, 17pp., 1992.

- [87] Schaap, J. Mapping water dynamics in heterogeneous porous media by neutron tomography. Forschungsbericht, Master's Thesis, Wageningen University, ETH Zürich, 2005.
- [88] Schaap, J., Lehmann, P., Kaestner, A., Vontobel, P., Hassanein, R., Frei, G., de Rooij, G., Lehmann, E., and Flühler, H. Measuring the effect of structural connectivity on the water dynamics in heterogeneous porous media using fast neutron tomography. *Advances in Water Resources*, preprint submitted, 2007.
- [89] Schiegg, H. O. *Verdrängungs-Simulation dreier nicht mischbarer Fluide in poröser Matrix*. Dissertation, ETH Zürich, 1979.
- [90] Scott, P. S., Farquhar, G. J., and Kouwen, N. Hysteretic effects on net infiltration. *American Society of Agricultural Engineers*, 11-83:163 – 171, 1983.
- [91] Setterfield, M. *Rapid Growth and Relative Decline: Modelling Macroeconomic Dynamics with Hysteresis*. Palgrave Macmillan, 1997.
- [92] Sheta, H. *Simulation von Mehrphasenvorgängen in porösen Medien unter Einbeziehung von Hysterese-Effekten*. Dissertation, University of Stuttgart, Institute of Hydraulic Engineering, 1999.
- [93] Solymar, M., Lehmann, E., Vontobel, P., and Nordlund, A. Relating variations in water saturation of a sandstone sample to pore geometry by neutron tomography and image analysis of thin sections. *Bull.Eng.Geol.Env.*, 62:85–88, 2003.
- [94] Stauffer, F. and Dracos, T. Experimental and numerical study of water and solute infiltration in layered porous media. *J. Hydrology*, 84(1):9 – 34, 1986.
- [95] Tölke, J., Freudiger, S., and Krafczyk, M. An adaptive scheme for the multiphase flow simulations on hierarchical grids. *Comput. Fluids*, 35:820–830, 2006.
- [96] Tölke, J., Krafczyk, M., Schulz, M., and Rank, E. Lattice Boltzmann Simulations of binary fluid flow through porous media. *Phil. Trans. R. Soc. Lond. A*, 360(1792), 2002.
- [97] Ursino, N. and Gimmi, T. Combined effect of heterogeneity, anisotropy and saturation on steady-state flow and transport: Structure recognition and numerical simulation. *Water Resources Research*, 40:W01514, doi:10.1029/2003WR002180, 2004.

- [98] Ursino, N., Gimmi, T., and Flühler, H. Combined effects of heterogeneity, anisotropy and saturation on steady-state flow and transport: A laboratory tank experiment. *Water Resources Research*, 37:201–208, 2001.
- [99] van Genuchten, M. T. A closed-form equation for predicting the hydraulic conductivity of unsaturated soils. *Soil Sci. Soc. Am. J.*, 44:892–898, 1980.
- [100] Vasin, M., Lehmann, P., Kaestner, A., Hassanein, R., Nowak, W., Helmig, R., and Neuweiler, I. Drainage in heterogeneous sand columns with different geometric structures. *Advances in Water Resources*, preprint submitted, 2007.
- [101] Vogel, H.-J. and Roth, K. A new approach for determining effective soil hydraulic functions. *European Journal of Soil Science*, 49:547–556, 1998.
- [102] Vogel, H.-J., Toelke, J., Schulz, V., Krafczyk, M., and Roth, K. Comparison of a lattice-Boltzmann model, a full-morphology model and a pore network model for determining capillary pressure-saturation relationships. *Vadose Zone Journal*, 4:380–388, 2005.
- [103] Wardlaw, N. C. The effect of geometry, wettability, viscosity and interfacial tension on trapping in single pore-throat pairs. *Journal of Canadian Petroleum Technology*, 21(3), 1982.
- [104] Wei, C. and Dewoolkar, M. Formulation of capillary hysteresis with internal state variables. *Water Resources Research*, 42:W07405, 2006.
- [105] Whitaker, S. Flow in porous media i: A theoretical derivation of Darcy's law. *Transport in Porous Media*, 1:3–25, 1986.
- [106] Wildenschild, D. and Jensen, K. H. Laboratory investigation of effective flow behaviour in unsaturated heterogeneous sands. *Water Resources Research*, 35:17–21, 1999.
- [107] Winkler, A. *Prozesse des Wärme- und Stofftransports bei der In-situ-Sanierung mit festen Wärmequellen*. Dissertation, Universität Stuttgart, 2002.



## Institut für Wasserbau Universität Stuttgart

Pfaffenwaldring 61  
70569 Stuttgart (Vaihingen)  
Telefon (0711) 685 - 64717/64749/64752/64679  
Telefax (0711) 685 - 67020 o. 64746 o. 64681  
E-Mail: [iws@iws.uni-stuttgart.de](mailto:iws@iws.uni-stuttgart.de)  
<http://www.iws.uni-stuttgart.de>

### Direktoren

Prof. Dr. rer. nat. Dr.-Ing. András Bárdossy  
Prof. Dr.-Ing. Rainer Helmig  
Prof. Dr.-Ing. Silke Wieprecht

### Vorstand (Stand 1.2.2008)

Prof. Dr. rer. nat. Dr.-Ing. A. Bárdossy  
Prof. Dr.-Ing. R. Helmig  
Prof. Dr.-Ing. S. Wieprecht  
Prof. Dr.-Ing. habil. B. Westrich  
Jürgen Braun, PhD  
Dr.-Ing. H. Class  
Dr.-Ing. S. Hartmann  
Dr.-Ing. H.-P. Koschitzky  
PD Dr.-Ing. W. Marx  
Dr. rer. nat. J. Seidel

### Emeriti

Prof. Dr.-Ing. Dr.-Ing. E.h. Jürgen Giesecke  
Prof. Dr.h.c. Dr.-Ing. E.h. Helmut Kobus, PhD

### Lehrstuhl für Wasserbau und Wassermengenwirtschaft

Leiter: Prof. Dr.-Ing. Silke Wieprecht  
Stellv.: PD Dr.-Ing. Walter Marx, AOR

### Lehrstuhl für Hydromechanik und Hydrosystemmodellierung

Leiter: Prof. Dr.-Ing. Rainer Helmig  
Stellv.: Dr.-Ing. Holger Class, AOR

### Lehrstuhl für Hydrologie und Geohydrologie

Leiter: Prof. Dr. rer. nat. Dr.-Ing. András Bárdossy  
Stellv.: Dr. rer. nat. Jochen Seidel

### VEGAS, Versuchseinrichtung zur Grundwasser- und Altlastensanierung

Leitung: Jürgen Braun, PhD  
Dr.-Ing. Hans-Peter Koschitzky, AD

### Versuchsanstalt für Wasserbau

Leiter: apl. Prof. Dr.-Ing. Bernhard Westrich

## Verzeichnis der Mitteilungshefte

- 1 Röhnisch, Arthur: *Die Bemühungen um eine Wasserbauliche Versuchsanstalt an der Technischen Hochschule Stuttgart, und*  
Fattah Abouleid, Abdel: *Beitrag zur Berechnung einer in lockeren Sand gerammten, zweifach verankerten Spundwand, 1963*
- 2 Marotz, Günter: *Beitrag zur Frage der Standfestigkeit von dichten Asphaltbelägen im Großwasserbau, 1964*
- 3 Gurr, Siegfried: *Beitrag zur Berechnung zusammengesetzter ebener Flächen-tragwerke unter besonderer Berücksichtigung ebener Stauwände, mit Hilfe von Randwert- und Lastwertmatrizen, 1965*
- 4 Plica, Peter: *Ein Beitrag zur Anwendung von Schalenkonstruktionen im Stahlwasserbau, und* Petrikat, Kurt: *Möglichkeiten und Grenzen des wasserbaulichen Versuchswesens, 1966*

- 5 Plate, Erich: *Beitrag zur Bestimmung der Windgeschwindigkeitsverteilung in der durch eine Wand gestörten bodennahen Luftschicht, und*  
Röhnisch, Arthur; Marotz, Günter: *Neue Baustoffe und Bauausführungen für den Schutz der Böschungen und der Sohle von Kanälen, Flüssen und Häfen; Gesteungskosten und jeweilige Vorteile, sowie Unny, T.E.: Schwingungsuntersuchungen am Kegelstrahlschieber, 1967*
- 6 Seiler, Erich: *Die Ermittlung des Anlagenwertes der bundeseigenen Binnenschiffahrtsstraßen und Talsperren und des Anteils der Binnenschifffahrt an diesem Wert, 1967*
- 7 *Sonderheft anlässlich des 65. Geburtstages von Prof. Arthur Röhnisch mit Beiträgen von* Benk, Dieter; Breitling, J.; Gurr, Siegfried; Haberhauer, Robert; Honekamp, Hermann; Kuz, Klaus Dieter; Marotz, Günter; Mayer-Vorfelder, Hans-Jörg; Miller, Rudolf; Plate, Erich J.; Radomski, Helge; Schwarz, Helmut; Vollmer, Ernst; Wildenhahn, Eberhard; 1967
- 8 Jumikis, Alfred: *Beitrag zur experimentellen Untersuchung des Wassernachschubs in einem gefrierenden Boden und die Beurteilung der Ergebnisse, 1968*
- 9 Marotz, Günter: *Technische Grundlagen einer Wasserspeicherung im natürlichen Untergrund, 1968*
- 10 Radomski, Helge: *Untersuchungen über den Einfluß der Querschnittsform wellenförmiger Spundwände auf die statischen und rammtechnischen Eigenschaften, 1968*
- 11 Schwarz, Helmut: *Die Grenztragfähigkeit des Baugrundes bei Einwirkung vertikal gezogener Ankerplatten als zweidimensionales Bruchproblem, 1969*
- 12 Erbel, Klaus: *Ein Beitrag zur Untersuchung der Metamorphose von Mittelgebirgsschneedecken unter besonderer Berücksichtigung eines Verfahrens zur Bestimmung der thermischen Schneequalität, 1969*
- 13 Westhaus, Karl-Heinz: *Der Strukturwandel in der Binnenschifffahrt und sein Einfluß auf den Ausbau der Binnenschiffskanäle, 1969*
- 14 Mayer-Vorfelder, Hans-Jörg: *Ein Beitrag zur Berechnung des Erdwiderstandes unter Ansatz der logarithmischen Spirale als Gleitflächenfunktion, 1970*
- 15 Schulz, Manfred: *Berechnung des räumlichen Erddruckes auf die Wandung kreiszylindrischer Körper, 1970*
- 16 Mobasseri, Manoutschehr: *Die Rippenstützmauer. Konstruktion und Grenzen ihrer Standsicherheit, 1970*
- 17 Benk, Dieter: *Ein Beitrag zum Betrieb und zur Bemessung von Hochwasserrückhaltebecken, 1970*

- 18 Gál, Attila: *Bestimmung der mitschwingenden Wassermasse bei überströmten Fischbauchklappen mit kreiszylindrischem Staublech*, 1971, vergriffen
- 19 Kuz, Klaus Dieter: *Ein Beitrag zur Frage des Einsetzens von Kavitationserscheinungen in einer Düsenströmung bei Berücksichtigung der im Wasser gelösten Gase*, 1971, vergriffen
- 20 Schaak, Hartmut: *Verteilleitungen von Wasserkraftanlagen*, 1971
- 21 *Sonderheft zur Eröffnung der neuen Versuchsanstalt des Instituts für Wasserbau der Universität Stuttgart mit Beiträgen von* Brombach, Hansjörg; Dirksen, Wolfram; Gál, Attila; Gerlach, Reinhard; Giesecke, Jürgen; Holthoff, Franz-Josef; Kuz, Klaus Dieter; Marotz, Günter; Minor, Hans-Erwin; Petrikat, Kurt; Röhnisch, Arthur; Rueff, Helge; Schwarz, Helmut; Vollmer, Ernst; Wildenhahn, Eberhard; 1972
- 22 Wang, Chung-su: *Ein Beitrag zur Berechnung der Schwingungen an Kegelstrahlschiebern*, 1972
- 23 Mayer-Vorfelder, Hans-Jörg: *Erdwiderstandsbeiwerte nach dem Ohde-Variationsverfahren*, 1972
- 24 Minor, Hans-Erwin: *Beitrag zur Bestimmung der Schwingungsanfachungsfunktionen überströmter Stauklappen*, 1972, vergriffen
- 25 Brombach, Hansjörg: *Untersuchung strömungsmechanischer Elemente (Fluidik) und die Möglichkeit der Anwendung von Wirbelkammerelementen im Wasserbau*, 1972, vergriffen
- 26 Wildenhahn, Eberhard: *Beitrag zur Berechnung von Horizontalfilterbrunnen*, 1972
- 27 Steinlein, Helmut: *Die Eliminierung der Schwebstoffe aus Flußwasser zum Zweck der unterirdischen Wasserspeicherung, gezeigt am Beispiel der Iller*, 1972
- 28 Holthoff, Franz Josef: *Die Überwindung großer Hubhöhen in der Binnenschifffahrt durch Schwimmerhebwerke*, 1973
- 29 Röder, Karl: *Einwirkungen aus Baugrundbewegungen auf trog- und kastenförmige Konstruktionen des Wasser- und Tunnelbaues*, 1973
- 30 Kretschmer, Heinz: *Die Bemessung von Bogenstaumauern in Abhängigkeit von der Talform*, 1973
- 31 Honekamp, Hermann: *Beitrag zur Berechnung der Montage von Unterwasserpipelines*, 1973
- 32 Giesecke, Jürgen: *Die Wirbelkammertriode als neuartiges Steuerorgan im Wasserbau*, und Brombach, Hansjörg: *Entwicklung, Bauformen, Wirkungsweise und Steuereigenschaften von Wirbelkammerverstärkern*, 1974

- 33 Rueff, Helge: *Untersuchung der schwingungserregenden Kräfte an zwei hintereinander angeordneten Tiefschützen unter besonderer Berücksichtigung von Kavitation*, 1974
- 34 Röhnisch, Arthur: *Einpreßversuche mit Zementmörtel für Spannbeton - Vergleich der Ergebnisse von Modellversuchen mit Ausführungen in Hüllwellrohren*, 1975
- 35 *Sonderheft anlässlich des 65. Geburtstages von Prof. Dr.-Ing. Kurt Petrikat mit Beiträgen von:* Brombach, Hansjörg; Erbel, Klaus; Flinspach, Dieter; Fischer jr., Richard; Gál, Attila; Gerlach, Reinhard; Giesecke, Jürgen; Haberhauer, Robert; Hafner Edzard; Hausenblas, Bernhard; Horlacher, Hans-Burkhard; Hutarew, Andreas; Knoll, Manfred; Krummet, Ralph; Marotz, Günter; Merkle, Theodor; Miller, Christoph; Minor, Hans-Erwin; Neumayer, Hans; Rao, Syamala; Rath, Paul; Rueff, Helge; Ruppert, Jürgen; Schwarz, Wolfgang; Topal-Gökceli, Mehmet; Vollmer, Ernst; Wang, Chung-su; Weber, Hans-Georg; 1975
- 36 Berger, Jochum: *Beitrag zur Berechnung des Spannungszustandes in rotations-symmetrisch belasteten Kugelschalen veränderlicher Wandstärke unter Gas- und Flüssigkeitsdruck durch Integration schwach singulärer Differentialgleichungen*, 1975
- 37 Dirksen, Wolfram: *Berechnung instationärer Abflußvorgänge in gestauten Gerinnen mittels Differenzenverfahren und die Anwendung auf Hochwasserrückhaltebecken*, 1976
- 38 Horlacher, Hans-Burkhard: *Berechnung instationärer Temperatur- und Wärmespannungsfelder in langen mehrschichtigen Hohlzylindern*, 1976
- 39 Hafner, Edzard: *Untersuchung der hydrodynamischen Kräfte auf Baukörper im Tiefwasserbereich des Meeres*, 1977, ISBN 3-921694-39-6
- 40 Ruppert, Jürgen: *Über den Axialwirbelkammerverstärker für den Einsatz im Wasserbau*, 1977, ISBN 3-921694-40-X
- 41 Hutarew, Andreas: *Beitrag zur Beeinflußbarkeit des Sauerstoffgehalts in Fließgewässern an Abstürzen und Wehren*, 1977, ISBN 3-921694-41-8, vergriffen
- 42 Miller, Christoph: *Ein Beitrag zur Bestimmung der schwingungserregenden Kräfte an unterströmten Wehren*, 1977, ISBN 3-921694-42-6
- 43 Schwarz, Wolfgang: *Druckstoßberechnung unter Berücksichtigung der Radial- und Längsverschiebungen der Rohrwandung*, 1978, ISBN 3-921694-43-4
- 44 Kinzelbach, Wolfgang: *Numerische Untersuchungen über den optimalen Einsatz variabler Kühlsysteme einer Kraftwerkskette am Beispiel Oberrhein*, 1978, ISBN 3-921694-44-2
- 45 Barczewski, Baldur: *Neue Meßmethoden für Wasser-Luftgemische und deren Anwendung auf zweiphasige Auftriebsstrahlen*, 1979, ISBN 3-921694-45-0

- 46 Neumayer, Hans: *Untersuchung der Strömungsvorgänge in radialen Wirbelkammerverstärkern*, 1979, ISBN 3-921694-46-9
- 47 Elalfy, Youssef-Elhassan: *Untersuchung der Strömungsvorgänge in Wirbelkammerdioden und -drosseln*, 1979, ISBN 3-921694-47-7
- 48 Brombach, Hansjörg: *Automatisierung der Bewirtschaftung von Wasserspeichern*, 1981, ISBN 3-921694-48-5
- 49 Geldner, Peter: *Deterministische und stochastische Methoden zur Bestimmung der Selbstdichtung von Gewässern*, 1981, ISBN 3-921694-49-3, vergriffen
- 50 Mehlhorn, Hans: *Temperaturveränderungen im Grundwasser durch Brauchwassereinleitungen*, 1982, ISBN 3-921694-50-7, vergriffen
- 51 Hafner, Edzard: *Rohrleitungen und Behälter im Meer*, 1983, ISBN 3-921694-51-5
- 52 Rinnert, Bernd: *Hydrodynamische Dispersion in porösen Medien: Einfluß von Dichteunterschieden auf die Vertikalvermischung in horizontaler Strömung*, 1983, ISBN 3-921694-52-3, vergriffen
- 53 Lindner, Wulf: *Steuerung von Grundwasserentnahmen unter Einhaltung ökologischer Kriterien*, 1983, ISBN 3-921694-53-1, vergriffen
- 54 Herr, Michael; Herzer, Jörg; Kinzelbach, Wolfgang; Kobus, Helmut; Rinnert, Bernd: *Methoden zur rechnerischen Erfassung und hydraulischen Sanierung von Grundwasserkontaminationen*, 1983, ISBN 3-921694-54-X
- 55 Schmitt, Paul: *Wege zur Automatisierung der Niederschlagsermittlung*, 1984, ISBN 3-921694-55-8, vergriffen
- 56 Müller, Peter: *Transport und selektive Sedimentation von Schwebstoffen bei gestautem Abfluß*, 1985, ISBN 3-921694-56-6
- 57 El-Qawasmeh, Fuad: *Möglichkeiten und Grenzen der Tropfbewässerung unter besonderer Berücksichtigung der Verstopfungsanfälligkeit der Tropfelemente*, 1985, ISBN 3-921694-57-4, vergriffen
- 58 Kirchenbaur, Klaus: *Mikroprozessorgesteuerte Erfassung instationärer Druckfelder am Beispiel seegangbelasteter Baukörper*, 1985, ISBN 3-921694-58-2
- 59 Kobus, Helmut (Hrsg.): *Modellierung des großräumigen Wärme- und Schadstofftransports im Grundwasser*, Tätigkeitsbericht 1984/85 (DFG-Forschergruppe an den Universitäten Hohenheim, Karlsruhe und Stuttgart), 1985, ISBN 3-921694-59-0, vergriffen
- 60 Spitz, Karlheinz: *Dispersion in porösen Medien: Einfluß von Inhomogenitäten und Dichteunterschieden*, 1985, ISBN 3-921694-60-4, vergriffen
- 61 Kobus, Helmut: *An Introduction to Air-Water Flows in Hydraulics*, 1985, ISBN 3-921694-61-2



- 62 Kaleris, Vassilios: *Erfassung des Austausches von Oberflächen- und Grundwasser in horizontalebene Grundwassermodellen*, 1986, ISBN 3-921694-62-0
- 63 Herr, Michael: *Grundlagen der hydraulischen Sanierung verunreinigter Porengrundwasserleiter*, 1987, ISBN 3-921694-63-9
- 64 Marx, Walter: *Berechnung von Temperatur und Spannung in Massenbeton infolge Hydratation*, 1987, ISBN 3-921694-64-7
- 65 Koschitzky, Hans-Peter: *Dimensionierungskonzept für Sohlbelüfter in Schußbrinnen zur Vermeidung von Kavitationsschäden*, 1987, ISBN 3-921694-65-5
- 66 Kobus, Helmut (Hrsg.): *Modellierung des großräumigen Wärme- und Schadstofftransports im Grundwasser*, Tätigkeitsbericht 1986/87 (DFG-Forschergruppe an den Universitäten Hohenheim, Karlsruhe und Stuttgart) 1987, ISBN 3-921694-66-3
- 67 Söll, Thomas: *Berechnungsverfahren zur Abschätzung anthropogener Temperaturanomalien im Grundwasser*, 1988, ISBN 3-921694-67-1
- 68 Dittrich, Andreas; Westrich, Bernd: *Bodenseeufererosion, Bestandsaufnahme und Bewertung*, 1988, ISBN 3-921694-68-X, vergriffen
- 69 Huwe, Bernd; van der Ploeg, Rienk R.: *Modelle zur Simulation des Stickstoffhaushaltes von Standorten mit unterschiedlicher landwirtschaftlicher Nutzung*, 1988, ISBN 3-921694-69-8, vergriffen
- 70 Stephan, Karl: *Integration elliptischer Funktionen*, 1988, ISBN 3-921694-70-1
- 71 Kobus, Helmut; Zilliox, Lothaire (Hrsg.): *Nitratbelastung des Grundwassers, Auswirkungen der Landwirtschaft auf die Grundwasser- und Rohwasserbeschaffenheit und Maßnahmen zum Schutz des Grundwassers*. Vorträge des deutsch-französischen Kolloquiums am 6. Oktober 1988, Universitäten Stuttgart und Louis Pasteur Strasbourg (Vorträge in deutsch oder französisch, Kurzfassungen zweisprachig), 1988, ISBN 3-921694-71-X
- 72 Soyeaux, Renald: *Unterströmung von Stauanlagen auf klüftigem Untergrund unter Berücksichtigung laminarer und turbulenter Fließzustände*, 1991, ISBN 3-921694-72-8
- 73 Kohane, Roberto: *Berechnungsmethoden für Hochwasserabfluß in Fließgewässern mit überströmten Vorländern*, 1991, ISBN 3-921694-73-6
- 74 Hassinger, Reinhard: *Beitrag zur Hydraulik und Bemessung von Blocksteinrampen in flexibler Bauweise*, 1991, ISBN 3-921694-74-4, vergriffen
- 75 Schäfer, Gerhard: *Einfluß von Schichtenstrukturen und lokalen Einlagerungen auf die Längsdispersion in Porengrundwasserleitern*, 1991, ISBN 3-921694-75-2
- 76 Giesecke, Jürgen: *Vorträge, Wasserwirtschaft in stark besiedelten Regionen; Umweltforschung mit Schwerpunkt Wasserwirtschaft*, 1991, ISBN 3-921694-76-0

- 77 Huwe, Bernd: *Deterministische und stochastische Ansätze zur Modellierung des Stickstoffhaushalts landwirtschaftlich genutzter Flächen auf unterschiedlichem Skalenniveau*, 1992, ISBN 3-921694-77-9, vergriffen
- 78 Rommel, Michael: *Verwendung von Klufdaten zur realitätsnahen Generierung von Klufnetzen mit anschließender laminar-turbulenter Strömungsberechnung*, 1993, ISBN 3-92 1694-78-7
- 79 Marschall, Paul: *Die Ermittlung lokaler Stofffrachten im Grundwasser mit Hilfe von Einbohrloch-Meßverfahren*, 1993, ISBN 3-921694-79-5, vergriffen
- 80 Ptak, Thomas: *Stofftransport in heterogenen Porenaquiferen: Felduntersuchungen und stochastische Modellierung*, 1993, ISBN 3-921694-80-9, vergriffen
- 81 Haakh, Frieder: *Transientes Strömungsverhalten in Wirbelkammern*, 1993, ISBN 3-921694-81-7
- 82 Kobus, Helmut; Cirpka, Olaf; Barczewski, Baldur; Koschitzky, Hans-Peter: *Versucheinrichtung zur Grundwasser und Altlastensanierung VEGAS, Konzeption und Programmrahmen*, 1993, ISBN 3-921694-82-5
- 83 Zang, Weidong: *Optimaler Echtzeit-Betrieb eines Speichers mit aktueller Abflußregenerierung*, 1994, ISBN 3-921694-83-3, vergriffen
- 84 Franke, Hans-Jörg: *Stochastische Modellierung eines flächenhaften Stoffeintrages und Transports in Grundwasser am Beispiel der Pflanzenschutzmittelproblematik*, 1995, ISBN 3-921694-84-1
- 85 Lang, Ulrich: *Simulation regionaler Strömungs- und Transportvorgänge in Karst-aquiferen mit Hilfe des Doppelkontinuum-Ansatzes: Methodenentwicklung und Parameteridentifikation*, 1995, ISBN 3-921694-85-X, vergriffen
- 86 Helmig, Rainer: *Einführung in die Numerischen Methoden der Hydromechanik*, 1996, ISBN 3-921694-86-8, vergriffen
- 87 Cirpka, Olaf: *CONTRACT: A Numerical Tool for Contaminant Transport and Chemical Transformations - Theory and Program Documentation -*, 1996, ISBN 3-921694-87-6
- 88 Haberlandt, Uwe: *Stochastische Synthese und Regionalisierung des Niederschlages für Schmutzfrachtberechnungen*, 1996, ISBN 3-921694-88-4
- 89 Croisé, Jean: *Extraktion von flüchtigen Chemikalien aus natürlichen Lockergesteinen mittels erzwungener Luftströmung*, 1996, ISBN 3-921694-89-2, vergriffen
- 90 Jorde, Klaus: *Ökologisch begründete, dynamische Mindestwasserregelungen bei Ausleitungskraftwerken*, 1997, ISBN 3-921694-90-6, vergriffen
- 91 Helmig, Rainer: *Gekoppelte Strömungs- und Transportprozesse im Untergrund - Ein Beitrag zur Hydrosystemmodellierung-*, 1998, ISBN 3-921694-91-4

- 
- 92 Emmert, Martin: *Numerische Modellierung nichtisothermer Gas-Wasser Systeme in porösen Medien*, 1997, ISBN 3-921694-92-2
- 93 Kern, Ulrich: *Transport von Schweb- und Schadstoffen in staugeregelten Fließgewässern am Beispiel des Neckars*, 1997, ISBN 3-921694-93-0, vergriffen
- 94 Förster, Georg: *Druckstoßdämpfung durch große Luftblasen in Hochpunkten von Rohrleitungen* 1997, ISBN 3-921694-94-9
- 95 Cirpka, Olaf: *Numerische Methoden zur Simulation des reaktiven Mehrkomponententransports im Grundwasser*, 1997, ISBN 3-921694-95-7, vergriffen
- 96 Färber, Arne: *Wärmetransport in der ungesättigten Bodenzone: Entwicklung einer thermischen In-situ-Sanierungstechnologie*, 1997, ISBN 3-921694-96-5
- 97 Betz, Christoph: *Wasserdampfdestillation von Schadstoffen im porösen Medium: Entwicklung einer thermischen In-situ-Sanierungstechnologie*, 1998, ISBN 3-921694-97-3
- 98 Xu, Yichun: *Numerical Modeling of Suspended Sediment Transport in Rivers*, 1998, ISBN 3-921694-98-1, vergriffen
- 99 Wüst, Wolfgang: *Geochemische Untersuchungen zur Sanierung CKW-kontaminierter Aquifere mit Fe(0)-Reaktionswänden*, 2000, ISBN 3-933761-02-2
- 100 Sheta, Hussam: *Simulation von Mehrphasenvorgängen in porösen Medien unter Einbeziehung von Hysterese-Effekten*, 2000, ISBN 3-933761-03-4
- 101 Ayros, Edwin: *Regionalisierung extremer Abflüsse auf der Grundlage statistischer Verfahren*, 2000, ISBN 3-933761-04-2, vergriffen
- 102 Huber, Ralf: *Compositional Multiphase Flow and Transport in Heterogeneous Porous Media*, 2000, ISBN 3-933761-05-0
- 103 Braun, Christopherus: *Ein Upscaling-Verfahren für Mehrphasenströmungen in porösen Medien*, 2000, ISBN 3-933761-06-9
- 104 Hofmann, Bernd: *Entwicklung eines rechnergestützten Managementsystems zur Beurteilung von Grundwasserschadensfällen*, 2000, ISBN 3-933761-07-7
- 105 Class, Holger: *Theorie und numerische Modellierung nichtisothermer Mehrphasenprozesse in NAPL-kontaminierten porösen Medien*, 2001, ISBN 3-933761-08-5
- 106 Schmidt, Reinhard: *Wasserdampf- und Heißluftinjektion zur thermischen Sanierung kontaminierter Standorte*, 2001, ISBN 3-933761-09-3
- 107 Josef, Reinhold: *Schadstoffextraktion mit hydraulischen Sanierungsverfahren unter Anwendung von grenzflächenaktiven Stoffen*, 2001, ISBN 3-933761-10-7

- 108 Schneider, Matthias: *Habitat- und Abflussmodellierung für Fließgewässer mit unscharfen Berechnungsansätzen*, 2001, ISBN 3-933761-11-5
- 109 Rathgeb, Andreas: *Hydrodynamische Bemessungsgrundlagen für Lockerdeckwerke an überströmbaren Erddämmen*, 2001, ISBN 3-933761-12-3
- 110 Lang, Stefan: *Parallele numerische Simulation instationärer Probleme mit adaptiven Methoden auf unstrukturierten Gittern*, 2001, ISBN 3-933761-13-1
- 111 Appt, Jochen; Stumpp Simone: *Die Bodensee-Messkampagne 2001, IWS/CWR Lake Constance Measurement Program 2001*, 2002, ISBN 3-933761-14-X
- 112 Heimerl, Stephan: *Systematische Beurteilung von Wasserkraftprojekten*, 2002, ISBN 3-933761-15-8
- 113 Iqbal, Amin: *On the Management and Salinity Control of Drip Irrigation*, 2002, ISBN 3-933761-16-6
- 114 Silberhorn-Hemminger, Annette: *Modellierung von Kluftaquifersystemen: Geostatistische Analyse und deterministisch-stochastische Kluftgenerierung*, 2002, ISBN 3-933761-17-4
- 115 Winkler, Angela: *Prozesse des Wärme- und Stofftransports bei der In-situ-Sanierung mit festen Wärmequellen*, 2003, ISBN 3-933761-18-2
- 116 Marx, Walter: *Wasserkraft, Bewässerung, Umwelt - Planungs- und Bewertungsschwerpunkte der Wasserbewirtschaftung*, 2003, ISBN 3-933761-19-0
- 117 Hinkelmann, Reinhard: *Efficient Numerical Methods and Information-Processing Techniques in Environment Water*, 2003, ISBN 3-933761-20-4
- 118 Samaniego-Eguiguren, Luis Eduardo: *Hydrological Consequences of Land Use / Land Cover and Climatic Changes in Mesoscale Catchments*, 2003, ISBN 3-933761-21-2
- 119 Neunhäuserer, Lina: *Diskretisierungsansätze zur Modellierung von Strömungs- und Transportprozessen in geklüftet-porösen Medien*, 2003, ISBN 3-933761-22-0
- 120 Paul, Maren: *Simulation of Two-Phase Flow in Heterogeneous Porous Media with Adaptive Methods*, 2003, ISBN 3-933761-23-9
- 121 Ehret, Uwe: *Rainfall and Flood Nowcasting in Small Catchments using Weather Radar*, 2003, ISBN 3-933761-24-7
- 122 Haag, Ingo: *Der Sauerstoffhaushalt staugeregelter Flüsse am Beispiel des Neckars - Analysen, Experimente, Simulationen -*, 2003, ISBN 3-933761-25-5
- 123 Appt, Jochen: *Analysis of Basin-Scale Internal Waves in Upper Lake Constance*, 2003, ISBN 3-933761-26-3

- 124 Hrsg.: Schrenk, Volker; Batereau, Katrin; Barczewski, Baldur; Weber, Karolin und Koschitzky, Hans-Peter: *Symposium Ressource Fläche und VEGAS - Statuskolloquium 2003, 30. September und 1. Oktober 2003*, 2003, ISBN 3-933761-27-1
- 125 Omar Khalil Ouda: *Optimisation of Agricultural Water Use: A Decision Support System for the Gaza Strip*, 2003, ISBN 3-933761-28-0
- 126 Batereau, Katrin: *Sensorbasierte Bodenluftmessung zur Vor-Ort-Erkundung von Schadensherden im Untergrund*, 2004, ISBN 3-933761-29-8
- 127 Witt, Oliver: *Erosionsstabilität von Gewässersedimenten mit Auswirkung auf den Stofftransport bei Hochwasser am Beispiel ausgewählter Stauhaltungen des Oberrheins*, 2004, ISBN 3-933761-30-1
- 128 Jakobs, Hartmut: *Simulation nicht-isothermer Gas-Wasser-Prozesse in komplexen Kluft-Matrix-Systemen*, 2004, ISBN 3-933761-31-X
- 129 Li, Chen-Chien: *Deterministisch-stochastisches Berechnungskonzept zur Beurteilung der Auswirkungen erosiver Hochwasserereignisse in Flusstauhaltungen*, 2004, ISBN 3-933761-32-8
- 130 Reichenberger, Volker; Helmig, Rainer; Jakobs, Hartmut; Bastian, Peter; Niessner, Jennifer: *Complex Gas-Water Processes in Discrete Fracture-Matrix Systems: Upscaling, Mass-Conservative Discretization and Efficient Multilevel Solution*, 2004, ISBN 3-933761-33-6
- 131 Hrsg.: Barczewski, Baldur; Koschitzky, Hans-Peter; Weber, Karolin; Wege, Ralf: *VEGAS - Statuskolloquium 2004*, Tagungsband zur Veranstaltung am 05. Oktober 2004 an der Universität Stuttgart, Campus Stuttgart-Vaihingen, 2004, ISBN 3-933761-34-4
- 132 Asie, Kemal Jabir: *Finite Volume Models for Multiphase Multicomponent Flow through Porous Media*. 2005, ISBN 3-933761-35-2
- 133 Jacoub, George: *Development of a 2-D Numerical Module for Particulate Contaminant Transport in Flood Retention Reservoirs and Impounded Rivers*, 2004, ISBN 3-933761-36-0
- 134 Nowak, Wolfgang: *Geostatistical Methods for the Identification of Flow and Transport Parameters in the Subsurface*, 2005, ISBN 3-933761-37-9
- 135 Süß, Mia: *Analysis of the influence of structures and boundaries on flow and transport processes in fractured porous media*, 2005, ISBN 3-933761-38-7
- 136 Jose, Surabhin Chackiath: *Experimental Investigations on Longitudinal Dispersive Mixing in Heterogeneous Aquifers*, 2005, ISBN: 3-933761-39-5
- 137 Filiz, Fulya: *Linking Large-Scale Meteorological Conditions to Floods in Mesoscale Catchments*, 2005, ISBN 3-933761-40-9

- 138 Qin, Minghao: *Wirklichkeitsnahe und recheneffiziente Ermittlung von Temperatur und Spannungen bei großen RCC-Staumauern*, 2005, ISBN 3-933761-41-7
- 139 Kobayashi, Kenichiro: *Optimization Methods for Multiphase Systems in the Sub-surface - Application to Methane Migration in Coal Mining Areas*, 2005, ISBN 3-933761-42-5
- 140 Rahman, Md. Arifur: *Experimental Investigations on Transverse Dispersive Mixing in Heterogeneous Porous Media*, 2005, ISBN 3-933761-43-3
- 141 Schrenk, Volker: *Ökobilanzen zur Bewertung von Altlastensanierungsmaßnahmen*, 2005, ISBN 3-933761-44-1
- 142 Hundecha, Hirpa Yesheatesfa: *Regionalization of Parameters of a Conceptual Rainfall-Runoff Model*, 2005, ISBN: 3-933761-45-X
- 143 Wege, Ralf: *Untersuchungs- und Überwachungsmethoden für die Beurteilung natürlicher Selbstreinigungsprozesse im Grundwasser*, 2005, ISBN 3-933761-46-8
- 144 Breiting, Thomas: *Techniken und Methoden der Hydroinformatik - Modellierung von komplexen Hydrosystemen im Untergrund*, 2006, 3-933761-47-6
- 145 Hrsg.: Braun, Jürgen; Koschitzky, Hans-Peter; Müller, Martin: *Ressource Untergrund: 10 Jahre VEGAS: Forschung und Technologieentwicklung zum Schutz von Grundwasser und Boden*, Tagungsband zur Veranstaltung am 28. und 29. September 2005 an der Universität Stuttgart, Campus Stuttgart-Vaihingen, 2005, ISBN 3-933761-48-4
- 146 Rojanschi, Vlad: *Abflusskonzentration in mesoskaligen Einzugsgebieten unter Berücksichtigung des Sickerraumes*, 2006, ISBN 3-933761-49-2
- 147 Winkler, Nina Simone: *Optimierung der Steuerung von Hochwasserrückhaltebecken-systemen*, 2006, ISBN 3-933761-50-6
- 148 Wolf, Jens: *Räumlich differenzierte Modellierung der Grundwasserströmung alluvialer Aquifere für mesoskalige Einzugsgebiete*, 2006, ISBN: 3-933761-51-4
- 149 Kohler, Beate: *Externe Effekte der Laufwasserkraftnutzung*, 2006, ISBN 3-933761-52-2
- 150 Hrsg.: Braun, Jürgen; Koschitzky, Hans-Peter; Stuhmann, Matthias: *VEGAS-Statuskolloquium 2006*, Tagungsband zur Veranstaltung am 28. September 2006 an der Universität Stuttgart, Campus Stuttgart-Vaihingen, 2006, ISBN 3-933761-53-0
- 151 Niessner, Jennifer: *Multi-Scale Modeling of Multi-Phase - Multi-Component Processes in Heterogeneous Porous Media*, 2006, ISBN 3-933761-54-9
- 152 Fischer, Markus: *Beanspruchung eingeeerdeter Rohrleitungen infolge Austrocknung bindiger Böden*, 2006, ISBN 3-933761-55-7

- 153 Schneck, Alexander: *Optimierung der Grundwasserbewirtschaftung unter Berücksichtigung der Belange der Wasserversorgung, der Landwirtschaft und des Naturschutzes*, 2006, ISBN 3-933761-56-5
- 154 Das, Tapash: *The Impact of Spatial Variability of Precipitation on the Predictive Uncertainty of Hydrological Models*, 2006, ISBN 3-933761-57-3
- 155 Bielinski, Andreas: *Numerical Simulation of CO<sub>2</sub> sequestration in geological formations*, 2007, ISBN 3-933761-58-1
- 156 Mödinger, Jens: *Entwicklung eines Bewertungs- und Entscheidungsunterstützungssystems für eine nachhaltige regionale Grundwasserbewirtschaftung*, 2006, ISBN 3-933761-60-3
- 157 Manthey, Sabine: *Two-phase flow processes with dynamic effects in porous media - parameter estimation and simulation*, 2007, ISBN 3-933761-61-1
- 158 Pozos Estrada, Oscar: *Investigation on the Effects of Entrained Air in Pipelines*, 2007, ISBN 3-933761-62-X
- 159 Ochs, Steffen Oliver: *Steam injection into saturated porous media – process analysis including experimental and numerical investigations*, 2007, ISBN 3-933761-63-8
- 160 Marx, Andreas: *Einsatz gekoppelter Modelle und Wetterradar zur Abschätzung von Niederschlagsintensitäten und zur Abflussvorhersage*, 2007, ISBN 3-933761-64-6
- 161 Hartmann, Gabriele Maria: *Investigation of Evapotranspiration Concepts in Hydrological Modelling for Climate Change Impact Assessment*, 2007, ISBN 3-933761-65-4
- 162 Kebede Gurmessa, Tesfaye: *Numerical Investigation on Flow and Transport Characteristics to Improve Long-Term Simulation of Reservoir Sedimentation*, 2007, ISBN 3-933761-66-2
- 163 Trifković, Aleksandar: *Multi-objective and Risk-based Modelling Methodology for Planning, Design and Operation of Water Supply Systems*, 2007, ISBN 3-933761-67-0
- 164 Götzing, Jens: *Distributed Conceptual Hydrological Modelling - Simulation of Climate, Land Use Change Impact and Uncertainty Analysis*, 2007, ISBN 3-933761-68-9
- 165 Hrsg.: Braun, Jürgen; Koschitzky, Hans-Peter; Stuhmann, Matthias: *VEGAS – Kolloquium 2007*, Tagungsband zur Veranstaltung am 26. September 2007 an der Universität Stuttgart, Campus Stuttgart-Vaihingen, 2007, ISBN 3-933761-69-7
- 166 Freeman, Beau: *Modernization Criteria Assessment for Water Resources Planning; Klamath Irrigation Project, U.S.*, 2008, ISBN 3-933761-70-0

- 167 Dreher, Thomas: *Selektive Sedimentation von Feinstschwebstoffen in Wechselwirkung mit wandnahen turbulenten Strömungsbedingungen*, 2008, ISBN 3-933761-71-9
- 168 Yang, Wei: *Discrete-Continuous Downscaling Model for Generating Daily Precipitation Time Series*, 2008, ISBN 3-933761-72-7
- 169 Kopecki, Ianina: *Calculational Approach to FST-Hemispheres for Multiparametrical Benthos Habitat Modelling*, 2008, ISBN 3-933761-73-5
- 170 Brommundt, Jürgen: *Stochastische Generierung räumlich zusammenhängender Niederschlagszeitreihen*, 2008, ISBN 3-933761-74-3
- 171 Papafotiou, Alexandros: *Numerical Investigations of the Role of Hysteresis in Heterogeneous Two-Phase Flow Systems*, 2008, ISBN 3-933761-75-1

Die Mitteilungshefte ab dem Jahr 2005 stehen als pdf-Datei über die Homepage des Instituts: [www.iws.uni-stuttgart.de](http://www.iws.uni-stuttgart.de) zur Verfügung.